# Ground moving target tracking with space-time adaptive radar

DISSERTATION
zur Erlangung des Grades eines Doktors
der Ingenieurwissenschaften

vorgelegt von
Dipl.-Ing. Robert Kohlleppel

eingereicht bei der Naturwissenschaftlich-Technischen Fakultät
der Universität Siegen
Siegen 2014

| | |
|---|---|
| Erster Gutachter: | Prof. Dr.-Ing. Joachim Ender |
| Zweiter Gutachter: | Prof. Dr.-Ing. Otmar Loffeld |
| Tag der mündlichen Prüfung: | 23. März 2015 |

## Acknowledgements

In the process of writing a PHD thesis there are many challenging times. At these moments I received help from colleagues, friends and my family. I would like to thank:

My supervisor Prof. Dr. Ender for sharing the wealth of his knowledge on radar with me, for reserving time for frequent discussions and for motivating me with his enthusiasm towards radar research.

My referee Prof. Dr. Loffeld for examining the thesis, for the welcoming reception at his institute at the university of Siegen and for providing a platform for the presentation of ideas and discussion.

My head of department Dr. Brenner for creating good conditions to enable me to write this PHD thesis and his effort to provide the best conditions to the members of his department.

Dr. Koch for introducing me to target tracking and his enthusiasm towards this topic.

Dr. Nickel and Dr. Gierull for giving the important advise to acquire experimental data as early as possible.

My team leader Dr. Delphine Cerutti-Maori for giving valuable advice concerning the focus of the thesis, for allowing time for me to write this thesis, for her support and advice as I was becoming a father.

Dr. Wolfram Bürger for always helping whenever I asked.

My colleagues at Fraunhofer FHR for building the experimental radar PAMIR and for conducting the elaborate measurement campaigns. Without the data acquired during these campaigns, this thesis would not have been possible.

My colleagues both at Fraunhofer FHR and FKIE who participated as drivers, assistants and for radio communication in the measurement campaigns.

My colleague Dr. Ludger Prünte for many fruitful discussion that often let to greater insight or exposed the core of a problem.

My colleagues at the institute, in particular Dr. Diego Cristallini, Mario Witter and Dr. Michael Mertens for being friends and many discussions not only on research matters.

My friends Dennis, Tilman, Matthias and Tillmann.

My parents, my brother and sister, Zhao Jun.

# Zusammenfassung

Bodenzielverfolgung mit luftgestütztem Radar liefert das Lagebild von Fahrzeugbewegungen innerhalb des beobachteten Gebiets. Fahrzeuge werden durch die Anwendung von Raum-Zeit adaptiver Signalverarbeitung (STAP) entdeckt. Die Entdeckungen werden dann von einem Zielverfolgungsalgorithmus zu Zielspuren verarbeitet.

In der Literatur werden Radarsignalverarbeitung und Zielverfolgung als zwei getrennte Forschungsfelder behandelt und die Bodenzielverfolgung wird nicht anhand von Realdaten validiert. Das erste Ziel dieser Arbeit ist, eine engere Verbindung zwischen beiden Feldern herzustellen. Das zweite Ziel ist zu zeigen, dass die Qualität der Zielverfolgung durch das Verwenden zusätzlicher, durch die Radarsignalverarbeitung gewonnene Information verbessert werden kann. Das dritte Ziel ist, die Funktionalität der Zielverfolgung und die Verbesserung der Leistung durch experimentelle Realdaten zu belegen.

Somit stellt diese Arbeit eine Gesamtbehandlung der Bodenzielverfolgung von den Radar-Rohdaten bis zu Zielspuren dar. Es wird ein vollständiger, auf dem Gaussian Mixture Probability Hypothesis Density Filter basierender Referenzalgorithmus für die Bodenzielverfolgung entwickelt. Insbesondere werden Jacobimatrizen der Beobachtungsfunktion hergeleitet. Sie werden in der Arbeit so dargestellt, dass sie direkt in einer Programmiersprache implementiert werden können.

Im Zuge dieser Arbeit wurde ein Zielverfolgungs-Experiment mit dem Experimentalsystem PAMIR des Fraunhofer FHR durchgeführt. In dem Experiment wurden neben einer Vielzahl von Gelegenheitszielen zwei mit GPS-Geräten ausgerüstete Fahrzeuge von dem Radar beobachtet. Auf Basis dieses Experiments und des Referenzalgorithmus werden Zielverfolgungsergebnisse vorgestellt.

Darüber hinaus erweitert diese Arbeit den Referenzalgorithmus um einen Parameter, der die Varianz der Richtungsschätzung des Zielsignals charakterisiert. Dieser Parameter wird adaptiv anhand der geschätzten Signalstärke und der Stärke störender Bodenrückstreuungen festgelegt. Der wesentliche Beitrag dieser Arbeit in Bezug auf diese Erweiterung ist eine gründliche experimentelle Validierung. Erstens zeigt der Vergleich von GPS- und Radar-basierten Richtungsschätzungen, dass dieser Parameter die Verteilung des Messfehlers exzellent beschreibt. Zweitens werden Zielverfolgungsergebnisse mit den GPS-Spuren verglichen. Es zeigt sich, dass der erweiterte Algorithmus sowohl in Bezug auf die Spurgenauigkeit als auch in Bezug auf die Spurkontinuität die Zielverfolgung verbessert.

## Abstract

Ground moving target tracking by airborne radar provides situational awareness of vehicle movements in the supervised region. Vehicles are detected by applying space time adaptive processing to the received multi channel radar data. The detections are then fed to a tracking algorithm that processes them to tracks. In literature, radar signal processing and ground target tracking are treated as two separate topics and results are not validated by experimental data. The first objective of this thesis is to provide a closer link between these fields. The second objective is to show that tracking performance can be improved by providing additional data from the radar signal processing to the tracking step. The third objective is to validate the algorithm and the performance improvement using experimental data.

As a result this thesis presents a unified treatment of ground moving target tracking from radar raw data to established tracks. A complete reference algorithm for ground moving target tracking based on the Gaussian mixture probability hypothesis density filter is presented. In particular, Jacobians of the observation process are derived. They are presented in such a form that immediate implementation in a programming language is possible.

In the course of this thesis a measurement campaign with the experimental radar PAMIR of Fraunhofer FHR was conducted. The experiment included two GPS equipped reference vehicles and a multitude of targets of opportunity. Tracking results obtained with this experimental data and the reference tracking algorithm of this thesis are shown.

The thesis also enhances the reference target tracking algorithm by a parameter that characterizes the variance of the direction of arrival measurement of the target signal. This parameter is determined adaptively depending on the estimated signal strength and the clutter background. The major contribution with regard to this enhancement is a thorough experimental validation: Firstly, a comparison between GPS based measurements and radar based measurements of the direction of arrival shows that this variance captures the distribution of measurement errors excellently. Secondly, tracking results are compared to the GPS tracks of the ground truth vehicles. It is found that the enhanced algorithm yields superior track quality with respect to both track accuracy and track continuity.

# Contents

# 1. Introduction

Knowledge of the landscape, its forests, villages and roads combined with information about movement of vehicles yields *situational awareness* of a region. Obtaining this awareness is crucial in many circumstances, both in civilian and military context. In the civilian context, situational awareness is needed in particular in the case of natural disaster, e.g. an earthquake or flooding. Initially, supervisors of relief efforts will not know in which direction survivors are heading, which roads are still usable or where locally organized aid convoys are progressing.

Situational awareness may be acquired by several means. Maps provide information about the stationary features of a landscape and historically reports by personnel on the ground have provided information about the movement of persons and vehicles. Especially to access the dynamic development of the situation, knowledge of *vehicle movements* is of particular importance.

Within the last decades, technical equipment for generating situational awareness and especially for obtaining information about vehicle movements has been developed. Different types of sensors are available, e.g. optical sensors, infrared sensors and radar. Among these sensors, radar is an excellent tool both for mapping a region with an airborne radar and for detecting moving objects on the ground. Radar systems of commonly used frequencies are not impeded by clouds, fog and rain and as active systems can operate at night.

The task of locating moving objects on the earth's surface is denoted as ground moving target indication (GMTI). As often in history, military requirements have been the original driver for developing radar based GMTI systems. Such systems usually comprise an airborne platform – i.e. a converted passenger plane in the case of Joint STARS of the United States – equipped with radar systems. The radar antennas transmit electromagnetic waves to the ground where they are reflected and backscattered. Part of the emitted energy is reflected to the radar antenna where it is recorded. The data can then be digitally processed to gain information about the structure of and movements on the ground.

Ground moving target indication with radar is particularly difficult for slowly moving vehicles whose returns must compete with the overwhelmingly large reflections by the stationary ground, *clutter*. This difficulty has given rise to Space Time Adaptive Processing (STAP) that requires radar systems that are equipped with multiple receiving channels. In most implementations of STAP, the radar processor attempts to learn the characteristics of the ground returns from radar data that are free of moving target signals. It is then able to construct a filter that enhances the detectability of ground moving targets.

For every detection target parameters are estimated. These include the range to the target, its

radial velocity with respect to the radar antenna and the direction of arrival of the signal. Linear antenna arrays enable the estimation of the azimuth angle with which the target signal impinges on the antenna. Combined with a digital elevation model of the earth's surface, the range and azimuth angle estimates enable the geolocation of a detection.

As a result of the radar signal processing, the location of detections may be displayed on a map of the area of interest. While this already constitutes an improvement of situational awareness, it is truly desired to display the paths of movements of the ground vehicles. To this end, tracking algorithms that process the large number of detections to separate tracks are employed. Historically, tracking algorithms have first been applied to the tracking of airborne targets. In comparison, tracking of ground moving targets is more challenging since ground targets might perform more abrupt maneuvers, may be very closely spaced, can be masked by ground clutter and exhibit a small radar cross section. The most challenging aspect in target tracking is the fact that the origin of detections is unclear, i.e. there is no prior association between existing tracks and detections.

Target detections with associated parameter estimates form the link between the radar signal processing and target tracking. In general the target parameter estimates are erroneous. Tracking algorithms take this into account by modeling the measurements as realizations of random variables. The variance of the random variable qualifies of how the tracking algorithm perceives the measurements: A small variance value signifies that the measurement error is small. A large variance implies that the measurement errors may be large.

In standard tracking algorithms a single value for the measurement variance is set in the configuration of the tracking algorithm. It is not adapted during the run time of the algorithm. However, in practice the configured variance may fail to capture the true behavior of the measurement errors. For example, the measurements of different targets may be of varying accuracy. Furthermore, changes of the true measurement error variance over time are possible.

In radar signal processing the estimation accuracy depends on the signal to noise and clutter ratio (SCNR) of the target signal [72, Sec. 18.10]. The target signal power itself is a function of several factors: The range between the target and the antenna, its location within the antenna beam and its radar cross section. The radar cross section can fluctuate extremely rapidly due to its strong dependence on the incidence angle [58]. For small values of the radial velocity, the target signal is very similar to returns by the stationary ground, i.e. the clutter signal. This reduces the signal to noise and clutter ratio. Thus, in ground moving target tracking there is a strong variability of the target SCNR due to fluctuations of the target RCS and due to target parameter dependent effects. This in turn causes strong fluctuations of the measurement error variance between different detections. This effect has lead to the proposal of ground moving target tracking algorithms that adapt the modeled measurement error variance for each detection ([35] and [38]). The adapted measurement error variance is obtained by a theoretical model for monopulse estimates [54]. In these works it has been shown with Monte Carlo simulations that the tracking error decreases due to the proposed detection dependent adaptation. However, these

results have not yet been validated with experimental data: No analysis whether the adaptively modeled estimation error variance does indeed conform to the distribution of errors with real radar data has been published. Furthermore, no results with real radar data that prove an improved tracking performance due to the adaptively modeled variance have been published.

This thesis provides the experimental validation for the case of modeling the direction of arrival (DOA) measurement error. The model for the DOA measurement error variance is based on inserting estimated parameters into the expression for the Cramer-Rao lower bound (CRB). In comparison to evaluating the Monopulse variance as in [54] this approach can be implemented much more conveniently as it does not require a numerical integration. It is shown with experimental radar data that the introduced adaptive modeling of the measurement error variance does indeed capture the empirical distribution of the measurement error. Furthermore, it is shown with experimental data that the inclusion of this model in a tracking algorithm does significantly improve the tracking performance.

In order to obtain these results several intermediate tasks had to be completed: The author of this thesis designed and organized ground moving target tracking experiments with the experimental system PAMIR of Fraunhofer FHR. Data that was acquired during these experiments was used in the experimental validation. A ground moving target indication algorithm and a tracking algorithm were implemented. The tracking algorithm without signal dependent adaptation of the measurements serves as a reference algorithm to which tracking with detection adaptive measurement variance is compared. For the error calculation Jacobian matrices of the functions that determine the geolocation of a detection based on the radar measurements were determined. Additionally to radar measurement errors, the error model also includes errors in the antenna position, attitude and velocity determination.

**Major contributions** The major contributions of this thesis are:

- ⋆ A complete treatment of ground moving target tracking including both the radar signal processing step and the tracking step.
- ⋆ Published algorithms for ground moving target tracking assume simplified models for the radar measurements. While the simplification is often appropriate for the investigated question, such algorithms cannot be directly applied to real tracking scenarios. In contrast, this thesis includes a complete realistic measurement model in the target tracking algorithm. This model accounts for measurement errors that are detection specific – range, DOA and radial velocity – and measurement errors of the antenna location, attitude and velocity vector. In particular, this includes the cumbersome computation of Jacobians of the geolocation of targets which are required in tracking algorithms performing a linearization as in an extended Kalman filter.
- ⋆ The distribution of the direction of arrival measurement error is investigated with an experimental data set. It is shown that the variance of the DOA error can be modeled

excellently by inserting target parameter and clutter covariance matrix estimates into an expression for the Cramer-Rao lower bound. As a result, it can be indicated for which detections the estimation error is particularly small and for which detections the estimation error may be very large.

⋆ It is shown on the basis of experimental data that signal adaptive modeling of the DOA measurement error improves the ground moving target tracking performance. This result is significant because it gives confidence to use this technique in future tracking algorithms.

⋆ In the course of this thesis the author designed and organized a ground moving target tracking experiment with the experimental radar PAMIR of Fraunhofer FHR. The data of this experiment is the basis for the experimental validations of this thesis. While it is not publicly available, it is shared with Fraunhofer FKIE. It is leading to the experimental validation of ground target tracking techniques that have previously only been validated by simulations [51].

**State of the art** In GMTI, the detection of ground moving targets usually involves STAP. An overview of basic STAP techniques has been given in [83]. [34] provides a comprehensive overview of publications and developments within the field of STAP up to the year 2005. Furthermore [49] is a comprehensive tutorial. Space-Time Adaptive Processing in its mathematically optimum form is infeasible, since it requires more training data than is available and it is computationally too demanding for implementation. Thus, [83] gives a comprehensive overview of subspace processing techniques for reducing the computational burden and training requirements. Detection in heterogeneous terrain [48] [24], [61], [52] i.e. in areas where the characteristics of the ground vary strongly with location is one of the most challenging cases because the radar processor is unable to adapt to a specific type of terrain. One technique to counter this difficulty is knowledge aided STAP (KA-STAP) that employs prior knowledge like ground maps to aid in the adaption of the radar processor [50]. In most cases, the radar antennas are mounted such that they are side looking. If this is not the case, further difficulties arise [42, 49].

Usually, as part of the STAP processing, a detector is applied to the filtered receive data. It is attempted to design the detector such that a specified false alarm probability is obtained. This false alarm probability is directly related to the detection threshold. However, the link is not always obvious. In [64] a method for determining the detection threshold for the adaptive matched filter (AMF) is given. In general the type of detector that is employed depends on the model of the target.

A field that is related to GMTI is Synthetic Aperture Radar (SAR). SAR is a technique for generating ground images based on the observation of the ground with radar. Contrary to GMTI, SAR can be performed with systems that comprise only one recording channel. However, data of multi channel SAR can also be used for GMTI [18]. Some systems like PAMIR of Fraunhofer FHR are capable of performing both GMTI and SAR functions.

In general, the identical tracking algorithms can be applied for tracking airborne targets and for ground moving target tracking. If applied to single target scenarios without false alarms and no missed detections, most tracking filters are at the core Kalman filters. An important challenge for tracking algorithms is the association of detections to tracks. An obvious simplistic solution is to associate the detection which lies most closely to a predicted track position. Filters that employ this technique are denoted as Nearest Neighbor (NN) or Global Nearest Neighbor (GNN). Other than nearest neighbor filters, probabilistic data association filter (PDAF) update the track with a weighted mean of measurements [3] [43]. Multiple hypotheses tracking methods (MHT) [8] [62] form tracks for multiple hypothesis of measurement to track associations. In effect, this delayed association decision increases the tracking performance at the cost of computational load. All of the above methods may be extended to employ interacting multiple models (IMM) to predict the target motion [47]. The target motion model is within a discrete set of states – e.g accelerating or linear motion. Tracking filters based on the probability hypothesis density (PHD) avoid the difficulty of associating targets with detections. Instead of forming target tracks, they track the density of expected number of targets. For linear, Gaussian target and measurement models a closed form solution, the GM-PHD filter has been found [80]. Most tracking techniques are formulated for targets that move according to Gaussian and linear dynamics. If this is not the case, linearizations according to the form of the extended Kalman filter or the unscented Kalman filter may be used. Other, however computationally much more demanding approaches for dealing with non-Gaussianity and non-linearities are grid based and particle filters / sequential Monte Carlo methods [2] [81].

Track-before-Detect denotes techniques that perform tracking of targets directly with measurement data that has not been thresholded. Thus, dim targets that are otherwise lost due to the thresholding within the detection process may still be tracked. Several approaches for track before detect exist [16]: The dynamic programming approach (Viterbi algorithm) is a computationally efficient method for performing maximum likelihood tests with a huge number of possible target trajectories (tracks) on the data [5]. This method is grid based, i.e. the likelihood of the most likely path that leads to states on a grid is computed. Other methods for Track-before-Detect are grid or particle based Bayesian filters [67], [82] and histogram probabilistic multiple hypotheses tracking (H-PMT) [76].

In relation to ground moving target tracking, some adaptations have been investigated. An important topic is to model the 'clutter notch', i.e. the effect that targets below a minimum detectable velocity cannot be detected by STAP methods [14] [15] [37] [45] [78]. Other publications deal with using terrain information, in particular road map information [1] [6] [12] [23] [32] [33] [60] and general terrain information [22] [28] [59] . Furthermore, the use of high range resolution profiling (HRR) has been investigated [27], [65] .

**Systems for ground moving target tracking** The most widely known operational system for ground surveillance is the U.S. Joint STARS [20] systems. It comprises a Boeing 707 carrier

aircraft equipped with computer stations for reconnaissance personal [30]. Its radar system (APY-6 or APY-7 of 24 foot length) is mounted below the aircraft.

SOSTAR-X was a European program that attempted to meet the requirements of the NATO Allied Ground Surveillance (AGS) programs. Within SOSTAR-X a demonstration radar system was developed and mounted on a Fokker 100 aircraft. The transmit-receive moduls were taken from the AMSAR program. Fraunhofer FHR contributed two radar operating modes to this program. Experiments were performed with up to 25, mostly GPS equipped ground truth vehicles [85].

MP-RTIP (Multi-Platform Radar Technology Insertion Program) is a U.S. program to develop advanced radar technique for new platforms and possibly for upgrading the Joint STARS system. MP-RTIP technology is for example used for the unmanned reconnaissance aircraft Global Hawk.

Outside of the U.S., the Selex Galileo Seaspray 7000E and the Selex Galileo PICOSAR are two electronically scanned surveillance systems for SAR and GMTI.

Among research radars the AER-II system [18] and the PAMIR system [9] of Fraunhofer FHR are notable for combining high resolution SAR imaging and multi channel GMTI modes in a single system. F-SAR is a newly developed airborne research SAR system of Germany's DLR that can be operated in X, C, S, L and P band [29, 63]. Recently, Airbus has developed the research system "SmartRadar" for airborne imaging and ground moving target detection. The French aerospace lab ONERA has airborne SAR systems for operation in VHF-UHF, L and X band (SETHI) and Ka band (BUSARD) [66].

**Previous publications of thesis results** Parts of this thesis have been presented by the author at various conferences. In [39] the general structure of the tracking algorithm and tracking results have been shown. In [40] and [41] it is shown by simulations that the use of a signal adaptive DOA measurement model improves the tracking results. In [41] a subset of the results with respect to the experimental validation of the measurement model and the improved tracking results with experimental data has been shown.

# 2. Fundamentals of ground moving target indication

This thesis treats tracking based on detections that are acquired with an airborne radar system. As defined in [70, Sec. 1.1] a radar is an "electromagnetic sensor for detection and location of reflecting objects". It emits electromagnetic waves into free space. When objects lie in the propagation path, these objects reflect some of the energy. A portion of this energy is reflected exactly into the direction of the radar receiver. Through the antenna, the radar receiver records the impinging electromagnetic waves. Depending on the type of radar and waveform that is emitted by the radar, the received signal can be processed to deduce the presence of the object or target and to measure the distance or range to the target [70, Sec. 1.1]. Due to a relative motion between the radar and the target, the receive waveform may be modulated by the Doppler frequency. If the Doppler frequency can be measured by the radar system, it enables to determine the radial velocity of the target with respect to the radar.

The first use of electromagnetic waves for detecting objects was due to Christian Hülsmeyer in the early 1900s [84, p. 10.2]. His device could detect the presence of ships up to large distances but was not able to provide range measurements [73, Sec. 1.6]. This application of electromagnetic waves for the detection of objects was forgotten, but prior to the second world war the radar principle was rediscovered in various countries. From then on, a rapid development in radar technology and theory ensued. One of the most notable relatively recent developments is the now extensive use of digital signal processing.

## 2.1. Airborne MTI radar

As of today a large variety of radars exist [70, Sec. 1.2]. The type of radar that is maybe most known in the general public is the surface based moving target indication (MTI) radar with a rotating antenna [68]. Its purpose is the detection of airborne moving targets. As such it is desired, that the energy emitted by the radar is reflected mostly by airborne targets. However, it is unavoidable that some of the energy that is emitted by the radar is reflected by the ground, buildings, woodland, etc. Undesired reflections due to these stationary targets make the detection of airborne targets more difficult. Hence, they are called clutter. Often, clutter echoes are much larger than returns from the target [73, Sec. 3.1, p. 105] and can thus completely hide targets. In order to overcome this problem, MTI radars are designed to detect moving targets based on the

Doppler frequency shift. Ideally, the Doppler shift of return signals due to stationary clutter is zero while the Doppler shift of reflections by moving objects is proportional to the radial velocity of the target.

MTI radars may be realized as pulse Doppler radars [75, Table 4.2, p. 4.3]. A pulse Doppler radar is a radar that is capable of exploiting the Doppler effect and that uses pulsed transmissions. It periodically emits pulses of electromagnetic waves according to the pulse repetition frequency (PRF). During the emission of a pulse, no reception is possible. Reception is only possible in between the transmission of pulses. By using a pulsed transmission it is possible to employ the same antenna both for reception and transmission. For a pulse of a given duration, each of the reflections by various objects are of the same duration. For closely spaced objects the reflected signals will overlap at the receiver, making it impossible to recognize individual objects. The use of shorter pulses is not a satisfying solution, as it reduces the amount of energy that is transmitted per pulse and the average transmit power. A solution is to use a technique called pulse compression [17].

In order to obtain the coverage of a large area, radars for ground moving target indication have to be placed in airborne carriers. Among these, the most common carrier type is the airplane. There are dedicated surveillance planes as for the Joint-STARS program. In the case of fighter radars, GMTI is one of many radar functions. As a GMTI radar must direct the transmitted wave towards the ground, reflections which are due to the ground and not to targets, will be much stronger than in the case of air control radars. Thus, an effective method is needed to distinguish between target returns and clutter.

This task is very similar to the problem faced by surface based MTI radars. The successful use of the Doppler effect in MTI radar suggests a similar approach for airborne GMTI. However, due to the motion of the carrier platform, the earth's surface is also in motion with respect to the radar. The radial velocity of a point on the ground depends on its position. Points that lie on a line that is perpendicular to the flight path have a radial velocity of zero. The radial velocity of points that lie far ahead of the platform in the flight direction attains almost the platform velocity; a point far behind the platform attains almost the negative of the platform velocity. This range of radial velocity corresponds to a range of Doppler frequencies that can potentially be received by the radar. Figure 2.1a shows iso Doppler lines that indicate which ground reflections have identical Doppler shifts. The area which is illuminated by the main beam of the radar is encircled in blue. The corresponding extent of reflections by the ground in range and Doppler is encircled in Figure 2.1b. Thus, this part of the range-Doppler map is covered with clutter. Without further measures, target reflections are masked by clutter reflections within this area. To illustrate this point, locations and velocity vectors of three ground targets have been inserted into Figure 2.1a. The corresponding range-Doppler location of the targets are plotted in Figure 2.1b. Two of the targets are within the clutter area and cannot be detected. Only the target with a high radial velocity component lies outside of the clutter area.

In surface based MTI radars the Doppler frequency was introduced to indicate targets that

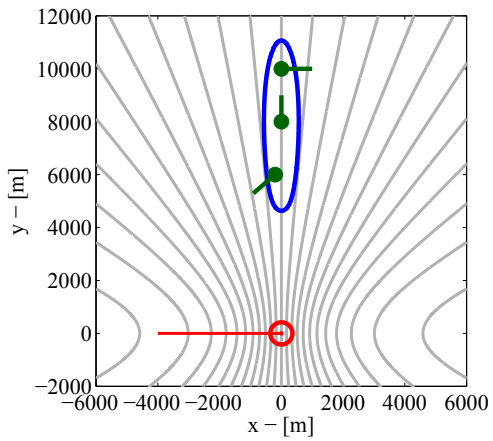


**(a)** An antenna footprint contour line is plotted in blue and iso Doppler lines are shown in gray. The location and velocity vector of three targets is indicated in green.

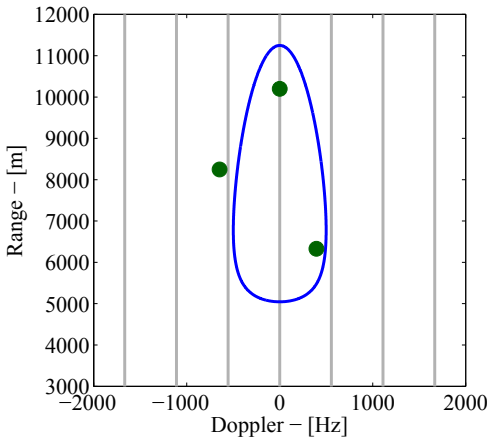


**(b)** The range and Doppler frequency of the antenna footprint contour line is shown in blue. Iso Doppler lines are plotted in gray. The location of the three targets of (a) are plotted in green.

**Figure 2.1.:** Extension of the antenna footprint on the earth's surface and corresponding area in range-Doppler. The contour line is given for a signal power that is at -13 dB with respect to the maximum received signal power. In Figure (b) the extension of Doppler frequencies that is covered by clutter is a function of range due to the shape of the antenna pattern and the attenuation of a signal as a function of range. As a target signal suffers the same attenuation, this does not imply that its detection is easier for large ranges. Additionally, the location and velocity vector of several targets in Cartesian coordinates and their corresponding range and Doppler values are shown.

could not be distinguished by range alone. The question arises: Is it possible to use another variable to indicate targets that cannot be detected based on range and Doppler by airborne radar? The answer to this question has led to multichannel radars that are equipped with several receiving antennas. Such systems are able to distinguish targets with the *direction of arrival* (DOA), i.e. the direction from which a signal impinges on the antenna.

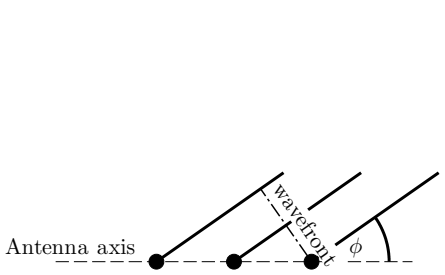


**(a)** For a linear antenna the direction of arrival is the angle $\phi$ between the antenna axis and the vector that points from the antenna to the origin of the signal.

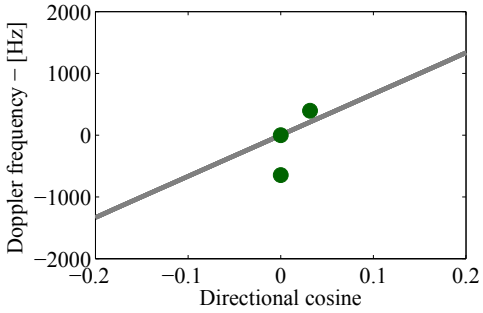


**(b)** Clutter Doppler frequency vs. directional cosine. The range Doppler location of the targets of Figure 2.1b are marked by green dots.

**Figure 2.2.:** Definition of the direction of arrival and relation between the directional cosine and Doppler frequency for clutter returns.

For a linear antenna, the direction of arrival is the angle between the antenna axis and the line which points into the direction of the propagation of the electromagnetic wave (see Figure 2.2a). The cosine of the DOA angle $\phi$ is called *directional cosine*.

As the direction of arrival is determined by the line of sight (LOS), the directional cosine is given by the line of sight (between the target and antenna) and the orientation of the antenna axis. On the other hand, the Doppler frequency of a clutter reflection is proportional to the cosine of the angle between the LOS to the clutter reflector and the velocity vector of the antenna. Thus, if the orientation of the velocity vector and the orientation of the antenna axis coincide, then – for clutter – there exists a linear relation between the Doppler frequency and the directional cosine [83, Sec. 2.6.2]. This relation signifies that more targets can now be distinguished from clutter. To illustrate this point Figure 2.2b shows this linear relation and the locations of the targets in a coordinate system of Doppler frequency and directional cosine. One of the targets is located exactly on the so called clutter ridge [83, Sec. 2.6.2] and remains indistinguishable from clutter. The other target that was covered by clutter in Figure 2.1b is now potentially detectable as it lies off the ridge.

If a target can truly be detected depends among other factors on the actual radar system, the recording parameters, the signal processing and the strength of the signal which is reflected by the target.

## 2.2. The radar signal

At this point the basic variables – range, Doppler and DOA – which combined distinguish ground moving targets from clutter have been introduced. The radar signal that enables to exploit these variables has yet to be presented: Airborne GMTI systems are realized as pulse-Doppler radars. Pulses are emitted periodically and in between the emission of the pulses the reflected echoes are recorded. The delay between the transmission of a pulse and the reception of an echo is proportional to the range (distance) to a target. There is one recorded signal per receive channel of the radar. For a single channel, Figure 2.3 schematically visualizes a pulse train and echos of a scene with only a few targets. In order to detect ground moving targets, the receive data

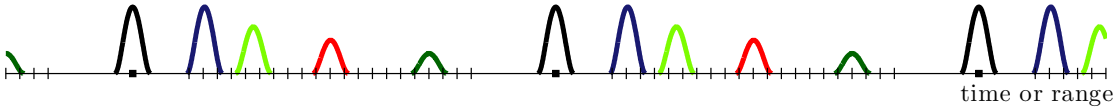


**Figure 2.3.:** Schematic representation of the transmit pulse train and received echos. The transmit pulses are colored black and the received echos in various colors. The transmit times are marked with a solid square and the times at which the received signal is sampled are marked with dashes.

of several consecutive pulses is grouped into a so called coherent processing interval (CPI). [75, p. 4.9]. It is then processed with a technique called Space Time Adaptive Processing (STAP) [83, 34]. The naming of this technique indicates that a spatial and a temporal dimension of the receive data is used. The spatial dimension is obtained by the fact that the radar is equipped with multiple receive channels with antennas at various locations. A single channel radar cannot perform STAP. The temporal dimension is spanned by the transmit times of the pulses within the CPI.

For typical radars and recording configurations, the range to the targets during the duration of a CPI varies little in comparison to the range resolution of the radar. Thus, the scatterers that contribute to the target signal at a specific range remain identical during the CPI. This fact can be recognized more clearly if the data of one CPI is rearranged into a matrix. Each column of this matrix is given by the received data that corresponds to one transmit pulse. The rearrangement is visualized in Figure 2.4. Figures 2.3 and 2.4 show that the echo of each signal is a time shifted and scaled version of the original transmit signal.

Due to the specific manner in which the radar operates, both the transmit and receive signals are in fact complex valued (see [83, Sec. 2.3] and [73, p. 5.4]). A complex valued signal comprises an imaginary and a real part of different magnitudes. It can also be given by its absolute value and an angle. The angle is also denoted as *phase*. As the transmitted and received signals are complex, in schemata as in Figure 2.3 the plots show in fact the absolute value of the signal versus time whereas the phase of the signal is not shown. Still, the phase is an important carrier of information. This is due to the fact that the phase of a received signal is shifted proportionally to the distance of the target. The phase reacts very sensitively to changes of the distance. If the

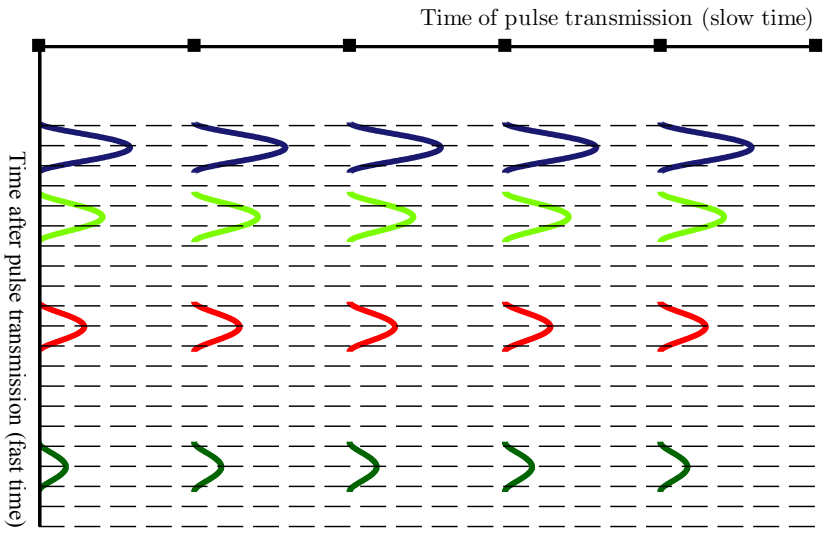


**Figure 2.4.:** Arrangement of the receive data of one channel into a matrix

target range is changed by only a quarter of the wavelength of the radar signal, this corresponds to a phase shift of 180 degrees. As the wavelength of a typical GMTI system is in the order of only 3 cm, this indicates that very small distance changes become measurable. However, if an object is displaced further, for example by another quarter of a wavelength, the total phase shift is 360 or 0 degrees – as if no target displacement has occurred. Hence, an absolute range measurement based on the phase is unsuitable as it is highly ambiguous.

As the Doppler effect is due to the relative velocity between the transmitter and the target – hence a change in range –, it manifests itself in a linear change of the phase of the received signal over time. In the example of Figure 2.4 the targets are in fact moving away from the radar. Even though the displacement is too small to be visible as shift of the received signals, the displacement causes a linear progression of the phase in the time axis of the pulse emission. By performing a discrete Fourier transform – independently for each range line – on the data matrix of Figure 2.4, this change of phase can be exploited to split the signal into Doppler frequencies components. The resulting two dimensional representation of the received data in range and Doppler is called *range-Doppler map*. Figure 2.5 schematically represents the range-Doppler map for the set of example targets. For better visibility, the signal is only plotted for the range lines where a target is present.

In a multichannel radar, the data matrix and range-Doppler map of Figures 2.4 and 2.5 will be available for each channel. Thus, the total dataset of a CPI is a data cube where the first dimension is spanned by the receive channels, the second dimension is spanned by the pulse

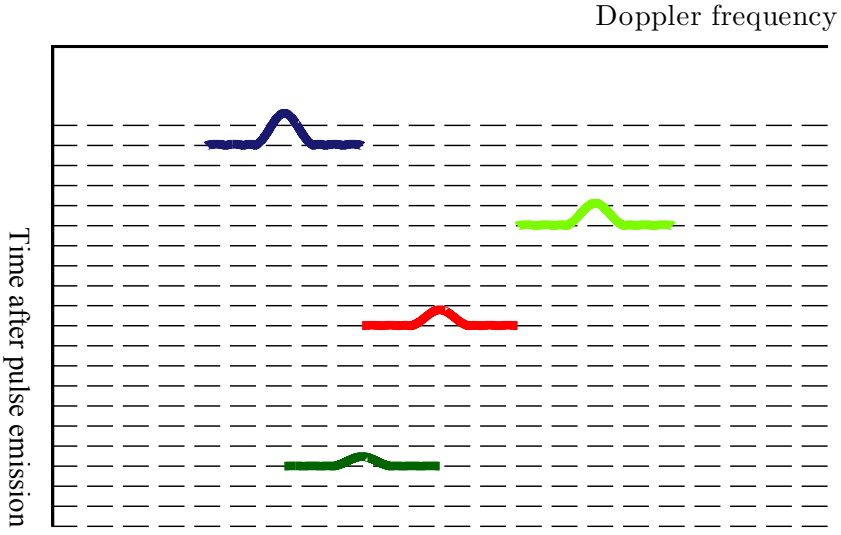


**Figure 2.5.:** Schematical representation of a range-Doppler map

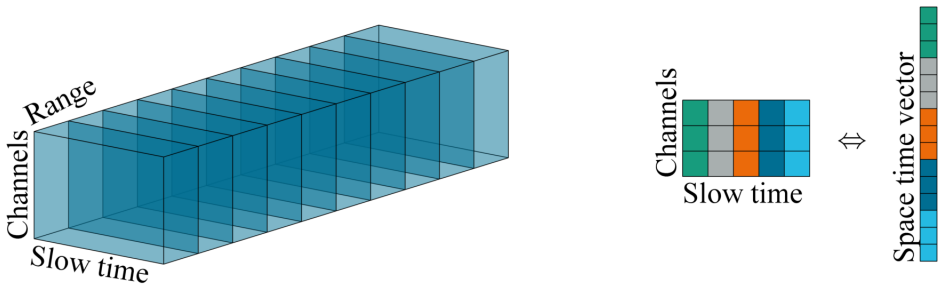


**(a)** The received data can be presented as a cube with dimensions: receive channel, slow time, range

**(b)** Arrangement of the data matrix of a single range into a vector

**Figure 2.6.:** Visualization of the data structure of the received radar signal of a multichannel radar system.

emission time or Doppler and the third dimension is the range to the target.

For multichannel data, the phase of the received signal enables the estimation of the direction of arrival of a signal. In the situation which is visualized in Figure 2.2a the distance to a target is slightly different for the antennas of the different receiving channels. The exact amount in which the distance differs is a function of the angle of arrival. For example, for a signal which impinges with a 90 degree angle on the antenna axis, the difference is zero. The difference in range to target for the receive antennas causes also a phase difference between the channels of the received signal. This phase difference can be exploited in order to estimate the direction of arrival.

In a realistic situation, the received data will be due to many more echoes than the four of the example. The data matrix of a single channel of a more realistically simulated data will look similar to the one of Figure 2.7a. In this Figure, the amplitude of the receive signal is represented on a color scale. Due to the superposition of echoes from a very large number of scatterers, no structure in the data is discernible. The same data represented as range-Doppler map is shown in Figure 2.7b. In this Figure, the strong clutter signal in the frequency band between -0.025 and 0.025 is visible. Outside of the clutter band, the signal is mostly dominated by receiver noise. The reflection of a single moving object is located at (-0.2, 8500 m) and the reflection of two other moving objects are submerged in clutter.

The transformation to the Doppler domain can be understood as the change of representation of the signal. For a multichannel data set it is similarly possible to represent the data in the so called beamspace [83, Sec. 6.1]. The beamspace dimension corresponds to the direction of arrival. Figure 2.8 shows a representation of a single range line of the data in beamspace-Doppler.

## 2.3. Data processing and target detection

The goal of the signal processing is to indicate ground moving targets based on the received radar data. Traditionally, this task has been cast as a detection and estimation problem [64].

The detection of a target is equivalent to deciding between two hypotheses [77, Ch. 2]. Hypothesis 0 states that the received data is due to clutter and receiver noise only. Hypothesis 1 is that the received data additionally contains the reflection of a target with specific parameters. The detection should be performed independently for each range line of the data.

$$\textbf{received data} = \begin{cases} \textbf{clutter and noise} & \text{Hypothesis } H_0 \\ \textbf{target signal} + \textbf{clutter and noise} & \text{Hypothesis } H_1 \end{cases}$$

Upon considering Figure 2.2b making this decision seems to be simple. If the data contains components that do not lie on the clutter ridge, then they must be due to targets and a detection (hypothesis 1) can be declared. However, the representation of a realistic receive signal versus the DOA and Doppler frequency is similar to the example of Figure 2.8. It can be seen that – due to the limited resolution of the radar – signal energy leaks from the clutter ridge into the

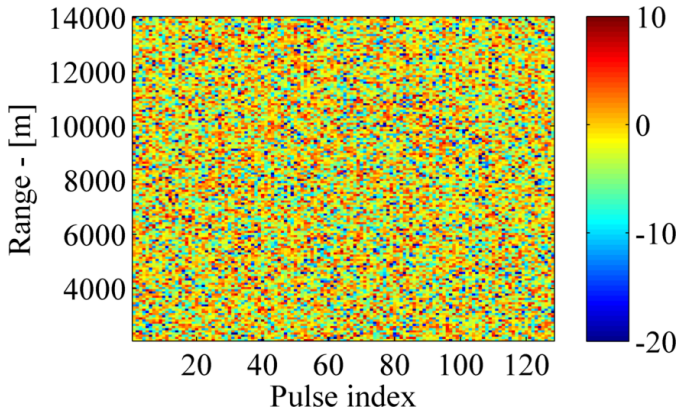


**(a)** Time domain signal of a single channel

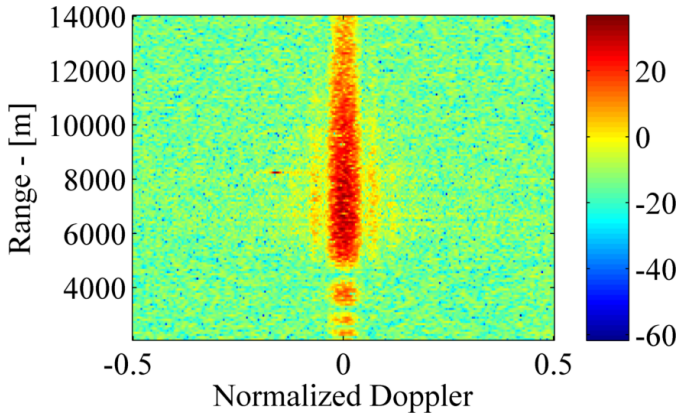


**(b)** Range Doppler map of the sum channel

**Figure 2.7.:** Visual representation of simulated data sets

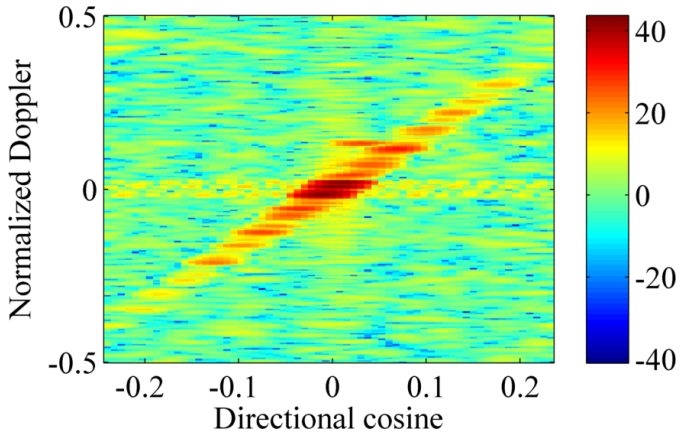


**Figure 2.8.:** Beamspace Doppler plot of a simulated signal

normally clutter free region. A certain amount of "contamination" of the clutter free space in the Doppler-DOA domain is virtually unavoidable. Furthermore, noise is present in the entire domain and weak target signals might be mistaken for receiver noise. Thus, the distinction between the two hypotheses is blurred.

In order to be still be able to decide between the hypotheses, statistical models, i.e. random variables are used to describe the characteristics of clutter and noise signals more precisely. Based on these models, statistical decision theory will enable to derive a decision rule or test [77].

Several observations lead to a formulation for the clutter model: First, the clutter signal can be understood as independent sum of countless individual signals, each due to a single reflection, be it by a rock, leave, part of a building, etc. The amplitude and the phase of these signals are random since the position and sizes of the reflecting objects are random. According to the central limit theorem [10, Sec. 2.1.3], the sum of a large number of independent random variables approaches a Gaussian distribution. Hence, at least as an approximation, it is appropriate to model clutter as a Gaussian random variable. The second observation is that the clutter signals at different range lines are due to different individual reflecting objects. As the location and sizes of these objects are stochastically independent from one another, so are the clutter signals of different range lines. Third, the clutter signal of different pulses at the same range line is highly correlated as it is due to the same reflecting objects, only recorded at different times. Furthermore, there is a strong correlation between the clutter signal that is recorded by the different channels (see [83, Fig. 8]).

As a result of the first two statements, the clutter of each range line can be modeled independently of other range lines as a Gaussian random variable. The third statement signifies that data of the same range line should be processed jointly. In doing so, it is convenient to rearrange the data of a single range line into a vector as visualized in Figure 2.6b. The probability distribution of this vector is parameterized by its expected value and its covariance matrix. The expected value is in fact a vector of zeros and the covariance matrix captures the correlation of the clutter signal within one CPI.

Statistical decision theory provides two basic principles for deriving a detection test: The Bayes criterion [77, p. 24] which minimizes the expected cost of making a wrong decision and the Neyman-Pearson criterion [77, p. 33] which constraints the probability of a *false alarm*. In ground moving target detection, usually the second criterion is chosen. For the case of testing between two hypotheses without additional parameters, the optimum test for this criterion is the Neyman-Person test [77, p. 33]. In this test problem, however, hypothesis 1 comes with an unknown parameter, the complex valued signal amplitude. As a result, hypothesis 1 is a composite hypothesis [77, Sec. 2.5]. For composite hypotheses a type of test called generalized likelihood ratio test [77, p. 92] can be used.

## 2.4. Signal model

In order to present the target detection in more detail, it is at this point necessary to introduce a signal model for the received data.

**Target signal** The model is given for the data at the range of the target. The data of pulse $p$ and channel $n$ is modeled as [83, p. 15]

$$y_{np} = \alpha_\mathrm{t} \mathrm{e}^{\mathrm{j}n2\pi\vartheta_\mathrm{t}} \mathrm{e}^{\mathrm{j}p2\pi f_\mathrm{t}} \,. \tag{2.1}$$

Here $\alpha_\mathrm{t}$ is the complex valued amplitude of the target signal, $\vartheta_t$ is the normalized spatial frequency and $f_\mathrm{t}$ is the normalized frequency of the target. The target's spatial frequency is related to the target's location via

$$\vartheta_\mathrm{t} = \frac{\boldsymbol{u}_\mathrm{at}^T \boldsymbol{d}_\mathrm{antAxis}}{\lambda_0} \tag{2.2}$$

where $\boldsymbol{u}_\mathrm{at}$ is a unit vector pointing from the antenna to the target and $\boldsymbol{d}_\mathrm{antAxis}$ is a vector that points into the direction of the antenna axis. Its length $\|\boldsymbol{d}_\mathrm{antAxis}\|$ is equal to the distance between the antenna elements. The normalized target frequency is

$$f_\mathrm{t} = \frac{F_\mathrm{t}}{F_\mathrm{pr}} \tag{2.3}$$

where $F_\mathrm{t}$ is the Doppler frequency of the target signal (in Hz) and $F_\mathrm{pr}$ is the pulse repetition frequency of the radar. The complex amplitude of the target signal can be modeled as realization of a scalar complex normal random variable, i.e.

$$\alpha_\mathrm{t} \sim \mathcal{N}^\mathcal{C}(0, \sigma_\mathrm{n}^2 r_\mathrm{snr,sp,se}) \,. \tag{2.4}$$

Here, $\sigma_\mathrm{n}^2$ is the power of noise of a single pulse and a single element. The signal to noise ratio is given by

$$r_\mathrm{snr,sp,se} = \frac{P_\mathrm{tx} T_\mathrm{p} \lambda_0^2}{N_0 \left(4\pi\right)^3 r^4} D_\mathrm{tx} D_\mathrm{rx} A_\mathrm{t} \tag{2.5}$$

where $P_\mathrm{tx}$ is the transmit power, $T_\mathrm{p}$ is the pulse duration, $\lambda_0$ is the wavelength of the transmit signal, $N_0$ is the spectral density of the noise at the receiver, $A_\mathrm{t}$ is the radar cross section of the target. The variables $D_\mathrm{tx}$ and $D_\mathrm{rx}$ are the array transmit and element receive power gains of the antenna. The subscript "snr,sp,se" stands for SNR of a single pulse and single element.

The indices are in the range $p = 0, ..., M_\mathrm{cpi}$ and $n = 0, ..., N_\mathrm{chan}$, where $M_\mathrm{cpi}$ is the number of pulses of the CPI and $N_\mathrm{chan}$ is the number of receive channels of the radar system. The data of equation (2.1) can be reassembled to the spatial snapshot of pulse $p$ and all channels [83, eq. (29)

with eq. (13)]

$$\boldsymbol{y}_p = \alpha \mathrm{e}^{\mathrm{j}p2\pi f_\mathrm{t}} \boldsymbol{a}(\vartheta_\mathrm{t}) \tag{2.6}$$

Here,

$$\boldsymbol{a}(\vartheta) = \begin{bmatrix} 1 \\ \mathrm{e}^{\mathrm{j}2\pi\vartheta} \\ \vdots \\ \mathrm{e}^{\mathrm{j}2\pi(N_\mathrm{chan}-1)\vartheta} \end{bmatrix} \tag{2.7}$$

is the spatial steering vector. Furthermore, as visualized in Figure 2.6b, the spatial snapshots of the received data can be stacked to space time snapshots of the data.

$$\boldsymbol{\chi}_\mathrm{t} = \begin{bmatrix} \boldsymbol{a}(\vartheta_\mathrm{t}) \\ \mathrm{e}^{\mathrm{j}2\pi f_\mathrm{t}} \boldsymbol{a}(\vartheta_\mathrm{t}) \\ \vdots \\ \mathrm{e}^{\mathrm{j}2\pi(M_\mathrm{cpi}-1)f_\mathrm{t}} \boldsymbol{a}(\vartheta_\mathrm{t}) \end{bmatrix} \tag{2.8}$$

With the definition of the temporal steering vector

$$\boldsymbol{b}(f_\mathrm{t}) = \begin{bmatrix} 1 \\ \mathrm{e}^{\mathrm{j}2\pi f_\mathrm{t}} \\ \vdots \\ \mathrm{e}^{\mathrm{j}2\pi(M_\mathrm{cpi}-1)f_\mathrm{t}} \end{bmatrix} \tag{2.9}$$

and the space time steering vector

$$\boldsymbol{v}(\vartheta_\mathrm{t}, f_\mathrm{t}) = \boldsymbol{b}(f_\mathrm{t}) \otimes \boldsymbol{a}(\vartheta_\mathrm{t}) \tag{2.10}$$

(where $\otimes$ denotes the Kronecker product) the space time snap shot of the target signal is given by

$$\boldsymbol{v}_\mathrm{t} = \boldsymbol{\chi}_\mathrm{t} = \alpha_\mathrm{t} \boldsymbol{v}(\vartheta_\mathrm{t}, f_\mathrm{t})\,. \tag{2.11}$$

**Noise** Receiver noise is modeled as spatially and temporally white Gaussian random variable. Its space time covariance matrix is given by

$$\mathbf{R}_\mathrm{n} = \mathrm{E}\left[\boldsymbol{\chi}_\mathrm{n} \boldsymbol{\chi}_\mathrm{n}^H\right] = \sigma_\mathrm{n}^2 \mathbf{I}_{M_\mathrm{cpi}} \otimes \mathbf{I}_{N_\mathrm{chan}}\,, \tag{2.12}$$

where $\mathbf{I}_{M_\mathrm{cpi}}$ is a $M_\mathrm{cpi} \times M_\mathrm{cpi}$ identity matrix, $\mathbf{I}_{M_\mathrm{cpi}}$ is a $N_\mathrm{chan} \times N_\mathrm{chan}$ identity matrix and $\otimes$ denotes the Kronecker product.

**Clutter** As laid out above, clutter is the sum of a great number of backscattered signals due to vegetation and other surface scatterers. Due to this, clutter of a single range line is modeled as a Gaussian random variable with $M_{\mathrm{cpi}}N_{\mathrm{chan}} \times M_{\mathrm{cpi}}N_{\mathrm{chan}}$ covariance matrix $\mathbf{R}_{\mathrm{c}}$. A model for the clutter covariance matrix is given in [83, Sec. 2.6.1, eq. (61)].

**Decomposition of the space time snapshot** The entire space time snap shot of the data is decomposed as

$$\boldsymbol{\chi} = \alpha_{\mathrm{t}}\boldsymbol{v}_{\mathrm{t}} + \boldsymbol{\chi}_{\mathrm{q}} \tag{2.13}$$

where $\boldsymbol{\chi}_{\mathrm{q}}$ is the sum of the clutter and the noise components $\boldsymbol{\chi}_{\mathrm{c}}$ and $\boldsymbol{\chi}_{\mathrm{n}}$.

## 2.5. Space time adaptive processing

### 2.5.1. Fully adaptive space time processing

With this signal model, the detection test can be formulated as the decision between $|\alpha_{\mathrm{t}}| = 0$ (Hypothesis $H_0$) and $|\alpha_{\mathrm{t}}| > 0$ (Hypothesis $H_1$). For a set of target parameters $\vartheta_{\mathrm{t}}$ and $f_{\mathrm{t}}$, the generalized likelihood ratio test is given by [64, eq. (7)]

$$\frac{\left|\boldsymbol{v}_s^H\mathbf{R}_{\mathrm{q}}^{-1}\boldsymbol{\chi}\right|^2}{\boldsymbol{v}_s^H\mathbf{R}_{\mathrm{q}}^{-1}\boldsymbol{v}_s} \underset{H_0}{\overset{H_1}{\gtrless}} t_{\mathrm{th}}\,. \tag{2.14}$$

where $\boldsymbol{v}_{\mathrm{s}}$ is the target model vector. This model vector may differ from the vector $\boldsymbol{v}_{\mathrm{t}}$ of the target signal that is actually present in the data. According to the above expression, the received data is effectively filtered with

$$\boldsymbol{w}_{\mathrm{s}} = \mathbf{R}_{\mathrm{q}}^{-1}\boldsymbol{v}_{\mathrm{s}} \tag{2.15}$$

and the square of the absolute value of the filter output is compared to a threshold. The identical filtering of the data can also be derived by designing a linear filter which yields the optimum signal to noise ratio of the filtered signal [25, Sec. 2.2.1].

The covariance matrix $\mathbf{R}_{\mathrm{q}}$ of clutter and noise can be obtained based on signal models [83, Sec. 2.6.1], but these models assume an ideal radar system. In practice, the true signal properties will deviate from the theoretically modeled. Thus, instead of relying on a model for the covariance matrix, in STAP it is typically estimated from the data. The resulting test which is obtained by replacing the true covariance matrix by an estimate is an *adaptive matched filter* [64].

The process of estimating the clutter and noise covariance matrix is called *training*. Different training strategies have been developed among which the most basic approach is sliding window training. As stated above, the covariance matrix is given for the data of a single range line and range lines are stochastically independent. However, they share similar signal properties. Hence,

the data for training can be taken from range lines that are in the vicinity of the range which is tested for the presence of the target. It should be avoided, that the target itself is included in the training data, otherwise an effect called *self nulling* will occur. To avoid this effect, a number of range lines within a *guard gate* around the range under test are excluded from the training. Thus, the covariance estimate is given by

$$\hat{\mathbf{R}}_{\mathrm{q}} = \sum_{l=1}^{K_{\mathrm{e}}} \boldsymbol{\chi}_l \boldsymbol{\chi}_l^H \tag{2.16}$$

Here, $\boldsymbol{\chi}_l$ is the data of the range gates that is used for training and $K_{\mathrm{e}}$ is the number of training samples. The adaptive adaptive matched filter [64] is then given by

$$\frac{\left|\boldsymbol{v}_s^H \hat{\mathbf{R}}_{\mathrm{q}}^{-1} \boldsymbol{\chi}\right|^2}{\boldsymbol{v}_s^H \hat{\mathbf{R}}_{\mathrm{q}}^{-1} \boldsymbol{v}_s} \underset{H_0}{\overset{H_1}{\gtrless}} t_{\mathrm{th}} \,. \tag{2.17}$$

The computation of detection thresholds that take into account the fact that the covariance matrix is estimated from the data are given in [64].

### 2.5.2. Partially adaptive space time processing

With training one attempts capture the true signal properties closer than with a theoretical model. On the other hand, the accuracy of the estimate of the covariance matrix depends on the amount of training samples that are employed [83, Sec. 3.5]. An insufficient amount of training samples will incur a large loss of SNR. To keep the loss limited, the number of training samples should theoretically be at least be 3 to 5 times larger than the dimension of the clutter and noise covariance matrix. In practice, even more samples should be used.

As a result, for typical CPI lengths and number of receiving channels, there is not sufficient training data available. Furthermore, in fully adaptive STAP the covariance matrix is very large. As a result, the computation of the filter, which has to be repeated for every range line and which involves the inversion of the estimated covariance matrix, is numerically too demanding in fully adaptive STAP.

Thus, a method called partially adaptive STAP has been developed [83]. In partially adaptive STAP, for each test with individual target parameters of $u$ for the cosine of the direction of arrival angle and $F_{\mathrm{D}}$ for the Doppler frequency, a transformed set of the received data is used. The important point is that the dimension of the data is reduced in the transformation. Hence, the dimension of the covariance matrix and required amount of training data is reduced accordingly. The reduction of the data leads to a loss in SNR. For an appropriate transformation of the data, this SNR loss is much smaller than the training loss for fully adaptive STAP.

In general, the subspace transformation in partially adaptive STAP can be expressed by the

matrix multiplication [83, Sec. 4.2]

$$\tilde{\boldsymbol{\chi}} = \mathbf{T}^H \boldsymbol{\chi} \,. \tag{2.18}$$

The transformed data is decomposed as

$$\tilde{\boldsymbol{\chi}} = \alpha_\mathrm{t} \tilde{\boldsymbol{v}}_\mathrm{t} + \tilde{\boldsymbol{\chi}}_\mathrm{q} \tag{2.19}$$

where $\tilde{\boldsymbol{v}}_\mathrm{t} = \mathbf{T}^H \boldsymbol{v}_\mathrm{t}$ is the transformed target steering vector and $\tilde{\boldsymbol{\chi}}_\mathrm{q}$ is the transformed clutter and noise data. The AMF test is found by replacing the full dimension variables in 2.17 with the reduced dimension versions

$$\frac{\left| \tilde{\boldsymbol{v}}_s^H \hat{\tilde{\mathbf{R}}}_\mathrm{q}^{-1} \tilde{\boldsymbol{\chi}} \right|^2}{\tilde{\boldsymbol{v}}_s^H \hat{\tilde{\mathbf{R}}}_\mathrm{q}^{-1} \tilde{\boldsymbol{v}}_s} \underset{H_0}{\overset{H_1}{\gtrless}} t_\mathrm{th} \,. \tag{2.20}$$

Here $\hat{\tilde{\mathbf{R}}}_\mathrm{q}$ is the covariance matrix of the transformed data set. It has to be estimated separately for every different transformation.

#### Adjacent bin post Doppler STAP

Among the different subspace projections, the one that leads to *adjacent bin post Doppler* STAP shall be presented in greater detail here, since it is employed in the processing of this thesis. In adjacent bin post Doppler STAP, the data is transformed to the Fourier domain. For the detection of a target with a given frequency, only the Doppler bins in the vicinity of the Doppler frequency are used. The motivation for adjacent bin Doppler processing lies in two facts:

- According to the signal model of equation (2.1), the signal power is identical at every pulse (index $m$). In the Fourier domain – however – the signal energy is concentrated in a few Doppler bins due to the constant frequency of the target signal.

- In the time domain the clutter signal is strongly correlated, even for time bins that are relatively far apart in time. In the Doppler domain, the correlation at the same distance (in Doppler frequency) is much smaller. Thus, in the Doppler domain a covariance matrix of much smaller dimensions captures the clutter properties.

For the filtering of a target with frequency $f_\mathrm{m}$, the transform to the Fourier domain and subsequent selection of $2P+1$ adjacent Fourier bins is expressed by multiplication with the matrix [83, eq. (203), p. 119]

$$\mathbf{T}_m = \tilde{\mathbf{F}}_m \otimes \mathbf{I}_{N_\mathrm{chan}} \,, \tag{2.21}$$

where $\mathbf{I}_{N_{\text{chan}}}$ is a $N_{\text{chan}} \times N_{\text{chan}}$ identity matrix. The matrix

$$\tilde{\mathbf{F}}_{\text{m}} = \begin{bmatrix} \boldsymbol{f}_{m-P} & \cdots & \boldsymbol{f}_m & \cdots & \boldsymbol{f}_{m+P} \end{bmatrix} \tag{2.22}$$

consists of a subset of the columns of a discrete Fourier transform (DFT) matrix, i.e. $\boldsymbol{f}_m$ is the $m$-th column of

$$\mathbf{F} = \text{diag}(\boldsymbol{t}_{\text{f}})\mathbf{U}^H \tag{2.23}$$

In this definition of the DFT matrix, $\boldsymbol{t}_{\text{f}}$ is a time domain taper.

The transformed space time snapshot for the detection of a target with frequency $f_m$ is

$$\boldsymbol{\chi}_m = \mathbf{T}_m \boldsymbol{\chi} \tag{2.24}$$

and the transformed target component is

$$\tilde{\boldsymbol{\chi}}_{\text{t},m} = \alpha_{\text{t}} \left( \tilde{\mathbf{F}}_m \boldsymbol{b}(f_{\text{t}}) \right) \otimes \boldsymbol{a}(\vartheta_{\text{t}}) \,. \tag{2.25}$$

The transformed steering vector is

$$\tilde{\boldsymbol{v}}_{\text{s},m} = \mathbf{T}_m \boldsymbol{v}_{\text{s}} \tag{2.26}$$

where

$$\boldsymbol{v}_{\text{s}} = \boldsymbol{v}(\vartheta_s, f_m) \tag{2.27}$$

The transformed data is decomposed as

$$\boldsymbol{\chi}_m = \tilde{\boldsymbol{\chi}}_{\text{t},m} + \boldsymbol{\chi}_{\text{q},m} \tag{2.28}$$

The test for the present of a target at Doppler bin $m$ is the defined as

$$\frac{\left| \tilde{\boldsymbol{v}}_{\text{s},m}^H \hat{\tilde{\mathbf{R}}}_{\text{q},m}^{-1} \tilde{\boldsymbol{\chi}}_m \right|^2}{\tilde{\boldsymbol{v}}_{\text{s},m}^H \hat{\tilde{\mathbf{R}}}_{\text{q}}^{-1} \tilde{\boldsymbol{v}}_{\text{s},m}} \underset{H_0}{\overset{H_1}{\gtrless}} t_{\text{th}} \,. \tag{2.29}$$

### 2.5.3. Performance of STAP

The performance of STAP can be measured by the signal to clutter and noise ratio (SCNR) that is obtained after applying the STAP filter [83, Sec. 3.4.2]. The SCNR is a function of the target's frequency. For untapered fully adaptive STAP (assuming a known clutter and noise covariance

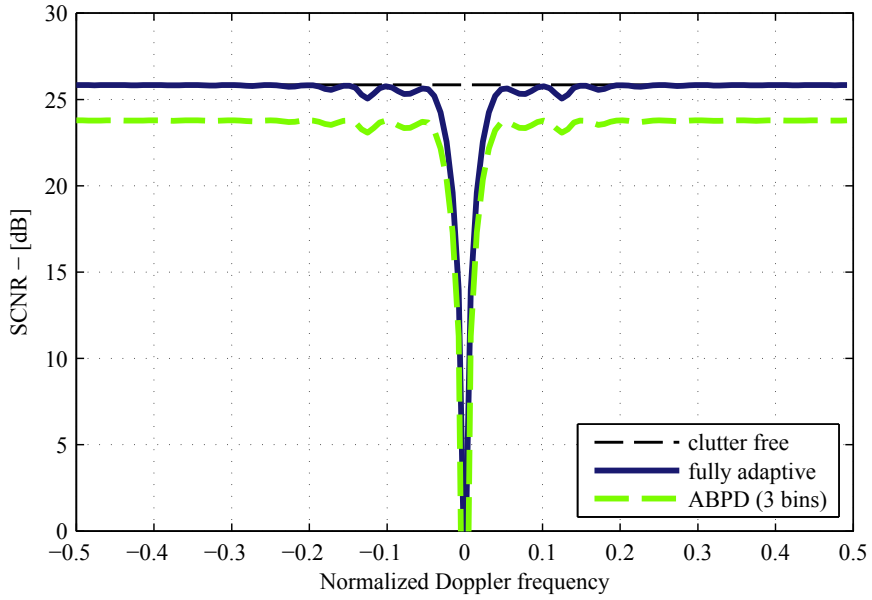


**Figure 2.9.:** Example for the signal to clutter and noise ratio (SCNR) after Space Time Adaptive Filtering for fully adaptive STAP and adjacent bin post Doppler STAP (ABPD). In generating this Figure no taper was used for fully adaptive STAP while a 40 dB Chebyshev window was employed for adjacent bin post Doppler STAP. The number of receiving channels is 3 and the number of pulses is 128. The SNR of a single pulse and channel is 0 dB and the respective single pulse, single channel CNR is 12 dB.

matrix) it is given by [83, eq. (111), p. 62]

$$r_{\mathrm{scnr}} = \frac{\sigma_n^2 r_{\mathrm{snr,sp,se}} \left| \boldsymbol{w}_s^H \boldsymbol{v}_{\mathrm{t}} \right|^2}{\boldsymbol{w}_s^H \mathbf{R}_{\mathrm{q}}^{-1} \boldsymbol{w}_s}, \tag{2.30}$$

where $\boldsymbol{w}_s$ is defined in equation (2.15). For partially adaptive STAP it is

$$r_{\mathrm{scnr}} = \frac{\left| \tilde{\boldsymbol{v}}_s^H \hat{\tilde{\mathbf{R}}}_{\mathrm{q}}^{-1} \tilde{\boldsymbol{v}}_{\mathrm{t}} \right|^2}{\tilde{\boldsymbol{v}}_s^H \hat{\tilde{\mathbf{R}}}_{\mathrm{q}}^{-1} \tilde{\boldsymbol{v}}_s}. \tag{2.31}$$

Figure 2.9 shows the SCNR that is obtained for a clutter free case, fully adaptive STAP and adajacent bin post Doppler STAP. Well visible at a Doppler frequency of zero is the so called clutter notch, a sharp drop in SCNR. It signifies that targets with very small velocities cannot be detected. Its width is related to the minimum detectable velocity [83, Sec. 3.4.5].

### 2.5.4. Parameter estimation

In addition to the detection of targets, GMTI also comprises the estimation of target parameters. The target parameters that are typically estimated with a radar are range, Doppler frequency and the direction of arrival [71, p. 2]. Due to the fact that the test is already constructed for a grid in range and Doppler, each detection automatically yields estimates of these parameters. A very coarse estimate of the DOA is also obtained as it can be assumed that the target was located in the main beam of the antenna. It is possible to refine this estimate further by techniques such as maximum likelihood estimation [77, p. 65] or adaptive monopulse [53].

# 3. Ground moving target indication and geolocation

This thesis considers ground moving target tracking based on data acquired by a single airborne platform such as an aircraft. It is assumed that the radar is mounted on the aircraft in a side looking configuration, i.e. it is capable of illuminating the ground to the side of the aircraft but not in the front or back. Furthermore, it is assumed that the radar is equipped with a linear, multichannel, electronically steerable antenna. The data that is recorded by the radar system is partitioned into *coherent processing intervals* (CPIs). For each CPI with index $k$, estimates of the antenna location, velocity and attitude are given by

$$\hat{\boldsymbol{x}}^{\mathcal{E}}_{\mathrm{ant},k} = \begin{bmatrix} \hat{x}^{\mathcal{E}}_{\mathrm{ant},k,1} \\ \hat{x}^{\mathcal{E}}_{\mathrm{ant},k,2} \\ \hat{x}^{\mathcal{E}}_{\mathrm{ant},k,3} \end{bmatrix}, \hat{\boldsymbol{v}}^{\mathcal{E}}_{\mathrm{ant},k} = \begin{bmatrix} \hat{v}^{\mathcal{E}}_{\mathrm{ant},k,1} \\ \hat{v}^{\mathcal{E}}_{\mathrm{ant},k,2} \\ \hat{v}^{\mathcal{E}}_{\mathrm{ant},k,3} \end{bmatrix} \tag{3.1}$$

and

$$\hat{\boldsymbol{\gamma}}^{\mathcal{A}\leftarrow\mathcal{E}}_{k} = \begin{bmatrix} \hat{\gamma}^{\mathcal{A}\leftarrow\mathcal{E}}_{\mathrm{yaw},k} \\ \hat{\gamma}^{\mathcal{A}\leftarrow\mathcal{E}}_{\mathrm{pitch},k} \\ \hat{\gamma}^{\mathcal{A}\leftarrow\mathcal{E}}_{\mathrm{roll},k} \end{bmatrix} \tag{3.2}$$

Here, $\hat{\boldsymbol{x}}^{\mathcal{E}}_{\mathrm{ant},k}$ and $\hat{\boldsymbol{v}}^{\mathcal{E}}_{\mathrm{ant},k}$ are given with respect to an *east-north-up* (ENU) coordinate system. The origin of this coordinate system is defined by a coordinate in WGS-84, i.e by a latitude, longitude and height. The axes of the coordinate system point east (x), north (y) and up (z). Additionally, an antenna coordinate system with time dependent origin at the location of the antenna is defined. The x-axis of the antenna coordinate system is given by the principal axis of the antenna. Together, the x- and y-axes span the planar aperture of the antenna. The z-axis points exactly into the direction into which the antenna transmits the highest proportion of the energy if no steering is applied. Superscripts $\mathcal{E}$ (ENU) and $\mathcal{A}$ (antenna) indicate the coordinate system that is used for a specific variable. The attitude of the antenna coordinate system and hence the antenna is given by the Euler angles of $\hat{\boldsymbol{\gamma}}^{\mathcal{A}\leftarrow\mathcal{E}}_{k}$ [21, Sec. 4.3, p. 112]. A rotation matrix can be constructed based on these angles (see Appendix A.7.1). Multiplication with this matrix will rotate a vector from the ENU coordinate system into antenna coordinates; hence the notation $\mathcal{A} \leftarrow \mathcal{E}$ is used. For some computations, only the yaw and pitch angles are required. In this case, the vector $\boldsymbol{\gamma}^{\mathcal{A}\leftarrow\mathcal{E}}_{\mathrm{yp},k}$ which contains only the first two elements of $\hat{\boldsymbol{\gamma}}^{\mathcal{A}\leftarrow\mathcal{E}}_{k}$ is passed as function argument.

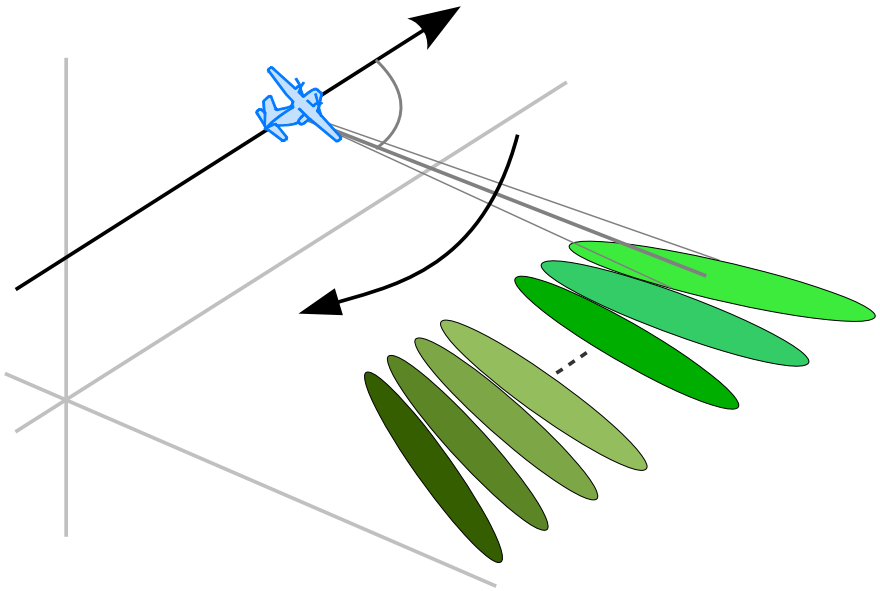

**Figure 3.1.:** Visualization of the subsquent steering of the antenna beam to different antenna footprints in a scan mode acquisition.

In this work it is assumed that the steering of the antenna remains constant during one CPI and it is denoted by $u_{\mathrm{st},k}$. Furthermore, the radar uses a constant pulse repetition frequency $F_{\mathrm{pr}}$ and a CPI dependent carrier wavelength $\lambda_{0,k}$. Each CPI contains $M_{\mathrm{cpi}}$ pulses. It is assumed that the CPIs are sufficiently short such that the same ground area is illuminated during its entire duration. The sequence of steering values $u_{\mathrm{st},k}$ may be programmed in an arbitrary fashion. For a scanning mode, the radar system will steer the antenna between minimum and maximum values such that a scan illuminates a set of ground areas as visualized in Figure 3.1. The distribution of the transmitted radar energy versus angle is captured by the antenna gain patterns. The transmit gain pattern is denoted by the function $D_{\mathrm{tx}}(\boldsymbol{\gamma}^{\mathrm{dir}}, u_{\mathrm{st}}, \lambda_0)$, where $\boldsymbol{\gamma}^{\mathrm{dir}}$ and the receive gain pattern is $D_{\mathrm{rx}}(\boldsymbol{\gamma}^{\mathrm{dir}}, u_{\mathrm{st}}, \lambda_0)$. These patterns must be determined based on the specific configuration and parameters of the radar antenna.

Additionally to the platform location and recording parameters, the received data of each CPI is given. As illustrated in Chapter 2, it consists of a data cube with the dimensions pulse number (within the CPI), range and recording channel.

**Data notation** After range compression, the complex scalar data sample of CPI $k$, range $l$, pulse $p$ and channel $n$ is denoted as $y_{\mathrm{trpc}}(k, l, p, n)$. The data of all channels of a specific pulse is given by

$$\boldsymbol{y}_{\mathrm{trp}}(k, l, p) = [y_{\mathrm{trpc}}(k, l, p, n)]_{n=0}^{N_{\mathrm{chan}}-1} \ , \tag{3.3}$$

which is obtained by arranging the samples of the different channels. Here, the subscript "trpc" stands for time, range, pulse, channel. The corresponding slow time of a pulse is $t_p = \frac{p}{F_{\mathrm{pr}}}$, the range is $r_l = r_0 + l\Delta r$ and the position of the receive channel in the antenna coordinate system is $x_{\mathrm{ph},n}$.

The data of an entire range line $l$ of CPI $k$ is obtained by stacking the vector data of the different pulses

$$\boldsymbol{y}_{\mathrm{tr}}(k,l) = \left[\boldsymbol{y}_{\mathrm{trp}}(k,l,p)\right]_{p=0}^{M_{\mathrm{cpi}}-1} . \tag{3.4}$$

The dimension of this vector is $M_{\mathrm{cpi}} N_{\mathrm{chan}} \times 1$.

For subsequent processing of the data and for visualization, a range Doppler representation of the received data is useful. It is found by applying the discrete Fourier transform across the third dimension (pulse index) to the data [56, Sec. 8.5, eq. (8.67), p. 669], i.e. the pair of the Doppler domain and time domain signal is

$$y^{\Omega}_{\mathrm{trpc}}(k,l,m,n) \quad \bullet\!\!-\!\!\circ \quad w(p) y_{\mathrm{trpc}}(k,l,p,n) . \tag{3.5}$$

Here $m$ is the index of the frequency bin and $w(p)$ is a window function that is applied to the data before computing the discrete Fourier transform. The window function is defined by the product

$$w(p) = w_{\mathrm{taper}}(p) w_0(p) , \tag{3.6}$$

where $w_{\mathrm{taper}}(p)$ is set according to the desired Taper, for example Taylor tapering. The second factor

$$w_0(p) = \mathrm{e}^{-\mathrm{j}2\pi f_0^{\mathrm{ft}} p} \tag{3.7}$$

determines the origin of the frequency vector after applying the Fourier transform. The normalized frequency vector is given by

$$f_m^{\mathrm{ft}} = f_0^{\mathrm{ft}} + \frac{m}{M_{\mathrm{fft}}} , \; m = 0, ..., M_{\mathrm{fft}} - 1 . \tag{3.8}$$

Here $M_{\mathrm{fft}}$ is the number of Fourier bins in the frequency domain. For $M_{\mathrm{fft}} > M_{\mathrm{cpi}}$ the received signal is zero-padded in the time domain before performing the Fourier transform. The frequency domain data can be stacked similarly to the time domain data to $\boldsymbol{y}^{\Omega}_{\mathrm{trp}}(k,l,m)$ (data of all channels of one frequency bin) and $\boldsymbol{y}^{\Omega}_{\mathrm{tr}}(k,l)$ (data of an entire range line).

# 3.1. Application of space time adaptive processing to a received data set

In order to apply the adjacent bin post Doppler algorithm of Section 2.5.2 to the received data set, the signal model of Section 2.4 is adapted to the notation of the received data set (which accounts for the range dependence).

## 3.1.1. Signal model of the received data set

The received data is decomposed into a target signal, a clutter signal and receiver noise

$$\boldsymbol{y}_{\mathrm{tr}}(k,l) = \alpha_{\mathrm{t}}\boldsymbol{y}_{\mathrm{tr,t}}(k,l) + \boldsymbol{y}_{\mathrm{tr,c}}(k,l) + \boldsymbol{y}_{\mathrm{tr,n}}(k,l) \tag{3.9}$$

The sum of receiver noise and clutter is denoted by $\boldsymbol{y}_{\mathrm{tr,q}}(k,l)$. Here $k$ is the index of the CPI and $l$ is the index of range gates within the CPI. The index $k$ is within the interval [1, number of CPIs] and the index $l$ is in the interval [1, number of range gates].

### Target signal

The target signal is modeled as

$$\boldsymbol{y}_{\mathrm{tr,t}}(k,l) = \begin{cases} \boldsymbol{v}(\vartheta_{\mathrm{t},k}, f_{\mathrm{t},k}), \text{ if } l = l_{\mathrm{t},k} \\ \boldsymbol{0}, \text{ otherwise} \end{cases} \tag{3.10}$$

where $\boldsymbol{v}(\cdot,\cdot)$ has already been defined in equation (2.11) of Section 2.4, $\vartheta_{\mathrm{t},k}$ is the spatial frequency of the target at the time of recording CPI $k$ and $f_{\mathrm{t},k}$ is the Doppler frequency of the target at CPI $k$. In comparison to the signal model of Section 2.4 the additional range gate parameter $l_{\mathrm{t}}$ has been introduced. It determines the range gate in which the target signal is present.

These target parameters are related to the Cartesian location and velocity coordinate of the target during CPI $k$ as follows. For clarity of notation, the CPI index $k$ is dropped now. For a target with location $\boldsymbol{x}_{\mathrm{t}}^{\mathcal{E}}$ and velocity vector $\boldsymbol{v}_{\mathrm{t}}^{\mathcal{E}}$, the range to the target is given by

$$r_{\mathrm{t}} = \|\boldsymbol{x}_{\mathrm{t}}^{\mathcal{E}} - \boldsymbol{x}_{\mathrm{ant}}^{\mathcal{E}}\| \tag{3.11}$$

The range bin of the target is given by

$$l_{\mathrm{t}} = \mathrm{round}\left(\frac{r_{\mathrm{t}} - r_0}{\Delta r}\right) \tag{3.12}$$

The direction vector pointing from the antenna to the target is

$$\boldsymbol{u}_{\mathrm{t}}^{\mathcal{E}} = \frac{\boldsymbol{x}_{\mathrm{t}}^{\mathcal{E}} - \boldsymbol{x}_{\mathrm{ant}}^{\mathcal{E}}}{r_{\mathrm{t}}} \tag{3.13}$$

and it is related to the target's spatial frequency by

$$\vartheta_{\mathrm{t}} = \left[\boldsymbol{u}_{\mathrm{t}}^{\mathcal{E}}\right]^{T} \boldsymbol{u}_{\mathrm{ant}}^{\mathcal{E}} \frac{d_{\mathrm{sub}}}{\lambda_0} \tag{3.14}$$

Here, the antenna axis is given by

$$\boldsymbol{u}_{\mathrm{ant}}^{\mathcal{E}} = \left[\mathbf{T}^{\mathcal{A}\leftarrow\mathcal{E}}\right]^{-1} \begin{bmatrix} 1 \\ 0 \\ 0 \end{bmatrix} \tag{3.15}$$

In this equation, the matrix

$$\mathbf{T}^{\mathcal{A}\leftarrow\mathcal{E}} = \mathbf{T}_{\mathrm{Euler}}(\boldsymbol{\gamma}_{\mathrm{ypr}}) \tag{3.16}$$

rotates from the ENU coordinate system to the antenna coordinate system. The radial velocity of the target

$$v_{\mathrm{t,rad}} = \left[\boldsymbol{u}_{\mathrm{t}}^{\mathcal{E}}\right]^{T} \left(\boldsymbol{v}_{\mathrm{t}}^{\mathcal{E}} - \boldsymbol{v}_{\mathrm{ant}}^{\mathcal{E}}\right) \tag{3.17}$$

yields the target signal Doppler frequency

$$F_{\mathrm{t}} = -\frac{2v_{\mathrm{t,rad}}}{\lambda_0} \tag{3.18}$$

The normalized target frequency is

$$f_{\mathrm{t}} = \frac{F_{\mathrm{t}}}{f_{\mathrm{pr}}} \tag{3.19}$$

The angles of arrival are given as

$$\begin{aligned} \varphi_{\mathrm{t}} &= \operatorname{atan2}\left(u_2^{\mathcal{A}}, u_1^{\mathcal{A}}\right),\ \pi \in (-\pi, \pi) \\ \theta_{\mathrm{t}} &= \arccos\left(u_3^{\mathcal{A}}\right),\ \pi \in (0, \pi) \end{aligned} \tag{3.20}$$

and combined to the vector

$$\boldsymbol{\gamma}^{\mathrm{dir}} = \begin{bmatrix} \theta_{\mathrm{t}} \\ \varphi_{\mathrm{t}} \end{bmatrix} \tag{3.21}$$

#### Clutter signal and receiver noise

Both clutter and noise are modeled as realizations of Gaussian random variables, i.e.

$$\boldsymbol{y}_{\mathrm{tr,n}}(k,l) \sim \mathcal{N}^{\mathcal{C}}\left(\mathbf{0}, \mathbf{R}_{\mathrm{n}}\right) \tag{3.22}$$

and

$$\boldsymbol{y}_{\mathrm{tr,c}}(k,l) \sim \mathcal{N}^{\mathcal{C}}\left(\mathbf{0}, \mathbf{R}_{\mathrm{c}}(k,l)\right) \tag{3.23}$$

This notation shows that the clutter covariance matrix is a function of the CPI (index $k$) and range (index $l$).

### 3.1.2. Data preprocessing

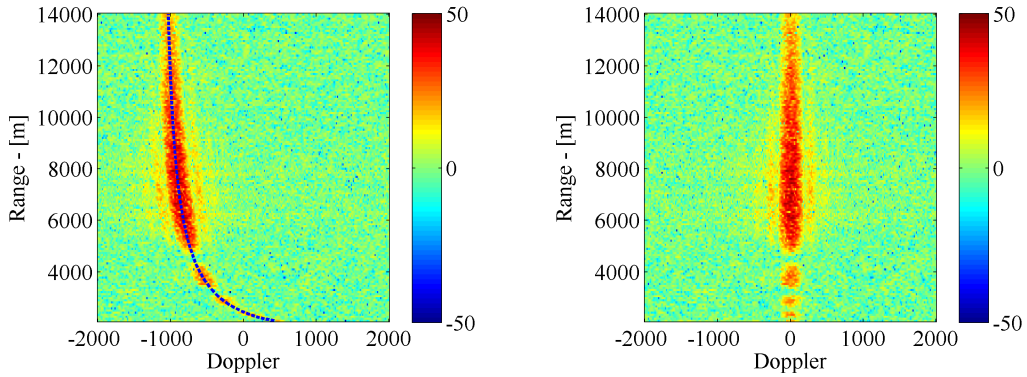


**(a)** Simulated data with J-hook **(b)** Simulated data after J-Hook removal

**Figure 3.2.:** Visualization of simulated received radar data in the range Doppler domain before and after removal of the J-Hook.

With STAP, the covariance matrix is estimated using data of the same CPI, but different range lines. It is important, that the statistical properties of these data are as close as possible to those of the cell under test. Otherwise, the performance will degrade. If the antenna axis is coaxial with the direction of flight, the relation between DOA and frequency for ground clutter is range independent. The only range dependence in clutter is then that of clutter power.

However, if the antenna and the flight direction are not coaxial, the relation between the direction of arrival and the clutter Doppler frequency becomes range dependent. For example, this is visible in Figure 3.2a of a simulated data set with a a yaw angle 10 degrees and a squint angle of 7 degrees. At high ranges, the clutter centroid, i.e clutter impinging from the steering direction lies at -1000 Hz. For small ranges, there is a curvature in the clutter frequency, the so called J-hook.

Thus, in general, the statistical similarity between data of different range lines is not given. To remedy this, in a preprocessing step the J-hook is removed by a range dependent frequency shift of the data. After the frequency shift, the clutter centroid of the data is located at 0 Hz, regardless of the range. The magnitude of the frequency shift is equivalent to the range dependent

frequency value of the clutter centroid. It is determined with the function

$$f_{\text{centroid}}(k,l) = f_n^{\text{f}\leftarrow\text{ur}}\left(u_{\text{st},k}, r_l, \boldsymbol{x}_{\text{ant},k}^{\mathcal{E}}, \boldsymbol{\gamma}_{\text{yp},k}^{\mathcal{A}\leftarrow\mathcal{E}}, \boldsymbol{n}_{\text{plane}}^{\mathcal{E}}, d_{\text{plane}}^{\mathcal{E}}; \lambda_{0,k}\right) , \tag{3.24}$$

which is given in Appendix A.4. This function is defined with the help of another function, $\boldsymbol{f}_{\text{rc},n}^{\mathcal{E}\leftarrow\text{ur}}$ that locates a measurement of range and direction of arrival on a surface plane that serves as approximation for the ground. This function is also used for geolocating targets (see Section 3.3.1). Once that the located position of a range DOA pair has been found, the computation of the corresponding radial velocity and range Doppler frequency is straight forward. After the removal of the J-hook, the data is given by

$$y^{\text{trp,dcs}}(k,l,m,n) = \mathrm{e}^{-\mathrm{j}2\pi t_m f_{\text{centroid}}(k,l)} y^{\text{trp}}(k,l,m,n) \tag{3.25}$$

where $t_{\text{m}} = \frac{m}{f_{\text{pr}}}$ is the slow time within the CPI of pulse $m$. The stacked version and the frequency domain version of the received signal after Doppler centroid shift (DCS) are found as above. The frequency vector of the DCS signal is given by $f_{\text{dcs},m} = -\frac{f_{\text{pr}}}{2} + \frac{m}{M_{\text{fft}}}$. To visualize the effect of DCS, Figure 3.2a shows the simulated data set after removal of the J-hook.

### 3.1.3. Target detection with adjacent bin post Doppler processing

After DCS, the data is processed with the adjacent bin post Doppler algorithm that has been presented in Section 2.5.2. The spacial steering vector is given by

$$\boldsymbol{a}(\vartheta_{\text{st},k}) \tag{3.26}$$

where

$$\vartheta_{\text{st},k} = u_{\text{st},k,1}^{\mathcal{A}} \frac{d_{\text{sub}}}{\lambda_0} \tag{3.27}$$

is the spatial frequency that corresponds to the steering direction of the antenna at CPI $k$. Thus, the space time steering vector for a target with normalized frequency $f_m$ is

$$\boldsymbol{v}_{\text{s},m} = \boldsymbol{v}(\vartheta_{\text{st},k}, f_{\text{m}}) = \boldsymbol{b}(f_m) \otimes \boldsymbol{a}(\vartheta_{\text{st},k}) \,. \tag{3.28}$$

This space time steering vector is independent of the target range. The transformed data for the detection of a target with frequency $f_m$ is given by

$$\tilde{\boldsymbol{y}}(k,l,m) = \mathbf{T}_{\text{m}} \boldsymbol{y}_{\text{tr}}(k,l) \tag{3.29}$$

where $\mathbf{T}_m$ is constructed according to equations (2.21) to (2.23) of Section 2.5.2. The transformed steering vector is

$$\tilde{\boldsymbol{v}}_{\mathrm{s},m} = \mathbf{T}_m \boldsymbol{v}_{\mathrm{s},m} \,. \tag{3.30}$$

The estimate of the clutter covariance matrix for the detection of a target at range gate $l$ and frequency $f_m$ is given by

$$\hat{\tilde{\mathbf{R}}}_{\mathrm{q}}(k,l,m) = \frac{1}{|\mathcal{M}_{\mathrm{t}}|} \sum_{\mathcal{M}_{\mathrm{t}}} \tilde{\boldsymbol{y}}(k,l,m) \left[\tilde{\boldsymbol{y}}(k,l,m)\right]^H \tag{3.31}$$

Here $\mathcal{M}_{\mathrm{t}}$ is the set of range gates that is used for training and $|\mathcal{M}_{\mathrm{t}}|$ is the number of training samples. The test variable for detecting a target of CPI $k$, range gate $l$ and Doppler bin $m$ is given by

$$z(k,l,m) = \frac{\left| \left[\tilde{\boldsymbol{v}}_{\mathrm{s},m}\right]^H \left[\hat{\tilde{\mathbf{R}}}_{\mathrm{q}}(k,l,m)\right]^{-1} \tilde{\boldsymbol{y}}(k,l,m) \right|^2}{\left[\tilde{\boldsymbol{v}}_{\mathrm{s},m}\right]^H \left[\hat{\tilde{\mathbf{R}}}_{\mathrm{q}}(k,l,m)\right]^{-1} \tilde{\boldsymbol{v}}_{\mathrm{s},m}} \,. \tag{3.32}$$

This test variable is compared to the detection threshold $t_{\mathrm{th}}$ [64]

$$z(k,l,m) \underset{H_0}{\overset{H_1}{\gtrless}} t_{\mathrm{th}} \tag{3.33}$$

Detections are numbered in an arbitrary order and indexed by $p = 1, ..., N_{\mathrm{z},k}$, where $N_{\mathrm{z},k}$ is the number of detections at CPI $k$. The range bin where the detection has been made is $l_p$ and the Doppler bin is $m_p$. Each target detection is associated with the covariance matrix

$$\hat{\mathbf{R}}_{\mathrm{q},k,p} = \hat{\tilde{\mathbf{R}}}_{\mathrm{q}}(k, l_p, m_p) \tag{3.34}$$

and the data vector is

$$\boldsymbol{y}_{k,p} = \tilde{\boldsymbol{y}}(k, l_p, m_p) \tag{3.35}$$

**Practical implementation** In practice, the Fourier transform is done with the fast Fourier transform in parallel for all Fourier bins and not by matrix multiplication, see equation (3.5).

**Clustering of detections** Often a single target causes multiple detections in adjacent test cells, either in range or in Doppler. For a cluster of detections, the detections can be sorted by significance, i.e. the detection with the largest valued test variable is the most significant one. In the detection clustering step, only this most significant detection is retained.

## 3.2. Parameter estimation

### 3.2.1. Target radial velocity

Each detection implicitly provides estimates of the target range and target Doppler frequency with the range gate and Doppler bin of detection. Due to frequency folding, the Doppler estimate is ambiguous, i.e. for a detection $p$ at time step $k$ at Doppler bin $m_p$ and range gate $l_p$, any of the normalized Doppler estimates

$$\hat{f}_{\mathrm{amb},k,p}(q) = f_{m_p} + \frac{f_{\mathrm{centroid}}(k, l_p)}{F_{\mathrm{pr}}} + q \text{ , where } q = ..., -1, 0, 1, ... \tag{3.36}$$

is valid. Here, $\frac{f_{\mathrm{centroid}}(k,l_p)}{F_{\mathrm{pr}}}$ accounts for the shift of the Doppler centroid during preprocessing and the possible values of $q$ represent the ambiguity. These estimates correspond to the ambiguous radial velocity estimate

$$\hat{v}_{\mathrm{rad,amb},k,p}(q) = -\frac{\lambda_{0,k}}{2} F_{\mathrm{pr}} \hat{f}_{\mathrm{amb},k,p}(q) \text{ , where } q = ..., -1, 0, 1, ... \tag{3.37}$$

For recording configurations with small pulse repetition frequencies, tracking algorithms have to take the ambiguity in estimating the Doppler frequency/radial velocity into account. If the pulse repetition frequency is sufficiently large, all but one of the possible radial velocity estimates in equation (3.37) are unlikely – these radial velocities are too small or large for a realistic target. In this case, it is desirable to provide the tracking algorithm only with the likely estimate and this most likely estimate shall be the output of the estimation step.

In order to determine the most likely velocity estimate, one recalls that the radial velocity of a target (see equation (3.17)) is the sum

$$v_{\mathrm{rad}} = v_{\mathrm{rad,a}} + v_{\mathrm{rad,t}} \tag{3.38}$$

of a component which is due to the antenna motion $v_{\mathrm{rad,a}} = -\left[\boldsymbol{u}_{\mathrm{at}}^{\mathcal{E}}\right]^{\mathrm{T}} \boldsymbol{v}_{\mathrm{ant}}^{\mathcal{E}}$ and a component caused by the target motion itself $v_{\mathrm{rad,t}} = \left[\boldsymbol{u}_{\mathrm{at}}^{\mathcal{E}}\right]^{\mathrm{T}} \boldsymbol{v}_{\mathrm{t}}^{\mathcal{E}}$. Since the target detections are most likely in the antenna main beam, the antenna component of the radial velocity is approximately the radial velocity of the clutter centroid, i.e.

$$v_{\mathrm{rad,a}} \approx -\frac{\lambda_{0,k}}{2} f_{\mathrm{centroid}}(k, l_{\mathrm{t}}) \,. \tag{3.39}$$

The radial velocity estimates shall be centered at $v_{\mathrm{rad,a}}$. Thus, the Doppler frequency and radial velocity estimates are

$$\hat{f}_{k,p} = f_{m_p} + \frac{f_{\mathrm{centroid}}(k, l_p)}{F_{\mathrm{pr}}} \tag{3.40}$$

and

$$\hat{v}_{\mathrm{rad},k,p} = -\frac{\lambda_{0,k}}{2} F_{\mathrm{pr}} \hat{f}_{k,p} \,. \tag{3.41}$$

### 3.2.2. Target range

Similarly to the Doppler estimate, the range estimate of a pulse Doppler radar is ambiguous. This is due to the fact, that a received signal is potentially due to backscattering of *any* of the previously emitted pulses [83, p. 22]. Thus, for a detection $p$ with range bin $l_p$ at time step $k$, the range estimates

$$\hat{r}_{\mathrm{amb},k,p}(q) = r_{l_p} + pR_{\mathrm{U}} \text{ ,where } q = 0, 1, 2, ... \tag{3.42}$$

is valid. Here, $R_{\mathrm{u}} = \frac{c}{2F_{\mathrm{pr}}}$ is the unambiguous range [83, p. 22]. For large values of the pulse repetition frequency these ambiguities have to be taken into account by the tracking algorithm. If the pulse repetition frequency is sufficiently small, then it is reasonable to assume that the detection is within the first unambiguous range. Thus, the output of the estimation step is given by

$$\hat{r}_{k,p} = r_{l_p} \,. \tag{3.43}$$

### 3.2.3. Direction of arrival estimation

The direction of arrival estimation is performed with the central Doppler bin of the test data; the adjacent Doppler bins are discarded. The data of the central Doppler bin is of the dimension $N_{\mathrm{chan}} \times 1$. For detection $p$ of time step $k$ it is extracted from the multiple bin data by the matrix multiplication

$$\boldsymbol{y}_{\mathrm{sb},k,p} = \mathbf{T}_{\mathrm{sb}}^{T} \boldsymbol{y}_{k,p} \,, \tag{3.44}$$

where

$$\mathbf{T}_{\mathrm{sb}} = \begin{bmatrix} \mathbf{0}_{P\times 1} \\ 1 \\ \mathbf{0}_{P\times 1} \end{bmatrix} \otimes \mathbf{I}_{N_{\mathrm{chan}}} \tag{3.45}$$

is the central Doppler bin selector matrix. The estimate of the clutter covariance matrix of the central Doppler bin is given by

$$\hat{\mathbf{R}}_{\mathrm{q,sb},k,p} = \mathbf{T}_{\mathrm{sb}}^{H} \hat{\mathbf{R}}_{\mathrm{q},k,p} \mathbf{T}_{\mathrm{sb}} \,. \tag{3.46}$$

The signal model for the received data of the central Doppler bin is

$$\boldsymbol{y}_{\mathrm{sb},k,p} = a_{\mathrm{t},k,p} \mathrm{e}^{\mathrm{j}\phi_{\mathrm{t},k,p}} \boldsymbol{d}\left(u_{\mathrm{t},k,p}\right) + \boldsymbol{q}_{\mathrm{sb},k,p}\,, \tag{3.47}$$

where $a_{\mathrm{t},k,p}$ is the amplitude of the target signal, $\phi_{\mathrm{t},k,p}$ is its phase, $u_{\mathrm{t},k,p}$ is the directional cosine of the target and $\boldsymbol{q}_{\mathrm{sb},k,p}$ is the clutter and noise signal at the range Doppler bin of detection. The direction of arrival vector $\boldsymbol{d}$ is related to the spatial steering vector of equation (2.7) according to

$$\boldsymbol{d}(u) = \boldsymbol{b}\left(u\frac{d_{\mathrm{sub}}}{\lambda_0}\right)\,. \tag{3.48}$$

The DOA vector is periodic in $u$, i.e. $\boldsymbol{d}(u) = \boldsymbol{d}(u + u_{\mathrm{rep}})$, where $u_{\mathrm{rep}} = \frac{\lambda_0}{d_{\mathrm{sub}}}$. Thus, an estimate of $u$ will be ambiguous with $u_{\mathrm{rep}}$. Since $|u| \leq 1$ ambiguities can be excluded, if $u_{\mathrm{rep}} < 2$.

An estimate of the directional cosine is found with a maximum likelihood estimator or with the monopulse technique [53]. The maximum likelihood estimate is given by

$$\hat{u}_{k,p} = \arg\max_{u} \left\{ \frac{\left| \boldsymbol{d}(u)^H \left[\hat{\mathbf{R}}_{\mathrm{q,sb},k,p}\right]^{-1} \boldsymbol{y}_{\mathrm{sb},k,p} \right|^2}{\boldsymbol{d}(u)^H \left[\hat{\mathbf{R}}_{\mathrm{q,sb},k,p}\right]^{-1} \boldsymbol{d}(u)} \right\}\,, \text{where } |\hat{u}_{k,p} - u_{\mathrm{st},k}| < \frac{u_{\mathrm{rep}}}{2}\,. \tag{3.49}$$

The constraint $|\hat{u}_{k,p} - u_{\mathrm{st},k}| < \frac{u_{\mathrm{rep}}}{2}$ ensures that – among all the ambiguous estimates – $\hat{u}_{k,p}$ is the estimate which lies the closest to the main beam. In general, the ambiguous estimates are given by

$$\hat{u}_{\mathrm{amb},k,p}(q) = \hat{u}_{k,p} + q u_{\mathrm{rep}}\ \text{, where }\ |\hat{u}_{\mathrm{amb},k,p}(q)| < 1 \tag{3.50}$$

**Impact of the DOA estimation ambiguities** The significance of the DOA estimation ambiguities depends on the value of $u_{\mathrm{rep}}$ and the antenna power pattern. Obviously, for $u_{\mathrm{rep}} > 2$ there are no ambiguities at all. For smaller values of $u_{\mathrm{rep}}$, the question is whether ambiguous measurements can be excluded due to the antenna power pattern.

This point shall be illustrated with Figure 3.3 that shows the two way power pattern of the PAMIR array for $u_{\mathrm{st}} = 0$. It is the pattern of an untapered linear array as the PAMIR system cannot be tapered in the Scan-MTI mode (since the antenna is not calibrated for tapered receive). The pattern shows that signals impinging from the main lobe are about 26 db stronger than signals from the first side lobe and 36 dB stronger than signals from the second side lobe. Vertical, dashed lines – spaced $u_{\mathrm{rep}}$ apart – indicate the edges of the ambiguity intervals, i.e. the directional cosine can only be estimated with respect to the position of the dashed lines.

This pattern shows that targets in the third or fourth antenna side lobe are suppressed by about 40 dB with respect to main lobe targets. Thus, it is most likely that a target that is placed in the main lobe by its estimate $\hat{u}_k^{(p)}$ is in fact from the main lobe area. However, strong stationary targets, e.g. large buildings may cause detections, even if their reflections impinge from the side

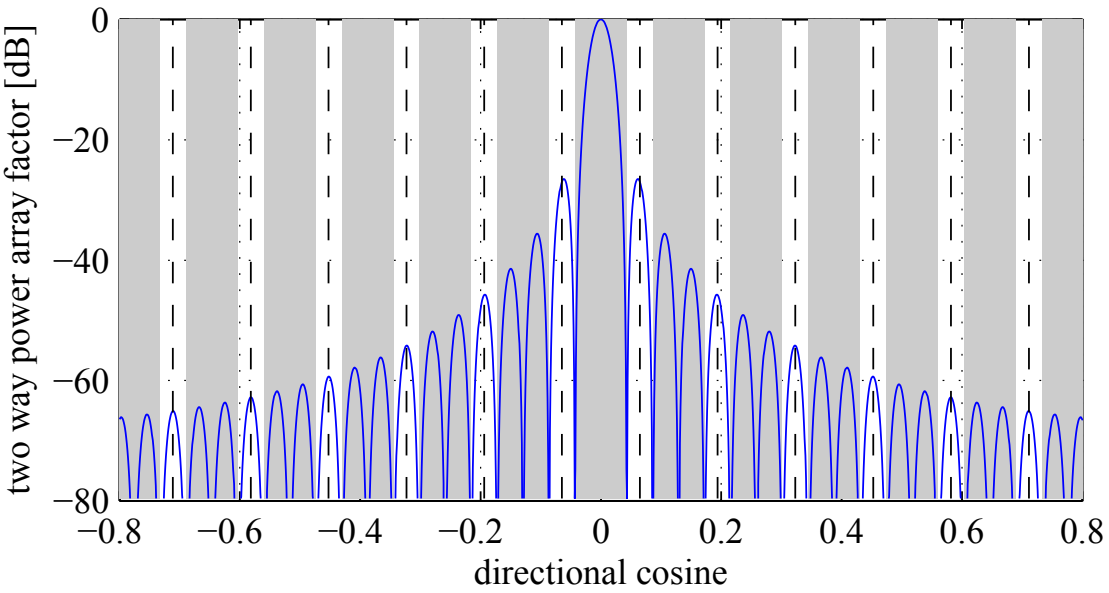


**Figure 3.3.:** Two way antenna pattern of PAMIR of the Scan-MTI mode. Due to the lack of tapering, high side lobes are present. Dashed vertical lines indicate the width of the unambiguous DOA estimation interval. Shaded intervals (in gray) correspond to DOA angles that seemingly are due to targets in the main lobe. For example, targets that are located in the third and fourth sidelobes – if detected – cannot be distinguished from targets in the main lobe. Targets in the first, fourth side lobe, etc. can be distinguished.

lobes. In this case, the above reasoning will lead to an incorrect geolocation of the detection.

## 3.3. Geolocation of detections

As a result of the target detection and parameter estimation step $N_{z,k}$ detections are made for each CPI. Each of these detections $p = 1, ...N_{z,k}$ is associated with estimates of the direction of arrival, the range and the radial velocity. Combined, the measurements yield the measurement vector $\boldsymbol{z}_{k,p} = [\hat{u}_{k,p} \quad \hat{r}_{k,p} \quad \hat{v}_{\mathrm{rad},k,p}]^{\mathrm{T}}$, where $p$ is the index of the detection. This section presents the geolocation of these detections, i.e. how these measurements are used to compute a Cartesian position.

The task of geolocation of a detection consists of converting the measurements of range and DOA to a location in the 3 dimensional ENU coordinate system. Due to the DOA measurement, the target location is constrained to a cone whose central axis is given by the orientation of the linear array. The range measurement constraints to a sphere. The combination of both constraints signifies that the detection is located on a circle. Clearly, an additional constraint is necessary for the geolocation a detection

### 3.3.1. Geolocation of the detections with a plane earth assumption

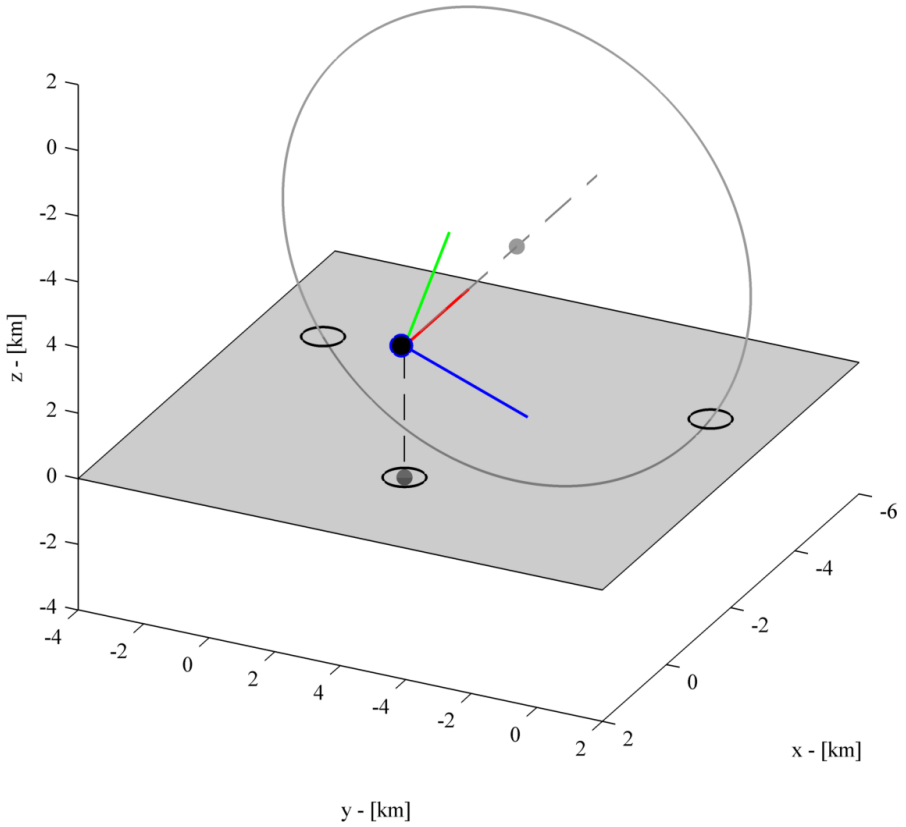


**Figure 3.4.:** A target is geolocated by combining the range measurement, i.e. distance to the radar antenna, the direction of arrival measurement and the information that it lies on a plane that approximates the earth's surface. In general, there are two solutions. In this Figure, the $x$, $y$ and $z$ axes of the antenna coordinate system are colored red, green and blue, respectively.

If only a coarse geolocation in a relatively small area is required, modeling the earth's surface as a plane provides the additional information. The detection is then constrained to a plane and the located position is the intersection of the plane with the circle.

As there are in general (except of the degenerate case that the circle lies within the plane) 0, 1 or 2 intersections of the circle with the plane, there are also, in general, 0, 1 or two possible locations of the target. A sample case is illustrated by Figure 3.4. In the case of this Figure the circle intersects the plane at two location. In case that there are two solutions, both solutions, for $n = 1, 2$ are found with the function

$$\hat{\boldsymbol{x}}^{\mathcal{E}}_{\mathrm{tgt},k,p,n} = \boldsymbol{f}^{\mathcal{E}\leftarrow\mathrm{ur}}_{\mathrm{rc},n}\left(\hat{u}_{k,p}, \hat{r}_{k,p}; \hat{\boldsymbol{x}}^{\mathcal{E}}_{\mathrm{ant},k}, \hat{\boldsymbol{e}}^{\mathcal{E}}_{\mathrm{ant},k,1}, \boldsymbol{n}^{\mathcal{E}}_{\mathrm{plane}}, d^{\mathcal{E}}_{\mathrm{plane}}\right) \tag{3.51}$$

which is given in an implementable algorithmic form in Appendix A.1.1. In most practical cases

and in all situations that are investigated here, one of these solutions places the target in the back lobe area of the antenna, i.e. in a location where a target detection is highly unlikely. In order to obtain a unique solution, the other solution, which is not in the back lobe, is selected. If both solutions are in the back lobe or not in the back lobe, then an arbitrary solution is chosen. In any case, in function form, the unique target geolocation is given by

$$\hat{\boldsymbol{x}}^{\mathcal{E}}_{\mathrm{tgt},k,p} = \boldsymbol{f}^{\mathcal{E}\leftarrow\mathrm{ur}}_{\mathrm{rc}}\left(\hat{u}_{k,p}, \hat{r}_{k,p}, \hat{\boldsymbol{x}}^{\mathcal{E}}_{\mathrm{ant},k}, \hat{\boldsymbol{e}}^{\mathcal{E}}_{\mathrm{ant},k,1}, \boldsymbol{n}^{\mathcal{E}}_{\mathrm{plane}}, d^{\mathcal{E}}_{\mathrm{plane}}\right) , \tag{3.52}$$

which is defined in Section A.1.4.

### 3.3.2. Conversion of the Doppler measurement with a plane earth assumption

The radial velocity $v_{\mathrm{rad}}$ of a target is related to the target velocity $\boldsymbol{v}^{\mathcal{E}}_{\mathrm{tgt}}$ and platform velocity $\boldsymbol{v}^{\mathcal{E}}_{\mathrm{ant}}$ by

$$v_{\mathrm{rad}} = \left[\boldsymbol{u}^{\mathcal{E}}_{\mathrm{at}}\right]^{\mathrm{T}} \left(\boldsymbol{v}^{\mathcal{E}}_{\mathrm{tgt}} - \boldsymbol{v}^{\mathcal{E}}_{\mathrm{ant}}\right) , \tag{3.53}$$

where

$$\boldsymbol{u}^{\mathcal{E}}_{\mathrm{at}} = \frac{\boldsymbol{x}^{\mathcal{E}}_{\mathrm{tgt}} - \boldsymbol{x}^{\mathcal{E}}_{\mathrm{ant}}}{\|\boldsymbol{x}^{\mathcal{E}}_{\mathrm{grd},n} - \boldsymbol{x}^{\mathcal{E}}_{\mathrm{ant}}\|} , \tag{3.54}$$

is the direction vector pointing from the antenna to the target location $\boldsymbol{x}^{\mathcal{E}}_{\mathrm{tgt}}$. The component of the radial velocity which is due to the motion of the target itself is given by

$$v_{\mathrm{t,rad}} = \left[\boldsymbol{u}^{\mathcal{E}}_{\mathrm{at}}\right]^{\mathrm{T}} \boldsymbol{v}^{\mathcal{E}}_{\mathrm{tgt}} = v_{\mathrm{rad}} + \left[\boldsymbol{u}^{\mathcal{E}}_{\mathrm{at}}\right]^{\mathrm{T}} \boldsymbol{v}^{\mathcal{E}}_{\mathrm{ant}} . \tag{3.55}$$

Thus, the estimate of the radial velocity can be converted to an estimate of the target component of the radial velocity by

$$\hat{v}_{\mathrm{t,rad},k,p} = \hat{v}_{\mathrm{rad},k,p} + \left[\hat{\boldsymbol{u}}^{\mathcal{E}}_{\mathrm{at},k,p}\right]^{\mathrm{T}} \hat{\boldsymbol{v}}^{\mathcal{E}}_{\mathrm{ant},k} , \tag{3.56}$$

where

$$\hat{\boldsymbol{u}}^{\mathcal{E}}_{\mathrm{at},k,p} = \frac{\hat{\boldsymbol{x}}^{\mathcal{E}}_{\mathrm{tgt},k,p} - \hat{\boldsymbol{x}}^{\mathcal{E}}_{\mathrm{ant},k}}{\|\hat{\boldsymbol{x}}^{\mathcal{E}}_{\mathrm{tgt},k,p} - \hat{\boldsymbol{x}}^{\mathcal{E}}_{\mathrm{ant},k}\|} . \tag{3.57}$$

is the estimate of the direction vector. Thus, one of the 3 Cartesian velocity components of the target – i.e. the one aligned with the line of sight between antenna and target – can be directly estimated from the detection data. Additionally, the fact that the target's motion is constrained to the plane provides the information that the target's velocity perpendicular to the plane is 0. Thus, the target's radial velocity can be converted to the component of the target velocity which

is parallel to the projection of the direction vector onto the plane

$$\boldsymbol{u}^{\mathcal{E}}_{\mathrm{at,p}} = \mathbf{P}^{\mathcal{E}}_{\mathrm{plane}} \boldsymbol{u}^{\mathcal{E}}_{\mathrm{at}} \tag{3.58}$$

$$= \boldsymbol{u}^{\mathcal{E}}_{\mathrm{at}} - \rho_{\mathrm{pl,at}} \boldsymbol{n}^{\mathcal{E}}_{\mathrm{plane}} \,. \tag{3.59}$$

(see Figure 3.5 and Figure 3.6) The magnitude of this target velocity component is related to the full target velocity vector according to

$$v_{\mathrm{t,pl}} = \left[\boldsymbol{v}^{\mathcal{E}}_{\mathrm{tgt}}\right]^{\mathrm{T}} \frac{\boldsymbol{u}^{\mathcal{E}}_{\mathrm{at,p}}}{\|\boldsymbol{u}^{\mathcal{E}}_{\mathrm{at,p}}\|} = \frac{v_{\mathrm{t,rad}}}{\|\boldsymbol{u}^{\mathcal{E}}_{\mathrm{at,p}}\|} \,. \tag{3.60}$$

An estimate of this velocity component is obtained with

$$\hat{v}_{\mathrm{t,pl},k,p} = \frac{\hat{v}_{\mathrm{t,rad},k,p}}{\|\hat{\boldsymbol{u}}^{\mathcal{E}}_{\mathrm{at,p}}\|} \,, \tag{3.61}$$

where

$$\hat{\boldsymbol{u}}^{\mathcal{E}}_{\mathrm{at,p}} = \mathbf{P}^{\mathcal{E}}_{\mathrm{plane}} \hat{\boldsymbol{u}}^{\mathcal{E}}_{\mathrm{at}} \tag{3.62}$$

is the estimate of the projection of the direction vector on the surface plane. The estimate of this target velocity component is given in function form in Section A.2.1 and A.2.3 by

$$\hat{v}_{\mathrm{t,pl},k,p} = \boldsymbol{f}^{\mathrm{v}\leftarrow\mathrm{urv}} \left( \hat{u}_{k,p}, \hat{r}_{k,p}, \hat{v}_{\mathrm{rad},k,p}, \hat{\boldsymbol{x}}^{\mathcal{E}}_{\mathrm{ant},k}, \hat{\boldsymbol{e}}^{\mathcal{E}}_{\mathrm{ant},k,1}, \boldsymbol{n}^{\mathcal{E}}_{\mathrm{plane}}, d^{\mathcal{E}}_{\mathrm{plane}} \right) \,. \tag{3.63}$$

### 3.3.3. Geolocation with a digital elevation model

In cases where the approximation of the ground as plane is not sufficiently accurate, a digital elevation model (DEM) is required for the geolocation. In this thesis the DEM is given as z values for a grid of x-y coordinates in the ENU coordinate system. This representation is possible for small areas as long as there is a unique z value for every location. For an arbitrary x-y coordinate, the z value is found by bilinear interpolation

$$f_{\mathrm{bilin}} \left( \begin{bmatrix} x \\ y \end{bmatrix}, \boldsymbol{\theta}_{\mathrm{dem}} \right) \,, \tag{3.64}$$

where the definition of the bilinear interpolation is given in Appendix A.7.3.

#### Intersection of the DEM surface and the circle

Due to the constraints, the detection must be located at the intersection of the surface that is defined by the DEM and the circle. Any position on the circle can be represented by the angle $\phi$;

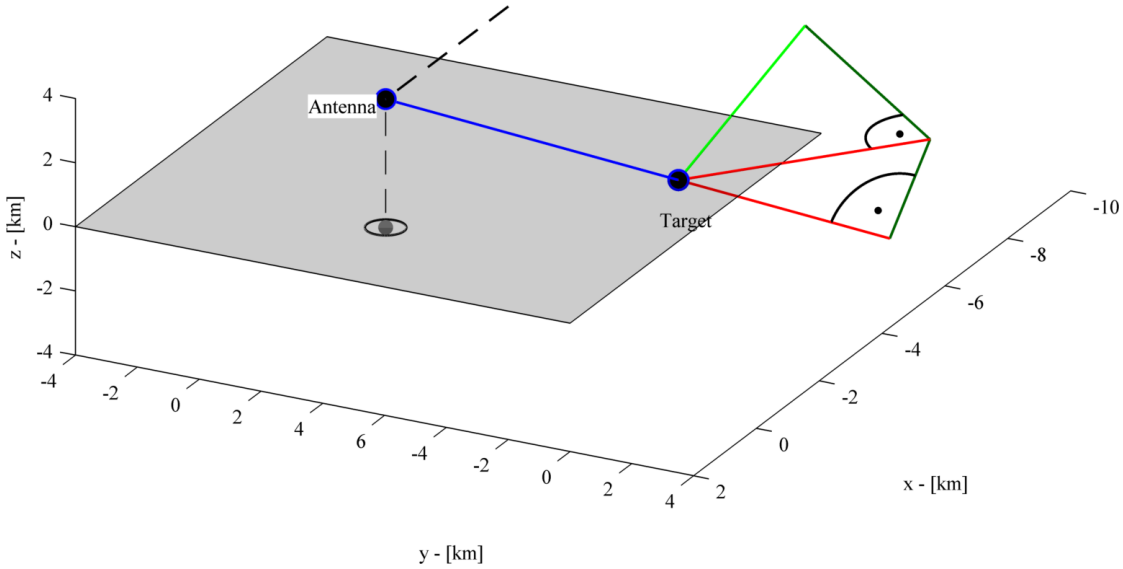


**Figure 3.5.:** A 3D view of the conversion of the velocity measurement. Due to the information that the target motion is constrained to a plane, the line of sight velocity of the target can be converted to a component of the target velocity that lies within the plane. In this Figure the line of sight between the antenna and the target is shown in blue and the true target velocity is represented in light green. Velocity components that cannot be measured are shown in dark green and velocity components that can be measured in red.

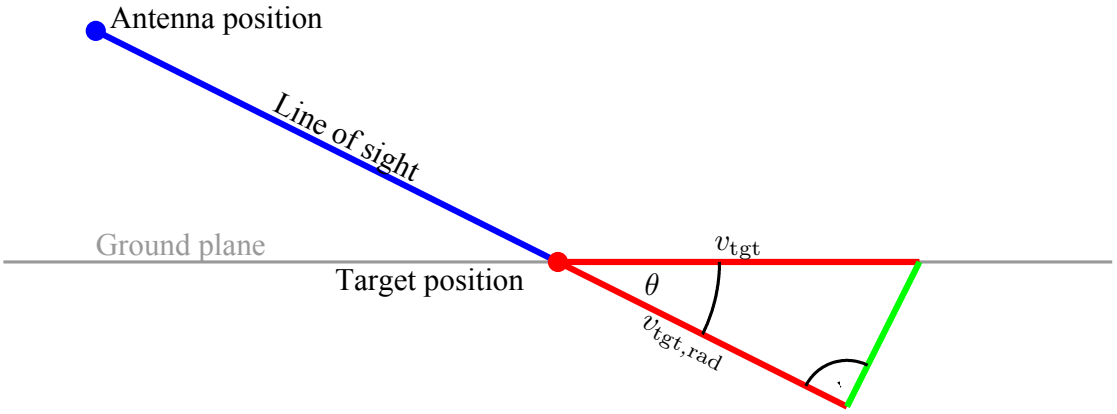


**Figure 3.6.:** A cut through the 3d view of Figure 3.5: The velocity component $v_{\mathrm{tgt,rad}}$ of the target that lies along the line of sight between the target and the antenna is converted into a velocity component that lies within the plane.

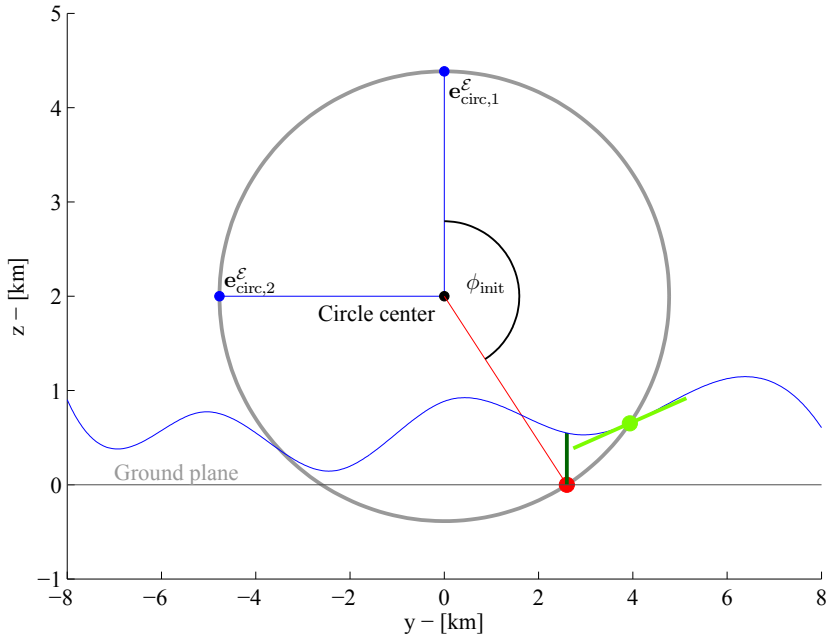


**Figure 3.7.:** Geolocation with a digital elevation model. The location of the detection must lie at the intersection of the circle and the surface that is defined by the DEM.

the corresponding position in the ENU coordinate system is

$$\boldsymbol{x}_{\text{phi}}(\phi) = \boldsymbol{m}^{\mathcal{E}}_{\text{circ}} + r_{\text{circ}}\boldsymbol{e}^{\mathcal{E}}_{\text{circ},1}\cos(\phi) + r_{\text{circ}}\boldsymbol{e}^{\mathcal{E}}_{\text{circ},2}\sin(\phi)\ . \tag{3.65}$$

For the first two components of this coordinate $\boldsymbol{x}_{\text{phi},(1,2)}(\phi)$ the corresponding point on the DEM surface can be computed. If $\boldsymbol{x}_{\text{phi}}(\phi)$ lies on the surface, then these points are identical and

$$f_{\text{bilin}}\left(\boldsymbol{x}_{\text{phi},(1,2)}(\phi), \boldsymbol{z}_{\text{dem}}\right) = x_{\text{phi},3}(\phi)\,. \tag{3.66}$$

For other values of $\phi$, there is a difference in the elevation which is given by

$$f_{\text{error}}(\phi) = f_{\text{bilin}}\left(\boldsymbol{x}_{\text{phi},(1,2)}(\phi), \boldsymbol{z}_{\text{dem}}\right) - x_{\text{phi},3}(\phi)\,. \tag{3.67}$$

Thus, numerically solving

$$f_{\text{error}}(\phi_{\text{int}}) = 0 \tag{3.68}$$

finds one of the solutions for the geolocation. (see Figure 3.7) The coordinate of this solution is

$$\boldsymbol{x}_{\text{sol},1} = \boldsymbol{f}_{\text{surf}}\left(\boldsymbol{x}_{\text{phi},(1,2)}(\phi_{\text{int}}), \boldsymbol{z}_{\text{dem}}\right) = \boldsymbol{x}_{\text{phi}}(\phi_{\text{int}}) \tag{3.69}$$

A second solution may be found by selecting a different starting value for $\phi$ for solving equation (3.68). At the location of the solution a tangent plane to the DEM surface exists. It is spanned by the vectors

$$\boldsymbol{r}_{\mathrm{x}}(\boldsymbol{x}^{\mathrm{2d}}, \boldsymbol{z}_{\mathrm{dem}}) = \frac{\partial \boldsymbol{f}_{\mathrm{surf}}}{\partial x_1^{\mathrm{2d}}}(\boldsymbol{x}^{\mathrm{2d}}, \boldsymbol{z}_{\mathrm{dem}}) = \begin{bmatrix} 1 \\ 0 \\ \frac{\partial f_{\mathrm{bilin}}}{\partial x_1^{\mathrm{2d}}}(\boldsymbol{x}, \boldsymbol{\theta}_{\mathrm{grid}}) \end{bmatrix} \tag{3.70}$$

and

$$\boldsymbol{r}_{\mathrm{y}}(\boldsymbol{x}^{\mathrm{2d}}, \boldsymbol{z}_{\mathrm{dem}}) = \frac{\partial \boldsymbol{f}_{\mathrm{surf}}}{\partial x_1^{\mathrm{2d}}}(\boldsymbol{x}^{\mathrm{2d}}, \boldsymbol{z}_{\mathrm{dem}}) = \begin{bmatrix} 0 \\ 1 \\ \frac{\partial f_{\mathrm{bilin}}}{\partial x_2^{\mathrm{2d}}}(\boldsymbol{x}, \boldsymbol{\theta}_{\mathrm{grid}}) \end{bmatrix} \tag{3.71}$$

The partial derivatives of $f_{\mathrm{bilin}}$ are derived later and given by equation (A.62b). The normal vector of the tangent plane is given by

$$\boldsymbol{n}^{\mathcal{E}}_{\mathrm{tangent}}(\boldsymbol{x}^{\mathrm{2d}}, \boldsymbol{z}_{\mathrm{dem}}) = \boldsymbol{r}_{\mathrm{x}}(\boldsymbol{x}^{\mathrm{2d}}, \boldsymbol{z}_{\mathrm{dem}}) \times \boldsymbol{r}_{\mathrm{y}}(\boldsymbol{x}^{\mathrm{2d}}, \boldsymbol{z}_{\mathrm{dem}}) \tag{3.72}$$

and the distance to the coordinate system origin is

$$d^{\mathcal{E}}_{\mathrm{tangent}} = \left[\boldsymbol{n}^{\mathcal{E}}_{\mathrm{tangent}}(\boldsymbol{x}^{\mathrm{2d}}, \boldsymbol{z}_{\mathrm{dem}})\right]^{\mathrm{T}} \boldsymbol{f}_{\mathrm{surf}}\left(\boldsymbol{x}^{\mathrm{2d}}, \boldsymbol{z}_{\mathrm{dem}}\right) . \tag{3.73}$$

For the specific detection, the same ENU location is found either by performing the geolocation with the tangent plane according to Section 3.3.1 or by using the DEM based geolocation. Thus, error calculations of the DEM based geolocation can be performed with the geolocation for a planar surface.

# 4. Fundamentals of target tracking

The task of target tracking is to reconstruct the motion of targets or objects based on measurement data [7, Sec. 1.1]. In general, the measurements may be provided by radar, infrared sensors, sonar or other sensors. Most tracking algorithms do not receive the full measurement data that is recorded by the device. In most cases, it would be computationally infeasible to do so. Instead, in between the sensor and the tracking algorithm there is usually a detection and parameter estimation step. In this step the received data is processed in order to detect targets of interest. For each target, some parameters such as its location or velocity are estimated. Over time the tracking algorithm is provided with a sequence of target detections.

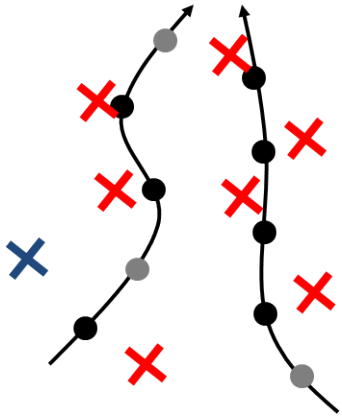

**Figure 4.1.:** An illustration of a complicated tracking situation: The tracking algorithm receives erroneous – due to noise and clutter – location measurements (red), a false alarm (blue) of two closely spaced targets. The locations of the targets where detections are made are marked by black circles, locations when a detection is missed are marked in grey.

Thus, the task of target tracking can be formulated more precisely: it is to reconstruct the motion of targets based on a sequence of target detections with associated parameter estimates. In doing so, tracking algorithms encounter several challenges: The parameter estimates are in general erroneous, at some times targets may not be detected, closely spaced targets might be detected as one target only, false detections or false alarms occur. Furthermore, for most sensors the detections are not labeled, i.e. it is unclear which detection originates from which target.

In order to introduce an important technique for tracking, it is useful to imagine a situation in which only one of these difficulties exists, i.e. erroneous measurements. This means, that there

exists only one target, the target is detected at every observation time step and there are no false alarms. This problem is in fact identical to estimating the state of a discrete time dynamic system [4, Sec. 5.2.1]; the state is the entity of the location, velocity, possibly the acceleration of the tracked target. The target parameter estimates correspond to the measurements in the state estimation problem.

There are two important classes of estimation problems. One is the estimation of an unknown non-random parameter of which there exists no prior knowledge. The other is the estimation of a parameter which is modeled as random variable, i.e. Bayes estimation [77, Sec. 2.4.1]. In Bayes estimation, prior knowledge of the parameter is expressed in form of a probability distribution. The measurement data modifies the prior probability distribution in order to yield a *posterior probability* density function. The posterior probability distribution then captures the complete information that is available on the random parameter.

The tracking of a single target can be understood as a sequential Bayes estimation problem [2, Sec. II]. Starting from an initial probability distribution for the target state, each incoming measurement refines the probability density of the state. On the other hand, the possibility of target maneuvers like turning, accelerating, stopping decreases the knowledge of the state and counteracts the refinement. In general, there exists no implementable solution to Bayesian tracking based on an analytical derivation [2, Sec. IV]. Approximative solutions can for example be found with a computationally demanding *particle filter* [2, Sec. V].

For a specific case, an analytical solution of the dynamic state estimation problem exists: The initial probability distribution of the state has to be assumed as Gaussian, the target dynamics and measurement model must be linear, [4, Sec. 5.2.1] [2, Sec. III.A], the prior probability of a state must be defined completely by the state at the preceding time step (Markov property), the measurement error and unknown target state changes due to maneuvers must be modeled as Gaussian random variables. In this case, the solution to the state estimation is given by the *Kalman filter*. Due to the linearity and Gaussianity of the state dynamics and measurements, the probability density of the target state is at all times Gaussian. As the density of Gaussian random variables is completely determined by its mean and covariance matrix, the output of the Kalman filter is the mean and covariance matrix of the target state density. The Kalman filter is a recursive algorithm and every recursion step contains a *prediction* and an *update* state. In the prediction step, the prior probability density of the state at time step $k+1$ is computed, taking only into account the measurements up to time step $k$. In the update step, the measurement at time step $k+1$ is used to refine the predicted probability using the Bayes principle. As the densities are Gaussian, the Kalman filter performs these computations by simple algebraic operations on matrices and vectors.

A two dimensional Gaussian distribution can be represented graphically by plotting the mean and the region where realizations occur with a certain probability. This enables to schematically represent one recursion of the Kalman filter as in Figure 4.2.

The Kalman filter serves as basis for tracking algorithms that are able to handle multiple

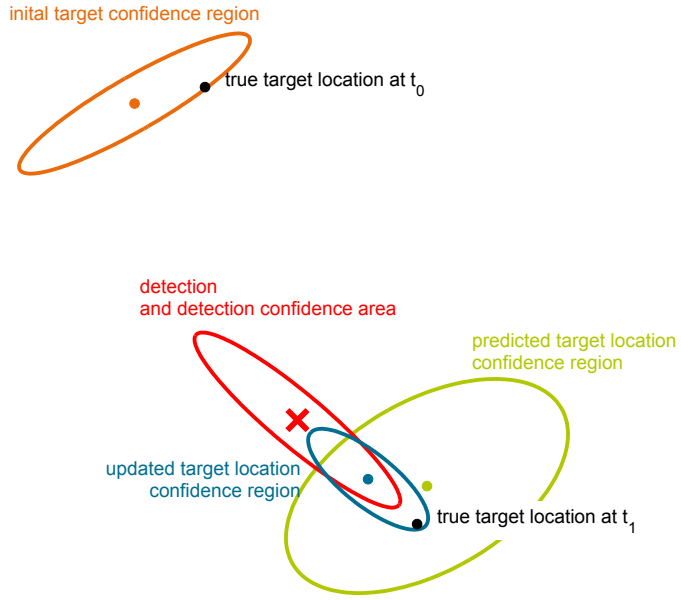


**Figure 4.2.:** Schematic representation of one time step of the Kalman filter recursion. The probability density of the location component of the target state at time step $k$ is represented by the orange ellipse (top left). The ellipse represents a specific confidence region; in this plot all ellipses are for a confidence level of 50 %. The velocity component of the state is not visualized. Based on this density and the target motion model, the Kalman filter predicts a prior probability density for the target state at time step $k+1$ – visualized by the green confidence interval ellipse. The measurement consists of a location and of a confidence interval of the measurement, shown by the red ellipse. Taking into account both the measurement and the predicted location, the posterior target state probability density for time step $k+1$ is obtained – graphically represented by the blue confidence ellipse.

targets, missed detections and false alarms. In the *assignment* based approach, detections are assigned to tracked targets. At every time step at most one detection is assigned to every track. This assignment is based on the probability that a given detection originates from a certain target. If there is no suitable detection for a tracked target, then a missed detection is assumed. Due to the assignment, the Kalman filter can be used to track the target state. For time steps with a missed detection, the update step is simply omitted and the covariance matrix of the predicted density is used directly. Of course, before detections can be assigned to tracks, tracks have to be established. Thus, detections that are not assigned to any existing track are allowed to initialize new tracks. For every track, a track score [7, Sec. 6.2] is computed. The higher the track score, the more likely that a track is not due to false alarms. Tracks with low track scores will be deleted. The assignment of detections to tracks is performed based on the distance of the detections to the predicted measurement. *Gating* excludes detections that are far from the predicted measurement. If a detection could possibly be due to multiple targets, then a technique called *global nearest neighbor* (GNN) [7, Sec. 6.4] can be used to find the optimal assignment.

In some situations, the assignment based approach might be problematic. For closely spaced targets the assignment might be wrong and false alarms might incorrectly be considered as detections. With a technique called *probabilistic data association* (PDA) all detections within the gated region are used to update a track [7, Sec. 6.6.1] [3]. The update due to a detection is weighted with the probability that the detection originates in fact from the target. In an extension of PDA, called *joint probabilistic data association* (JPDA), the probabilities are computed taking into account the presence of multiple targets.

The above methods are similar in that they perform the association or computation of association probabilities based on the information of a single time step. In some situations, it might be useful to take into account information from multiple time steps. In order to do so, a technique called *multiple hypothesis tracking* (MHT) has been developed [7, Sec. 6.7]. With MHT tracks are computed for different possible assignment hypotheses. For each hypothesis the probability that it represents the correct assignment of measurements is computed. Due to the combinatorial nature of assignment, without countermeasures there is an exponential growth of the number of hypotheses. To make MHT computationally feasible, hypotheses with low probabilities are deleted (pruning) and similar hypotheses are merged.

The above techniques are extensions of the Kalman filter. A relatively recent method for multiple target tracking is based on a mathematically more stringent derivation: In multiple target tracking, both the measurements and target states can best be described as finite random sets (RFS) [81]. The sets are random because the number of elements in the sets – i.e. the number of measurements or target states – are random and because the values that these elements assume are random as well. The alternative of stacking the measurements or states to vectors is not appropriate, since the ordering of the measurements or states is not of importance. In [81, Sec. II.B] probability densities are defined for RFS and based on these probability densities a Bayes recursion for RFSs is derived. The mathematical formulation of the RFS Bayes recursion is in principle identical to the Bayes recursion of a single target. The major difference is that the single target state and measurement have been replaced by multi target state and measurement random finite sets.

While it is possible to use a particle filter for solving the RFS Bayes recursion, this approach is in general computationally infeasible. A different approach to multiple target tracking as been derived with the RFS formalism [81, Sec. III]: The probability density of a target RFS determines the probability distribution of the number of targets and where they are located. Hence, it enables to derive the expected number of targets that are located in a specific region of the state space. It also enables to determine the density of expected targets in the state space. This density of expected targets is denoted *intensity* or *probability hypothesis density* (PHD). It is a scalar, nonnegative function; its input are vector valued points of the target state space. The integral of the PHD function over a region of the target state space yields the number of targets that are expected within this region. An integral over the entire state space yields the total number of expected targets.

Under some assumptions, a recursion of the PHD is possible without having to perform the Bayes recursion of the RFS. One of the assumptions for the PHD recursion is that false alarms are distributed according to a Poisson RFS and that the predicted RFS (of the Bayes recursion) is also a Poisson RFS. Poisson RFS are random finite sets for which the number of targets obeys a Poisson distribution and where the targets are distributed in the state space according to the PHD function. Thus, a Poisson RFS is completely defined by the PHD function similar to a Poisson distributed random variable that is completely defined by its expected value. Since the PHD is a function of the single target state space, the PHD recursion is significantly more simple than the full RFS recursion. Furthermore, it does not require an association of measurements to targets. Thus, particle filter implementations of the PHD are computationally more feasible [81]. For linear Gaussian target dynamics and measurements, a Gaussian mixture implementation of th PHD recursion has been presented in [80]. This recursion is denoted the *Gaussian mixture probability hypothesis density* (GM-PHD) filter. The GM-PHD filter also does not require an association of detections to targets. In comparison to the tracking algorithms that have been presented before, the output of the GM-PHD are not tracks, but Gaussian sums that represent the scalar PHD function. Thus, an additional track extraction algorithm is necessary to process the GM-PHD output to tracks. In this thesis such an algorithm is presented in Section 5.2.8.

Since the GM-PHD filter is the algorithm of choice for this thesis, it merits a more detailed introduction. In the next section, the mathematical formulation of the PHD recursion and the GM-PHD filter are introduced.

## 4.1. Probability Hypothesis Density Filter

At first, a more formal definition of the intensity or PHD is in order. The state of a single target at time step $k$ is defined by its position $\boldsymbol{x}_k$ in the single target state space $\mathcal{E}$. A multiple target state at time step $k$ is given by the set

$$X_k = \left\{\boldsymbol{x}_{k,1}, ..., \boldsymbol{x}_{k,M(k)}\right\} \in \mathcal{F}(\mathcal{E}) \,, \tag{4.1}$$

where $M(k)$ is the number of targets at time step $k$ and $\mathcal{F}(\mathcal{E})$ is the set that comprises all finite subsets of $\mathcal{E}$. The counting measure

$$N_{X_k}(S) = \sum_{x \in X_k} \mathbf{1}_S(\boldsymbol{x}) = |X_k \cap S| \,, \tag{4.2}$$

where $\mathbf{1}_S(x) = 1$,if $x \in S$ and 0 otherwise returns the number of elements of $X_k$ that are in $S$. Here $S$ is a Borel subset of the single target state space $\mathcal{E}$ [81].

In the random finite set framework for target tracking, the number and state of targets at time step $k$ are represented by a random finite set $\Xi_k$. Similarly as above, for the random finite set a random counting measure $N_{\Xi_k}(S)$ is defined [81, Sec. IIIA]. This measure is a random variable.

The expectation of this random variable [81, eq. (14)]

$$V_{\Xi_k}(S) = \mathrm{E}\left[N_{\Xi_k}(S)\right] = \int \left( \sum_{x \in X_k} \mathbf{1}_S(\boldsymbol{x}) \right) P_{\Xi_k}(\mathrm{d}\, X) \tag{4.3}$$

is the expected number of targets in $S$. The integral of equation (4.3) is a Lebesque integral that is defined in the random finite set theory [81, Appendix B]. The density of $V_{\Xi_k}(S)$ is precisely the intensity or PHD of the random finite set $\Xi_k$. Thus, the expectation and intensity measure of equation (4.3) can also be expressed as

$$\mathrm{E}\left[N_{\Xi_k}(S)\right] = \int_{\mathcal{S}} v_k(\boldsymbol{x})\, \mathrm{d}\, \boldsymbol{x} = \text{expected nb. of targets in } \mathcal{S} \text{ at time index } k\,. \tag{4.4}$$

This illustration clearly shows that the intensity $v_k(\boldsymbol{x})$ is *not* a probability density function. In particular, the integral over the entire state space is not equal to one, but the total expected number of targets.

As equation (4.3) shows, the PHD $v_k(\boldsymbol{x})$ is defined by the corresponding random finite set $\Xi_k$. For Poisson RFSs, a recursion of the PHD that does not require a prior evaluation of the probability distribution of $\Xi_k$ has been found [81]. This is the PHD filter.

Over time the PHD filter is provided with measurements or detections. At each time step $k$, there are a total of $N_{z,k}$ detections and $\boldsymbol{z}_{k,p}$ denotes the $p$th vector valued measurement. Assembled into sets, the measurements are given by

$$\mathcal{Z}_k = \left\{ \boldsymbol{z}_{k,1},\, ...,\, \boldsymbol{z}_{k,N_{z,k}} \right\}\,. \tag{4.5}$$

These measurements may be due to false alarms or targets.

The PHD filter requires the definition of a single target measurement and state transition model similar to that of other tracking algorithms. The measurement for a target with state $\boldsymbol{x}_k$ a time step $k$ is modeled as random variable $\boldsymbol{Z}(k)|\boldsymbol{X}(k)$. The probability density function of the measurement is denoted as

$$f_{\boldsymbol{Z}(k)|\boldsymbol{X}(k)}(\boldsymbol{z}_k|\boldsymbol{x}_k)\,. \tag{4.6}$$

The target dynamics are captured by the state transition probability density

$$f_{\boldsymbol{X}(k)|\boldsymbol{X}(k-1)}(\boldsymbol{x}_k|\boldsymbol{x}_{k-1}) \tag{4.7}$$

i.e. the probability density of the target state at time $k$ given the state $\boldsymbol{x}_{k-1}$ at the previous time step. The probability that a target with state $\boldsymbol{x}$ at time step $k$ still exists at time step $k+1$ is the survival probability $p_{S,k}(\boldsymbol{x})$. New targets may appear within the target state space. The appearance of new targets is modeled by the birth intensity $\gamma_k(\boldsymbol{x})$, i.e new targets are more likely to appear where $\gamma_k(\boldsymbol{x})$ assumes high values. Depending on the location of the target within the

taret state space, the probability of detection is $p_{\mathrm{D},k}(\boldsymbol{x})$.The intensity of false alarms is given by $\kappa_k(\boldsymbol{z})$ and is a function of the coordinate of the measurement.

Similarly to other target tracking algorithms, the PHD recursion also includes a prediction and update step. A major difference is that the PHD filter predicts and updates the target intensity which is not a probability density function. Given the intensity $v_{k-1}(\boldsymbol{x})$ at time step $k-1$, the predicted PHD at time step $k$ is given by [80, eq. (14)]

$$v_{k|k-1}(\boldsymbol{x}) = \int_{\mathcal{E}} p_{S,k}(\boldsymbol{\zeta}) f_{\boldsymbol{X}(k)|\boldsymbol{X}(k-1)}(\boldsymbol{x}|\boldsymbol{\zeta}) v_{k-1}(\boldsymbol{\zeta}) \,\mathrm{d}\,\boldsymbol{\zeta} + \gamma_k(\boldsymbol{x}) \,. \tag{4.8}$$

In equation (4.8) the first summand represents the PHD of surviving targets and the second summand $\gamma_k(\boldsymbol{x})$ stands for birth targets. The domain of the integration in the first summand is the entire target state space $\mathcal{E}$. The integrand is the product of the survival probability, the state transition density and the PHD at time step $k-1$. In the update step the measurements are processed according to

$$\begin{aligned} v_k(\boldsymbol{x}) = &\left[1 - p_{\mathrm{D,k}}(\boldsymbol{x})\right] v_{k|k-1}(\boldsymbol{x}) \\ &+ \sum_{z \in \mathcal{Z}_k} \frac{p_{D,k}(\boldsymbol{x}) f_{\boldsymbol{Z}(k)|\boldsymbol{X}(k)}(\boldsymbol{z}|\boldsymbol{x}) v_{k|k-1}(\boldsymbol{x})}{\kappa_k(\boldsymbol{z}) + \int_{\mathcal{E}} p_{D,k}(\boldsymbol{\xi}) f_{\boldsymbol{Z}(k)|\boldsymbol{X}(k)}(\boldsymbol{z}|\boldsymbol{\xi}) v_{k|k-1}(\boldsymbol{\xi}) \,\mathrm{d}\,\boldsymbol{\xi}} \,. \end{aligned} \tag{4.9}$$

to yield the updated posterior intensity. This equation is also the sum of two parts. The first part accounts for the proportion of the intensity that is propagated even in the absence of any detection. It is weighted by $1 - p_{\mathrm{D,k}}(\boldsymbol{x})$, i.e. the probability that a target with state $\boldsymbol{x}$ is not detected. The second part of the equation is itself a sum with one summand for every element of $\mathcal{Z}_k$, i.e. detection. These summands are basically the normalized product of the predicted intensity, the probability of detection and the likelihood function. Due to these summands, the intensity is augmented in regions where target detections occur.

The PHD recursion also allows for spawning targets [80], i.e. the creation of new targets from existing targets. For clarity and since spawning is not used in this thesis, it has been omitted in the presentation of the PHD.

## 4.2. Gaussian Mixture Probability Hypothesis Density Filter

For linear Gaussian target dynamics and measurements, a closed form for the PHD recursion, the Gaussian Mixture Probability Hypothesis Density Filter (GM-PHD) has been derived in [80]. For nonlinear target motion and measurement models, a linearizion similar to that of the extended Kalman filter (EKF) can be used. In this section, the GM-PHD is presented for this linearized

form. The target dynamics and the measurement equations are modeled as nonlinear functions

$$\boldsymbol{x}_k = \boldsymbol{\phi}_k(\boldsymbol{x}_{k-1}, \boldsymbol{\nu}_{k-1}) \tag{4.10}$$

$$\boldsymbol{z}_k = \boldsymbol{h}_k(\boldsymbol{x}_k, \boldsymbol{\epsilon}_k)\,, \tag{4.11}$$

where $\boldsymbol{x}_k$ is the state of the target at time step $k$ that is derived from the state $\boldsymbol{x}_{k-1}$ at the preceding time step and process noise $\boldsymbol{\nu}_k$ with the deterministic, nonlinear state propagation function $\boldsymbol{\phi}_k$. The measurement $\boldsymbol{z}_k$ is related to the target state and measurement noise $\boldsymbol{\epsilon}_k$ via the nonlinear measurement function $\boldsymbol{h}_k$. The covariance matrix of the process noise is $\mathbf{Q}_{k-1}$ and the measurement noise covariance matrix is $\mathbf{R}_k$.

The GM-PHD filter propagates the posterior multi-target intensity, also denoted as probability hypothesis density (PHD) in time. The PHD is a function of the target state and gives the density of the number of expected targets at a point in the target state space. Hence, an integral over an area of the target state space yields the number of expected target in that area. In the Gaussian mixture implementation of this filter, the PHD at time step $k$ is given by the Gaussian mixture

$$v_k(\boldsymbol{x}) = \sum_{i=1}^{J_k} w_k^{(i)} f\left(\boldsymbol{x}; \boldsymbol{m}_k^{(i)}, \mathbf{P}_k^{(i)}\right) \tag{4.12}$$

of $J_k$ components, where

$$f\left(\boldsymbol{x}; \boldsymbol{m}_k^{(i)}, \mathbf{P}_k^{(i)}\right) = \frac{1}{(2\pi)^{\frac{N_x}{2}} |\mathbf{P}_k^{(i)}|^{\frac{1}{2}}} \mathrm{e}^{-\frac{1}{2}(\boldsymbol{x}-\boldsymbol{m}_k^{(i)})^{\mathrm{T}} \left[\mathbf{P}_k^{(i)}\right]^{-1} (\boldsymbol{x}-\boldsymbol{m}_k^{(i)})} \tag{4.13}$$

is the probability density function for a normal random variable with mean $\boldsymbol{m}_k^{(i)}$ and covariance matrix $\mathbf{P}_k^{(i)}$ [46, Sec. 3.2.3, p. 88]. Each Gaussian component $i$ is weighted with $w_k^{(i)}$ and parameterized by its mean $\boldsymbol{m}_k^{(i)}$ and covariance $\mathbf{P}_k^{(i)}$. At this point, one should note that the sum of the weights $w_k^{(i)}$ is not 1, since $v_k(\boldsymbol{x})$ is not a probability density. Based on the intensity function at time step $k-1$, the prediciton

$$v_{k|k-1}(\boldsymbol{x}) = v_{S,k|k-1}(\boldsymbol{x}) + \gamma_k(\boldsymbol{x}) \tag{4.14}$$

of the intensity at time step $k$ is found. It is a sum of two terms that represent surviving targets and the birth targets respectively. The first summand which represents surviving targets is the Gaussian mixture

$$v_{S,k|k-1}(\boldsymbol{x}) = p_{S,k} \sum_{j=1}^{J_{k-1}} w_{k-1}^{(i)} f\left(\boldsymbol{x}; \boldsymbol{m}_{S,k|k-1}^{(j)}, \mathbf{P}_{S,k|k-1}^{(j)}\right)\,. \tag{4.15}$$

This Gaussian mixture is parameterized by the means $\boldsymbol{m}_{S,k|k-1}^{(j)}$ and the covariance matrices $\mathbf{P}_{S,k|k-1}^{(j)}$. The means are found directly with the nonlinear state propagation function according

to

$$\boldsymbol{m}_{S,k|k-1}^{(j)} = \boldsymbol{\phi}_k(\boldsymbol{m}_{k-1}^{(j)}, \mathbf{0})\,. \tag{4.16}$$

The covariance matrices of the predicted mixture are given by

$$\mathbf{P}_{S,k|k-1}^{(j)} = \mathbf{G}_{k-1}^{(j)}\mathbf{Q}_{k-1}\left[\mathbf{G}_{k-1}^{(j)}\right]^T + \mathbf{F}_{k-1}^{(j)}\mathbf{P}_{k-1}^{(j)}\left[\mathbf{F}_{k-1}^{(j)}\right]^T\,, \tag{4.17}$$

where

$$\mathbf{F}_{k-1}^{(j)} = \left.\frac{\partial \boldsymbol{\phi}_k(\boldsymbol{x}, \mathbf{0})}{\partial \boldsymbol{x}}\right|_{\boldsymbol{x}=\boldsymbol{m}_{k-1}^{(j)}} \tag{4.18}$$

$$\mathbf{G}_{k-1}^{(j)} = \left.\frac{\partial \boldsymbol{\phi}_k(\boldsymbol{m}_{k-1}^{(j)}, \boldsymbol{\nu})}{\partial \boldsymbol{\nu}}\right|_{\boldsymbol{\nu}=\mathbf{0}} \tag{4.19}$$

are Jacobians of the state propagation function. The equations for the prediction of a single component of the Gaussian mixture are are identical to those of an extended Kalman filter.

The second summand of equation (4.14) – the birth intensity – is also a Gaussian mixture

$$\gamma_k(\boldsymbol{x}) = \sum_{i=1}^{J_{\gamma,k}} w_{\gamma,k}^{(i)} f(\boldsymbol{x}; \boldsymbol{m}_{\gamma,k}^{(i)}, \mathbf{P}_{\gamma,k}^{(i)})\,. \tag{4.20}$$

The number of elements $J_{\gamma,k}$ of this mixture, their means and their covariance matrices have to be set by the user of the GM-PHD filter.

After the prediction step, the two terms of equation (4.14) can be combined to the Gaussian sum

$$v_{k|k-1}(\boldsymbol{x}) = \sum_{i=1}^{J_k-1} w_{k|k-1}^{(i)} \left(\boldsymbol{x}; \boldsymbol{m}_{k|k-1}^{(i)}, \mathbf{P}_{k|k-1}^{(i)}\right) \tag{4.21}$$

of the predicted components. In the update step, the GM-PHD filter processes the set of measurements $\mathcal{Z}_k$. The updated intensity function is given by

$$v_k(\boldsymbol{x}) = (1 - p_{\mathrm{D},k}) v_{k|k-1}(\boldsymbol{x}) + \sum_{z \in Z_k} v_{\mathrm{D},k}(\boldsymbol{x}; \boldsymbol{z})\,, \tag{4.22}$$

where the first summand accounts for the PHD that is due to the possibility that targets might not be detected. Thus, the Gaussian components of this term are due to the missed detection assumption. The second part of the sum adds a new PHD component for every possible pairing of predicted components and detections, thus generating $N_z J_{k-1}$ new components. Consequently, this part of the updated intensity is due to the detections. For every detection with measurement $\boldsymbol{z}$ the sum of the new components is

$$v_{\mathrm{D},k}(\boldsymbol{x}; \boldsymbol{z}) = \sum_{j=1}^{J_{k|k-1}} w_k^{(j)}(\boldsymbol{z}) f\left(\boldsymbol{x}; \boldsymbol{m}_{k|k}^{(j)}(\boldsymbol{z}), \mathbf{P}_{k|k}^{(j)}\right)\,. \tag{4.23}$$

The mean and covariance of the new components is determined with

$$\boldsymbol{\eta}_{k|k-1}^{(j)} = \boldsymbol{h}_k(\boldsymbol{m}_{k|k-1}^{(j)}, \mathbf{0}) \tag{4.24}$$

$$\boldsymbol{m}_{k|k}^{(j)}(\boldsymbol{z}) = \boldsymbol{m}_{k|k-1}^{(j)} + \mathbf{K}_k^{(j)}(\boldsymbol{z} - \boldsymbol{\eta}_{k|k-1}^{(j)}) \tag{4.25}$$

$$\boldsymbol{P}_{k|k}^{(j)} = [\mathbf{I} - \mathbf{K}_k^{(j)}\mathbf{H}_k^{(j)}]\mathbf{P}_{k|k-1}^{(j)} \tag{4.26}$$

$$\mathbf{S}_k^{(j)} = \mathbf{H}_k^{(j)}\mathbf{P}_{k|k-1}^{(j)}\left[\mathbf{H}_k^{(j)}\right]^T + \mathbf{U}_k^{(j)}\mathbf{R}_{\epsilon,k}\left[\mathbf{U}_k^{(j)}\right]^T \tag{4.27}$$

$$\mathbf{K}_k^{(j)} = \mathbf{P}_{k|k-1}^{(j)}\left[\mathbf{H}_k^{(j)}\right]^T (\mathbf{S}_k^{(j)})^{-1} \tag{4.28}$$

in an identical fashion as in the extended Kalman filter. Here $\boldsymbol{\eta}_{k|k-1}^{(j)}$ is the predicted measurement and $\mathbf{K}_k^{(j)}$ the Kalman filter gain and $\mathbf{H}_k^{(j)}$ and $\mathbf{U}_k^{(j)}$ are the Jacobi matrices

$$\mathbf{H}_k^{(j)} = \left.\frac{\partial \boldsymbol{h}_k(\boldsymbol{x}, \mathbf{0})}{\partial \boldsymbol{x}}\right|_{\boldsymbol{x}=\boldsymbol{m}_{k|k-1}^{(j)}} \tag{4.29}$$

$$\mathbf{U}_k^{(j)} = \left.\frac{\partial \boldsymbol{h}_k(\boldsymbol{m}_{k|k-1}^{(j)}, \boldsymbol{\epsilon})}{\partial \boldsymbol{\epsilon}}\right|_{\boldsymbol{\epsilon}=\mathbf{0}} . \tag{4.30}$$

The weights of the new components are determined with

$$\breve{w}_k^{(j)}(\boldsymbol{z}) = p_{\mathrm{D},k} w_{k|k-1}^{(j)} f\left(\boldsymbol{z}; \boldsymbol{\eta}_{k|k-1}^{(j)}, \mathbf{S}_k^{(j)}\right) \tag{4.31}$$

$$w_k^{(j)}(\boldsymbol{z}) = \frac{\breve{w}_k^{(j)}(\boldsymbol{z})}{\kappa_k(\boldsymbol{z}) + \sum_{i=1}^{J_{k|k-1}} \breve{w}_k^{(i)}(\boldsymbol{z})} . \tag{4.32}$$

With respect to the weight equations it can be observed that the total new weight due to one detection is equal to 1 in the absence of false alarms, i.e. if $\kappa_k(\boldsymbol{z}) = 0$. The higher the product $w_{k|k-1}^{(j)} f\left(\boldsymbol{z}; \boldsymbol{\eta}_{k|k-1}^{(j)}, \mathbf{S}_k^{(j)}\right)$ of the prior weight and the likelihood of a component, the higher is its share of the new weight. If the detection is possibly a false alarm, then the weight of the new components is reduced. If the false alarm intensity is very high, almost no new weight might be added.

The number of components at time step $k$ is in the order of $J_{k-1}\,|\mathcal{Z}_k|$, the number of components at the previous time steps times the number of detections at the current time step [80, p. 4097]. In order to limit the number of components a *merging* and *pruning* step is necessary. In this step, similar components are merged to one with combined weight and components of insignificant weight are deleted.

# 5. Reference implementation of a ground moving target tracking algorithm

Historically, algorithms have first been developed for tracking airborne targets. Ground moving target tracking has become an important technique and research field since the introduction of GMTI sensors [13]. In principle, identical or similar algorithms as for airborne target tracking are applicable for ground target tracking. On the other hand, there are important differences in the tasks which have to be considered [13, Sec, 2.1]. First, the movement of ground targets is restricted to the two dimensional surface, while airborne targets can move in a three dimensional space. Second, the movement of ground targets is less predictable as they can accelerate, stop or reverse direction. In contrast, airborne targets are restricted by the flight dynamics, i.e. their velocity cannot fall below a minimum value. On the other hand, a lot of ground targets are confined to roads or are prohibited from entering unsuitable terrain. Third, ground targets can be obscured by vegetation or the terrain, i.e. there might be locations at which they cannot be detected. Furthermore, the ground clutter impedes the detection of ground targets if their radial velocity with respect to the radar system is below a minimum value.

These distinctive features have motivated substantial research on ground moving target tracking. In [32] an IMM algorithm is employed to take into account that target motion is mostly restricted to roads and to model target obscuration. A similar approach is used in [33] to track targets that temporarily come to a halt in order to avoid detection. Starting with [37] the clutter notch is modeled by providing the tracking algorithm with a reduced detection probability for targets with a low radial velocity. In [78] the target location is predicted using road map information. A different approach of including road and terrain map information is the use of maps of the 'hospitality for maneuver' [31].

In most publications on GMTT idealized models for the measurement process are employed. Sometimes, the Doppler measurement is not used [26, eq. 8], [57, eq. (38)]. While simplifications are well founded for the investigation of specific aspects, they prevent the direct application of these algorithms to real measurement data. Furthermore, the application of many tracking algorithms demand the cumbersome evaluation of Jacobians of the measurement function which are also not given in literature. Thus, in short, there is no functional complete implementation of a ground moving target tracking algorithm available in literature.

The aim of this chapter is to close this gap and to provide a reference implementation of a ground moving target tracking algorithm.

## 5.1. Basic design choices

For the implementation of the reference algorithm, design choices must be made. The principal goal has been to design an algorithm which is successful at tracking ground moving targets with experimental data. Evidently, different design choices might lead to algorithms with different performance properties. Of the following implementation, some design choices can be easily changed if it is desired.

Various types of tracking algorithms are available, e.g. the PDAF or JPDAF, multiple hypothesis tracking algorithms, the GM-PHD and the GMC-PHD. Among these, the GM-PHD algorithm was chosen due to its reported computational efficiency, elegant mathematical derivation and relatively simple implementation. However, its original form of [80] must be extended by an additional track extraction algorithm. For linear target dynamics and measurement models, the core prediction and update equations of the GM-PHD are identical to those of the Kalman filter. Nonlinearities can be treated by an extended Kalman filter (EKF) or unscented Kalman filter (UKF) like modification. As the measurement process of GMTI is nonlinear, it is clear that either the EKF or UKF version has to be used. Since the nonlinearities are fairly mild, the EKF version was selected.

In tracking targets, the choice has to be made between representing the target state in sensor coordinates [44, Sec. 3.3] or in Cartesian coordinates. The use of sensor coordinates has the advantage that no conversion of the measurements is required. The severe disadvantage is that the state propagation becomes nonlinear: A target that moves along a straight line in our world does not move along a line in the sensor coordinates. Furthermore, for a moving platform the conversion between the sensor coordinates and the Cartesian coordinates becomes time dependent, making the interpretation of the tracking results difficult. Thus, a Cartesian coordinate system is preferable for GMTT and chosen for the reference implementation.

The target state space can comprise position and velocity only or additionally an acceleration state. These states are per dimension, i.e. for a state space with a two dimensional location component, the total state space dimension is 4 without acceleration and 6 with acceleration. For a state space with a three dimensional location component, the total dimension is 6 or 9. For state space models with an acceleration state, the Singer model [69], [7, Sec. 4.2.1] is the most common choice for a state propagation model. If no acceleration state is used, then a constant velocity (CV) target model can be used [7, Sec. 4.2.2]. According to [7, Sec. 4.2.1] the use of an acceleration state is not advantageous, if the target velocity is not measured or if acceleration is only correlated over very short time steps. In the reference implementation no acceleration state is used, as it was assumed that the correlation time of acceleration of ground moving targets is small.

In ground moving target tracking, the position of the target is constrained to the earth's surface. As the location of a point on a surface can be given in two dimensions, a state space with a two dimensional location component is sufficient for fully specifying the three dimensional position of the target. In order to do so, a suitable conversion from three dimensional coordinates to

two dimensional coordinates and vice versa is needed. In the reference implementation, a two dimensional location coordinate is used and a conversion of tracking results to three dimensions is presented.

Furthermore, the measurement space needs to be determined. Similarly to the state space, the measurements may be given in Cartesian coordinates or sensor coordinates [44, Sec. 3.1 & Sec. 3.2], [7, p. 178]. In sensor coordinates, it is mostly very reasonable to model the measurement noise as Gaussian. In Cartesian coordinates, the Gaussian approximation is less appropriate, however it might still be justified. On the other hand, the observation model may become highly nonlinear for measurements in sensor coordinates. This may lead to divergence of the tracking algorithm if the tracking is initiated for off the true target position [7, p. 165 to 166]. Thus, for the reference algorithm the measurements are converted to the Cartesian space. This has the additional advantage of allowing a representation of the measurement in the space in which the tracking is performed.

In ground moving target detection, the target detection probability depends strongly on the location of the target. In this reference implementation, the probability of detection is determined by means of modeling the measurement noise of the radar system. This provides a link to the radar signal processing.

In the following, the reference implementation of the tracking algorithm according to these design choices is presented in detail. Section 5.2 presents modifications to the GM-PHD algorithm that are not specific to GMTT. Ground moving target tracking specific adaptations are presented in Section 5.3.

## 5.2. Modifications of the standard GM-PHD filter

In order to apply the GM-PHD algorithm of [80] for ground moving target tracking, some modifications of the algorithm have been necessary. These are not specific to ground target tracking and could also be useful in other tracking scenarios. A flow chart of the algorithm is given in Figure 5.1.

### 5.2.1. State dependent detection probability

The original article [80] already accounts for state dependent detection probability by modeling the probability of detections as a Gaussian sum. However, this approach may lead to negative components and increases the overall number of components. Thus, in an approximation it is resorted to using a constant value of the detection probability for entire PHD sum components.

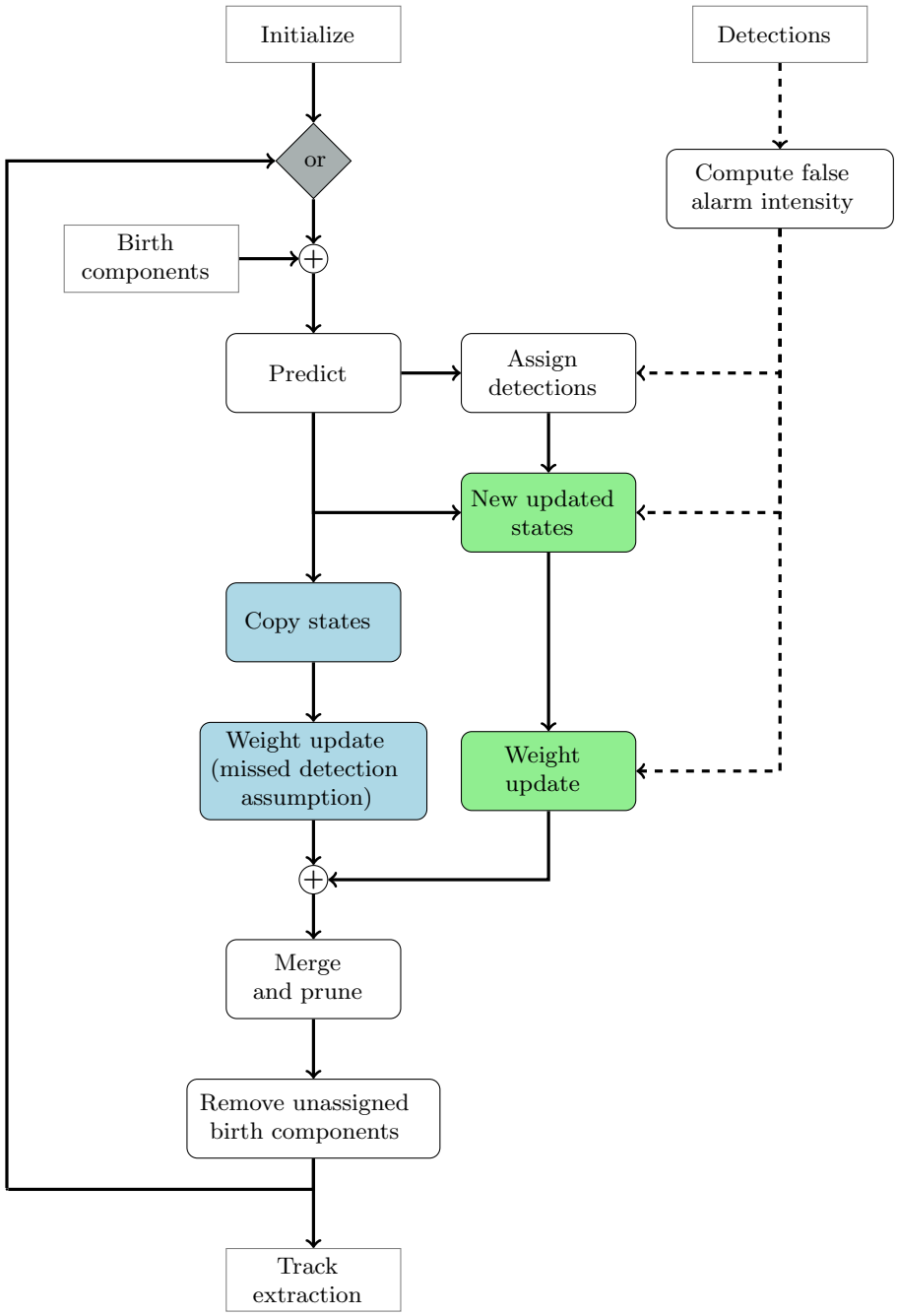


**Figure 5.1.:** Flow chart of the GM-PHD filter. Dashed lines indicate information flow related to target detections and solid lines indicate information flow related to components of the Gaussian mixture of the filter. Blocks of the update step that generate Gaussian sum components due to a missed detection assumption are colored light blue ( ). Update step blocks that generate new components for every association between predictions and detections are colored green ( ).

The update equations (4.31) and (4.32) are replaced by

$$\breve{w}_k^{(j)}(\boldsymbol{z}) = w_{k|k-1}^{(j)} f\left(\boldsymbol{z}; \boldsymbol{\eta}_{k|k-1}^{(j)}, \mathbf{S}_k^{(j)}\right) \tag{5.1}$$

$$w_k^{(j)}(\boldsymbol{z}) = \frac{p_{\mathrm{D},k}^{(j)} \breve{w}_k^{(j)}(\boldsymbol{z})}{\kappa_k(\boldsymbol{z}) + \sum_{i=1}^{J_{k|k-1}} p_{\mathrm{D},k}^{(i)} \breve{w}_k^{(i)}(\boldsymbol{z})}\,, \tag{5.2}$$

where the probability detection is computed with

$$p_{\mathrm{D},k}^{(j)} = p_{\mathrm{D},k}(\boldsymbol{m}_k^{(j)}) \tag{5.3}$$

for the updated state $\boldsymbol{m}_k^{(j)}$. This is possible since the updated location does not depend on the detection probability. In equation (5.2), $f(\boldsymbol{z}; \boldsymbol{m}, \mathbf{S})$ denotes the probability density function of a normal random vector with mean $\boldsymbol{m}$ and covariance matrix $\mathbf{S}$.

### 5.2.2. Association between detections and components

Without additional measures the number of newly created components in one GM-PHD recursion step is $N_z J_{k|k-1}$. Most of these new components will result from combinations of detections and prediction components that have a great distance. Thus, these components will exhibit very low weights and be removed in the pruning step. To increase the computational speed of the algorithm, it is thus advisable to prevent the creation of these components. To this end, the algorithm has been modified to associate measurements with prediction components. The first condition is that the detections lies within a gate around the predicted measurement as expressed with

$$\| w_{\mathrm{norm}}^T \left(\boldsymbol{z}_{k,p} - \boldsymbol{\eta}_{k|k-1}^{(j)}\right) \| \leq t_{\mathrm{gating}}\,, \tag{5.4}$$

where $w_{\mathrm{norm}}$ is a normalization vector. Additionally, for the weights of the new components given by equation (5.2) an upper bound can be derived. This upper bound is found based on the inequalities[1]

$$w_k^{(j)}(\boldsymbol{z}) = \frac{p_{\mathrm{D},k}^{(j)} \breve{w}_k^{(j)}(\boldsymbol{z})}{\kappa_k(\boldsymbol{z}) + \sum_{i=1}^{J_{k|k-1}} p_{\mathrm{D},k}^{(i)} \breve{w}_k^{(i)}(\boldsymbol{z})} \tag{5.5}$$

$$\leq \frac{p_{\mathrm{D},k}^{(j)} \breve{w}_k^{(j)}(\boldsymbol{z})}{\kappa_k(\boldsymbol{z}) + p_{\mathrm{D},k}^{(j)} \breve{w}_k^{(j)}(\boldsymbol{z})} \tag{5.6}$$

$$\leq \frac{\breve{w}_k^{(j)}(\boldsymbol{z})}{\kappa_k(\boldsymbol{z}) + \breve{w}_k^{(j)}(\boldsymbol{z})}\,. \tag{5.7}$$

[1] Here, the inequality of equation (5.6) is valid, since compared to equation (5.5) positive terms are removed from the denominator. The inequality of equation (5.7) can be derived starting from the inequality $p_{\mathrm{D},k}^{(j)} \kappa_k(\boldsymbol{z}) + p_{\mathrm{D},k}^{(j)} \breve{w}_k^{(j)}(\boldsymbol{z}) \leq \kappa_k(\boldsymbol{z}) + p_{\mathrm{D},k}^{(j)} \breve{w}_k^{(j)}(\boldsymbol{z})$ which is valid for $0 \leq p_{\mathrm{D},k}^{(j)} \leq 1$.

The upper bound for the weight of the new Gaussian mixture compnonent with index $(j)$ at time step $k$ is given by

$$w_{\mathrm{ub},k}^{(j)}(\boldsymbol{z}) = \frac{\breve{w}_k^{(j)}(\boldsymbol{z})}{\kappa_k(\boldsymbol{z}) + \breve{w}_k^{(j)}(\boldsymbol{z})}\,, \tag{5.8}$$

where $\breve{w}_k^{(j)}(\boldsymbol{z})$ is defined in equation (5.1). The computation of this upper bound does not require the evaluation of the probability of detection which may save a considerable amount of computation time. Thus, the second condition for the association of a measurement with a prediction component is

$$w_{\mathrm{ub},k}^{(j)}(\boldsymbol{z}) > t_{\mathrm{pruning}}\,, \tag{5.9}$$

i.e. that the maximum possible weight of a newly created component is larger than the pruning threshold $t_{\mathrm{pruning}}$.

### 5.2.3. Merging with the Kullback-Leibler divergence

The merging method as presented in the original paper on GM-PHD [80, Table II] may lead to merging of components with very different density functions. This is due to the fact that it uses the Mahalanobis distance as measure for the similarity between the components. The distance between two components $i$ and $j$, where component $i$ has the smaller weight is

$$d_{\mathrm{mahalanobis},i,j} = \left(\boldsymbol{m}_k^{(i)} - \boldsymbol{m}_k^{(j)}\right)^{\mathrm{T}} \left[\mathbf{P}_k^{(i)}\right]^{-1} \left(\boldsymbol{m}_k^{(i)} - \boldsymbol{m}_k^{(j)}\right)\,. \tag{5.10}$$

Thus, only the covariance matrix of the component with the smaller weight is taken into account. If the covariance matrix of this component is very 'large', then in this scheme it can be merged although the intensities of those components are very dissimilar.

The merging step is modified to use instead the symmetrized Kullback-Leibler divergence

$$\begin{aligned} d_{\mathrm{KL},i,j} =& \frac{1}{2}\left[\mathrm{tr}\left(\left[\mathbf{P}_k^{(i)}\right]^{-1}\mathbf{P}_k^{(j)}\right) + \mathrm{tr}\left(\left[\mathbf{P}_k^{(j)}\right]^{-1}\mathbf{P}_k^{(i)}\right)\right] \\ &+ \frac{1}{2}(\boldsymbol{m}_k^{(i)} - \boldsymbol{m}_k^{(j)})^T \cdot \left(\left[\mathbf{P}_k^{(j)}\right]^{-1} + \left[\mathbf{P}_k^{(i)}\right]^{-1}\right) \\ &\cdot (\boldsymbol{m}_k^{(i)} - \boldsymbol{m}_k^{(j)}) - N_{\text{dim of state}} \end{aligned} \tag{5.11}$$

(for Gaussian distributions) as distance measure. It measures the similarity between the densities of both components taking into account both covariance matrices.

The difference between those distances is illustrated by Figure 5.2. It shows two cases of merging two Gaussian sum components. In one case – Subfigure 5.2a – the Gaussians are relatively similar. As a result the single merged Gaussian approximates the sum of the original components well. In the second case – Subfigure 5.2b – the Gaussians are very different. Thus, the single Gaussian that is obtained through merging does not approximate the sum of the two Gaussians at all.

In both cases, the Mahalanobis distance is identical; it has a value of 2.7778. On the other

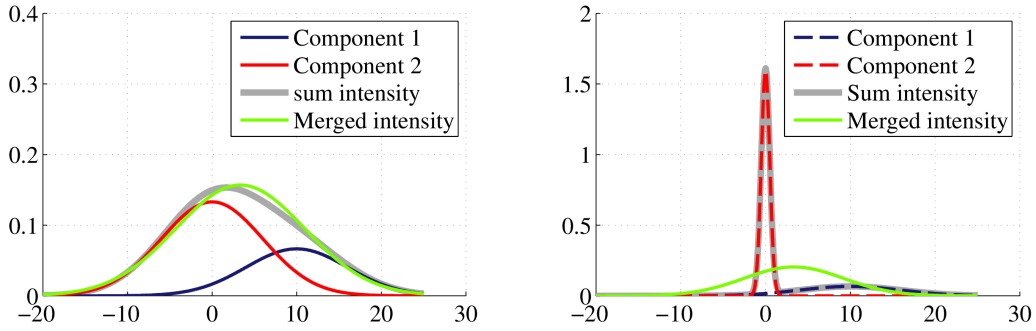


**(a)** Case 1: Similar Gaussians

**(b)** Case 2: Dissimilar Gaussians

**Figure 5.2.:** Two cases with two different Gaussian sum components each. In both cases the Mahalanobis distance is identical whereas the symmetrized Kullback-Leibler divergence is different.

hand, the symmetrized Kullback-Leibeler divergence is only 2.7778 in case 1 while it is 272.3924 in case 2. Hence, the symmetrized Kullback-Leibler divergence enables to distinguish between cases where merging is appropriate and where it is not. Consequently, the symmetrized Kullback-Leibler divergence rather than the Mahalanobis distance is used in the merging step of this implementation of the GM-PHD filter.

### 5.2.4. Ancestor relation

In the GM-PHD, at time step $k$ a new Gaussian sum component is created for every possible combination of detections to components at time step $k-1$ and to new birth components. Additionally, new components are formed for the missed detection assumption. Seen inversely, components at time step $k-1$ generate offspring components at time step $k$. Thus, there exists and offspring/ancestor relation between components of different time steps. The GM-PHD algorithm has been extended to recursively save the ancestor to descendant relations.

Figure 5.3 illustrates the ancestor relation by visualizing the different steps of a single GM-PHD recursion step and an overview of multiple GM-PHD recursion steps: Subfigure 5.3a shows that birth components are added in the prediction step, that new components are created due to incoming detections, that some components are deleted in the pruning step and that others are combined during the merging step. By tracing back the links from the right to the left, the ancestor relations are found. A component may have zero, one or multiple offspring components and inversely a component may have one or more ancestors. In some cases, the only ancestor is a birth component, i.e. in fact there exists no true ancestor. If a component has multiple ancestors, then a link strength for each ancestor is computed. For a specific ancestor this link strength is the ratio of the total weight of its post pruning components that contribute to the descendant to the total weight of the descendant. Subfigure 5.3b shows multiple steps of the GM-PHD genealogy.

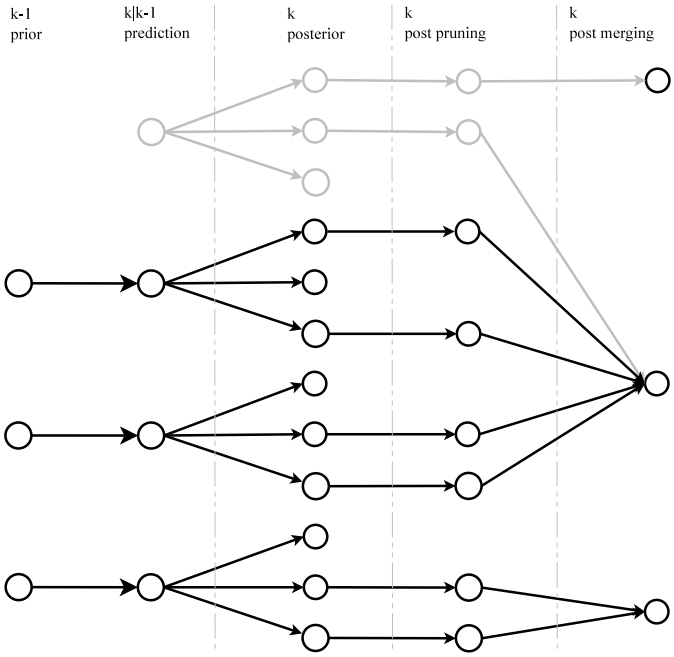


**(a)** Illustration of a single GM-PHD recursion step. In this example there exist three Gaussian sum components at time step $k-1$. Two detections are made at time step $k$. At time step $k$, 12 components are created during the update step, eight components remain after pruning and three components remain after merging. The birth component and its descendants (up to post pruning) are shown in gray.

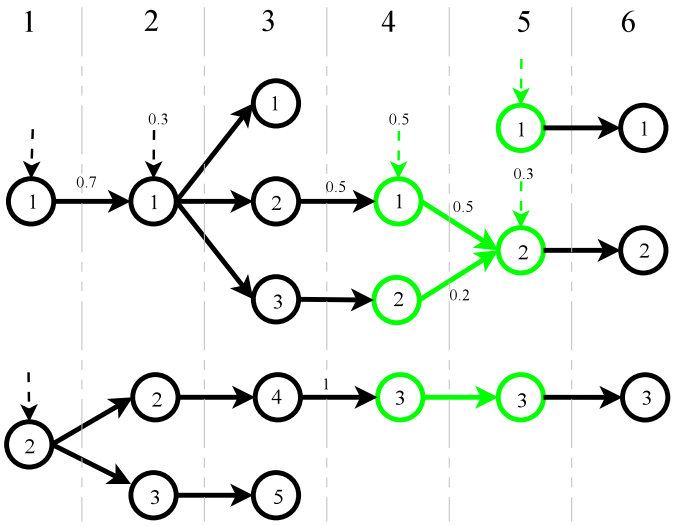


**(b)** Illustration of multiple GM-PHD recursion steps. Each circle represents one posteror Gaussian sum component with enclosed index number. Dashed errors indicate when a birth component is among the ancestors. For components whose fingerprints are given in Table 5.1, the weight of each ancestor is indicated.

**Figure 5.3.:** Visualization of the PHD recursion with an example.

For a subset of the genealogy numbers at the arrows between ancestors and descendants indicate the link strength.

The number of ancestors for component $i$ at time step $k$ is denoted $N_{\mathrm{A},k}^{(i)}$ and the indices of the ancestors at the preceding time step $k-1$ are denoted by $a_k^{(i)} = \left[a_{k,1}^{(i)}, ..., a_{k,N_{\mathrm{A},k}^{(i)}}^{(i)}\right]^{\mathrm{T}}$. As Figure 5.3 shows, every ancestor might contribute to a new post merging component via multiple posterior components, e.g. the missed detection assumption update and several detection update components. The number of posterior components derived from ancestor $j$ that are merged to the post merging component $i$ shall be denoted by $N_{\mathrm{p},k,j}^{(i)}$. The indices of these components shall be given by $p_{\mathrm{A},k,j}^{(i)} = [p_{\mathrm{A},k,j,1}^{(i)}, ..., p_{\mathrm{A},k,j,N_{\mathrm{p},k,j}^{(i)}}^{(i)}]^T$. The link strength between an ancestor $j$ and the post merging component $i$ is then defined as the sum

$$w_{\mathrm{A},k,j}^{(i)} = \sum_{l \in p_{\mathrm{A},k,j}^{(i)}} w_k^{(l)} \tag{5.12}$$

over the weights of all components given by the vector $p_{\mathrm{A},k,j}^{(i)}$. Combined for all ancestors, the link strength of component $i$ is written as

$$w_{\mathrm{A},k}^{(i)} = [w_{\mathrm{A},k,1}^{(i)}, .., w_{\mathrm{A},k,N_{\mathrm{A},k}^{(i)}}^{(i)}]^T . \tag{5.13}$$

Finally, for the post merging component $i$ the weight is distributed according

$$\sum_{n=1}^{N_{\mathrm{A},k}^{(i)}} w_{\mathrm{A},k,n}^{(i)} + w_{\mathrm{birth},k}^{(i)} = w_{\mathrm{ancestors},k}^{(i)} + w_{\mathrm{birth},k}^{(i)} = \tilde{w}_k^{(i)} , \tag{5.14}$$

between true ancestors and birth terms. If no birth components contribute to component $i$, then $w_{\mathrm{birth},k}^{(i)}$ is zero. The extended version of the GM-PHD filter saves the vectors $a_k^{(i)}$ and $w_{\mathrm{A},k}^{(i)}$.

### 5.2.5. Immediate deletion of missed detection birth component descendants

The number, placement, covariance matrices and weights of the birth components can be set independently for every time step. Through the update with measurements, they enable the generation of new components that are not descendants of components at the preceding time steps. In conjunction with the track extraction algorithm of Section 5.2.8 this is equivalent to the generation of new tracks.

A prerequisite for this capability is that the updated weight of a birth component (see equations (4.32) and (5.2)) is sufficiently high to survive the pruning step. If the influence of other components is negligible, this leads to the requirement of

$$w_{k|k-1}^{(j)} \mathcal{N}\left(\boldsymbol{z}; \boldsymbol{\eta}_{k|k-1}^{(j)}, \mathbf{S}_k^{(j)}\right) p_{D,k} > \frac{1}{\kappa_k(z)} \left(\frac{1}{t_{\mathrm{pruning}}} - 1\right) \tag{5.15}$$

for the product of detection probability, prior weight and value of the likelihood function.

Birth components should always be available when previously unobserved targets are likely to appear, e.g. if an area is observed for the first time or at the start of the tracking algorithm. Additionally, scenarios in which new targets can appear at all times in the tracking area are possible.

The most simple solution is to place one birth component with a large covariance matrix in the middle of the tracking area. Then the value of the likelihood function will be almost constant for all detections. Furthermore, in this case the measurement accuracy is much higher than the accuracy of the birth component. Hence, after the update step the state of the component will be almost entirely be defined by the measurement.

Additionally to birth components descendants that are due to detections, there are also the descendants due to the missed detection assumption. This signifies, that independently of the detections, intensity due to the birth process will build up in the tracking algorithm. This has to be taken into account when configuring the birth intensity, i.e. the birth intensity should be smaller in areas where already birth intensity due to previous time steps is present.

Thus, even though the evolution of the missed detection part of the birth intensity is deterministic, it makes designing the birth intensity $\gamma_k(\boldsymbol{x})$ more difficult. As a remedy, the GM-PHD algorithm has been extended to enable the deletion of the missed detection birth components at every time step. If this deletion is performed, the birth intensity can be configured independently for every time step according to the requirements of the respective time step.

### 5.2.6. Component fingerprints

For some analyses of the GM-PHD result it can be desirable to have a measure for how closely two components of the GM-PHD recursion at different or identical time steps are related. For example a component at time step $k_1$ could be a direct descendant of a component at time step $k_0$ without any other ancestors or contributions of birth components. In that case, these components have a very close relation. Two components at the same time step $k_1$ might share common ancestors at preceding time steps which also leads to a relation between these components.

In order to capture these relations, the events that a post merging component $i$ receives weight through a birth component (i.e. $w_{\text{birth},k}^{(i)} > 0$) are numbered consecutively. Via its ancestors the weight of a component can ultimately be traced back to the birth events. The distribution of a component's weight between birth events is characteristic of the component. Thus, in the following this distribution will be called 'fingerprint'.

Let the total number of birth events up to and including time step $k$ be denoted by $N_{\text{births},k}$. The fingerprint of a component with index $i$ at time step $k$ is given by a (sparse) $N_{\text{births},k} \times 1$ vector $\boldsymbol{q}_k^{(i)}$. The element indices of this vector correspond to the birth event indices and the entries give the weight associated with the respective birth event.

The fingerprint of the components is performed recursively by merging the fingerprints of the components' ancestors and the birth fingerprint. For a birth event at time step $k$ the birth

**Table 5.1.:** Fingerprints associated with the components of Figure 5.3

| Time | Comp. | Fingerprint |
|---|---|---|
| 1 | 1 | $[1\ 0]^T$ |
| 1 | 2 | $[0\ 1]^T$ |
| 2 | 1 | $[0.7\ 0\ 0.3]^T = 0.7\ [1\ 0\ 0]^T + 0.3\ [0\ 0\ 1]^T$ |
| 2 | 2 | $[0\ 1\ 0]^T$ |
| 2 | 3 | $[0\ 1\ 0]^T$ |
| 3 | 1 | $[0.7\ 0\ 0.3]^T$ |
| 3 | 2 | $[0.7\ 0\ 0.3]^T$ |
| 3 | 3 | $[0.7\ 0\ 0.3]^T$ |
| 3 | 4 | $[0\ 1\ 0]^T$ |
| 3 | 5 | $[0\ 1\ 0]^T$ |
| 4 | 1 | $[0.35\ 0\ 0.15\ 0.5]^T =$ $0.5[0.7\ 0\ 0.3\ 0]^T + 0.5\ [0\ 0\ 0\ 1]^T$ |
| 4 | 2 | $[0.7\ 0\ 0.3\ 0]^T$ |
| 4 | 3 | $[0\ 1\ 0\ 0]^T$ |
| 5 | 1 | $[0\ 0\ 0\ 0\ 1\ 0]^T$ |
| 5 | 2 | $[0.315\ 0\ 0.135\ 0.25\ 0\ 0.3]^T =$ $0.5\ [0.35\ 0\ 0.15\ 0.5\ 0\ 0]^T +$ $0.2\ [0.7\ 0\ 0.3\ 0\ 0\ 0]^T + 0.3\ [0\ 0\ 0\ 0\ 0\ 1]^T$ |
| 5 | 3 | $[0\ 1\ 0\ 0\ 0\ 0]^T$ |
| 6 | 1 | $[0\ 0\ 0\ 0\ 1\ 0]^T$ |
| 6 | 2 | $[0.315\ 0\ 0.135\ 0.25\ 0\ 0.3]^T$ |
| 6 | 3 | $[0\ 1\ 0\ 0\ 0\ 0]^T$ |

fingerprint is given by the $N_{\text{births},k} \times 1$ vector $\boldsymbol{q}^{(i)}_{\text{birth},k}$ whose elements are zero except the element at position given by the index of the birth element which is set to 1. In the first step of the computation of the fingerprint, the fingerprint vectors of the components at time step $k-1$ are extended from the length $N_{\text{births},k-1}$ to $N_{\text{births},k}$ by padding $\Delta N_{\text{births},k}$ zeros, i.e. for the $n$-th ancestor of component $i$ at time step $k$

$$\tilde{\boldsymbol{q}}^{(i)}_{k,n} = \begin{bmatrix} \boldsymbol{q}^{(j)}_{k-1}\Big|_{j=a^{(i)}_{k,n}} \\ \mathbf{0}_{\Delta N_{\text{births},k} \times 1} \end{bmatrix} . \tag{5.16}$$

Then the fingerprint vector of component $i$ is found as the weighted average

$$\boldsymbol{q}^{(i)}_k = \sum_{n=1}^{N^{(i)}_{\text{A},k}} \frac{w^{(i)}_{\text{A},k,n}}{\tilde{w}^{(i)}_k} \tilde{\boldsymbol{q}}^{(i)}_{k,n} + \frac{w^{(i)}_{\text{birth},k}}{\tilde{w}^{(i)}_k} \boldsymbol{q}^{(i)}_{\text{birth},k} . \tag{5.17}$$

The degree of relation between two components can be found by forming the correlation between their fingerprint vectors. If it is determined for components of different time steps, then the shorter fingerprint vector is zero padded. A correlation value of 1 signifies that the two components are

very closely related while a value of 0 indicates no relation at all. To illustrate this point, the example of Figure 5.3 is reused. The birth events are numbered from one to six. Table 5.1 gives the resulting fingerprints associated with the different components.

### 5.2.7. Visualization of the GM-PHD filter results

In some occasions it is advisable to directly visualize the GM-PHD filter result without passing through a track extraction step.. Two dimensional GM-PHD results can be visualized by plotting lines between all components and their respective ancestors. The link strength between component $i$ of time step $k$ and its $n$-th ancestor of time step $k-1$ is given by the proportion of the contribution of the $n$-th ancestor to the total component weight

$$w_{\text{link},k,n^{(i)}} = \frac{w_{\text{A},k,n}^{(i)}}{\tilde{w}_k^{(i)}} \,. \tag{5.18}$$

As this link strength lies between 0 and 1 it can be interpreted as transparency value for the plotted line, e.g. a link with a small value of $w_{\text{link},k,n^{(i)}}$ will be almost invisible. Additionally to choosing the transparency of the line, its basic color defined by its red, green and blue (RGB) color components can be chosen. One option is to base the line color on the fingerprint of the more recent component of the two components that are linked by a line. To this end, the element values of the fingerprint vector are interpreted as weights for the color contributions in a mixture of RGB colors. If the RGB values of the mixture colors are defined by the lines of the $N_{\text{births},k} \times 3$ matrix $\mathbf{A}_{\text{color},k}$, then the color

$$\tilde{\boldsymbol{c}}_{\text{rgb},k}^{(i)} = \left[\mathbf{A}_{\text{color},k}\right]^T \boldsymbol{q}_k^{(i)} \,. \tag{5.19}$$

is generated with the fingerprint. This corresponds to projecting the high dimensional fingerprint to a 3 dimensional space which can be displayed as color value. In order to perform a normalization with respect to the saturation and brightness of the color, $\tilde{c}_{\text{rgb},k}^{(i)}$ is converted to the HSV color space [74], value and hue are set to 1 and the color is converted back to the RGB color space.

The matrix $\mathbf{A}_{\text{color},k}$ can be generated by sampling independently from a uniform distribution between 0 and 1. For obtaining a consistent color for display at different time steps $k$, it can be constructed recursively according to

$$\mathbf{A}_{\text{color},k} = \begin{bmatrix} \mathbf{A}_{\text{color},k-1} \\ \boldsymbol{\Delta}\mathbf{A}_{\text{color},k} \end{bmatrix} . \tag{5.20}$$

If the final length of the fingerprints is known it can also be generated by selecting submatrices of a previously generated matrix. An example of this visualization technique is given in Section 6.3.

### 5.2.8. Track extraction

Unlike classical tracking algorithms such as the probabilistic data association filter (PDAF) or multiple hypotheses tracking (MHT) the GM-PHD filter does not yield a list of tracks with unique identifiers. Instead, the result of the GM-PHD is a Gaussian sum representation of the evolution of the posterior target intensity $v_k(\boldsymbol{x})$, $k = 0, ..., K-1$. Fortunately the Gaussian sum representation in combination with the saving of the ancestor relation as introduced above provides for a simple method of extracting tracks based on the GM-PHD result:

Based on the saved ancestor relation, for every Gaussian sum components its descendants are determined. For existing tracks, the component with the largest weight is chosen for continuing the track. Existing tracks are stopped if they have no descendants or if the weight of the descendants is below a threshold. Descendants that are not attributed to existing tracks start new tracks if their weight exceeds a threshold. As a result, each track is continuous in time and Gaussian sum components may only be attributed to a single track.

An extracted track is defined by a list of Gaussian sum components identifiers. In this list each component is identified by the time step and the index number within the Gaussian sum. E.g., a track with id 1 is given by the list $T_1 = \{(1,1),(2,4),(3,3)\}$. Based on the list, the state and the state covariance matrix are defined for all time steps of the track duration.

## 5.3. Ground moving target tracking specific adaptations of the GM-PHD

The target dynamics and measurement model enter the definition of the EKF version of the GM-PHD filter via generic models and the Jacobian matrices of these models. In order to apply the algorithm to any specific tracking task, the definition of these models and the derivation of the Jacobians are required. These are related to the definition of the measurement and target state space. The definition of the state propagation, measurement model and related Jacobians is not specific to the use of a GM-PHD algorithm, e.g. they could be reused if the GM-PHD filter were replaced by an MHT algorithm.

### 5.3.1. Definition of the target state space

As our world has 3 spatial dimensions, a 3 dimensional coordinate system is required for fully specifying the location of a tracked target. However, if an object or target is known to be constrained to a surface, for example the earth's surface, two dimensions are sufficient.

This motivates the use of a two dimensional coordinate system for specifying the location of a ground target in the tracking algorithm. Its definition is linked to functions that map from 2 dimensions to 3 dimensions and vice versa. For transforming the location, the mapping functions are denoted by $\boldsymbol{f}_{\mathrm{p}}^{2\leftarrow 3}$ for converting from 3D coordinates to 2D coordinates and by $\boldsymbol{f}_{\mathrm{p}}^{3\leftarrow 2}$ for converting from 2D to 3D coordinates.

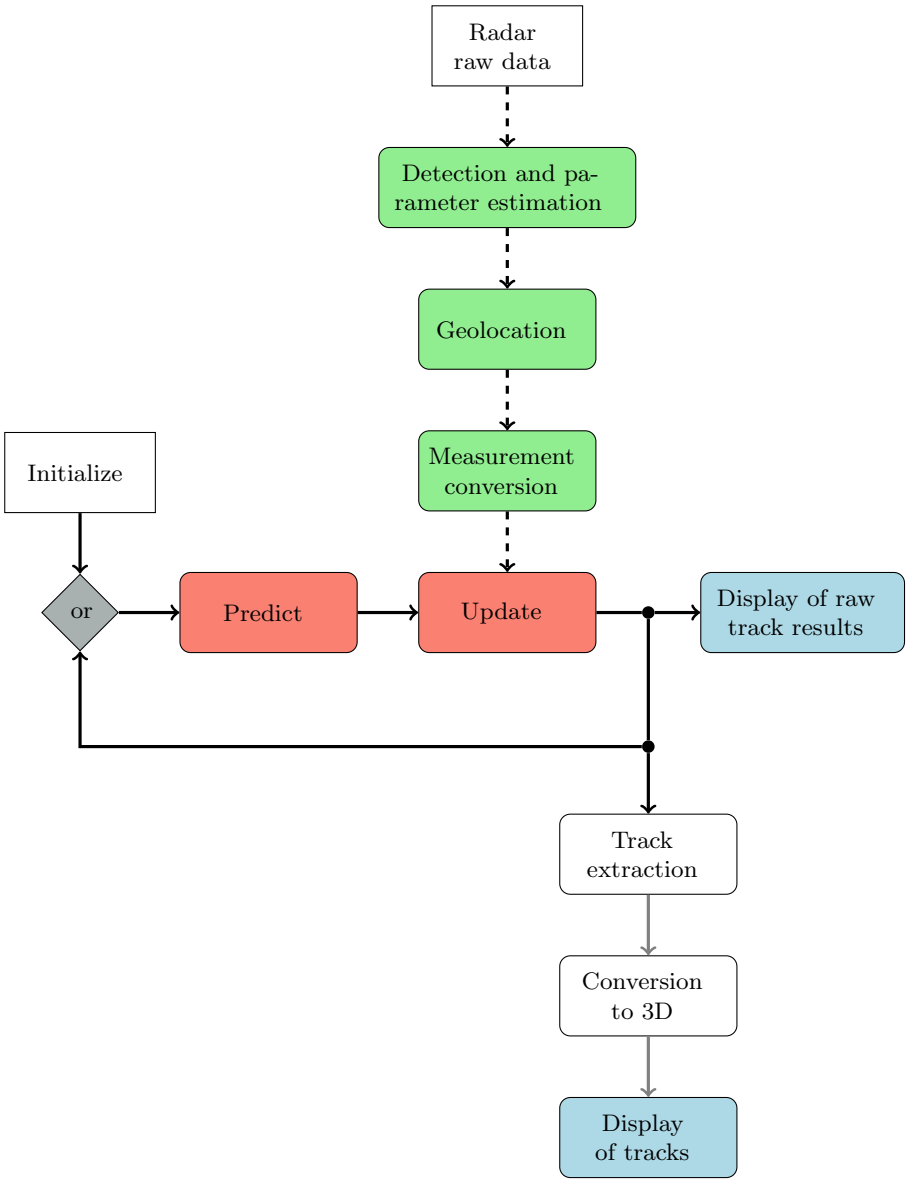


**Figure 5.4.:** Overview of the processing from the radar raw data to the display of tracks. Blocks related to radar signal processing and the conversion of detections are colored green ( ), blocks that belong to the GM-PHD tracking algorithm are shown in red ( ) and display blocks are colored blue ( ). Information flow related to detections is represented by a dashed line, information flow related to Gaussian mixture components is shown by a solid black line. Information flow in the form of extracted tracks is shown by a gray, solid line.

Additionally, the tracking algorithm shall track the velocity of the target, resulting in a four dimensional state vector

$$\boldsymbol{x}^{\mathcal{S}} = \begin{bmatrix} \boldsymbol{x}^{\mathcal{P}2} \\ \boldsymbol{v}^{\mathcal{P}2} \end{bmatrix} = \begin{bmatrix} x_1^{\mathcal{P}2} \\ x_2^{\mathcal{P}2} \\ v_1^{\mathcal{P}2} \\ v_2^{\mathcal{P}2} \end{bmatrix} = \begin{bmatrix} x_1^{\mathcal{S}} \\ x_2^{\mathcal{S}} \\ x_3^{\mathcal{S}} \\ x_4^{\mathcal{S}} \end{bmatrix} \tag{5.21}$$

where $\boldsymbol{x}^{\mathcal{P}2}$ and $\boldsymbol{v}^{\mathcal{P}2}$ give the position and target component of the track state in the surface's coordinate system. The superscript $^{\mathcal{S}}$ indicates that a variable is given with respect to the target state space.

The mapping functions for the location also define the transformation of the velocity state of a tracked target at given location. For example, as can be found with the chain rule by differentiating,

$$\boldsymbol{f}_{\mathrm{v}}^{3\leftarrow 2}(\boldsymbol{x}^{\mathcal{E}}, \boldsymbol{v}^{\mathcal{E}}) = \frac{\partial \boldsymbol{f}_{\mathrm{p}}^{3\leftarrow 2}}{\partial \boldsymbol{x}^{\mathcal{E}}}\left(\boldsymbol{x}^{\mathcal{E}}\right)\boldsymbol{v}^{\mathcal{E}} \tag{5.22}$$

maps a velocity vector from 2 to 3 dimensions. The mapping of the entire state vector is denoted by $\boldsymbol{f}_{\mathrm{s}}^{3\leftarrow 2}$. The conversion functions may depend on a parameter vector $\boldsymbol{\theta}_{\mathrm{conv}}$.

**Conversion of the tracking result to ENU coordinates** In the GM-PHD algorithm the tracking result is the Gaussian sum of equation (4.12). Extracted tracks consist of sequences of Gaussian sum components. In both cases, the tracking result is either given by or derived from the sequences $\boldsymbol{m}_k^{(j)}$ and $\mathbf{P}_k^{(j)}$.

These sequences are given in the track coordinate system $\mathcal{S}$. Often, it is desirable to represent the result with respect to the ENU coordinate system. To this end, the mapping functions that have been introduced above are used. The mean of the ENU location for component $j$ at time step $k$ is given by

$$\boldsymbol{m}_{\mathrm{p},k}^{\mathcal{E},(j)} = \boldsymbol{f}_{\mathrm{p}}^{3\leftarrow 2}\left(\boldsymbol{m}_{\mathrm{p},k}^{(j)}\right) \tag{5.23}$$

and the velocity vector in ENU coordinates is

$$\boldsymbol{m}_{\mathrm{v},k}^{\mathcal{E},(j)} = \boldsymbol{f}_{\mathrm{v}}^{3\leftarrow 2}\left(\boldsymbol{m}_{\mathrm{p},k}^{(j)}, \boldsymbol{m}_{\mathrm{v},k}^{(j)}\right). \tag{5.24}$$

Here, $\boldsymbol{m}_{\mathrm{p},k}^{(j)}$ and $\boldsymbol{m}_{\mathrm{v},k}^{(j)}$ are defined by the partitioning

$$\boldsymbol{m}_k^{(j)} = \begin{bmatrix} \boldsymbol{m}_{\mathrm{p},k}^{(j)} \\ \boldsymbol{m}_{\mathrm{v},k}^{(j)} \end{bmatrix} \tag{5.25}$$

of the original state vector into a location and a velocity component. The entire, converted six

dimensional state vector that comprises both three dimensional location and three dimensional velocity is obtained by

$$\boldsymbol{m}_k^{\mathcal{S}3,(j)} = \boldsymbol{f}_{\mathrm{s}}^{3\leftarrow 2}\left(\boldsymbol{m}_k^{(j)}\right). \tag{5.26}$$

The covariance matrix of the converted state is of the dimension $6 \times 6$. For component $j$ at time step $k$ it is given by

$$\mathbf{P}_k^{\mathcal{S}3,(j)} = \frac{\partial \boldsymbol{f}_{\mathrm{s}}^{3\leftarrow 2}}{\partial \boldsymbol{\theta}_{\mathrm{s}}}\left(\boldsymbol{m}_k^{(j)}\right)\mathbf{R}_{\mathrm{s},k}^{(j)}\left[\frac{\partial \boldsymbol{f}_{\mathrm{s}}^{3\leftarrow 2}}{\partial \boldsymbol{\theta}_{\mathrm{s}}}\left(\boldsymbol{m}_k^{(j)}\right)\right]^{\mathrm{T}}. \tag{5.27}$$

Here $\frac{\partial \boldsymbol{f}_{\mathrm{s}}^{3\leftarrow 2}}{\partial \boldsymbol{\theta}_{\mathrm{s}}}$ is the Jacobian of $\boldsymbol{f}_{\mathrm{s}}^{3\leftarrow 2}$ with respect to the vector

$$\boldsymbol{\theta}_{\mathrm{s}} = \begin{bmatrix} \boldsymbol{x}^{\mathcal{S}} \\ \boldsymbol{\theta}_{\mathrm{conv}} \end{bmatrix} \tag{5.28}$$

that comprises the target state and the parameter vector $\boldsymbol{\theta}_{\mathrm{conv}}$ that contains parameters for the conversion from 2 to 3 dimensions. The covariance matrix $\mathbf{R}_{\mathrm{s},k}^{(j)}$ is a block diagonal matrix comprising the error covariance matrix $\mathbf{P}_k^{(j)}$ of the tracking error and the error covariance matrix $\mathbf{R}_{\mathrm{conv}}$ of the conversion parameters.

**Conversion between tracking state space and full 3D Cartesian state** After these general considerations, a specific mapping between the 2 and 3 dimensional coordinate system must be chosen. The tracking algorithm is developed first for the most simple case, i.e. that – in the area of interest – the earth's surface can already be well approximated by a plane.

Then the two dimensional coordinate system spans this plane. Its relation to the 3 dimensional coordinate system is defined by its origin $\boldsymbol{x}_{\mathcal{P}3,\mathrm{origin}}^{\mathcal{E}}$ and the two orthogonal vectors of unit length, $\boldsymbol{e}_{\mathcal{P}3,1}^{\mathcal{E}}$ and $\boldsymbol{e}_{\mathcal{P}3,2}^{\mathcal{E}}$ which define the coordinate axes. The conversion from a 2 to 3 dimensional location coordinate is given by

$$\boldsymbol{f}_{\mathrm{p}}^{3\leftarrow 2}(\boldsymbol{x}^{\mathcal{P}2}) = \boldsymbol{x}_{\mathcal{P}3,\mathrm{origin}}^{\mathcal{E}} + \mathbf{T}^{\mathcal{E}\leftarrow\mathcal{P}2}\boldsymbol{x}^{\mathcal{P}2} \tag{5.29}$$

where the multiplication with the matrix

$$\mathbf{T}^{\mathcal{E}\leftarrow\mathcal{P}2} = \mathbf{T}^{\mathcal{E}\leftarrow\mathcal{P}3}\ \mathbf{T}^{D3\leftarrow D2} \tag{5.30}$$

adds an additional dimension and performs a rotation. Here

$$\mathbf{T}^{D3\leftarrow D2} = \begin{bmatrix} 1 & 0 \\ 0 & 1 \\ 0 & 0 \end{bmatrix} \tag{5.31}$$

and

$$\mathbf{T}^{\mathcal{E}\leftarrow\mathcal{P}3} = \begin{bmatrix} \boldsymbol{e}^{\mathcal{E}}_{\mathcal{P}3,1} & \boldsymbol{e}^{\mathcal{E}}_{\mathcal{P}3,2} & \boldsymbol{e}^{\mathcal{E}}_{\mathcal{P}3,3} \end{bmatrix}. \tag{5.32}$$

The inverse mapping is a projection onto the plane and is defined by

$$\boldsymbol{f}^{2\leftarrow 3}_{\mathrm{p}}(\boldsymbol{x}^{\mathcal{E}}) = \mathbf{T}^{\mathcal{P}2\leftarrow\mathcal{E}}\left(\boldsymbol{x}^{\mathcal{E}} - \boldsymbol{x}^{\mathcal{E}}_{\mathcal{P},\mathrm{origin}}\right) \tag{5.33}$$

where

$$\mathbf{T}^{\mathcal{E}\leftarrow\mathcal{P}2} = \mathbf{T}^{\mathcal{E}\leftarrow\mathcal{P}3}\ \mathbf{T}^{D3\leftarrow D2} \tag{5.34}$$

and

$$\mathbf{T}^{D2\leftarrow D3} = \begin{bmatrix} 1 & 0 & 0 \\ 0 & 1 & 0 \end{bmatrix}. \tag{5.35}$$

From these definition and with (5.22) follow the expression for the conversion of the velocity vectors

$$\boldsymbol{f}^{2\leftarrow 3}_{\mathrm{v}}(\boldsymbol{x}^{\mathcal{E}}, \boldsymbol{v}^{\mathcal{E}}) = \mathbf{T}^{\mathcal{P}2\leftarrow\mathcal{E}}\boldsymbol{v}^{\mathcal{E}} \tag{5.36}$$

and

$$\boldsymbol{f}^{3\leftarrow 2}_{\mathrm{v}}(\boldsymbol{x}^{\mathcal{E}}, \boldsymbol{v}^{\mathcal{E}}) = \mathbf{T}^{\mathcal{E}\leftarrow\mathcal{P}2}\boldsymbol{v}^{\mathcal{P}2} \tag{5.37}$$

### 5.3.2. State propagation

The state propagation of an object is governed by the classical equations of motion. These lead to the linear state propagation function

$$\boldsymbol{\phi}_k(\boldsymbol{x}_{k-1}, \boldsymbol{\nu}_{k-1}) = \mathbf{F}_k\boldsymbol{x}_{k-1} + \boldsymbol{\nu}_{k-1} \tag{5.38}$$

where

$$\mathbf{F}_k = \begin{bmatrix} 1 & \Delta t_k \\ 0 & 1 \end{bmatrix} \otimes \mathbf{I}_2 \tag{5.39}$$

and where $\Delta t_k = t_k - t_{k-1}$. Here, the Kronecker multiplication (denoted by $\otimes$) with an identity matrix $\mathbf{I}_2$ of dimension $2 \times 2$ expands the motion equations from one spatial dimension to two spatial dimensions.

The process noise term $\boldsymbol{\nu}_{k-1}$ is Gaussian with process noise covariance matrix [4, Sec. 6.2.2]

$$\mathbf{Q}_{\mathrm{pn},k-1} = \sigma_{\mathrm{a}}^2 \Delta t_k^2 \begin{bmatrix} \frac{1}{3}\Delta t_k^2 & \frac{1}{2}\Delta t_k \\ \frac{1}{2}\Delta t_k & 1 \end{bmatrix} \otimes \mathbf{I}_2 \tag{5.40}$$

$$\tag{5.41}$$

Here $\sigma_{\mathrm{a}}$ is the standard deviation of the white noise acceleration time series of the target. The choice of a variance for the acceleration is equivalent to a series of standard deviations of velocity changes $\sigma_{\mathrm{v},k} = \sigma_{\mathrm{a}} \Delta t_k$.

### 5.3.3. Definition of the measurement space

As stated in Chapter 3 each detection is associated with a measurement of target range, target DOA and target Doppler frequency. It is possible to formulate the extended Kalman filter version of the GM-PHD directly with this measurement set. However, in this case the linearization that is performed in the extended Kalman filter may have particularly negative effects. This is due to the state update, which is a weighted difference of the true measurement and predicted measurement (see equation (4.25)). The weighting is performed by multiplication with the Kalman gain matrix $\mathbf{K}_k^{(j)}$ which is computed with the Jacobian of the measurement function at the predicted target state (see equations (4.28), (4.27) and (4.29)). In particular during track initialization, the predicted state may differ strongly from the true target state. Thus, it is advisable to choose a measurement set for which the gain and hence measurement matrix do not depend strongly on the target state.

To this end, the DOA and range measurements are converted to a two dimensional measurement of the target location component of the target state space. Step I of this conversion is already given in Section 3.3.1 where the geolocation of a detection on a planar surface is described. Thus, a 3 dimensional ENU coordinate for the location of the detection is obtained. In step II the ENU coordinate is converted to a plane surface coordinate (see Section A.5.7)

$$\hat{\boldsymbol{x}}_{\mathrm{tgt},k}^{\mathcal{P}2,(j)} = \boldsymbol{f}^{\mathcal{P}2 \leftarrow \mathcal{E}} \left( \hat{\boldsymbol{x}}_{\mathrm{tgt},k}^{\mathcal{E},(j)}; \boldsymbol{x}_{\mathcal{P},\mathrm{origin}}^{\mathcal{E}}, \boldsymbol{\gamma}^{\mathcal{E} \leftarrow \mathcal{P}3} \right) . \tag{5.42}$$

The concatenation of both functions yields the function $\boldsymbol{f}^{\mathcal{P}2 \leftarrow \mathrm{ur}}$ such that the estimate in plane coordinates is given by (see Section A.5.9)

$$\hat{\boldsymbol{x}}_{\mathrm{tgt},k}^{\mathcal{P}2,(j)} = \boldsymbol{f}^{\mathcal{P}2 \leftarrow \mathrm{ur}} \left( \hat{u}_k^{(j)}, \hat{r}_k^{(j)}, \hat{\boldsymbol{x}}_{\mathrm{ant},k}^{\mathcal{E}}, \hat{\boldsymbol{e}}_{\mathrm{ant},k,1}^{\mathcal{E}}, \boldsymbol{n}_{\mathrm{plane}}^{\mathcal{E}}, d_{\mathrm{plane}}^{\mathcal{E}} \right) . \tag{5.43}$$

Furthermore, the velocity measurement of Section 3.3.2 is employed. The entire measurement

vector is then given by (see Section A.5.1)

$$\begin{aligned}\boldsymbol{z}_k^{(j)} &= \begin{bmatrix} \hat{\boldsymbol{x}}_{\mathrm{tgt},k}^{\mathcal{P}2,(j)} \\ v_{\mathrm{t,pl},k}^{(j)} \end{bmatrix} \\ &= \boldsymbol{f}^{\mathcal{M}\leftarrow\mathrm{urv}}\left(\hat{u}_k^{(j)}.\hat{r}_k^{(j)}, v_{\mathrm{rad},k}^{(j)}, \hat{\boldsymbol{x}}_{\mathrm{ant},k}^{\mathcal{E}}, \hat{\boldsymbol{e}}_{\mathrm{ant},k,1}^{\mathcal{E}}, \boldsymbol{n}_{\mathrm{plane}}^{\mathcal{E}}, d_{\mathrm{plane}}^{\mathcal{E}}\right). \end{aligned} \tag{5.44}$$

## 5.3.4. Definition of the observation process

In the extended Kalman filter version of the GM-PHD, the vector valued function $\boldsymbol{h}_k$ defines how a target state is converted to a synthetic measurement. It also specifies in what way a noise term $\boldsymbol{\epsilon}$ corrupts the measurement. The Jacobians of this function with respect to the target state and the noise term,

$$\mathbf{H}_k^{(j)} = \left.\frac{\partial \boldsymbol{h}_k(\boldsymbol{x},\mathbf{0})}{\partial \boldsymbol{x}}\right|_{\boldsymbol{x}=\boldsymbol{m}_{k|k-1}^{(j)}} \tag{5.45}$$

$$\mathbf{U}_k^{(j)} = \left.\frac{\partial \boldsymbol{h}_k(\boldsymbol{m}_{k|k-1}^{(j)},\boldsymbol{\epsilon})}{\partial \boldsymbol{\epsilon}}\right|_{\boldsymbol{\epsilon}=\mathbf{0}}, \tag{5.46}$$

are employed in the update step of this tracking filter. Thus, it is necessary, to define $\boldsymbol{h}_k$ and to find expressions for the respective Jacobians.

At this point it is pertinent to define the noise terms that should be considered. First of all, there are the noise terms that are directly related to each detection, i.e. the measurement noise of the DOA estimate $\epsilon_u$, the measurement noise of the range estimate $\epsilon_r$ and the measurement noise of the estimate of the radial velocity $\epsilon_v$. These errors are specific for each detection. Secondly, there are the measurement errors with respect to the antenna location $\boldsymbol{\epsilon}_{p,\mathrm{ant}}^{\mathcal{E}}$, the antenna velocity $\boldsymbol{\epsilon}_{v,\mathrm{ant}}^{\mathcal{E}}$ and the antenna attitude $\epsilon_{\mathrm{yp}}^{\mathcal{A}\leftarrow\mathcal{E}}$ which are identical for all detections of one time step. All of these measurement noise terms are combined into the vector

$$\boldsymbol{\epsilon} = [\epsilon_u\ \epsilon_r\ \epsilon_v\ \boldsymbol{\epsilon}_{p,\mathrm{ant}}^{\mathcal{E}}\ \boldsymbol{\epsilon}_{v,\mathrm{ant}}^{\mathcal{E}}\ \boldsymbol{\epsilon}_{\mathrm{yp}}^{\mathcal{A}\leftarrow\mathcal{E}}]^{\mathrm{T}}. \tag{5.47}$$

The covariance matrix $\mathbf{R}_{\epsilon,k}$ of these measurement errors is time step dependent.

### Observation function including the noise term

For incorporating all of these noise terms in the synthetic measurement (two dimensional position and a velocity term), it is computed in two steps. In the first step, the track state is converted to the DOA, range and radial velocity measurement without adding any measurement error. The track state $\boldsymbol{x}^{\mathcal{S}}$ is converted to the 3D target location and velocity variables $\boldsymbol{x}^{\mathcal{E}}$ and $\boldsymbol{v}^{\mathcal{E}}$. Then, the difference between the target location

$$\Delta\boldsymbol{x}^{\mathcal{E}} = \boldsymbol{x}^{\mathcal{E}} - \boldsymbol{x}_{\mathrm{ant}}^{\mathcal{E}} \tag{5.48}$$

can be used to determine the range

$$r = \|\Delta \boldsymbol{x}^{\mathcal{E}}\| \tag{5.49}$$

to the target and the direction vector in ENU coordinates

$$\boldsymbol{u}^{\mathcal{E}} = \frac{\Delta \boldsymbol{x}^{\mathcal{E}}}{\|\Delta \boldsymbol{x}^{\mathcal{E}}\|} \tag{5.50}$$

The radial velocity of the target is given by

$$v_{\mathrm{rad}} = \left[\boldsymbol{u}_{\mathrm{at}}^{\mathcal{E}}\right]^{\mathrm{T}} \left(\boldsymbol{v}_{\mathrm{tgt}}^{\mathcal{E}} - \boldsymbol{v}_{\mathrm{ant}}^{\mathcal{E}}\right) . \tag{5.51}$$

The orientation of the x-axis of the antenna coordinate system and hence the orientation of the linear array is given by

$$\boldsymbol{e}_{\mathrm{ant},1}^{\mathcal{E}} = \mathbf{T}^{\mathcal{E}\leftarrow\mathcal{A}} \begin{bmatrix} 1 \\ 0 \\ 0 \end{bmatrix} , \tag{5.52}$$

where

$$\mathbf{T}^{\mathcal{E}\leftarrow\mathcal{A}} = \mathbf{T}_{\mathrm{Euler}}^{\mathrm{inv}}(\boldsymbol{\gamma}_{\mathrm{ypr}}^{\mathcal{A}\leftarrow\mathcal{E}}) \tag{5.53}$$

is the Euler rotation matrix. With $\boldsymbol{\gamma}_{\mathrm{ypr}}^{\mathcal{A}\leftarrow\mathcal{E}} = [\gamma_{\mathrm{yaw}} \quad \gamma_{\mathrm{pitch}} \quad \gamma_{\mathrm{roll}}]^{\mathrm{T}}$ and the definition of the inverse Euler rotation matrix of A.7.1, the expression of equation (5.52) can be expanded to

$$\begin{aligned} \boldsymbol{e}_{\mathrm{ant},1}^{\mathcal{E}} &= \mathbf{T}_{\mathrm{y}}(-\gamma_{\mathrm{yaw}})\mathbf{T}_{\mathrm{p}}(-\gamma_{\mathrm{pitch}})\mathbf{T}_{\mathrm{r}}(-\gamma_{\mathrm{roll}}) \begin{bmatrix} 1 \\ 0 \\ 0 \end{bmatrix} \\ &= \begin{bmatrix} \cos(\gamma_{\mathrm{yaw}})\cos(\gamma_{\mathrm{pitch}}) \\ \sin(\gamma_{\mathrm{yaw}})\cos(\gamma_{\mathrm{pitch}}) \\ -\sin(\gamma_{\mathrm{pitch}}) \end{bmatrix} . \end{aligned} \tag{5.54}$$

The directional cosine of the target direction vector with respect to the linear antenna is given by

$$u_1^{\mathcal{A}} = \left[\boldsymbol{e}_{\mathrm{ant},1}^{\mathcal{E}}\right]^{\mathrm{T}} \boldsymbol{u}^{\mathcal{E}} . \tag{5.55}$$

These equations show that the roll angle of the antenna attitude is not required for computing the orientation of the antenna's x-axis. Thus, the vector

$$\boldsymbol{\gamma}_{\mathrm{yp}}^{\mathcal{A}\leftarrow\mathcal{E}} = [\gamma_{\mathrm{yaw}} \quad \gamma_{\mathrm{pitch}}]^{\mathrm{T}} \tag{5.56}$$

is introduced that contains only the the yaw and roll angle. All measurements are combined into

the vector

$$\boldsymbol{z}_{\mathrm{urv}} = \begin{bmatrix} u_1^{\mathcal{A}} \\ r \\ v_{\mathrm{rad}} \end{bmatrix} . \tag{5.57}$$

In function form, the computation of the radar measurement is given by (see Sections A.5.10 and A.3.1)

$$\boldsymbol{z}_{\mathrm{urv}} = \boldsymbol{f}^{\mathrm{urv}\leftarrow\mathcal{S}} \left( \boldsymbol{x}^{\mathcal{E}}, \boldsymbol{v}^{\mathcal{E}}; \boldsymbol{x}^{\mathcal{E}}_{\mathrm{ant}}, \boldsymbol{v}^{\mathcal{E}}_{\mathrm{ant}}, \boldsymbol{\gamma}^{\mathcal{A}\leftarrow\mathcal{E}}_{\mathrm{yp}} \right) . \tag{5.58}$$

In the second step, the synthetic measurement of DOA range and radial velocity is converted to the track measurement with function $\boldsymbol{f}^{\mathcal{M}\leftarrow\mathrm{urv}}$ which has already been defined above. In this step, the measurement noise is added to the parameters

$$\begin{aligned} \boldsymbol{z} = \boldsymbol{f}^{\mathcal{M}\leftarrow\mathrm{urv}} \big( & u + \epsilon_u, r + \epsilon_r, v_{\mathrm{rad}} + \epsilon_v, \boldsymbol{x}^{\mathcal{E}}_{\mathrm{ant}} + \boldsymbol{\epsilon}^{\mathcal{E}}_{\mathrm{p,ant}}, \\ & \boldsymbol{v}^{\mathcal{E}}_{\mathrm{ant}} + \boldsymbol{\epsilon}^{\mathcal{E}}_{\mathrm{v,ant}}, \boldsymbol{\gamma}^{\mathcal{A}\leftarrow\mathcal{E}}_{\mathrm{yp}} + \boldsymbol{\epsilon}_{\mathrm{yp,ant}}, \boldsymbol{n}^{\mathcal{E}}_{\mathrm{plane}}, d^{\mathcal{E}}_{\mathrm{plane}} \big) . \end{aligned} \tag{5.59}$$

Both steps combined are given in function form in Section A.5.3 as

$$\boldsymbol{z} = \boldsymbol{f}^{\mathcal{M}\leftarrow\mathcal{S}}_{\epsilon} \left( \boldsymbol{x}^{\mathcal{S}}; \boldsymbol{x}^{\mathcal{E}}_{\mathrm{ant}}, \boldsymbol{v}^{\mathcal{E}}_{\mathrm{ant}}, \boldsymbol{\gamma}^{\mathcal{A}\leftarrow\mathcal{E}}_{\mathrm{yp}}, \boldsymbol{\epsilon} \right) . \tag{5.60}$$

With this function, it is possible to define the observation function by (see Section A.5.2)

$$\boldsymbol{h}_k(\boldsymbol{x}^{\mathcal{S}}, \boldsymbol{\epsilon}) = \boldsymbol{f}^{\mathcal{M}\leftarrow\mathcal{S}}_{\epsilon} \left( \boldsymbol{x}^{\mathcal{S}}; \hat{\boldsymbol{x}}^{\mathcal{E}}_{\mathrm{ant},k}, \hat{\boldsymbol{v}}^{\mathcal{E}}_{\mathrm{ant},k}, \hat{\boldsymbol{\gamma}}^{\mathcal{A}\leftarrow\mathcal{E}}_{\mathrm{yp},k}, \boldsymbol{\epsilon} \right) . \tag{5.61}$$

#### Observation function in the absence of noise

Since the Jacobian of the observation function with respect to the target state is computed for a zero noise vector, it is useful to find a simplified expression of $\boldsymbol{f}^{\mathcal{M}\leftarrow\mathcal{S}}_{\epsilon}$ for $\boldsymbol{\epsilon} = \boldsymbol{0}$.

This is particularly easy in the case of the location measurement. In the absence of noise, it is simply given by the first two elements of the track state vector. The velocity measurement is found according to its definition in equation (3.60) as the scalar product between the normalized projection of the direction vector on the surface plane and the target velocity vector. The normalized projection vector is given by

$$\boldsymbol{u}^{\mathcal{E}}_{\mathrm{at,p,n}} = \frac{\mathbf{P}^{\mathcal{E}}_{\mathrm{plane}} \Delta\boldsymbol{x}^{\mathcal{E}}_{\mathrm{at}}}{\| \mathbf{P}^{\mathcal{E}}_{\mathrm{plane}} \Delta\boldsymbol{x}^{\mathcal{E}}_{\mathrm{at}} \|} = \frac{\Delta\boldsymbol{x}^{\mathcal{E}}_{\mathrm{at,p}}}{\| \Delta\boldsymbol{x}^{\mathcal{E}}_{\mathrm{at,p}} \|} \tag{5.62}$$

and the scalar product is

$$v_{\mathrm{t,pl}} = \left[ \boldsymbol{u}^{\mathcal{E}}_{\mathrm{at,p,n}} \right]^T \boldsymbol{v}^{\mathcal{E}} . \tag{5.63}$$

The results are arranged into the measurement vector

$$\boldsymbol{z} = \begin{bmatrix} x_1^{\mathcal{S}} \\ x_2^{\mathcal{S}} \\ v_{\mathrm{t,pl}} \end{bmatrix}. \tag{5.64}$$

The function form is given in Section A.5.4. It defines $\boldsymbol{h}_k$ for the special case of a zero noise term by (see Section A.5.2

$$\boldsymbol{h}_k(\boldsymbol{x}^{\mathcal{S}}, \mathbf{0}) = \boldsymbol{f}_0^{\mathcal{M}\leftarrow\mathcal{S}}\left(\boldsymbol{x}^{\mathcal{S}}; \hat{\boldsymbol{x}}_{\mathrm{ant},k}^{\mathcal{E}}, \hat{\boldsymbol{v}}_{\mathrm{ant},k}^{\mathcal{E}}, \hat{\boldsymbol{\gamma}}_{\mathrm{yp},k}^{\mathcal{A}\leftarrow\mathcal{E}}\right) \tag{5.65}$$

### 5.3.5. Jacobians of the observation process

The computation of the Jacobian

$$\mathbf{U}_k^{(j)} = \left.\frac{\partial \boldsymbol{h}_k(\boldsymbol{m}_{k|k-1}^{(j)}, \boldsymbol{\epsilon})}{\partial \boldsymbol{\epsilon}}\right|_{\boldsymbol{\epsilon}=\mathbf{0}} \tag{5.66}$$

is required for implementing the GM-PHD tracking algorithm. It requires a tedious but straight forward application of rules of differentiation, in particular the chain rule. The order in which different elements for its computation should be computed is

1. Jacobian of the 3D geolocation based on range-DOA measurement, see Section A.1.2
2. Jacobian of the conversion from 3 to 2 dimensions, see Section A.6.1
3. Jacobian of the measurable velocity component in the tracking plane based on range, DOA, radial velocity measurement, see Section A.2.2
4. Jacobian of the track measurement as function of the track state with respect to the noise vector $\boldsymbol{\epsilon}$, see Section A.6.4

This computation of the Jacobian is summarized as matrix valued function $\mathbf{f}_{J,\epsilon}^{\mathcal{M}\leftarrow\mathcal{S}}$ and given in Appendix A.6.4. With this definition, the Jacobian is

$$\mathbf{U}_k^{(j)} = \mathbf{f}_{J,\epsilon}^{\mathcal{M}\leftarrow\mathcal{S}}\left(\boldsymbol{m}_{k|k-1}^{(j)}; \hat{\boldsymbol{x}}_{\mathrm{ant},k}^{\mathcal{E}}, \hat{\boldsymbol{v}}_{\mathrm{ant},k}^{\mathcal{E}}, \hat{\boldsymbol{\gamma}}_{\mathrm{yp},k}^{\mathcal{A}\leftarrow\mathcal{E}}, \mathbf{0}\right). \tag{5.67}$$

Additionally, the computation of the Jacobian of the observation function

$$\mathbf{H}_k^{(j)} = \left.\frac{\partial \boldsymbol{h}_k(\boldsymbol{x}, \mathbf{0})}{\partial \boldsymbol{x}}\right|_{\boldsymbol{x}=\boldsymbol{m}_{k|k-1}^{(j)}} \tag{5.68}$$

with respect to the track state is required. In order to compute this Jacobian, the more simple definition $\boldsymbol{h}_k$ for the noise free case (see Section A.5.2) is used. Its derivation is straight forward

and the resulting Jacobian is given as matrix valued function $\mathbf{f}_{J,0}^{\mathcal{M}\leftarrow\mathcal{S}}$ in Section A.6.5. Thus, the measurement matrix is given by

$$\mathbf{H}_k^{(j)} = \mathbf{f}_{J,0}^{\mathcal{M}\leftarrow\mathcal{S}}\left(\boldsymbol{m}_{k|k-1}^{(j)}; \hat{\boldsymbol{x}}_{\mathrm{ant},k}^{\mathcal{E}}, \hat{\boldsymbol{v}}_{\mathrm{ant},k}^{\mathcal{E}}, \hat{\boldsymbol{\gamma}}_{\mathrm{yp},k}^{\mathcal{A}\leftarrow\mathcal{E}}\right) . \tag{5.69}$$

## 5.3.6. Modeling of the state dependent probability of detection

As evident in equation (5.3), the GM-PHD tracking filter requires an expression for the state dependent probability of detection in order to determine $p_{\mathrm{D},k}(\boldsymbol{m}_k^{(j)})$, the probability of detection of the GM-PHD element with index $j$ at time $k$. The 'true' probability of detection depends on the radar system, the detection algorithm, the radar cross section of the target, the target parameters and the clutter environment. However, as assumptions must be made for modeling the radar cross section and the clutter environment, the modeled detection probability will necessarily diverge from the 'true' solution. Furthermore, it is extremely important that the expression for detection probability is *numerically efficient* since it must be computed for every updated track state – before pruning and merging. Thus, it may be pertinent to use approximations that decrease the accuracy but increase the speed of computation.

### Signal and clutter model based evaluation of the detection probability

The GMTI of this thesis employs the AMF test (see equation (3.32) and (3.33)). The evaluation of the detection probability of the AMF test involves a numerical integration [64, equation (34)]. As an approximation, the detection probability of a GLRT can be used. This substitution corresponds to neglecting the loss of detection probability that occurs due to imperfect learning of the clutter and noise covariance matrix. The probability of detection of a GLRT is directly related to the SCNR that is obtained after filtering of the signal. For a Swerling I target model, the probability of detection simply is $p_{\mathrm{fa}}^{1/r_{\mathrm{scnr}}}$, where $p_{\mathrm{fa}}$ is the desired false alarm probability and $r_{\mathrm{scnr}}$ is the clutter to noise ratio.

The clutter to noise ratio depends on the target signal power, the clutter and noise covariance matrix and the mismatch between the target steering vector and the true target model vector. Due to the use of adjacent bin post Doppler processing, the interference covariance matrix is a function of the target location in range and Doppler.

By principle it is impossible to 'know' the true clutter and noise covariance matrix. Only an approximation can be obtained either by learning from the received radar data or by theoretical modeling. Regardless of how the interference covariance matrix is obtained, the process of determining the SCNR and hence the detection probability is similar:

**(a)** The tracking algorithm computes the state of the updated Gaussian sum components $\boldsymbol{m}_k^{(j)}$, $j = 1...N_k$.

**(b)** The corresponding range, Doppler and direction of arrival values for all predicted sum components are determined, yielding $u_k^{(j)}$, $r_k^{(j)}$ and $f_k^{(j)}$.

(**c**) The interference covariance matrix $\tilde{\mathbf{R}}_{\mathrm{q},k}^{(j)}$ is determined – either by learning from radar data or model based. The covariance matrix depends on the location of the target in range and Doppler.

(**d**) The steering vector $\tilde{\boldsymbol{v}}_{\mathrm{s},k}^{(j)}$ is constructed. For adjacent bin post Doppler processing, it is a function of the target's Doppler frequency.

(**e**) A model vector $\tilde{\boldsymbol{v}}_{\mathrm{t},k}^{(j)}$ for the target signal is constructed. It is a function of the target signal direction of arrival and Doppler frequency.

(**f**) The expected signal power $P_{\mathrm{t},k}^{(j)}$ is determined by multiplication of the target signal SNR of equation (2.5) with the noise power.

(**g**) The previously computed variables are used to determine the SCNR $r_{\mathrm{scnr},k}^{(j)}$ and the probability of detection.

**Model based determination of the clutter covariance matrix** If the tracking algorithm does not have access to the interference covariance matrices that are learned in the detection step, the covariance matrices can alternatively be determined by modeling. This can be performed with a clutter model such as given in [83, Sec. 2.6.1, eq. (61)]. The determination and subsequent inversion of the clutter covariance matrices are computationally demanding. The number of interference covariance matrices that have to be computed and inverted scales linearly with the number of posterior components of the Gaussian sum. Thus, especially for large numbers of components this might lead to excessive run times for the tracking algorithm.

For a significantly faster but approximative approach the clutter covariance matrices are only computed for a single bin post Doppler detector. Thus, there arises a difference between the actual detector and the one which is modeled for determining the clutter covariance matrix. The benefit of this approach is that single bin post Doppler covariance matrices can be obtained in a particularly efficient manner for entire range lines. Furthermore, inverting single bin covariance matrices is faster. Another speed up is obtained by determining the covariance matrices only for specific range lines as shown in Figure 5.5. For targets that lie outside of these range lines, the closest clutter covariance matrix is then chosen. Due to these modifications the computational load becomes independent of the actual number of Gaussian sum components.

**Model based evaluation of the detection probability**

An alternative to determining the probability of detection based on the SNCR (hence a complete clutter and signal model), is to use a simplified model for the probability of detection. Such a model has been proposed in [36, Sec. 4.1]. In this model the detection probability is determined by two parameters: A maximum detection probability outside of the clutter region and the minimum detectable velocity (MDV). If the target velocity falls below the MDV, the probability of detection reduces exponentially.

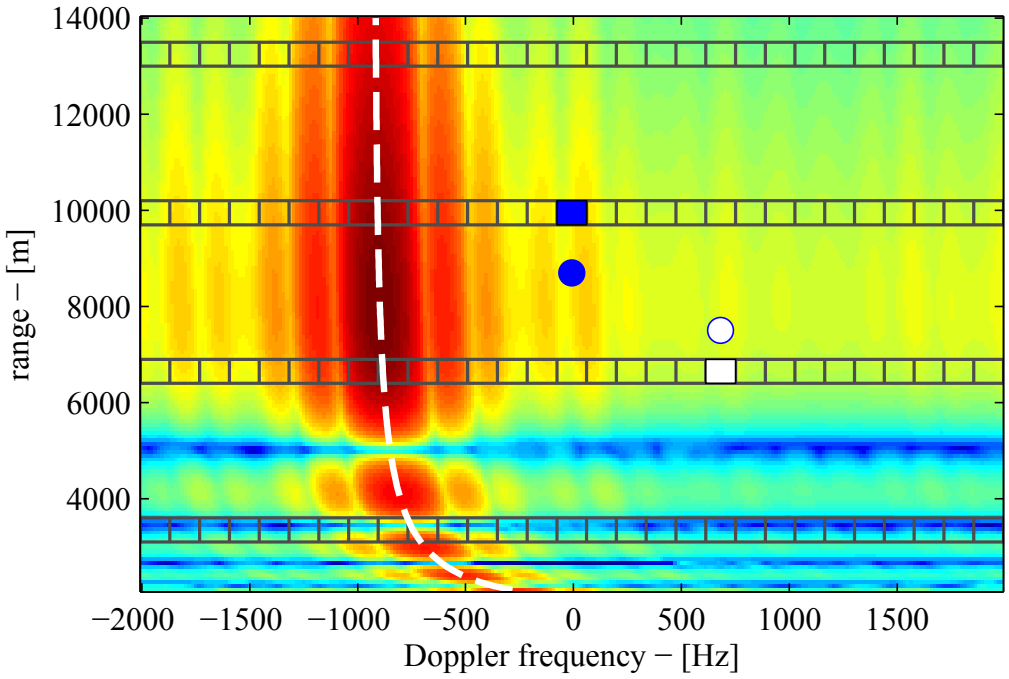


**Figure 5.5.:** Theoretical clutter power versus range and Doppler frequency. The range-Doppler bins for which the clutter covariance matrices are computed are indicated schematically by the squares. For a target that lies at an arbitrary location in the range Doppler map, the clutter covariance matrix of the closest range (for which the matrices are computed) substitutes for characterizing the clutter at the target location. This is shown exemplary for two targets whose locations in the range Doppler map are shown by circles in blue and white. The Doppler and range gates from which the clutter matrices are taken for these targets are indicated in the corresponding colors.

This approach of determining the detection probability offers the advantage of using 'negative' sensor information and is computationally fast. Still, in this reference implementation of the tracking algorithm the SCNR based approach has been chosen since it shows a clearer link to the radar signal processing. Provided that the clutter covariance matrix is determined from the radar data, it is likely that it is also more accurate.

### 5.3.7. An expression for the false alarm probability

The GM-PHD algorithm also requires the definition of the intensity of the random finite set of false alarms $\kappa_k(\boldsymbol{z})$. The intensity of false alarms gives the density of the expected number of false alarms in the track measurement space. Thus, the integral over the entire measurement space

yields the total expected number of false alarms, i.e.

$$N_{\text{falseAlarm}} = \int_x \int_y \int_{v_{\text{pl}}} \kappa(\boldsymbol{z}) \, \mathrm{d}\, v_{\text{t,pl}} \, \mathrm{d}\, x \, \mathrm{d}\, y \tag{5.70}$$

Since target detections and hence false alarms are possible only in a region of the target state space, it is clear that the integral can in fact be limited to this region.

As the detections are made in the range/Doppler domain, it is easier to define the intensity in the original radar measurement space. It can then be converted to the track measurement space. In the original radar measurement space, all false alarms lie between $r_{\min}$ and $r_{\max}$, the minimum and maximum range for which the data is recorded, the directional cosine values lie between $u_{\min,k}$ and $u_{\max,k}$ and the radial velocity estimate is in between $v_{\text{rad,min},k}$ and $v_{\text{rad,max},k}$. Within these bounds, the false alarm intensity is set to a constant since the detector employs a constant false alarm (CFAR) test. Thus, the false alarm intensity in the radar measurement space is given by

$$\kappa^{\text{urv}}(\boldsymbol{z}_{\text{urv}}) = \begin{cases} \frac{N_{\text{falseAlarm}}}{\Delta r \Delta u \Delta v_{\text{rad}}} & \text{, if } r_{\min} < r < r_{\max} \\ & \text{and } u_{\min,k} < u < u_{\max,k} \\ & \text{and } v_{\text{rad,min},k} < v_{\text{rad}} < v_{\text{rad,max},k} \\ 0 & \text{, otherwise} \end{cases} \tag{5.71}$$

where

$$\Delta r = r_{\max} - r_{\min}$$

$$\Delta u = v_{\text{rad,max},k} - v_{\text{rad,min},k} \tag{5.72}$$

$$\Delta v_{\text{rad}} = v_{\text{rad,max},k} - v_{\text{rad,min},k} \, . \tag{5.73}$$

The integral over the intensity with respect to the radar measurement space also yields the total expected number of false alarms.

$$N_{\text{falseAlarm}} = \int_u \int_r \int_{v_{\text{rad}}} \kappa^{\text{urv}}(\boldsymbol{z}_{\text{urv}}) \, \mathrm{d}\, v_{\text{rad}} \, \mathrm{d}\, r \, \mathrm{d}\, u \, . \tag{5.74}$$

The track measurement can be converted to the radar measurement with (see Section A.5.11)

$$\boldsymbol{f}^{\text{urv}\leftarrow\mathcal{M}} \left( \boldsymbol{z}, \boldsymbol{x}_{\text{ant}}^{\mathcal{E}}, \boldsymbol{v}_{\text{ant}}^{\mathcal{E}}, \boldsymbol{\gamma}_{\text{yp}}^{\mathcal{A}\leftarrow\mathcal{E}} \right) \, . \tag{5.75}$$

With this conversion and the identities (5.70) and (5.74), the rule of substitution provides the expression

$$\kappa \left( \boldsymbol{z} \right) = \kappa^{\text{urv}}(\boldsymbol{f}^{\text{urv}\leftarrow\mathcal{M}} \left( \boldsymbol{z}, ... \right)) \left| \det \left( \frac{\partial \boldsymbol{f}^{\text{urv}\leftarrow\mathcal{M}}}{\partial z} (\boldsymbol{z}, ...) \right) \right| \tag{5.76}$$

for the conversion from the false alarm intensity with respect to the radar measurement to the false alarm intensity with respect to the track measurement. An expression for the Jacobian $\frac{\partial \boldsymbol{f}^{\mathrm{urv}\leftarrow\mathcal{M}}}{\partial z}(\boldsymbol{z},...)$ of $\boldsymbol{f}^{\mathrm{urv}\leftarrow\mathcal{M}}\left(\boldsymbol{z},\boldsymbol{x}_{\mathrm{ant}}^{\mathcal{E}},\boldsymbol{v}_{\mathrm{ant}}^{\mathcal{E}},\boldsymbol{\gamma}_{\mathrm{yp}}^{\mathcal{A}\leftarrow\mathcal{E}}\right)$ is given in Section A.6.7 by

$$\boldsymbol{f}_{\mathrm{J}}^{\mathrm{urv}\leftarrow\mathcal{M}}\left(\boldsymbol{z},\boldsymbol{x}_{\mathrm{ant}}^{\mathcal{E}},\boldsymbol{v}_{\mathrm{ant}}^{\mathcal{E}},\boldsymbol{\gamma}_{\mathrm{yp}}^{\mathcal{A}\leftarrow\mathcal{E}}\right) . \tag{5.77}$$

## 5.4. Use of a digital elevation model

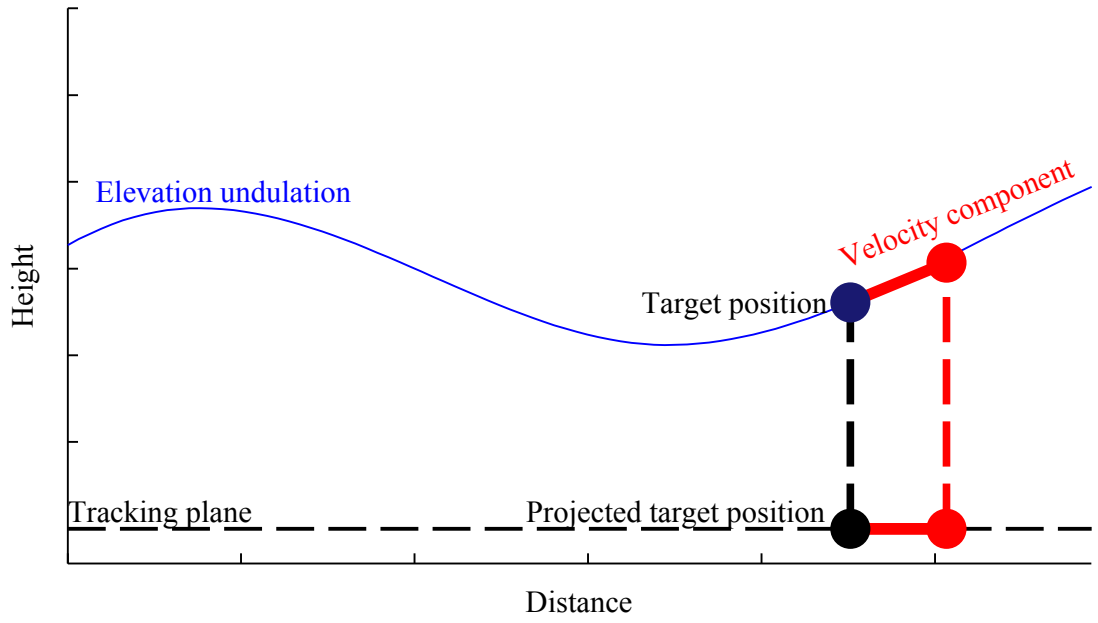


**Figure 5.6.:** Mapping between 2D and 3D coordinate systems

In the preceding sections, the tracking algorithm was designed for scenarios in which the earth's surface could be approximated by a plane. Now, the tracking algorithm is extended to incorporate a digital elevation model. This requires a modification of the mapping between the two dimensional tracking coordinate system $\mathcal{P}2$ and the three dimensional ENU coordinate system $\mathcal{E}$. The modified mapping is visualized in Figure 5.6: For the conversion of a location from $\mathcal{E}$ to $\mathcal{P}2$, the three dimensional target position is projected onto the x-y plane of the ENU coordinate system. For the inverse mapping, the z coordinate is found by interpolating with the DEM. Likewise, for the conversion of the velocity vector from 3D to 2D the target velocity is projected on the x-y plane of the ENU coordinate system. For the conversion of the velocity vector from 2D to 3D, the tangent plane of the DEM at the location of the target is used.

### 5.4.1. Conversion from an ENU state to a track state

Since the conversion from ENU coordinates to the tracking coordinate system is a simple projection, the mapping functions are given by the matrix multiplications

$$\boldsymbol{f}_{\mathrm{p,dem}}^{2\leftarrow 3}(\boldsymbol{x}^{\mathcal{E}}, \boldsymbol{v}^{\mathcal{E}}) = \mathbf{T}^{2\leftarrow 3}\boldsymbol{x}^{\mathcal{E}} \tag{5.78}$$

and

$$\boldsymbol{f}_{\mathrm{v,dem}}^{2\leftarrow 3}(\boldsymbol{x}^{\mathcal{E}}, \boldsymbol{v}^{\mathcal{E}}) = \mathbf{T}^{2\leftarrow 3}\boldsymbol{v}^{\mathcal{E}}\,. \tag{5.79}$$

### 5.4.2. Conversion from a track state to an ENU state

The track state location is converted to an ENU location by

$$\boldsymbol{f}_{\mathrm{p,dem}}^{3\leftarrow 2}\left(\boldsymbol{x}_{\mathrm{p}}^{\mathcal{P}2}, \boldsymbol{\theta}_{\mathrm{dem}}\right) = \begin{bmatrix} \boldsymbol{x}^{\mathcal{P}2} \\ f_{\mathrm{bilin}}\left(\boldsymbol{x}^{\mathcal{P}2}, \boldsymbol{\theta}_{\mathrm{dem}}\right) \end{bmatrix}, \tag{5.80}$$

where $f_{\mathrm{bilin}}$ is a function that performs a bilinar interpolation (see Appendix A.7.3). The velocity conversion is given by

$$\boldsymbol{f}_{\mathrm{v,dem}}^{3\leftarrow 2}(\boldsymbol{x}^{\mathcal{S}}, \boldsymbol{\theta}_{\mathrm{dem}}) = \frac{\partial \boldsymbol{f}_{\mathrm{dem}}^{3\leftarrow 2}}{\partial \boldsymbol{x}^{\mathcal{E}12}}(\boldsymbol{x}^{\mathcal{P}2}, \boldsymbol{\theta}_{\mathrm{dem}})\boldsymbol{v}^{\mathcal{P}2}\,. \tag{5.81}$$

Here, the computation of the Jacobian $\frac{\partial \boldsymbol{f}_{\mathrm{p,dem}}^{3\leftarrow 2}}{\partial \boldsymbol{x}^{\mathcal{E}12}}(\boldsymbol{x}^{\mathcal{P}2}, \boldsymbol{\theta}_{\mathrm{dem}})\boldsymbol{v}^{\mathcal{P}2}$ is given in Appendix A.9.1 Both conversions combined yield the function

$$\boldsymbol{f}_{\mathrm{s}}^{3\leftarrow 2}(\boldsymbol{x}^{\mathcal{S}}, \boldsymbol{\theta}_{\mathrm{dem}}) = \begin{bmatrix} \boldsymbol{f}_{\mathrm{p,dem}}^{3\leftarrow 2}(\boldsymbol{x}^{\mathcal{P}2}, \boldsymbol{\theta}_{\mathrm{dem}}) \\ \boldsymbol{f}_{\mathrm{v,dem}}^{3\leftarrow 2}(\boldsymbol{x}^{\mathcal{S}}, \boldsymbol{\theta}_{\mathrm{dem}}) \end{bmatrix}. \tag{5.82}$$

### 5.4.3. Error propagation

The computation of the error covariance matrix of the ENU location and velocity state according to equation (5.27) requires the Jacobian of $\boldsymbol{f}_{\mathrm{s}}^{3\leftarrow 2}$ with respect to $\boldsymbol{\theta}_{\mathrm{s}}$. This variable comprises the full track state and error terms of the digital elevation model. Without the introduction of errors due to the DEM, the resulting covariance matrix is singular. Since the elevation coordinate is found with a bilinear interpolation, only the errors of the four edges of the quadrant where the interpolation occurs are relevant. The computation of the Jacobian is given in Appendix A.9. The error covariance matrix of $\boldsymbol{\theta}_{\mathrm{s}}$ is of the form

$$\mathbf{R}_{\mathrm{s},k}^{(j)} = \begin{bmatrix} \mathbf{P}_{k}^{(j)} & \mathbf{0}_{4\times 4} \\ \mathbf{0}_{4\times 4} & \mathbf{R}_{\mathrm{dem}} \end{bmatrix}, \tag{5.83}$$

where $\mathbf{R}_{\mathrm{dem}}$ is the error covariance matrix of the four elevation values.

# 6. Tracking results with simulated data

In this chapter, the functionality of the reference implementation of the ground moving target tracking algorithm is tested with simulated data sets. The input to the tracking algorithm shall be similar to the input that it receives from real data sets. In order to generate this input, a simulator has been implemented.

## 6.1. Simulation of ground moving target detections by an airborne radar

As input, the simulator requires the motion model of the antenna, the steering of the antenna over time and radar parameters. It can simulate detections that originate from an arbitrary number of targets with arbitrary paths and RCS values. Additionally, false alarms are generated according to a user defined false alarm rate. It also corrupts the true motion parameters of the antenna with noise in order to simulate estimates of the antenna position, antenna velocity and attitude. The steps that are necessary for the data simulation are listed in Table 6.1.

**Setup of simulations with linear antenna motion** For a scenario with linear antenna motion, the position and velocity vector of the antenna is defined by its Cartesian position $\boldsymbol{x}^{\mathcal{E}}_{\text{ant,sc,0}}$ at time 0 and the velocity vector $\boldsymbol{v}^{\mathcal{E}}_{\text{ant,sc,0}}$. The antenna attitude is determined by the Euler angles $\boldsymbol{\gamma}^{\mathcal{A}\leftarrow\mathcal{E}}_{\text{ypr,sc,0}} = \begin{bmatrix} \gamma^{\mathcal{A}\leftarrow\mathcal{E}}_{\text{yaw,sc,0}} \\ \gamma^{\mathcal{A}\leftarrow\mathcal{E}}_{\text{pitch,sc,0}} \\ \gamma^{\mathcal{A}\leftarrow\mathcal{E}}_{\text{roll,sc,0}} \end{bmatrix}$. With these parameters the antenna location versus time is given by

$$\boldsymbol{x}^{\mathcal{E}}_{\text{ant},k} = \boldsymbol{x}^{\mathcal{E}}_{\text{ant,sc,0}} + \boldsymbol{v}^{\mathcal{E}}_{\text{ant,sc,0}} t_k \,, \tag{6.1}$$

where

$$t_k = t_0 + k\ \Delta t \tag{6.2}$$

is the vector that gives the recording time for CPI $k$. The antenna velocity is

$$\boldsymbol{v}^{\mathcal{E}}_{\text{ant},k} = \boldsymbol{v}^{\mathcal{E}}_{\text{ant,sc,0}} \tag{6.3}$$

**Table 6.1.:** Steps for data simulation

1. Determine the antenna position, velocity and attitude
2. Determine the target position, velocity and RCS
3. Determine direction vector pointing from the antenna to the target both in the ENU coordinate system and in the antenna coordinate system, compute the range to the target, angle with which the target signal impinges on the antenna and target Doppler frequency
4. Use the radar equation to determine the expected rx power (Swerling I),
5. Determine clutter covariance matrix at target range Doppler by employing the clutter model
6. Draw a sample from the clutter and noise covariance matrix
7. Generate the DOA vector for the target
8. Draw the target amplitude from a complex normal distribution with the expected target power that has been determined before
9. Generate $N_{\text{channel}} \times 1$ target signal vector
10. Compute the test variable for the AMF
11. Compare the test variable with detection threshold
12. If the target is detected:
    - Perform the DOA estimation
    - Generate range and radial velocity estimates. They are generated by adding Gaussian noise to the true values.
    - Estimate the target signal amplitude
13. Determine the number of false alarm as realization of a Poisson distributed random variable. The expected number of false alarms is determined with the false alarm rate.
14. Determine range, $v_{\text{rad}}$ and directional cosine of the false alarms according to the uniform distribution.
15. Determine the clutter and noise covariance matrix at the location of the false alarm.
16. Draw samples of the clutter and noise random variable and compute the test variable until the detection threshold is exceeded.
17. Determine the same estimates for this sample as for simulated target detections

and the attitude of the antenna is

$$\boldsymbol{\gamma}_{\mathrm{ypr},k}^{\mathcal{A}\leftarrow\mathcal{E}} = \boldsymbol{\gamma}_{\mathrm{ypr,sc},0}^{\mathcal{A}\leftarrow\mathcal{E}} \tag{6.4}$$

For the output, the true platform location, velocity and attitude are corrupted with noise in order to simulate the measurement errors by the inertial measurement unit (IMU) of the platform.

$$\begin{aligned}
\hat{\boldsymbol{x}}_{\mathrm{ant}}^{\mathcal{E}} &= \boldsymbol{x}_{\mathrm{ant},k}^{\mathcal{E}} + \boldsymbol{n}_{x,k} \\
\hat{\boldsymbol{v}}_{\mathrm{ant},k}^{\mathcal{E}} &= \boldsymbol{v}_{\mathrm{ant},k}^{\mathcal{E}} + \boldsymbol{n}_{v,k} \\
\hat{\boldsymbol{\gamma}}_{\mathrm{ypr},k}^{\mathcal{A}\leftarrow\mathcal{E}} &= \boldsymbol{\gamma}_{\mathrm{ypr},k}^{\mathcal{A}\leftarrow\mathcal{E}} + \boldsymbol{n}_{\gamma,k}
\end{aligned} \tag{6.5}$$

where the noise terms obey normal distributions with covariance matrices $\mathbf{R}_{x,\mathrm{ant}}^{\mathcal{E}}$, $\mathbf{R}_{v,\mathrm{ant}}^{\mathcal{E}}$ and $\mathbf{R}_{\gamma}$ respectively.

**Choice of the antenna attitude Euler angles** For the simulation, it is adequate to determine these angles by first defining the attitude of the carrier platform and the attitude of the antenna with respect to the platform.

The position and attitude of the carrier platform is equivalent to the position and attitude of the body fixed (BF) coordinate system [21, Sec. 4.2.6]. For an airplane, the origin of the BF coordinate system is located the center of gravity of the platform, its x-axis points into the direction of the noise of the plane, its y-axis is parallel to the right wing and its z-axis points to the bottom of the plane (see [21, Fig. 4.8]). In general, the attitude of an airplane cannot be determined based on its velocity vector. However, as a first approximation for a non maneuvering airplane it is reasonable to assume that the normalized velocity vector coincides with the x-axis of the BF coordinate system. Furthermore, one may assume as approximation that the wing is parallel to the ground.

While this approximation is not aerodynamically exact, it enables to configure the platform attitude based solely on the velocity vector and ground plane. In this configuration, the basis vectors of the BF coordinate system in the ENU system are found with

$$\begin{aligned}
\boldsymbol{e}_{\mathrm{bf,sc},0,1}^{\mathcal{E}} &= \frac{\boldsymbol{v}_{\mathrm{ant,sc},0}^{\mathcal{E}}}{\|\boldsymbol{v}_{\mathrm{ant,sc0}}^{\mathcal{E}}\|}\,, \\
\boldsymbol{e}_{\mathrm{bf,sc},0,2}^{\mathcal{E}} &= \boldsymbol{e}_{\mathrm{bf0},1}^{\mathcal{E}} \times \boldsymbol{n}_{\mathrm{plane}}^{\mathcal{E}}\,, \\
\boldsymbol{e}_{\mathrm{bf,sc},0,3}^{\mathcal{E}} &= \boldsymbol{e}_{\mathrm{bf0},1}^{\mathcal{E}} \times \boldsymbol{e}_{\mathrm{bf,sc},0,2}^{\mathcal{E}}
\end{aligned}$$

and

$$\mathbf{T}_{\mathrm{sc},0}^{\mathcal{E}\leftarrow\mathrm{bf}} = \left[\boldsymbol{e}_{\mathrm{bf,sc},0,1}^{\mathcal{E}}\ \boldsymbol{e}_{\mathrm{bf,sc},0,3}^{\mathcal{E}}\ \boldsymbol{e}_{\mathrm{bf0},3}^{\mathcal{E}}\right]\,. \tag{6.6}$$

is the rotation matrix. The orientation of the antenna with respect to the platforms BF coordinate system is defined by

$$\gamma_{\text{yaw}}^{\mathcal{A}\leftarrow\text{bf}} = \Phi_{\text{ant,yaw}} \tag{6.7}$$

$$\gamma_{\text{pitch}}^{\mathcal{A}\leftarrow\text{bf}} = \Phi_{\text{ant,pitch}} \tag{6.8}$$

$$\gamma_{\text{roll}}^{\mathcal{A}\leftarrow\text{bf}} = -\frac{\pi}{2} + \Phi_{\text{ant,dep}} \tag{6.9}$$

$$\boldsymbol{\gamma}_{\text{ypr}}^{\mathcal{A}\leftarrow\text{bf}} = \begin{bmatrix} \gamma_{\text{yaw}}^{\mathcal{A}\leftarrow\text{bf}} \\ \gamma_{\text{pitch}}^{\mathcal{A}\leftarrow\text{bf}} \\ \gamma_{\text{roll}}^{\mathcal{A}\leftarrow\text{bf}} \end{bmatrix} \tag{6.10}$$

$$\mathbf{T}_{\text{sc},0}^{\mathcal{A}\leftarrow\text{bf}} = \mathbf{T}_{\text{Euler}}\left(\boldsymbol{\gamma}_{\text{ypr}}^{\mathcal{A}\leftarrow\text{bf}}\right) , \tag{6.11}$$

where $\Phi_{\text{ant,dep}}$ is the depression angle of the antenna. A typical value for this parameter is $15°/180°\pi$ rad. If the antenna is mounted along the principal axis of the carrier platform, then $\Phi_{\text{ant,yaw}}$ and $\Phi_{\text{ant,pitch}}$ are both zero. For a forward looking antenna, $\Phi_{\text{antYaw}} = -\frac{\pi}{2}$. Both definitions can be combined to the yield the attitude of the antenna

$$\mathbf{T}_{\text{sc},0}^{\mathcal{A}\leftarrow\mathcal{E}} = \mathbf{T}_{\text{sc},0}^{\mathcal{A}\leftarrow\text{bf}}\left[\mathbf{T}_{\text{sc},0}^{\mathcal{E}\leftarrow\text{bf}}\right]^{-1} \tag{6.12}$$

as a rotation matrix and in Euler angles

$$\gamma_{\text{ypr,sc},0}^{\mathcal{A}\leftarrow\mathcal{E}} = \boldsymbol{f}_{\text{Euler}}^{\gamma\leftarrow T}\left(\mathbf{T}_{\text{sc},0}^{\mathcal{A}\leftarrow\mathcal{E}}\right) . \tag{6.13}$$

## 6.2. Tracking results with simulated scenarios

This Section presents tracking results with three simulated scenarios. All scenarios share a common, linear flight path that is simulated as described in Section 6.2. Table 6.2 gives the parameters for the simulation of the antenna flight path and Table 6.3 presents parameters of the simulated radar system and of the radar signal processing. The scenarios differ in the path of the single, simulated ground truth vehicle.

In all three scenarios, the antenna is electronically steered exactly towards the location of the target, mimicking a radar mode in which the target has been acquired and periodically revisited. This type of steering is made possible in the simulation by using the true ground target location for defining the steering direction.

The recording geometries of the scenarios are shown in Figures 6.1, 6.2 and 6.3. Figures 6.4, 6.5 and 6.6 present various aspects of each scenario:

**(a)** the geolocated detections and the ground truth

**(b)** the extracted track or tracks

**(c)** the true target SNR and SCNR

**Table 6.2.:** Antenna attitude and motion parameters

| Parameter name | Value | Unit |
|---|---|---|
| position at recording start (x) | 7000 | m |
| position at recording start (y) | 0 | m |
| position at recording start (z) | 2000 | m |
| velocity (x) | -80 | m/s |
| velocity (y) | 0 | m/s |
| velocity (z) | 0 | m/s |
| depression angle | 12 | deg |
| yaw angle | 0 | deg |
| pitch angle | 0 | deg |
| postion error std. deviation (x) | 0.08 | m |
| postion error std. deviation (y) | 0.08 | m |
| postion error std. deviation (z) | 0.08 | m |
| velocity error std. deviation (x) | 0.1 | m/s |
| velocity error std. deviation (y) | 0.1 | m/s |
| velocity error std. deviation (z) | 0.1 | m/s |
| depression angle error std. deviation | 0.1 | rad |
| yaw angle error std. deviation | 0.1 | rad |
| roll angle error std. deviation | 0.1 | rad |

**(d)** the true target component of the radial velocity and the target component of the radial velocity that is derived from the extracted track or tracks

**(e)** the true probability of detection and the probability of detection that the tracking algorithm reconstructs for the tracked target. Timesteps at which the target is not detected are highlighted with a red marker.

**(f)** the track weight

The true target SCNR and SNR is computed based on parameters that are only available in the simulations. It is not made accessible to the tracking algorithm. Likewise, the true target component of the radial velocity and the detection probability are computed with data that is only available in a simulation. Additionally, Subfigure (d) plots the target component of the radial velocity that is reconstructed from the tracking result. This is the radial velocity that the tracking algorithm "believes" the target to have. Likewise, Subfigure (e) also plots the probability of detection that the tracking algorithm attributes to the tracked target.

### 6.2.1. Scenario 1

In scenario 1 the target moves along a curved path. In this Scenario, the tracking algorithm succeeds almost perfectly in tracking the target. At 60 s into the simulation the radial velocity of the target is close to 0 due to the observation geometry. This leads to a decreased expected

**Table 6.3.:** Radar, recording and processing parameters

| Parameter name | Value | Unit |
|---|---|---|
| nb. of pulses per CPI | 128 | unitless |
| pulse repetition frequency | 4000 | Hz |
| wavelength of center frequency | 0.03 | m |
| revisit interval | 1 | s |
| nb. of transmit elements | 48 | unitless |
| nb. of receive elements per subarray | 16 | unitless |
| subarray 1 location (x-coordinate) | 0.25 | m |
| subarray 2 location (x-coordinate) | 0 | m |
| subarray 3 location (x-coordinate) | -0.25 | m |
| antenna width | 0.15 | m |
| range resolution | 7.5238 | m |
| desired false alarm rate for the detection test | $10^{-6}$ | unitless |
| minimum range | 6 | km |
| maximum range | 10 | km |

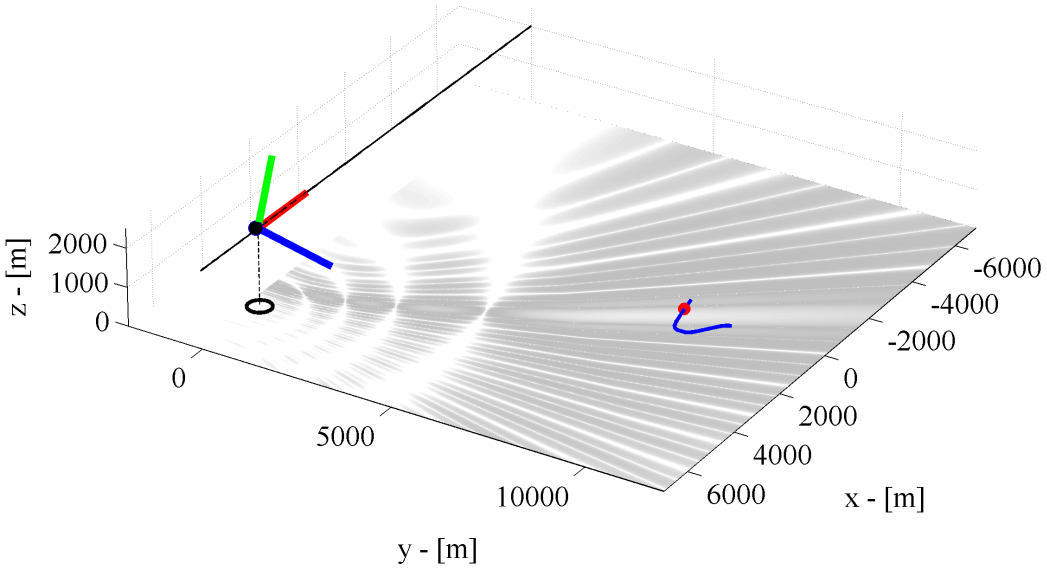


**Figure 6.1.:** Flight path and path of the ground vehicle for scenario 1. The footprint and attitude of the antenna and the location of the ground target is shown for a specific timestep.

SCNR of the target. As a result, the probability of detection around time step 60 drops sharply. The tracking algorithm models this drop relatively well and thus the track does not break.

Overall the tracking algorithm captures the probability of detection well. However, between seconds 150 and 160 of the simulation the tracking algorithm underestimates the probability of detection. This seems to be due to the fact that the algorithm also computes a radial velocity which is slightly inferior to the true value. As the true value of the radial velocity is close to velocities at which the detection probability drops sharply, even a small deviation in radial velocity signifies a large deviation in detection probability.

### 6.2.2. Scenario 2

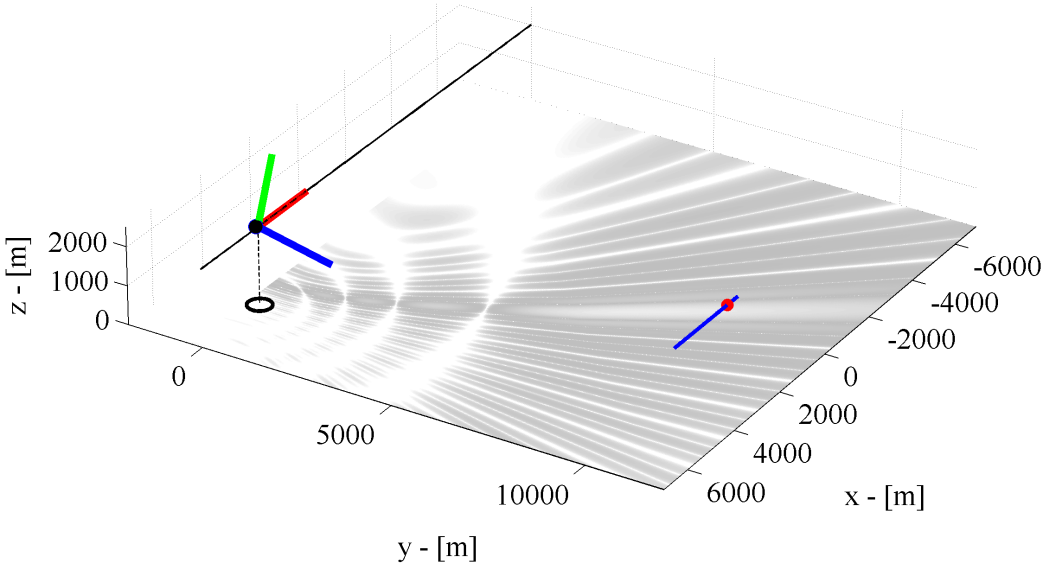


**Figure 6.2.:** Flight path and path of the ground vehicle for scenario 2. The footprint and attitude of the antenna and the location of the ground target is shown for a specific timestep.

In scenario 2 the target path is parallel to the path of the antenna. During the simulation the target component of the target's radial velocity increases starting from $-10\,\mathrm{m/s}$. At $90\,\mathrm{s}$ into the experiment the target component of the radial velocity is approximatively $0\,\mathrm{m/s}$. Thus, around

this time the SCNR decreases and detections are missed. Due to the fact that the target does not change course or its velocity while it cannot be observed, the track covers the true radial velocity and probability of detection perfectly. Thus, the track is successfully maintained despite the period without observation.

### 6.2.3. Scenario 3

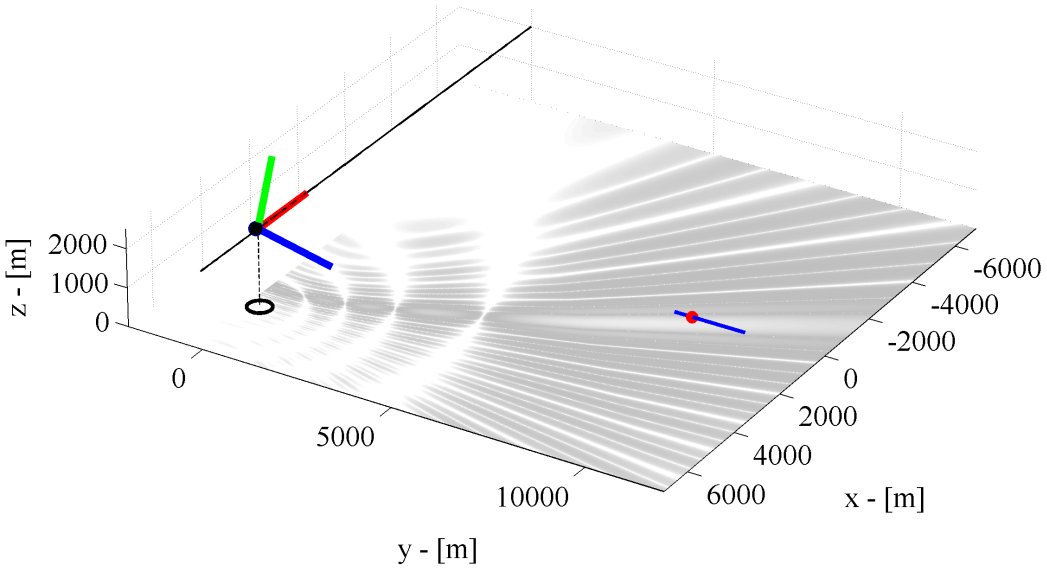


**Figure 6.3.:** Flight path and path of the ground vehicle for scenario 3. The footprint and attitude of the antenna and the location of the ground target is shown for a specific timestep.

In scenario 3 the target moves on a straight line which is perpendicular to the flight path. Between seconds 60 and 80 of the simulation the target comes to a complete stop before continuing into the same direction. The stop manifests itself in the drop of the radial velocity to zero in Subfigure 6.6d. As the deceleration and acceleration occurs rapidly, this stop is not visible as an area without detections in Figure 6.6a. Due to the stop of the target it is not detectable between seconds 60 and 80 of the experiment.

At the beginning of the simulation a target track is established. This tracks breaks at the stop

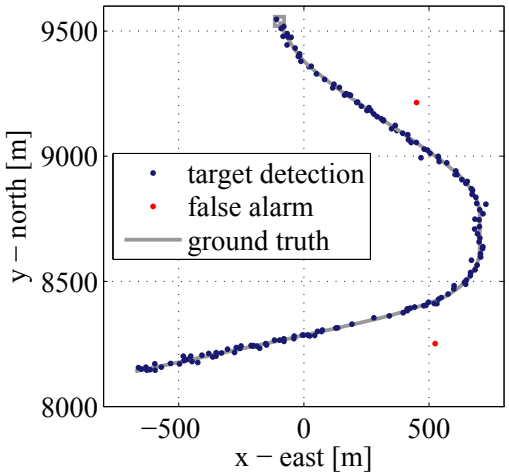


**(a)** Geolocated detections and ground truth target path

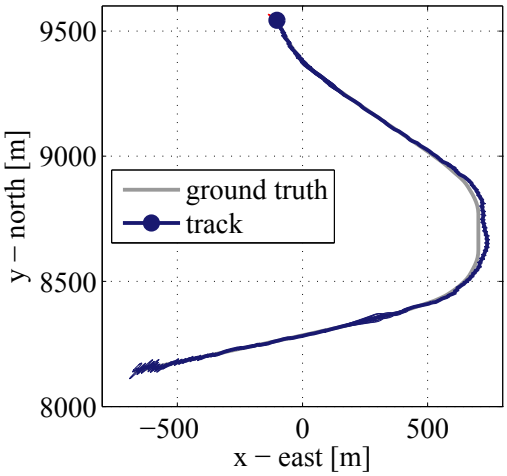


**(b)** Extracted track and ground truth target path

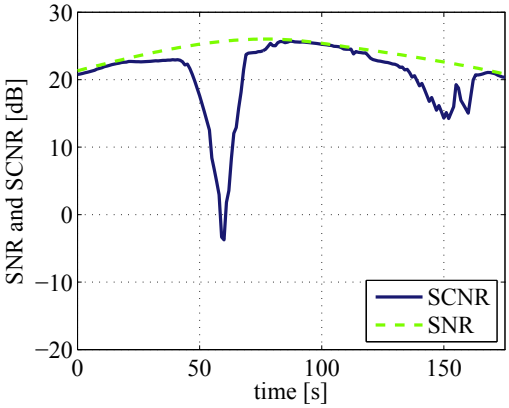


**(c)** Target SNR and SCNR vs. time

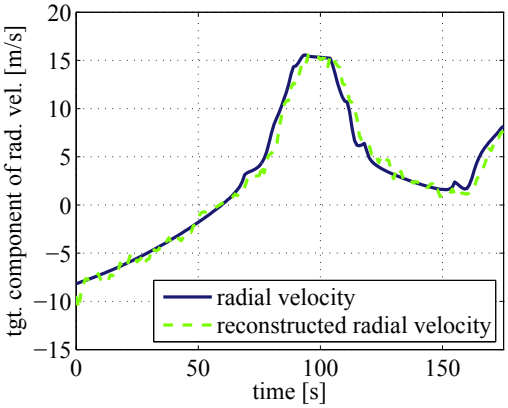


**(d)** Target radial velocity vs. time and target radial velocity assumed by the tracking algorithm

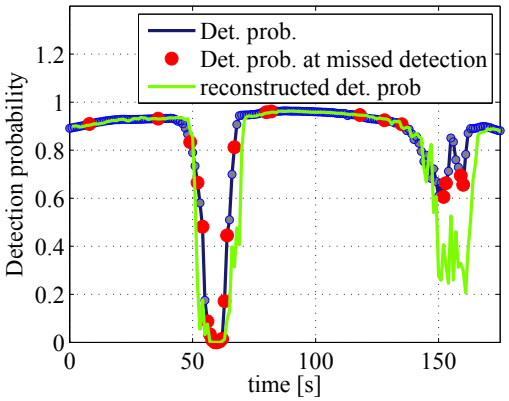


**(e)** Target detection probability vs. time

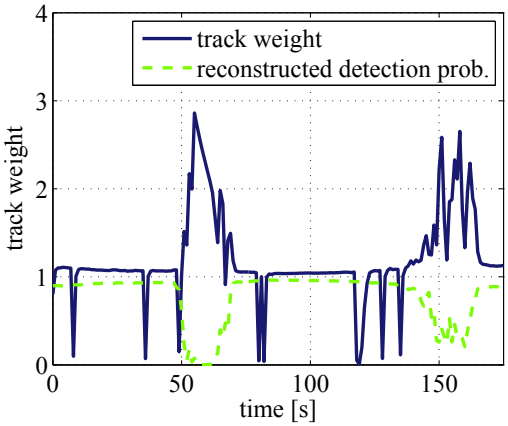


**(f)** Track weight and reconstructed detection probability vs. time

**Figure 6.4.:** Aspects of scenario 1

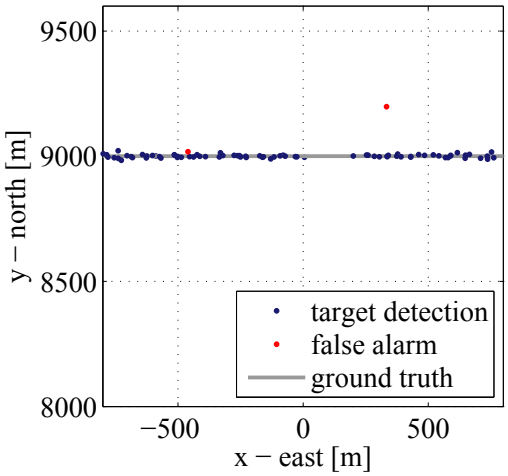


**(a)** Geolocated detections and ground truth target path

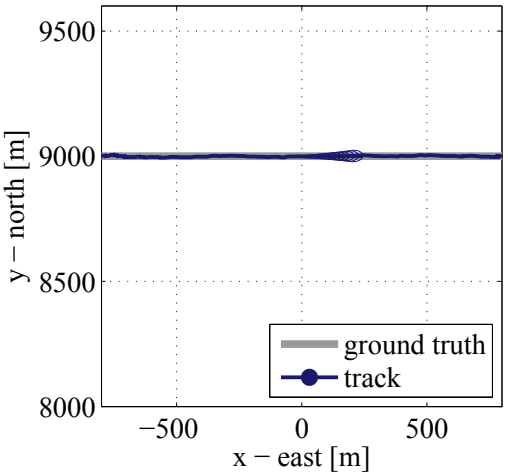


**(b)** Extracted track and ground truth target path

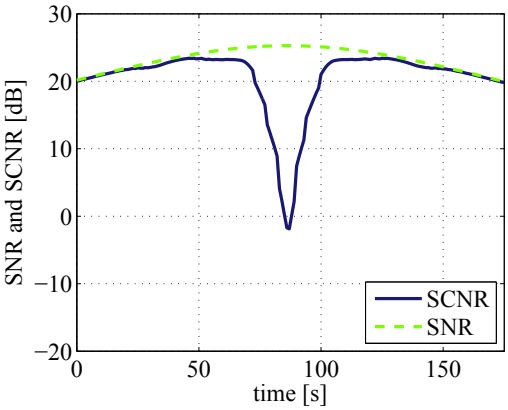


**(c)** Target SNR and SCNR vs. time

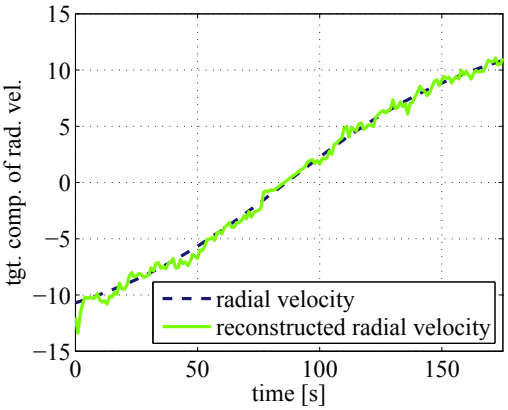


**(d)** Target radial velocity vs. time and target radial velocity assumed by the tracking algorithm

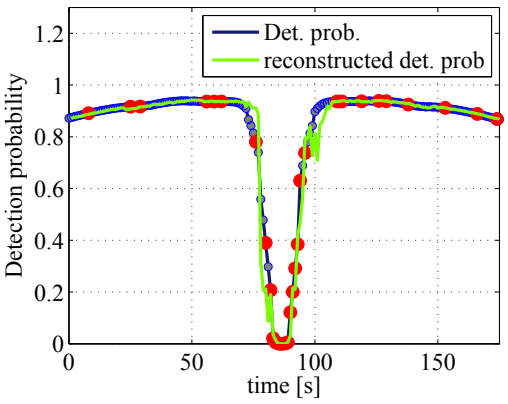


**(e)** Target detection probability vs. time

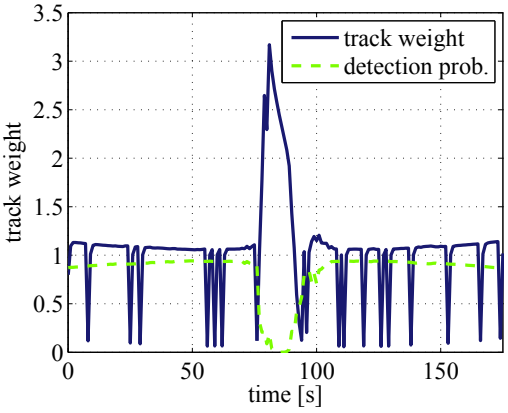


**(f)** Track weight and reconstructed detection probability vs. time

**Figure 6.5.:** Aspects of scenario 2

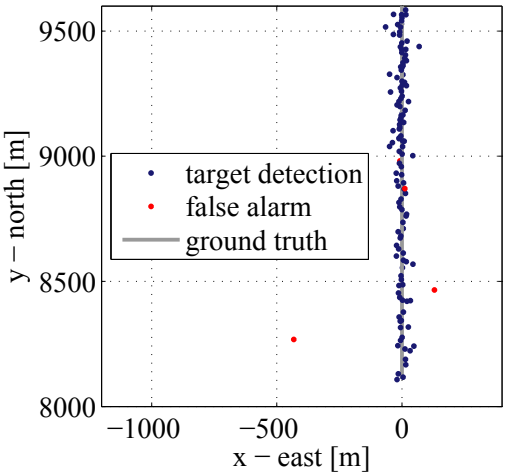


(a) Geolocated detections and ground truth target path

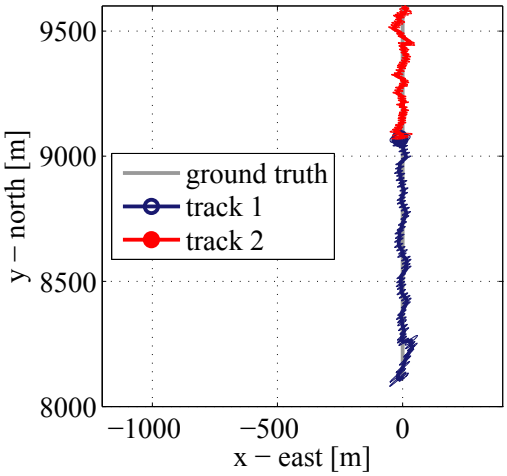


(b) Extracted track and ground truth target path

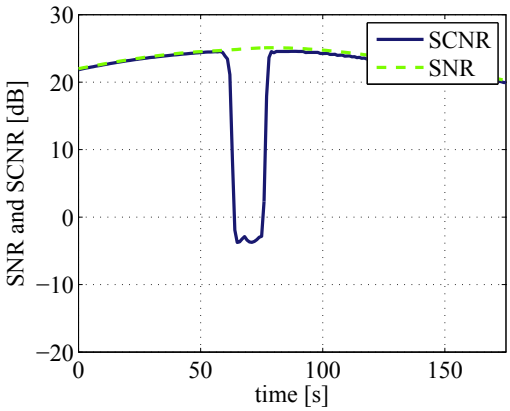


(c) Target SNR and SCNR vs. time

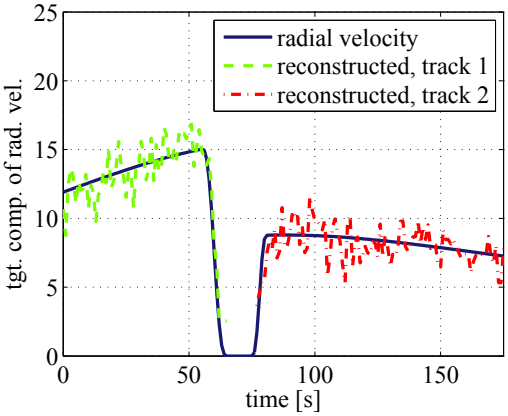


(d) Target radial velocity vs. time and target radial velocity assumed by the tracking algorithm

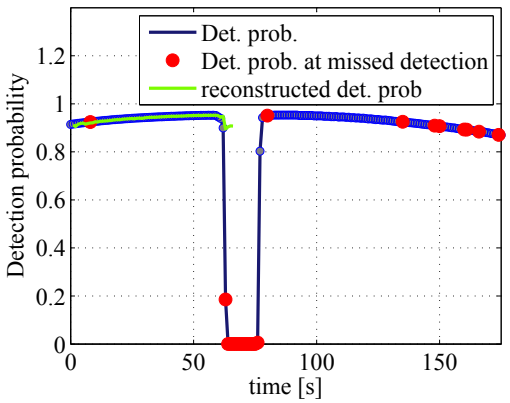


(e) Target detection probability vs. time

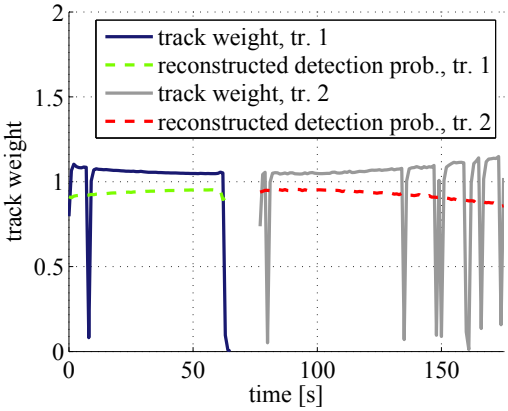


(f) Track weight and reconstructed detection probability vs. time

**Figure 6.6.:** Aspects of scenario 3

of the target. After the target resumes its course the target is picked up with a new track. The combination of Figures 6.6d and 6.6e explains why this track breakage occurs: The deceleration of the target is at first correctly captured by the tracking algorithm down to a radial velocity of 2.5 m/s. Up to this point the target is detectable. As the target decelerates further, it is no longer detected. Hence, the tracking algorithm cannot update the track state to a lower target velocity. As a result, it still assumes a high detection probability. In the absence of detections, the target track breaks.

## 6.3. Example of the direct visualization of GM-PHD filter results

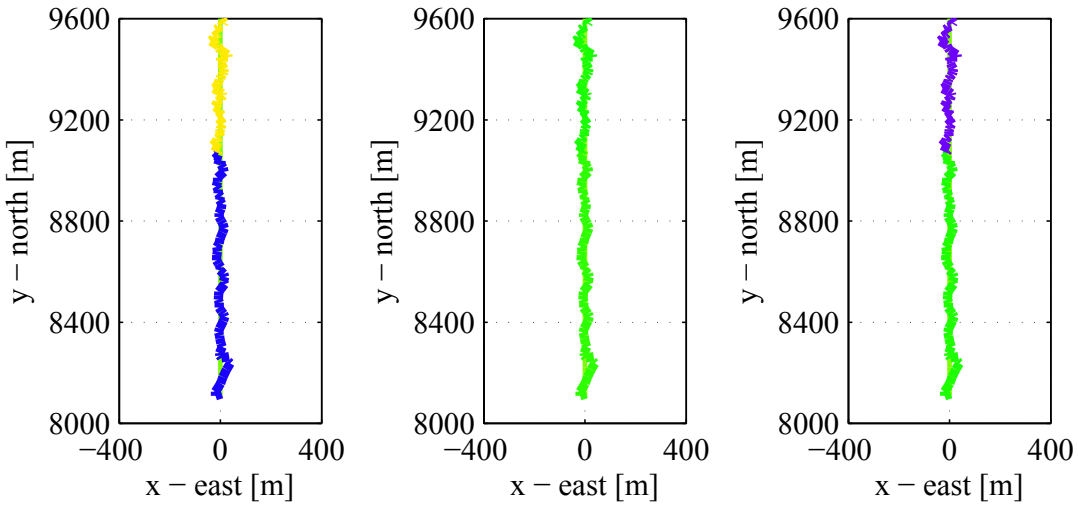


**Figure 6.7.:** A visualization of the GM-PHD filter result of Scenario 3 based on fingerprints prior to track extraction. The subfigures (a), (b) and (c) have been generated with three different matrices $\mathbf{A}_{\text{color}}$.

In Section 5.2.7 a method for visualizing the output of the GM-PHD filter prior to track extraction was presented. At that point, no example could be given since the simulation had not been presented. Figure 6.7 shows three different visualization of Scenario 3 with that method. The difference between the subfigures lies in the matrix $\mathbf{A}_{\text{color}}$ which is used for converting the

fingerprint value to a RGB color. For each subfigure, this matrix was randomly generated. In subfigures 6.7a and 6.7c the track breakage that occurs within this scenario is well visible at $y \approx 9000\,\mathrm{m}$. However for the choice of $\mathbf{A}_{\mathrm{color}}$ in subfigure 6.7b the track before and after the breakage receive the same coloring.

This example shows that the coloring depends strongly on the matrix $\mathbf{A}_{\mathrm{color}}$ that is used. This cannot be avoided, since a high dimensional fingerprint is converted to a single color value. In particular, the fact that two GM-PHD components receive the same color, does not signify that the fingerprints are almost identical. However, for analysis of the GM-PHD result this method is still highly useful, since the display is not affected by the track extraction step. To counter the problem that dissimilar components might receive the same coloring, it is useful to display the same result with different realizations of the coloring matrix.

## 6.4. Summary

From the simulations, one can conclude that the tracking algorithm is functional in the presented scenarios. Track breakage does however occur, if the the target changes its velocity while it cannot be observed, as in scenario 3. If the target continues to move on an approximatively straight line during a loss of observation as in scenario 1, the tracking algorithm can recover the track once the target becomes again visible.

# 7. Experimental results

Despite the large amount of publications on ground moving target tracking with airborne radar – to the knowledge of this author – there exists no openly available publication with experimental tracking results. However, in this field experimental results are severely needed. Published extension to standard algorithms are only verified with simulations. However, only the application to experimental data sets will reveal the problems that are encountered in target tracking.

## 7.1. Acquisition of the dataset

Thus, we designed an experiment in order to acquire airborne radar data especially for verifying ground moving target tracking algorithms. To this end, the experimental radar PAMIR of Fraunhofer FHR was employed [9]. PAMIR is a multichannel phased array radar. The fact that it has multiple channels is crucial for ground moving target tracking as this enables the detection of slowly moving ground targets. Furthermore, multiple channels enable the estimation of the direction of arrival of signals that are backscattered by the targets. Another important capability that was used in this experiment is the Scan-MTI mode of PAMIR. In this mode, the antenna beam periodically sweeps a range of angles that is determined during the design of the experiment. At each angle, two distinct carrier frequencies were used for recording data of two coherent processing intervals.

As carrier platform for the experimental radar, a Transall airplane was used. The radar system was mounted in the rear door of the Transall – the door that is also used by parachutist. The fact that the system was mounted in the door limited the maximum flight altitude to about 3000 m above sea level. The larger the distance to the radar, the longer is the radar "shadow" that is cast by an object. Thus, at large ranges, buildings and vegetation easily obscure moving objects. Thus, at the design phase of the experiment, it was deemed that targets at ranges between 6 km and 10 km range to the radar should be observed. Also, a larger swath would have resulted in a data rate beyond the recording capabilities of the PAMIR system.

While flying on a straight line, an area to the side of the platform can be observed. This area moves with the same velocity as the platform. For scanning a angles between $\pm 30°$ degree, the longest extension of this area in flight direction is about 10 km. For a platform velocity of 100 m/s, a target at this range can thus be observed for about 100 s. At shorter ranges, the observation time is smaller.

PAMIR is also equipped with a camera that points broadside. Photos were taken at intervals

**(a)** PAMIR mounted in the carrier platform Transall

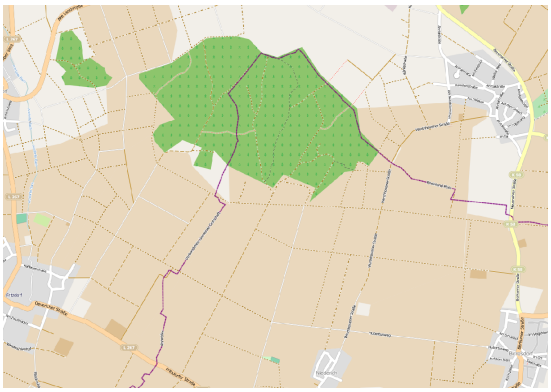

**(b)** Area of interest. Source: Openstreetmap

**(c)** VW Transporter

**(d)** VW Golf

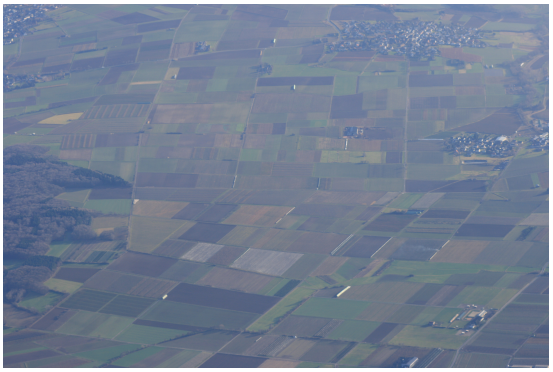

**(e)** View 1

**(f)** View 2

**Figure 7.1.:** Acquisiton of experimental data: Carrier platform, area of interest, reference vechicles and aerial views

**Table 7.1.:** Recording parameters of the experimental data acquisition

| Parameter name | Value | Unit |
|---|---|---|
| Pulse repetition frequency | 6002.4 | Hz |
| Sample frequency | 25 | MHz |
| Carrier frequency (local 1) | 8.73 | GHz |
| Carrier frequency (local 2) | 10.17 | GHz |
| Scan angles | 75 to 105 | deg |
| Looks per scan | 28 | unitless |
| Pulses per CPI | 128 | unitless |
| Scan duration | 1.19 | s |
| Number of subarrays | 3 | unitless |
| Phase center spacing | 26.56 | cm |
| Antenna length | 79.68 | cm |
| Antenna width | 15 | cm |
| Height over ground | 2600 | m |
| Minimum recorded range | 6145 | m |
| Maximum recorded range | 9869 | m |

of 9 s. During the experiment, a ground truth scenario was created with two GPS equipped reference vehicles and a bicycle. Staff of Fraunhofer FHR and Fraunhofer FKIE assisted in the ground truth scenario, for communication with the carrier platform, as drivers or assistants to the drivers. The vehicles operated in a previously defined area of interest. In order to obtain a long, continuous observation of these vehicles, a circular flight path around the ground truth area was chose. The radius of the circle was approximately 7 km. Due to wind drift and since a the autopilot does not allow for an automatic configuration of circular flight paths, the true platform track deviated from the circular path. As a result, the area of interest was outside of the scanned interval during two periods during the recording.

Figure 7.1 shows various aspects of the data acquisition – the PAMIR system mounted in the Transall (Figure 7.1a), a map of the area of interest (Figures 7.1b), photos of the reference vehicles (Figure 7.1c and 7.1d) and two aerial photographs that were taken during the recording. Table 7.1 lists recording parameters.

**Table 7.2.:** Radar processing parameters

| Parameter name | Value |
|---|---|
| FFT window | Taylor window, -50 dB |
| Number of training samples | 120 |
| Number of guard gates | 30 |
| Number of adjacent Doppler bins | 2 |
| Detection threshold | 14 dB |

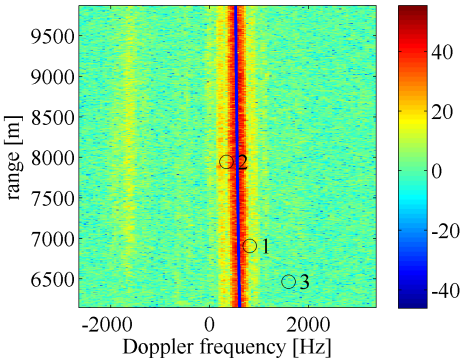


**(a)** Range-Doppler map of the receive data

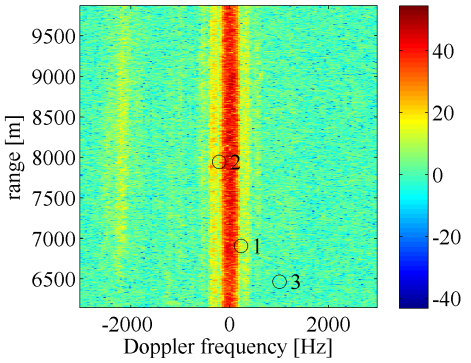


**(b)** Range-Doppler map after compensation for the J-hook

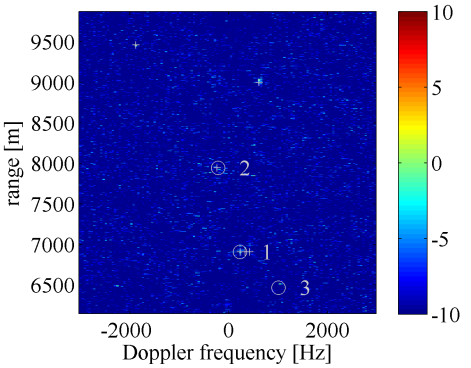


**(c)** Range-Doppler map of the test variable

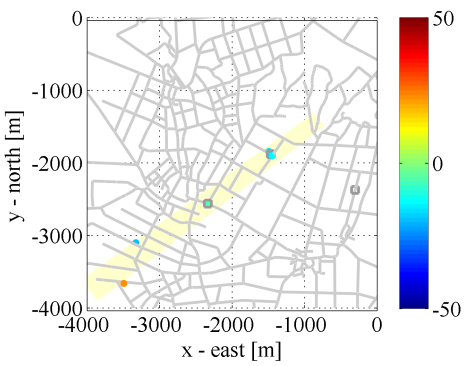


**(d)** Geolocated detections and 3dB antenna footprint

**Figure 7.2.:** Range-Doppler maps and geolocated detections

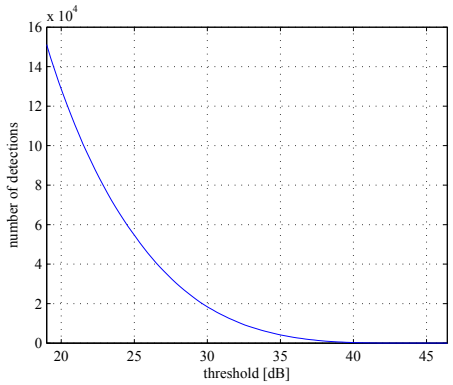


**(a)** Number of detections vs. detection threshold

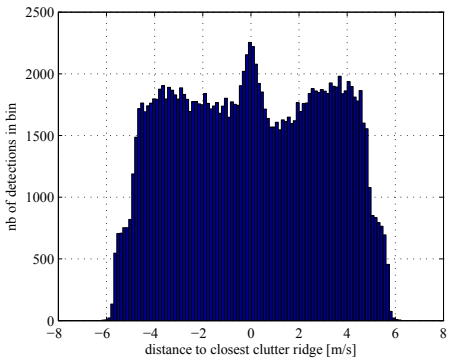


**(b)** Distance in radial velocity to the clutter ridge

**Figure 7.3.:** Test variable and distance to clutter ridge

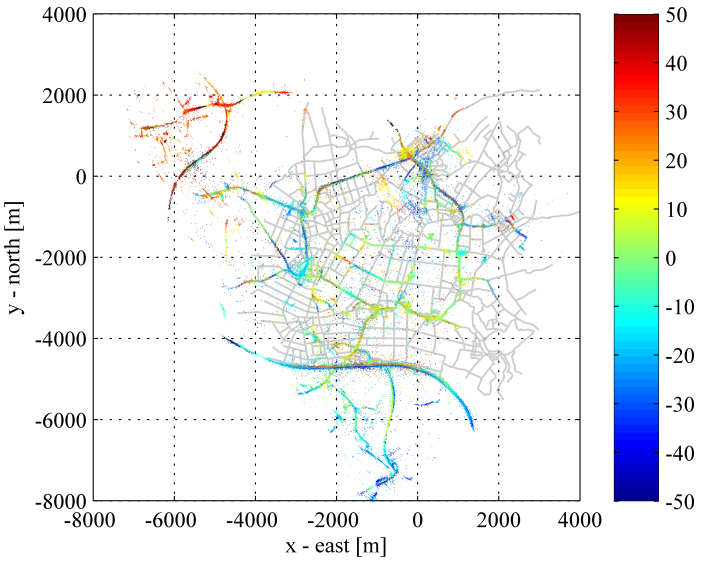


**(a)** All detections

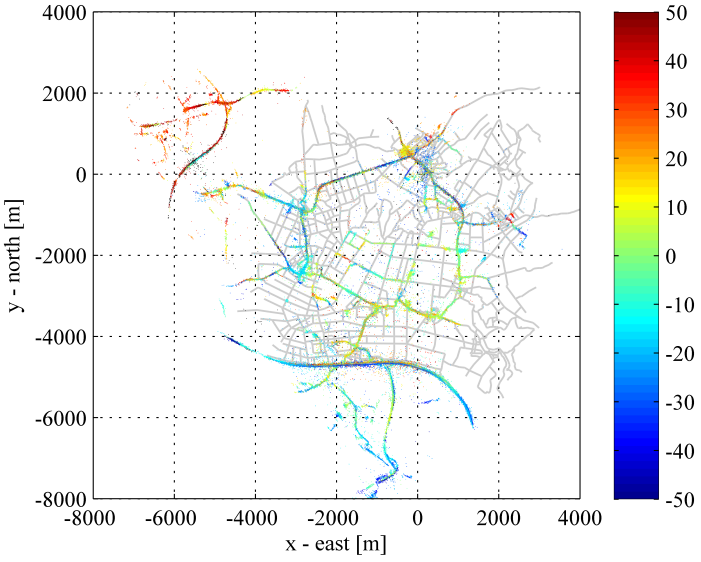


**(b)** Detections exceeding minimum distance to the clutter ridge

**Figure 7.4.:** Geolocated detections of the entire recording. The color of the detection plots indicates the estimate of the radial velocity. Source of the road map data: Openstreetmap

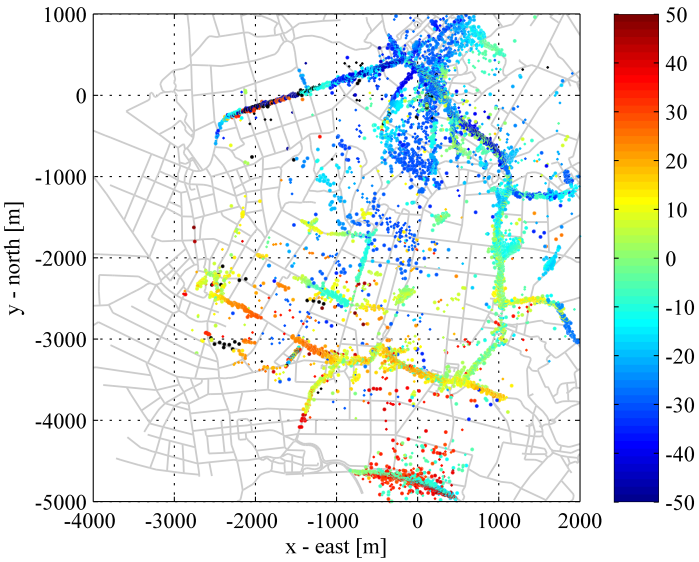


**(a)** All detections

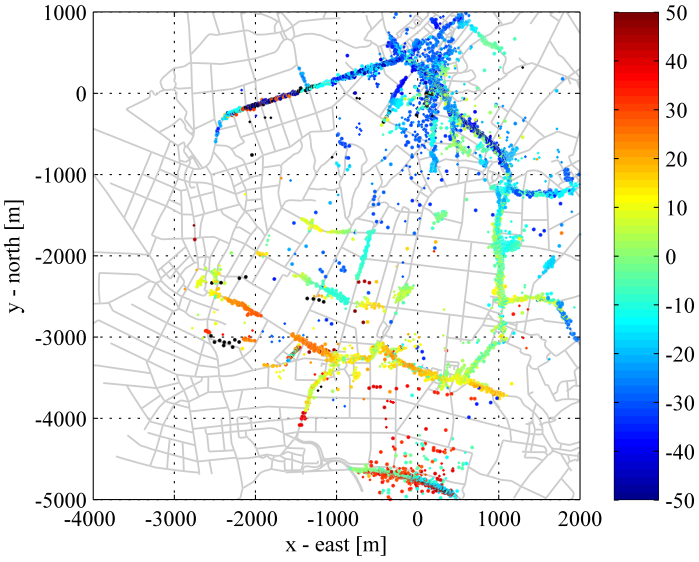


**(b)** Detections exceeding minimum distance to the clutter ridge

**Figure 7.5.:** Detections of the recording up to time step 6000. In Figure 7.5a all detections are plotted whereas detections with a distance of less than 1.5 m/s to the clutter ridge are not displayed in Figure 7.5b. The color of the detection plots indicates the estimate of the radial velocity. Source of the road map data: Openstreetmap

## 7.2. Target detections

The duration of the recording was 494 seconds. During this time data for a total of 23200 CPIs was recorded, i.e 11600 for each center frequency. About 414 entire scans, each comprising 28 different look directions and 56 CPIs were completed. The total data set size is about 17 GByte.

The received data was processed as outlined in Chapter 3. Figure 7.2 visualizes the different processing steps with data of look 4603 and local 1. This CPI was chosen for the example because two ground reference vehicles were detected in this CPI. In principle the processing and the results are similar to other CPIs of the recording. In Subfigure 7.2a the range-Doppler representation of this CPI is shown. In the center of this Figure the clutter band is visible, i.e. signal energy that is due to backscattering by the stationary ground. Circles indicate where energy due to the GPS equipped ground vehicles is possible. The positions of these circles has been computed based on the GPS data. As the bicycle (target 3) was not in the antenna beam, no signal for target 3 is expected. Subfigure 7.2b shows the range-Doppler representation after shifting the clutter centroid to 0 Hz. The expected locations of the targets have been adjusted accordingly. This is the data that was used for learning the clutter and noise covariance matrix. Subfigure 7.2c shows the test variable normalized by the detection threshold. Detections are marked by crosses. Indeed at the range-Doppler location of the reference vehicles two detections occur. The geolocated detections are plotted in Subfigure 7.2d. Here, the location of the reference vehicles is marked as well. It is visible that the detections are correctly located at the position of the vehicles. Additionally, in this Figure, the 3 dB antenna footprint is shown.

For a detection threshold of 19 dB a total of 157007 detections occured, i.e. on average 6.7 detections per CPI. After the removal from detections whose DOA estimates did not placed them in the main lobe area, 151147 detections remained.

Due to the fact that the PAMIR pattern was not tapered, the side lobes are relatively high in relation to the main lobe. Thus, large stationary scatterers (clutter discretes) with signals impinging from the side lobes are wrongly positioned in the main beam area. At the expense of also removing detections of moving targets, these detections can be discarded. The removal is performed by only retaining detections with a minimum distance to the clutter ridge. After discarding detections with a distance of less than 1.5 m/s, 107719 detections remained.

Figure 7.4 shows geolocated detections for the entire recording. Subfigure 7.4a all detections are shown, whereas only detections with a minimum distance of 1.5 m/s to the clutter ridge are plotted in Subfigure 7.4b. Figure 7.5 shows a zoom on a part of the observed area and detections only up to the time step 6000. In Subfigure 7.5a all detections are displayed, whereas in Subfigure 7.5b detections that are likely due to clutter discretes have been discarded. It is apparent, that especially in the center of the area, a lot of detections have been removed. These detections are due to strong returns by buildings that are misplaced due to the DOA estimation ambiguity.

Figure 7.3 plots the number of detections versus the detection threshold and the distance of the detections to the clutter ridge. Subfigure 7.3a shows that the number of detections decreases rapidly if the detection threshold is raised above 19 dB. For almost none of the detections does the

test variable exceed a value of 35 dB. In the histogram of Subfigure 7.3b there is a peak at a zero distance to the clutter ridge. This peak is likely due to clutter discretes that are falsely detected. The width of this peak was instrumental in selecting the threshold for removing detections that are likely due to clutter.

## 7.3. Tracking results

**Table 7.3.:** Parameterization of the tracking algorithm

| Parameter name | Value |
|---|---|
| Detection threshold | 18.7955 |
| Target survival probability | $0.95^{1/28}$ |
| Acceleration standard deviation | 3 m/s$^2$ |
| Merging threshold | 100 |
| Truncation threshold | $10^{-4}$ |
| Gating threshold | 300 |
| Association threshold | $10^{-4}$ |
| Birth particle weight | 100 |
| Birth particle location std. deviation | 8000 m |
| Birth particle velocity std. deviation | 120 m/s |
| Antenna location error std. deviation (all coordinates) | 0.08 m |
| Antenna velocity error std. deviation (all coordinates) | 0.1 m/s |
| Antenna attitude error std. deviation (all angles) | 0° |
| DOA estimation error std. deviation | 0.0022 |
| Range estimation errror std. deviation | 10 m |
| Radial velocity estimation error std. deviation | 2.5 m/s |

Figures 7.6 and 7.7 show tracking results for part of the observed area at time step 3000 and time step 6000 of the dataset. These time steps correspond to second 64 and 128, respectively, of the data set. For each of these time steps two plots of tracks are shown: In the first plot, tracks with a minimum length of 2 seconds are displayed, in the second plot tracks must have a minimum length of 10 seconds for display.

The plots requiring only a length of 2 seconds for display show a lot of false tracks. These false tracks are mainly due to clutter discrete detections, in particular clutter discretes that lie in the antenna side lobes. For example, in Subfigure 7.6a clusters of this kind of false tracks can be found around the location (0,-700) and (-500,-1500). In the Figures that require a minimum track length of 10 seconds for track display, only a few of these false tracks remain, for example at (0,-700) in Subfigure 7.6b and at (100,-800) in Subfigure 7.7b.

The remainder of the tracks is largely located on roads, indicating that these are not false tracks but indeed correctly tracked targets. An interesting question is, how many vehicles are missed, i.e. for how many vehicles no tracks have been generated. However, as no ground truth apart from the ground truth vehicles is avaialbe, this question cannot be answered here.

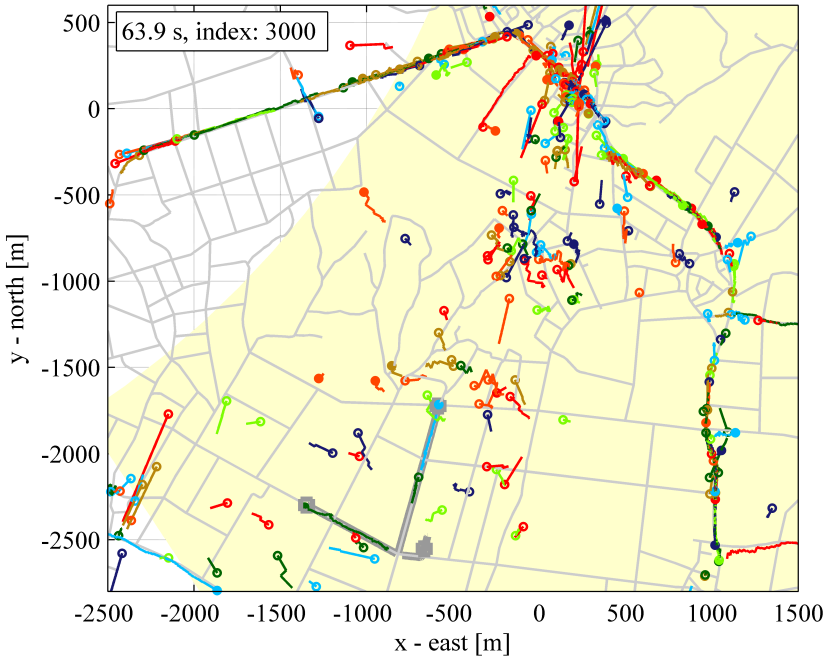


**(a)** Track length exceeding 2 seconds

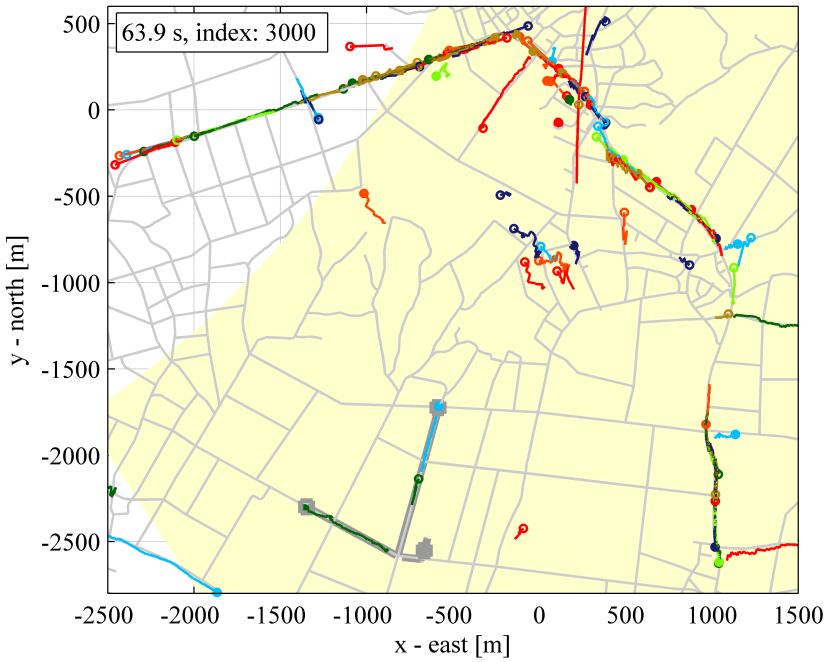


**(b)** Track length exceeding 10 seconds

**Figure 7.6.:** Tracking results for time steps 1 to 3000. The color for the display of each track is chosen arbitrarily. Source of the road map data: Openstreetmap

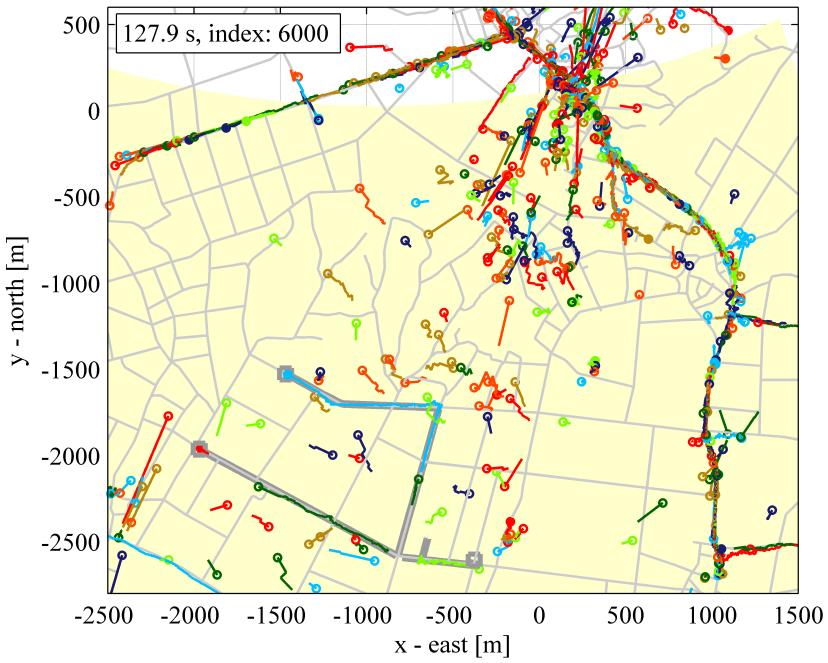


**(a)** Track length exceeding 2 seconds

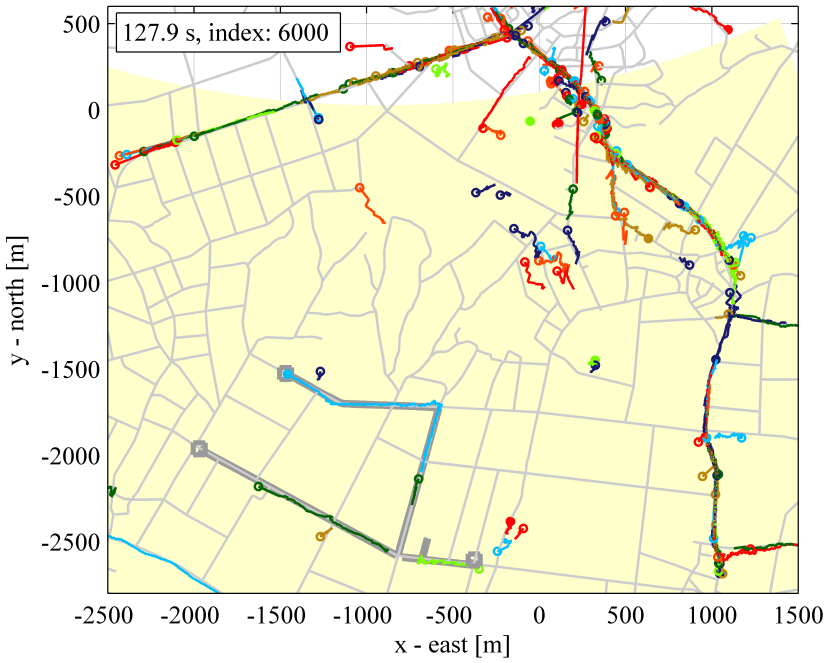


**(b)** Track length exceeding 10 seconds

**Figure 7.7.:** Tracking results up to time step 6000. The color for the display of each track is chosen arbitrarily. Source of the road map data: Openstreetmap

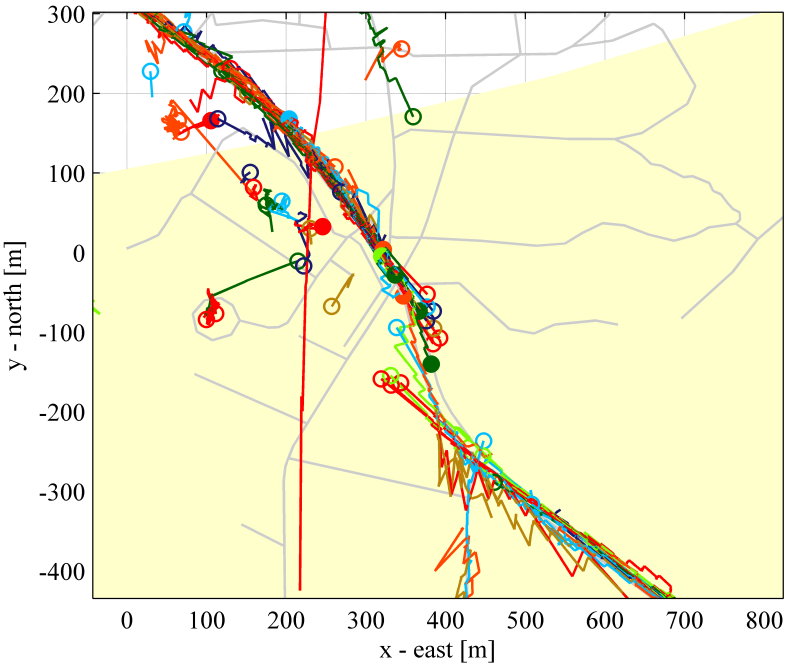


**Figure 7.8.:** Display of an area where a great number of track breakages occur. The minimum track length for display is 10 s. The color for the display of each track is chosen arbitrarily. Source of the road map data: Openstreetmap

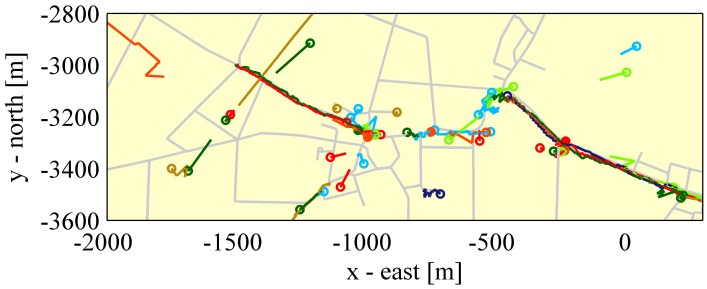


**Figure 7.9.:** Tracking results for the village of Oedingen. Two observations can be made here. Within the village, a lot of track breakage occurs, possibly due to obscuration. Furthermore, there are track breakages at the road curve at location (-500 m, -3200 m). The minimum track length for display is 5 s. The color for the display of each track is chosen arbitrarily. Source of the road map data: Openstreetmap

Figures 7.6 and 7.7 also indicate the paths of the GPS equipped vehicles (thick, gray lines) and the bicycle. In Subfigure 7.7b is is well visible that both ground truth vehicles are tracked. The bicycle is also tracked for a part of its path.

Figures 7.8 and 7.9 show situations in which the tracking results are not satisfactory. In Figure 7.8 a high number of track breakages occur. This is probably due to dense forests along both sides of the road at around (-350,-200). Thus, at this location no detections occur and the tracking algorithm cannot continue the track. As the tracked targets are road targets, the use of road map information might potentially alleviate this problem. The same Figure also shows false tracks at about (200 m, 50 m) and at (100 m,-100 m) that are due to detections of clutter discretes. Figure 7.9 shows tracking results for the area of the village of Oedingen. Probably due to obscuration of targets in the village, tracks of vehicles that enter the village are lost. Furthermore, at about (-500 m,-3200 m) several tracks are lost at the turn of the road. Again, road information might alleviate the problem of keeping track of vehicles on the curving road. However, no easy solution for tracking vehicles in the village with numerous obscuration is evident.

This section has presented the acquisition of an experimental radar data set that is well suited for ground moving target tracking. The functionality of this thesis' tracking algorithm has been shown with this data set. Two examples of non satisfactory tracking results have been given, providing incentives for further research.

# 8. Tracking with signal adaptive measurement error covariance matrix

As tracks are constructed based on parameter estimates, an accurate modeling of estimation errors is of great importance. It is known that the estimation accuracy of detection parameters is related to the SCNR of the received signal, i.e. it is signal dependent [72, Sec. 18.10]. In ground moving target tracking, the clutter power depends strongly on the location of the target in the range Doppler map. Furthermore, the power of the received signal depends on the radar cross section of the target which varies considerably between targets and as a function of the illumination angle. These two effects – the RCS variability and the clutter power variability – lead to a wide range of possible SCNR values for target detections. Hence it is to be expected that there is also a very wide range of target dependent measurement accuracies.

Some papers by Koch, Klemm and Nickel model the accuracy of the Doppler and DOA measurements for ground moving target tracking. In [37, Sec. 6.1] the accuracy is a function of the position of the detected target relative to the main beam. The highest accuracy is assumed in the center of the main beam where the expected signal power of the target is highest. In [35] and [38] the accuracy of the DOA and Doppler estimates is modeled more precisely. The modeling is based on an approach which is presented in [54] and which has been later refined in [55]. In this technique, the DOA and Doppler estimates are obtained by adaptive monopulse. The error covariance matrix of these measurements are then used as input for the tracking algorithm. The detection threshold is considered in the determination of the covariance matrix. Furthermore, the measurement error covariance matrix is computed based on the estimated clutter and noise covariance matrix. It is shown via Monte Carlo simulations that the use of the adaptive monopulse error covariance matrix improves the root mean square error of the tracking result. Furthermore, the tracking algorithm's estimates of the track state error covariance matrix are greatly improved. For an airborne target tracking application another approach to modeling the estimation accuracy is presented in [79]. Here, the variance of the direction of arrival estimate is inversely scaled by the signal power or *instantaneous SNR*. However, no results in how far this modeling improves the tracking performance are given.

The approach of [35] and [38] requires complicated, numerical evaluations of the covariance matrix of the monopulse estimator. Furthermore, these works do not validate with experimental data sets whether the modeling of the estimation error is appropriate and no experimental tracking results are given.

Here, a much simpler approach for modeling the DOA estimation error is presented. Experimental radar data in combination with target ground truth information is used to validate the DOA error modeling. Finally, experimental tracking results will be presented.

The proposed approach involves estimating the signal amplitude, the signal DOA and the clutter and noise covariance matrix during the radar signal processing. These estimates are then inserted into an expression of the Cramer-Rao bound of the DOA estimate. This expression of the Cramer-Rao bound is normally only valid for known target parameters. By inserting estimates instead, a signal adaptive estimate of the measurement error variance is found.

This chapter is organized as follows: First, a model for the DOA estimation error is presented. Second, this model is validated with an experimental data set. Third, the inclusion of the DOA measurement error model in the tracking algorithm of Chapter 5 is discussed. Monte Carlo simulation results for the tracking performance gains are given. Fourth, tracking results with experimental data results are presented for the algorithm that incorporates the proposed measurement error model and for various cases of tracking with standard error modeling.

## 8.1. Proposed model for the direction of arrival measurement error

As stated in Section 3.2.3, the information for estimating the DOA for detection $p$ at time step $k$ is the $N_{\text{chan}} \times 1$ data vector $\boldsymbol{y}_{\text{sb},k,p}$ at the range Doppler gate of the detection and the covariance matrix estimate $\hat{\mathbf{R}}_{\text{q,sb},k,p}$ that is associated with the detection. The data vector is modeled as

$$\boldsymbol{y}_{\text{sb},k,p} = \alpha_{\text{t},k,p} \mathrm{e}^{\mathrm{j}\phi_{\text{t},k,p}} \boldsymbol{d}\left(u_{\text{t},k,p}\right) + \boldsymbol{q}_{\text{sb},k,p}\,, \tag{8.1}$$

where $\alpha_{\text{t},k,p}$ is the real target amplitude, $\phi_{\text{t},k,p}$ is the target phase, $u_{\text{t},k,p}$ is the directional cosine of the target and $\boldsymbol{q}_{\text{sb},k,p}$ is the clutter and noise signal at the target's range Doppler gate. The clutter and noise covariance matrix is $\mathbf{R}_{\text{q,sb},k,p}$. According to Section 3.2.3, the DOA estimate is given by

$$\hat{u}_{k,p} = \arg\max_{u} \left\{ \frac{\left| \boldsymbol{d}(u)^H \left[\hat{\mathbf{R}}_{\text{q,sb},k,p}\right]^{-1} \boldsymbol{y}_{\text{sb},k,p} \right|^2}{\boldsymbol{d}(u)^H \left[\hat{\mathbf{R}}_{\text{q,sb},k,p}\right]^{-1} \boldsymbol{d}(u)} \right\}. \tag{8.2}$$

It is well known that the Cramer-Rao bound (CRB) gives the best possible performance for any unbiased estimator. Thus, investigating the CRB is the first step towards analyzing the estimation accuracy. The CRB of the target parameters is given by the inverse of the Fisher information matrix. For interferences that obey a Gaussian distribution an analytical expression of the Fisher information matrix and its inverse can be found. In particular, the CRB for the estimate of the directional cosine is a function of the true target directional cosine $u$, the target

signal amplitude $\alpha$ and the interference covariance matrix $\mathbf{R}_\mathrm{q}$, i.e. [19, Sec. VII.B]

$$\sigma^2_{u,\mathrm{crb}}(u,\alpha,\mathbf{R}_\mathrm{q}) = \frac{1}{2\left|\alpha\right|^2}\frac{p_\mathrm{crb}(u,\mathbf{R}_\mathrm{q})}{q_\mathrm{crb}(u,\mathbf{R}_\mathrm{q})} \tag{8.3}$$

with

$$\begin{aligned} p_\mathrm{crb}(u,\mathbf{R}_\mathrm{q}) &= \boldsymbol{d(u)}^H\mathbf{R}_\mathrm{q}^{-1}\boldsymbol{d(u)}\,, \\ q_\mathrm{crb}(u,\mathbf{R}_\mathrm{q}) &= \boldsymbol{d(u)}^H\mathbf{R}_\mathrm{q}^{-1}\boldsymbol{d(u)}\boldsymbol{d}_u(u)^H\mathbf{R}_\mathrm{q}^{-1}\boldsymbol{d}_u(u) \\ &\quad - \left|\boldsymbol{d}_u(u)^H\mathbf{R}_\mathrm{q}^{-1}\boldsymbol{d}(u)\right|^2\,, \end{aligned} \tag{8.4}$$

where $\boldsymbol{d}_u(u)$ is the derivative of the DOA vector with respect to $u$. Clearly, equations (8.3) and (8.4) show that the CRB is inversely proportional to the target power, i.e. the square of the amplitude. Thus, the CRB indicates that having estimates of $\alpha$ and the clutter and noise covariance matrix will help to identify those detections where the estimation accuracy may be particularly good and those where the estimation accuracy is low.

For this reason, the expression for the CRB shall serve for estimating the variance of the DOA estimate: First, for each detection the signal amplitude is estimated as

$$\hat{\alpha}_{k,p} = \frac{\left|\boldsymbol{d}(\hat{u}_{k,p})^H\left[\hat{\mathbf{R}}_{\mathrm{q,sb},k,p}\right]^{-1}\boldsymbol{y}_{\mathrm{sb},k,p}\right|}{\boldsymbol{d}(\hat{u}_{k,p})^H\left[\hat{\mathbf{R}}_{\mathrm{q,sb},k,p}\right]^{-1}\boldsymbol{d}(\hat{u}_{k,p})}\,. \tag{8.5}$$

Second, the estimate for the variance of directional cosine estimate is

$$\boxed{\hat{\sigma}^2_{u,k,p} = \sigma^2_{u,\mathrm{crb}}\left(\hat{u}_{k,p},\hat{\alpha}_{k,p},\hat{\mathbf{R}}_{\mathrm{q,sb},k,p}\right)}\,. \tag{8.6}$$

This is the *proposed model* for the DOA estimation error. This model is justified by the fact that for sufficiently high SNR values the maximum likelihood variance approaches the CRB. A significant contribution of this work, is to *validate* the proposed measurement accuracy model *with experimental data*.

## 8.2. Experimental validation of the direction of arrival measurment error model

To this end, the ground truth data shall be used to identify detections that are caused by the ground reference vehicles. An association of a detection to a specific ground reference vehicle shall be made, if the vehicle has been illuminated by the radar at the time step of the detection and if the range and Doppler measurements of the detection agree closely with the range and Doppler value that are obtained with the GPS information. If multiple detections fulfill these

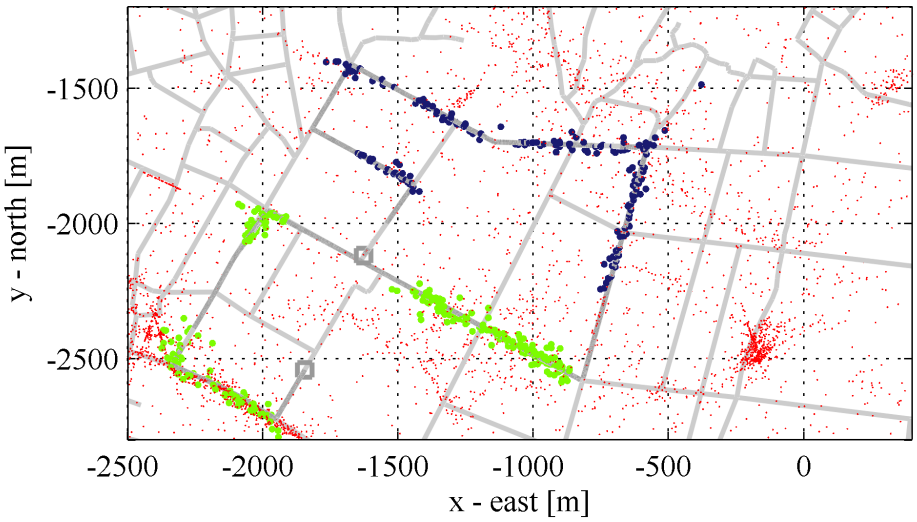


**(a)** Time steps 1 to 6000

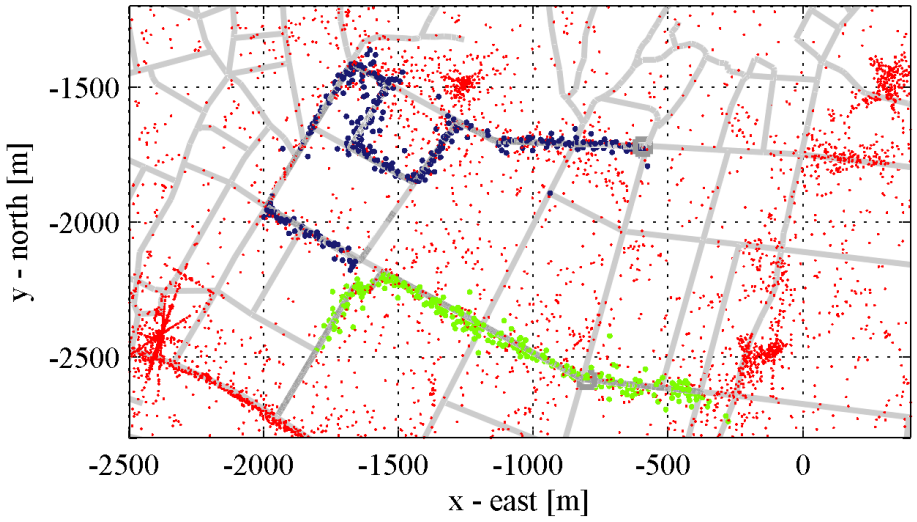


**(b)** Time steps 6001 to 11600

**Figure 8.1.:** Association of detections with ground truth targets (data of local 1). Detection plots that have been associated with the Volkswagen Transporter are colored blue whereas detection plots that have been associated with the Volkswagen Golf passenger car are colored green. Detection plots that are most likely due to false alarms or targets of opportunity are colored red.

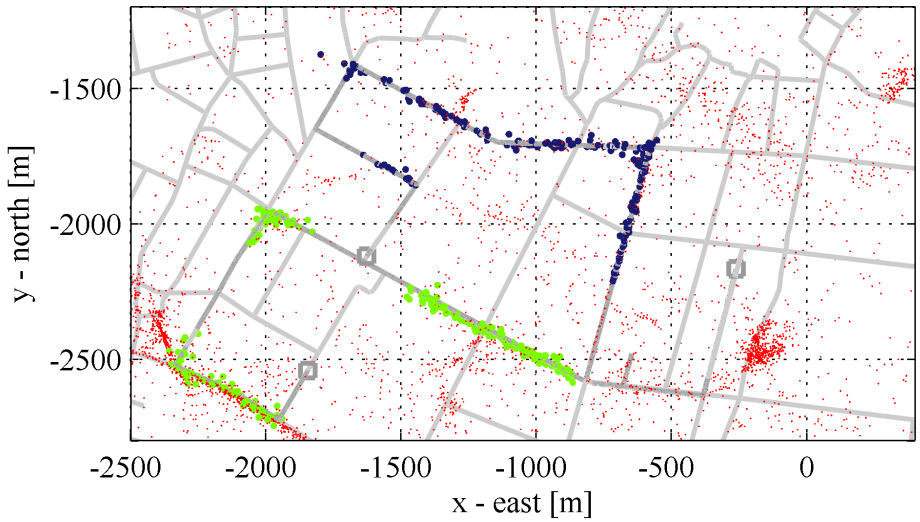


**(a)** Time steps 1 to 6000

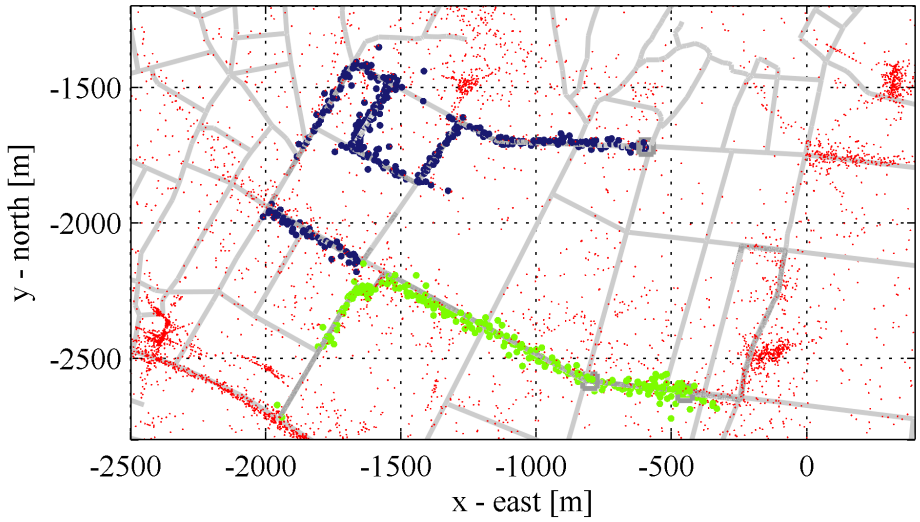


**(b)** Time steps 6001 to 11600

**Figure 8.2.:** Association of detections with ground truth targets (data of local 2). Detection plots that have been associated with the Volkswagen Transporter are colored blue whereas detection plots that have been associated with the Volkswagen Golf passenger car are colored green. Detection plots that are most likely due to false alarms or targets of opportunity are colored red.

criteria, the 'closest' detection shall be associated.

For each of the associated detections, the directional cosine will also be determined by using the position and attitude information of the platform and the GPS position information of the ground truth vehicles. Due to the high precision of the position and attitude data, it is expected that this measurement is in general much more precise than the radar based estimate of the DOA cosine. Thus, the deviation between both estimates can mostly be considered as error of the radar data based estimate of the directional cosine. A comparison of the DOA measurement error to the estimated error variance will show whether the proposed model captures the error distribution correctly.

### 8.2.1. Association between detections and ground reference vehicles

This method of associating detections, requires GPS derived estimates of the vehicle position and velocity. The estimates for the position and velocity of ground reference vehicle $\nu$ at time step $k$ are denoted $\hat{\boldsymbol{x}}^{\mathcal{E}}_{\mathrm{gps},k,\nu}(k)$ and $\hat{\boldsymbol{v}}^{\mathcal{E}}_{\mathrm{gps},k,\nu}$. The subscript "gps" indicates, that these estimates have been obtained via the vehicle's GPS device. Combined with the platform location and velocity at time step $k$, these estimates enable to compute estimates of the target range, the direction vector in ENU coordinates, the directional cosine and the target's radial velcoity.

$$\begin{aligned}
\hat{r}_{\mathrm{gps},k,\nu} &= \|\hat{\boldsymbol{x}}^{\mathcal{E}}_{\mathrm{gps},k,\nu} - \hat{\boldsymbol{x}}^{\mathcal{E}}_{\mathrm{ant},k}\|\,, \\
\hat{\boldsymbol{u}}^{\mathcal{E}}_{\mathrm{gps},k,\nu} &= \frac{\hat{\boldsymbol{x}}^{\mathcal{E}}_{\mathrm{gps},k,\nu} - \hat{\boldsymbol{x}}^{\mathcal{E}}_{\mathrm{ant},k}}{\hat{r}_{\mathrm{gps},k,\nu}}\,, \\
\hat{u}_{\mathrm{gps},k,\nu} &= \left[\boldsymbol{u}^{\mathcal{E}}_{\mathrm{gps},\nu}(k)\right]^{\mathrm{T}} \hat{\boldsymbol{u}}^{\mathcal{E}}_{\mathrm{ant},k}\,, \\
\hat{v}_{\mathrm{rad,gps},k,\nu} &= \left[\hat{\boldsymbol{u}}^{\mathcal{E}}_{\mathrm{gps},k,\nu}\right]^{T} \left(\hat{\boldsymbol{v}}^{\mathcal{E}}_{\mathrm{gps},k,\nu} - \hat{\boldsymbol{v}}^{\mathcal{E}}_{\mathrm{ant},k}\right)\,.
\end{aligned} \tag{8.7}$$

The computation of these variables is also given by the function $\boldsymbol{f}^{\mathrm{urv}\leftarrow\mathcal{E}}$ which is given in Section A.3.1

$$\begin{bmatrix} \hat{u}_{\mathrm{gps},k,\nu} \\ \hat{r}_{\mathrm{gps},k,\nu} \\ \hat{v}_{\mathrm{rad,gps},k,\nu} \end{bmatrix} = \boldsymbol{f}^{\mathrm{urv}\leftarrow\mathcal{E}}\left(\hat{\boldsymbol{x}}^{\mathcal{E}}_{\mathrm{gps},k,\nu}, \hat{\boldsymbol{v}}^{\mathcal{E}}_{\mathrm{gps},k,\nu}; \hat{\boldsymbol{x}}^{\mathcal{E}}_{\mathrm{ant},k}, \hat{\boldsymbol{v}}^{\mathcal{E}}_{\mathrm{ant},k}, \hat{\boldsymbol{\gamma}}^{\mathcal{A}\leftarrow\mathcal{E}}_{\mathrm{yp},k}\right)\,. \tag{8.8}$$

The distance between target $\nu$ and detection $p$ at time step $k$ is defined as

$$d_{p,k,\nu} = \sqrt{\left(\frac{\hat{r}_{\mathrm{gps},k,\nu} - \hat{r}_{k,p}}{\sigma_{\mathrm{assoc},r}}\right)^2 + \left(\frac{\hat{v}_{\mathrm{rad,gps},k,\nu} - \hat{v}_{\mathrm{rad},k,p}}{\sigma_{\mathrm{assoc},v}}\right)^2}\,, \tag{8.9}$$

where the range difference between the estimates is normalized by $\sigma_{\mathrm{assoc},r}$ and the velocity difference is normalized with $\sigma_{\mathrm{assoc},v}$. The index of the detection that is associated with ground

reference vehicle $\nu$ at time step $k$ is given by

$$p(k,\nu) = \begin{cases} \underset{p}{\operatorname{argmin}}\, d_{p,\nu}(k) & \text{, if tgt. } \nu \text{ detectable and } \min\limits_{p} d_{p,\nu}(k) < d_{\max} \\ \text{not defined} & \text{, otherwise} \end{cases} . \tag{8.10}$$

## 8.2.2. Deviation of the radar and GPS based DOA measurements

At time steps where an association can be performed, two different directional cosine estimates are available for each target. One based on the GPS data of the ground reference vehicles and another one based on the radar data. The radar data based DOA estimate for target $\nu$ at time step $k$ is

$$\hat{u}_{\text{radar},k,\nu} = \begin{cases} \hat{u}_{k,p(k,\nu)} & \text{, if valid detection available} \\ \text{not defined} & \text{, otherwise} \end{cases} . \tag{8.11}$$

The GPS based DOA measurement is found as in equations (8.7) and (8.8). Thus, the deviation between both measurements is

$$\Delta\hat{u}_{k,\nu} = \begin{cases} \hat{u}_{\text{radar},k,\nu} - \hat{u}_{\text{gps},k,\nu} & \text{, if valid detection available} \\ \text{not defined} & \text{, otherwise} \end{cases} . \tag{8.12}$$

## 8.2.3. Variance of the deviation between the DOA estimates

The proposed model of equation (8.6) for the radar based DOA estimation variance leads to the model

$$\hat{\sigma}^2_{\Delta u,k,\nu} = \hat{\sigma}^2_{\text{radar},k,\nu} + \sigma^2_{\text{gps},k,\nu} . \tag{8.13}$$

of the variance of the deviation between the radar and GPS based DOA measurements. Via the variance $\sigma^2_{\text{gps},k,\nu}$ it takes into account that the GPS measurements itself are not error free. The variance term for the radar based DOA estimate is given by the error model of equation (8.6)

$$\hat{\sigma}^2_{\text{radar},k,\nu} = \begin{cases} \hat{\sigma}^2_{u,k,p(k,\nu)} & \text{, if valid detection available} \\ \text{not defined} & \text{, otherwise} \end{cases} . \tag{8.14}$$

The variance of the GPS based measurement is determined by making use of the function $\boldsymbol{f}_{\text{J}}^{\text{urv}\leftarrow\mathcal{E}}$ of Section A.3.2. This function computes the Jacobian of the DOA, range and radial velocity measurement with respect to the parameter vector

$$\boldsymbol{\Phi} = \left[ \left[\boldsymbol{x}^{\mathcal{E}}_{\text{ant}}\right]^T \ \left[\boldsymbol{v}^{\mathcal{E}}_{\text{ant}}\right]^T \ \left[\boldsymbol{\gamma}^{\mathcal{A}\leftarrow\mathcal{E}}_{\text{yp}}\right]^T \ \left[\boldsymbol{x}^{\mathcal{E}}\right]^T \ \left[\boldsymbol{v}^{\mathcal{E}}\right]^T \right]^T . \tag{8.15}$$

For target $\nu$ at time step $k$ the Jacobian is given by

$$\mathbf{J}_{k,\nu}^{\mathrm{urv}\leftarrow\mathcal{E}} = \boldsymbol{f}_{\mathrm{J}}^{\mathrm{urv}\leftarrow\mathcal{E}}\left(\hat{\boldsymbol{x}}_{\mathrm{gps},k,\nu}^{\mathcal{E}}, \hat{\boldsymbol{v}}_{\mathrm{gps},k,\nu}^{\mathcal{E}}; \hat{\boldsymbol{x}}_{\mathrm{ant},k}^{\mathcal{E}}, \hat{\boldsymbol{v}}_{\mathrm{ant},k}^{\mathcal{E}}, \hat{\boldsymbol{\gamma}}_{\mathrm{yp},k}^{\mathcal{A}\leftarrow\mathcal{E}}\right) \tag{8.16}$$

Based on this result, the Jacobian of the directional cosine with respect to the parameter vector is

$$\mathbf{J}_{k,\nu}^{\mathrm{u}\leftarrow\mathcal{E}} = [0 \quad 0 \quad 1]\ \mathbf{J}_{k,\nu}^{\mathrm{urv}\leftarrow\mathcal{E}}\,. \tag{8.17}$$

With

$$\mathbf{R}_{\mathrm{gps},k,\nu} = \mathrm{diag}\left[\mathbf{R}_{x,\mathrm{ant},k}^{\mathcal{E}}, \mathbf{R}_{v,\mathrm{ant},k}^{\mathcal{E}}, \mathbf{R}_{\mathrm{yp},k}, \mathbf{R}_{x,\mathrm{gps},k,\nu}^{\mathcal{E}}, \mathbf{R}_{v,\mathrm{gps},k,\nu}^{\mathcal{E}}\right] \tag{8.18}$$

for the covariance matrix of the parameter vector $\boldsymbol{\Phi}$ the variance of the GPS based estimate of the directional cosine is

$$\sigma_{\mathrm{gps},k,\nu}^2 = \mathbf{J}_{k,\nu}^{\mathrm{u}\leftarrow\mathcal{E}}\mathbf{R}_{\mathrm{gps},k,\nu}\left[\mathbf{J}_{k,\nu}^{\mathrm{u}\leftarrow\mathcal{E}}\right]\,. \tag{8.19}$$

### 8.2.4. Experimental results

The association of detections to ground reference vehicles was performed for the data set that has been presented in Chapter 7. Figures 8.1 and 8.2 visualize which detections where tagged as having originated from the ground reference vehicles. In comparison to the Chapter 7, the detection threshold has been set to a lower value. Figures 8.3 and 8.4 show results that have been obtained with data from local 1 and local 2 respectively. In each of these Figures the left column presents results for ground reference vehicle 1 and the right column is for vehicle 2.

The DOA estimate is sensitive to phase offsets in the data of different receive channels. This is due to the fact that a non adaptive DOA vector is used for the direction of arrival estimation. In order to mitigate this problem, the phase offset between the channels was estimated from the received radar data and corrected. Despite this calibration procedure, a small bias in the DOA estimation remained for the experimental data set. This bias was estimated by forming the average over $\Delta\hat{u}_{k,\nu}$ of equation (8.12) for both targets ($\nu = 1, 2$). The average was then substracted from the estimates $\hat{u}_{\mathrm{radar},k,\nu}$ and $\hat{u}_{k,p(k,\nu)}$. In the following, all results are given for DOA estimates after bias removal.

Subfigures (a) and (b) of Figures 8.3 and 8.4 plot $\Delta\hat{u}_{k,\nu}$ of equation (8.12) and the estimated standard deviation $\hat{\sigma}_{\Delta u,k,\nu}$ of equation (8.13) versus time. These variables can only be plotted for time steps where a ground truth to detection association has been made. Furthermore, no data for the observation time steps intervals [1 150] and [7191 7623+150] was used. The data of the first 150 time steps (corresponds to 6.4 s) has been discarded since the IMU output of PAMIR is inaccurate at the beginning of the recording. The data of the second interval has been excluded due to a GPS outage during the interval [7191 7623]. Additional 150 time steps are allowed as settle in time for the IMU.

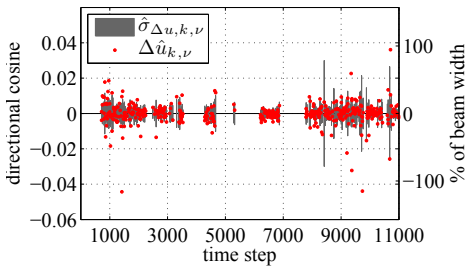


**(a)** Deviation vs. time step, target 1

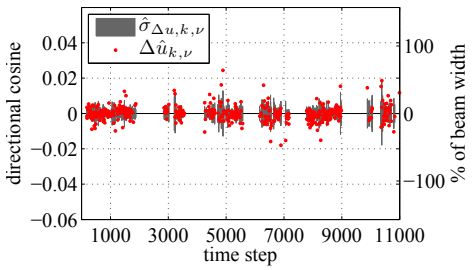


**(b)** Deviation vs. time step, target 2

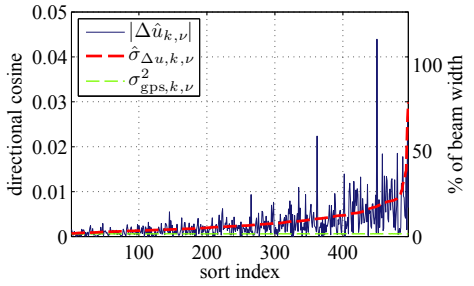


**(c)** Deviation of DOA estimates vs. sort index, target 1

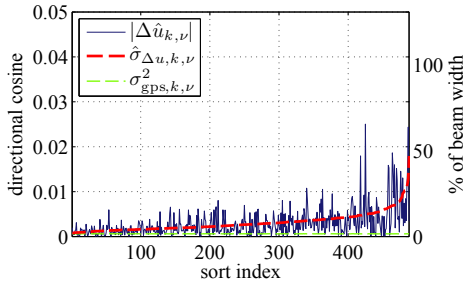


**(d)** Deviation of DOA estimates vs. sort index, target 2

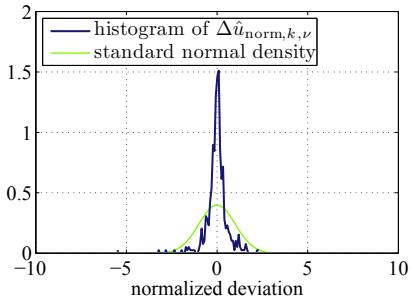


**(e)** Histogram and density of the DOA estimation deviation, target 1

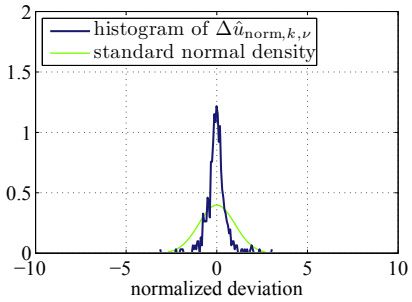


**(f)** Histogram and density of the DOA estimation deviation, target 2

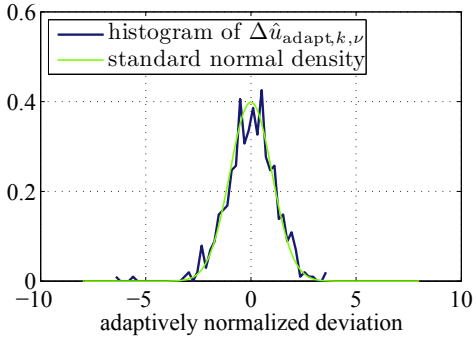


**(g)** Histogram and density of the adaptively normalized DOA estimation deviation, target 1

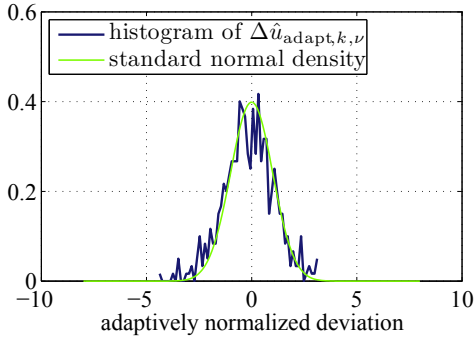


**(h)** Histogram and density of the adaptively normalized DOA estimation deviation, target 2

**Figure 8.3.:** Detection metrics for results with data of local 1

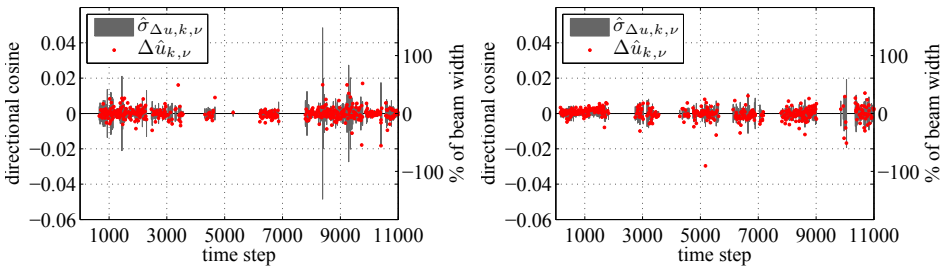


**(a)** Deviation vs. time step, target 1

**(b)** Deviation vs. time step, target 2

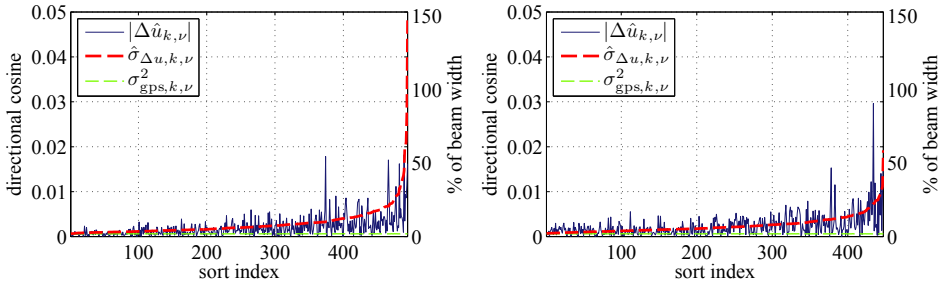


**(c)** Deviation of DOA estimates vs. sort index, target 1

**(d)** Deviation of DOA estimates vs. sort index, target 2

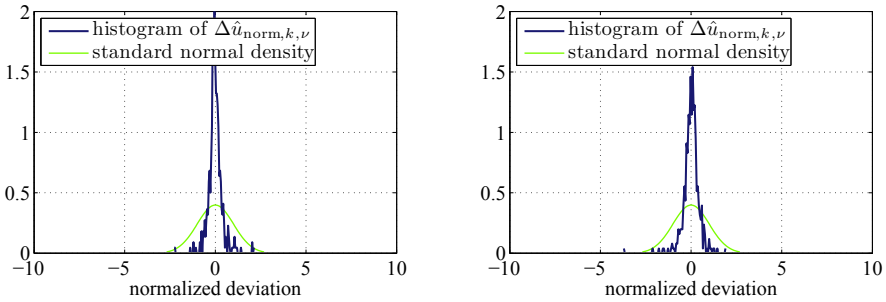


**(e)** Histogram and density of the DOA estimation deviation, target 1

**(f)** Histogram and density of the DOA estimation deviation, target 2

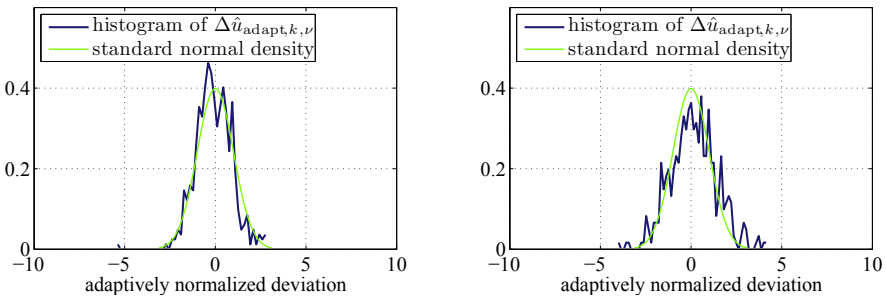


**(g)** Histogram and density of the adaptively normalized DOA estimation deviation, target 1

**(h)** Histogram and density of the adaptively normalized DOA estimation deviation, target 2

**Figure 8.4.:** Detection metrics for results with data of local 2

These Figures show that the DOA estimates deviation is indeed centered exactly at 0. Most notably, there is no time dependent bias of the DOA deviation. Furthermore, small values of the modeled standard deviation do indeed coincide with small deviations between the DOA estimates. For example, in Figure 8.3a the DOA deviations are much smaller between time steps 6000 and 7000 (where the modeled standard deviation is small) than at time steps 8000 to 11000 (where the modeled standard deviation is large).

Subfigures (c) and (d) shed further light on this point. Here, the detections are sorted by increasing values of the modeled standard deviation $\hat{\sigma}^2_{\Delta u,k,\nu}$. For both targets and data of both locals the likely magnitudes of the DOA measurement deviations are well predicted by the modeled standard deviation. If a small standard deviation is estimated, then the actual measurement deviations are indeed small. If a large standard deviation is computed, then large deviations occur. A comparison of $\hat{\sigma}^2_{\Delta u,k,\nu}$ with $\sigma^2_{\mathrm{gps},k,\nu}$ reveals that the deviation between the DOA measurements is mainly due to GPS and antenna attitude measurement errors for the best estimates. For most other estimates, the deviation between the DOA measurements is mainly caused by the radar data based DOA estimation. Thus, it is mostly correct to also call the deviation the radar data based "DOA measurement error".

In most target tracking algorithms it is assumed that the measurement errors obey a Gaussian distribution. Thus, it is pertinent to check in how far the deviation obeys a Guassian distribution. Subfigures (e) and (f) plot the histograms of the normalized DOA estimation deviation

$$\Delta\hat{u}_{\mathrm{norm},k,\nu} = \frac{\Delta\hat{u}_{k,\nu}}{\sqrt{\hat{\sigma}^2_{\mathrm{ave},\nu}}} \tag{8.20}$$

where

$$\hat{\sigma}^2_{\mathrm{ave},\nu} = \frac{1}{|\mathcal{M}_{\mathrm{ass},\nu}|} \sum_{k\in\mathcal{M}_{\mathrm{ass},\nu}} |\Delta\hat{u}_{k,\nu}|^2 \tag{8.21}$$

is the estimated standard deviation of this estimate. Here, $\mathcal{M}_{\mathrm{ass},\nu}$ is the set of time steps for which an association has been made, i.e. for which $\Delta\hat{u}_{k,\nu}$ is defined. Subfigures (g) and (h) plot the adaptively normalized deviation

$$\Delta\hat{u}_{\mathrm{adapt},k,\nu} = \frac{\Delta\hat{u}_{k,\nu}}{\sqrt{\hat{\sigma}^2_{\Delta u,k,\nu}}}\,. \tag{8.22}$$

For the adaptive normalization the proposed method of modeling the DOA estimation error variance is used. A comparison of the histograms of the two differently normalized deviations of equations (8.20) and (8.22) shows that the adaptively normalized deviations fit a Gaussian normal density much more closely. Thus, a tracking algorithm that uses the adaptive DOA measurement error variance will have a better error modeling.

## 8.3. Tracking with measurement covariance matrix adaptation

In order to process detections into tracks, the GM-PHD filter (as other tracking algorithms) requires the covariance matrix of the measurement errors. This covariance matrix has an important influence on the tracking result as it determines how strongly incoming measurements update the target state. In the standard extended Kalman filter version of the GM-PHD filter, the measurement error is modeled by a time step dependent random variable $\boldsymbol{\epsilon}_k$ with time step dependent covariance matrix $\mathbf{R}_{\epsilon,k}$.

In the type of tracking application that is investigated here, additional signal information is used to construct error covariance matrices that *depend on the detection*. For detection with index $p$ this covariance matrix is denoted $\mathbf{R}_{\epsilon,k,p}$. The goal of employing an adapted covariance matrix is to more accurately capture the error properties in order to increase the tracking performance. To employ the signal adapted covariance matrix in the the GM-PHD algorithm, equation (4.27) is exchanged with

$$\mathbf{S}_{k,p}^{(j)} = \mathbf{H}_k^{(j)} \mathbf{P}_{k|k-1}^{(j)} \left[\mathbf{H}_k^{(j)}\right]^T + \mathbf{U}_k^{(j)} \mathbf{R}_{\epsilon,k,p} \left[\mathbf{U}_k^{(j)}\right]^T \tag{8.23}$$

and the thus obtained algorithm is a MCMA GM-PHD filter. The covariance matrix is given by

$$\mathbf{R}_{\epsilon,k,p} = \begin{bmatrix} \hat{\sigma}_{u,k,p}^2 & \mathbf{0}^T \\ \mathbf{0} & \mathbf{R}_{\tilde{\epsilon}} \end{bmatrix}, \tag{8.24}$$

where $\hat{\sigma}_{u,k,p}^2$ is the modeled variance of the DOA estimation error and $\mathbf{R}_{\tilde{\epsilon}}$ is the covariance matrix of all other error terms.

## 8.4. Simulation results

The performance of the MCMA GM-PHD algorithm has been analyzed by Monte Carlo simulations. For comparison of the results, the standard GM-PHD algorithm has been used as well. It is identical to the MCMA GM-PHD except that $\hat{\sigma}_{u,k,p}^2$ in equation (8.24) is replaced by a constant value $\sigma_{u,\mathrm{std}}^2$.

The measurement simulator can model arbitrary platform flight paths and arbitrary target ground paths. The radar system is modeled in accordance with the parameters (e.g. antenna length, antenna pattern) of the system PAMIR of FHR [9, 11]. In order to generate the detections and measurements, the radar equation is used to determine the received clutter and signal power. These values are used to construct the single bin post Doppler received signals for clutter and for every target. A Rayleigh fluctuation model is assumed for the target signal strength (Swerling I). If the received signal passes the detection test, the DOA estimate is obtained with a maximum likelihood estimator.

A Monte Carlo simulation has been conducted for the scenario which is visualized in Figure 8.5.

| Parameter name | Value |
|---|---|
| Center frequency | 8.74 GHz |
| PRF | 6000 Hz |
| Pulses per CPI | 128 |
| Antenna element spacing | 0.2656 m |
| Number of channels | 3 |
| Platform velocity | 100 m/s |
| False alarm probability | $10^{-6}$ |
| Target SNR (Doppler) | 21.5 dB to 23.5 dB |
| CNR at target Doppler bin | 1.2 dB to 9.7 dB |
| Average DOA error at 7000 m | 10.5 m |
| $\sigma_R$ | 10 m |
| $\sigma_v$ | 0.5 m/s |
| $\sigma_{\text{yaw}}$ | 2/60 deg |
| $\sigma_{\text{pitch}}$, $\sigma_{\text{roll}}$ | 1/60 deg |
| $\sigma_{\text{east}}$, $\sigma_{\text{north}}$ | 0.08 m |
| $\sigma_{\text{up}}$ | 0.1 m |

**Table 8.1.:** Simulation parameters

In this scenario a Rayleigh-target moves with a constant velocity of 10 m/s along a curved path. The platform moves along the x-axis (east) at $y = 0$ with a velocity of 100 m/s and the starting x, y and z coordinates are -3000 m, 0 m and 2000 m, respectively. The antenna is steered to the location of the target with a revisit time of 1 s.

The parameters of the simulation are given in Table 8.1. As the signal to noise ratio (SNR) of the target varies during the simulation, the range of the SNR values assumed during the simulation is given. Likewise, the clutter to noise ratio (CNR) values vary strongly as a function of the target position and target radial velocity.

In the tracking algorithms, the same measurement variances are used as for the simulation. Additionally, the tracking algorithm without amplitude information needs a setting for the variance $\sigma^2_{u,\text{std}}$ of the DOA estimation. Here, the investigation was conducted for three different values of $\sigma^2_{u,\text{std}}$: in case 1, $\sigma_{u,\text{std}}$ is set to about five times the average DOA estimation variance $\sigma_{u,\text{ave}}$ of this scenario, in the second case $\sigma_{u,\text{std}} = \sigma_{u,\text{ave}}$ and in the third case $\sigma_{u,\text{std}} = \frac{1}{2}\sigma_{u,\text{ave}}$ . It is important to note that in real tracking scenarios a mismatch like in case 1 or 3 is more realistic as the average DOA estimation accuracy is unknown. On the other hand, the tracking algorithm with amplitude information does not require a choice of $\sigma_{u,\text{std}}$ as it is determined adaptively according to equation (8.6).

Figure 8.5 shows a tracking result for one run of the Monte Carlo simulation for the standard algorithm (case 1) and tracking with MCMA. It is apparent that tracking with MCMA follows the curved path more closely than the standard algorithm.

Figure 8.6 plots the position state error, i.e the distance between mean of the track and the target ground truth location. It has been established with 100 Monte Carlo runs versus time for the different tracking setups. Overall, the state error is lowest for the tracking with MCMA.

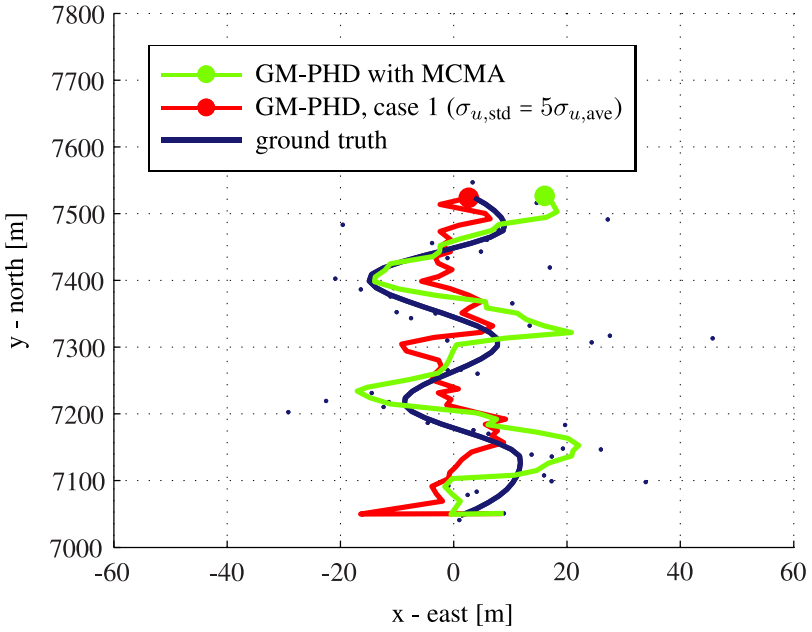


**Figure 8.5.:** Simulated ground truth path, detections of one Monte Carlo run, track with MCMA and standard tracking for case 1. Note the different scaling of the x- and y-axes.

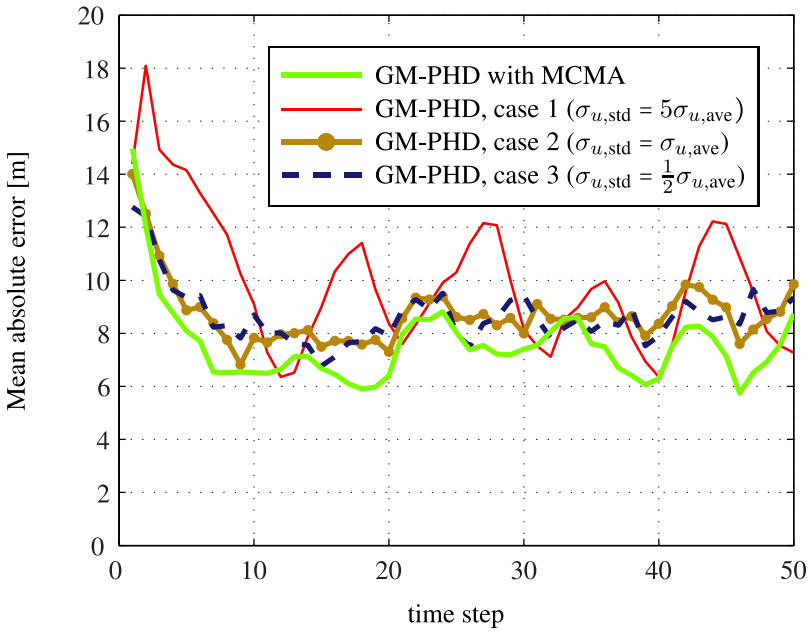


**Figure 8.6.:** State error vs. time for tracking with and without amplitude information averaged over 100 Monte Carlo simulation runs.

It is remarkable that – even though it has been provided with precise information about the average DOA estimation error – the performance of the standard algorithm in case 2 is slightly inferior to tracking with MCMA. This is likely due to the fact that the target return amplitude fluctuates according to the Rayleigh model leading to strong variations in the DOA estimation accuracy. Even for an almost optimal choice of $\sigma^2_{u,\mathrm{std}}$ as in case 2, tracking without MCMA cannot account for these variations. Furthermore Figure 8.6 suggests that choosing a variance value which is too optimistic as in case 3 has no negative effect on the tracking performance. However Figure 8.7 shows that this setting leads to a reduced average track length. This signifies that overly optimistic settings for the estimation accuracy cause track losses in the standard method.

An important measure for the evaluation of the tracking performance is track consistency: for every time step, the result of the tracking algorithm is not only a target state estimate but also the target state covariance that indicates the accuracy of the tracking result. Averaged over several Monte Carlo simulation runs, the tracking error should be distributed with a variance that agrees with the track covariance matrices. To investigate this, Figure 8.8 plots the normalized Mahalanobis distance between the simulated ground truth and the track state versus time [4, Sec. 5.4]. Ideally, the normalized Mahalanobis distance should be centered at 1 and not exit the 95% confidence region. Figure 8.8 shows that this is not achieved ideally for all tracking setups. However, both the standard algorithm configured with the true average estimation accuracy and tracking with MCMA yield results that lie mostly within the 95% confidence interval.

## 8.5. Tracking results with experimental data

Up to this point, the proposed model of the error variance has been successfully validated with experimental data in Section 8.2 and the positive impact of its incorporation into a tracking algorithm algorithm has been shown in Section 8.3. The goal of this section is to investigate the effect in target tracking with experimental data. To this end, the data set that has previously been presented in Chapter 7 and that has been used for the validation of the measurement accuracy model is employed.

Additionally to the MCMA tracking algorithm, the standard variant was applied to the same data for three distinct values of $\sigma^2_{u,\mathrm{std}}$. In the first case, $\sigma_{u,\mathrm{std}}$ is set to $3.7 \times 10^{-4}$ (which corresponds to 1 % of the antenna beam width for local 1), in the second case it is set to $18 \times 10^{-4}$ (5 % of the beam width for local 1) and in the third case it is set to $92 \times 10^{-4}$ (25 % of the beam width for local 1). Thus, in total there are four different configurations of the tracking algorithm. In case one the configuration of the standard tracking algorithm is *optimistic*, i.e. the tracking algorithm is set to assume that the DOA measurements are better than they are. In the third case, the configuration is *pessimistic* – the DOA measurements are mostly better than what the tracking algorithm believes. The second case is an intermediate configuration, neither pessimistic nor optimistic. For later reference, these four configurations are denoted as GM-PHD-MCMA,

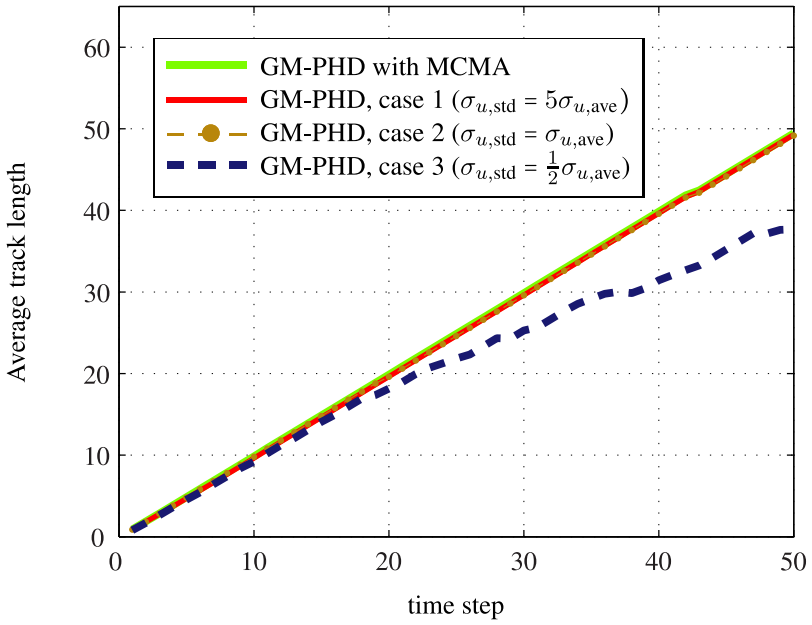


**Figure 8.7.:** Average track length versus time.

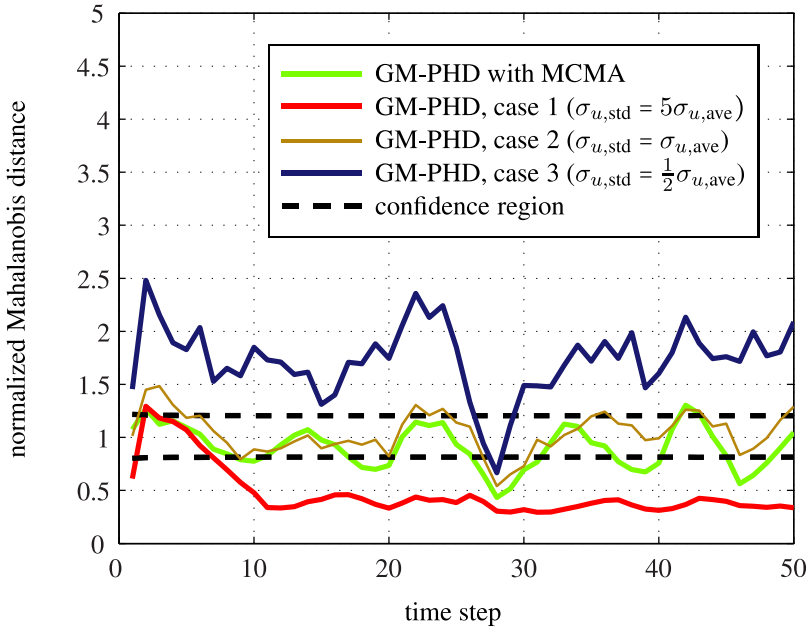


**Figure 8.8.:** Mahalanobis distance between the track and ground truth averaged over the Monte Carlo runs. The 95% confidence interval is plotted.

GM-PHD-OPT, GM-PHD-INT and GM-PHD-PESS.

Due to platform wind drift and squint angles the ground reference vehicles were not observed continuously. Thus, the data set is partitioned into three sub data sets. In each of these data sets one or two of the targets are (almost) continuously within the radar scan area:

(**a**) Almost continuous observation of targets 1 and 2 for time steps 1 to 6000 (127 s) of the experiment

(**b**) Continuous observation of target 1 for the time steps 14000 to 23200 (297 s to 492 s) of the experiment

(**c**) Continuous observation of target 2 for the time steps 14000 to 21000 (297 s to 446 s) of the experiment

Figures 8.9 and 8.10 show the tracking results for the different configurations of sub data set (**a**) and Figure 8.11 shows the tracking results for sub data set (**b**). Figures 8.12 and 8.13 show results for sub data set (**c**).

**Sub data set (a)** The following observations can be made: GM-PHD-MCMA tracks target 1 continuously for the complete duration of the data set. Target 2 is tracked while it is situated in scan area of the radar. Target 3, the bicycle is also tracked during a part of sub data set. GM-PHD-OPT experiences a track loss for target 1. Target 2 is tracked for the same amount of time as with GM-PHD-MCMA, but the deviation from the true ground truth track is larger. The bicycle causes a great number of very short tracks. In comparison GM-PHD-INT yields better results. Still, a track breakage for target 1 at a different location occurs. GM-PHD-PESS also suffers from a track breakage for target 1, again at a different location. The bicycle is tracked, but only for a very short duration.

**Sub data set (b)** Sub data set (**b**) enables to track ground reference vehicle 1. GM-PHD-MCMA tracks the target for the entire duration of the data set. However, at (-1700, -1400) a track breakage occurs. GM-PHD-OPT also establishes tracks for the entire duration, but it suffers a total of three breakages. Likewise GM-PHD-INT and GM-PHD-PESS experience three track breakages. Furthermore, at the turns of the vehicle GM-PHD-PESS generates tracks that deviate significantly more from the ground truth path.

**Sub data set (c)** This sub data set allows the tracking of ground reference vehicle 2. For all configurations the target is only tracked up to location (-800,-2600). After the turn at this location the radial velocity of the target decreases such that the tracking algorithm assumes a very low detection probability. Thus, even though detections are still made, no tracks is established anymore. No track breakages occur for the GM-PHD-MCMA and GM-PHD-OPT. For GM-PHD-INT and GM-PHD-PESS one track breakages each occurs at roughly the same location.

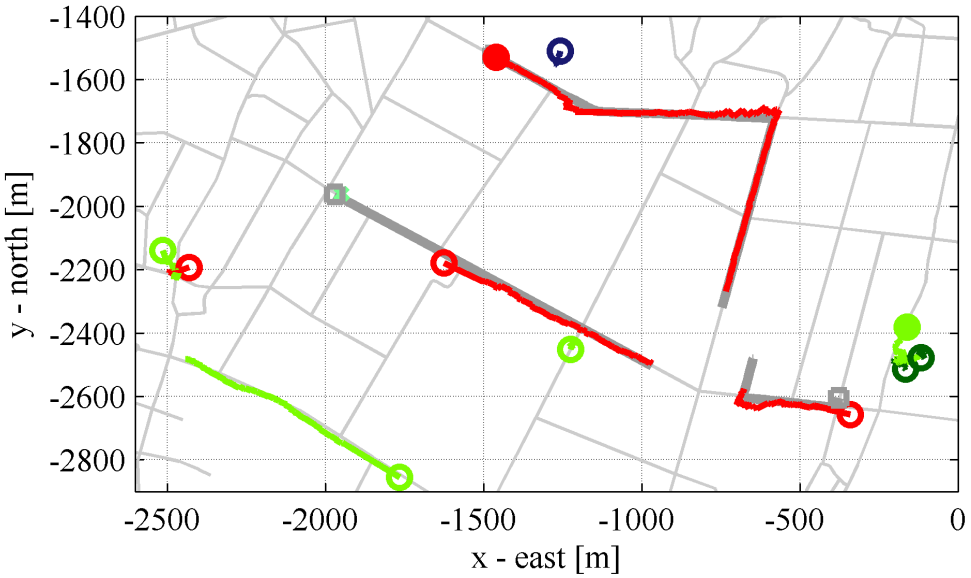


**(a)** MCMA

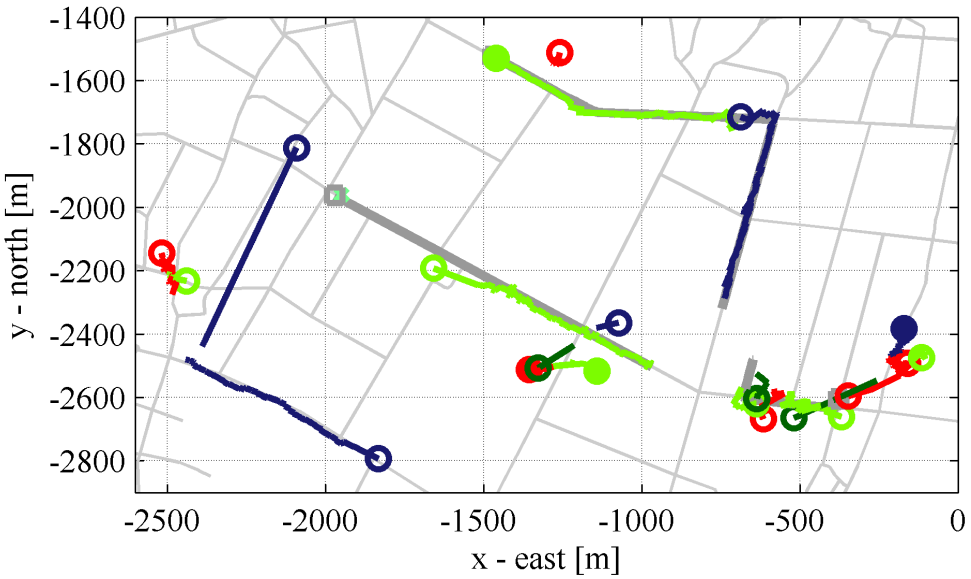


**(b)** 1 % of beamwidth

**Figure 8.9.:** Tracking results with two different configurations – MCMA and 1 % of the beam width – for the area with the ground truth targets up to time step 6000 (127 s). The minimum track duration for display is 10.6 s (500 time steps). The color for the display of each track is chosen arbitrarily. Source of the road map data: Openstreetmap

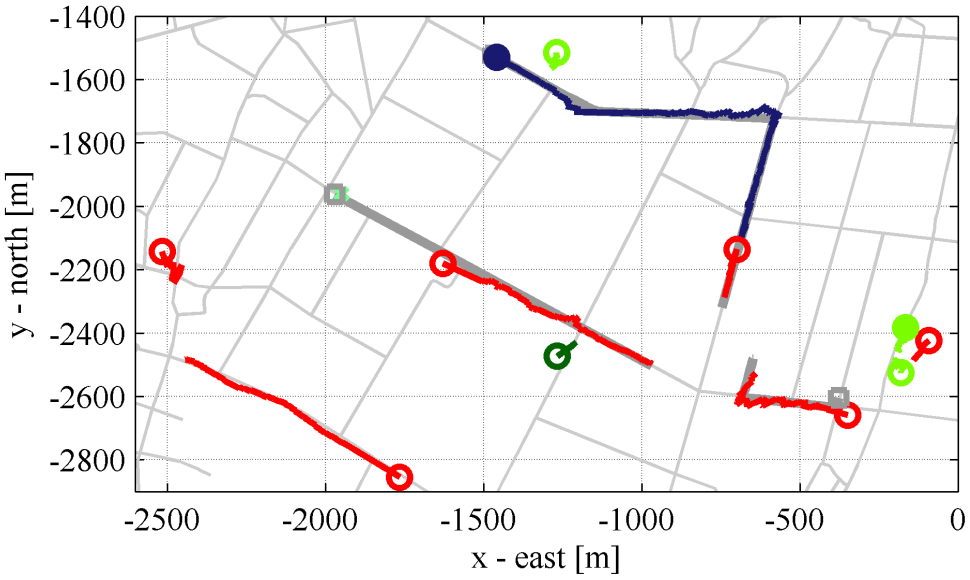


**(a)** 5 % of beamwidth

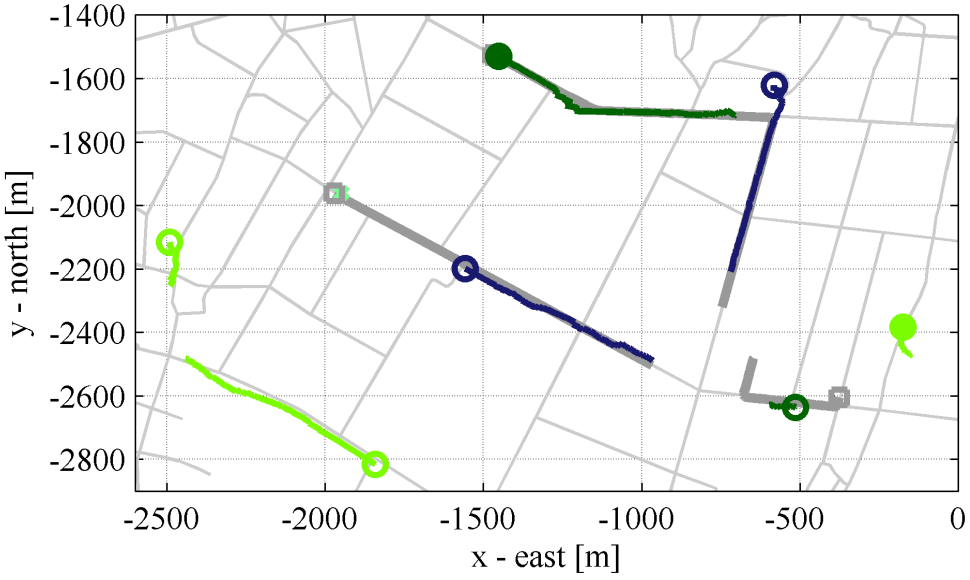


**(b)** 25 % of beamwidth

**Figure 8.10.:** Tracking results with two different configurations – 5% and 25 % of the beam width – for the area with the ground truth targets up to time step 6000 (127 s). The minimum track duration for display is 10.6 s (500 time steps). The color for the display of each track is chosen arbitrarily. Source of the road map data: Openstreetmap

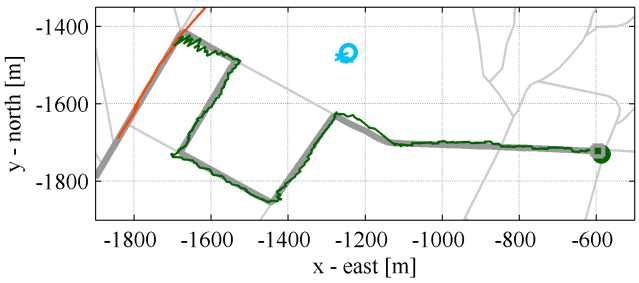


**(a)** MCMA

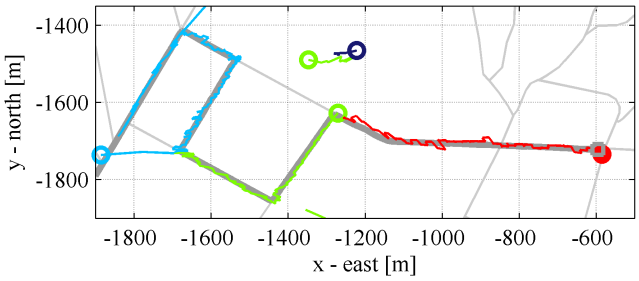


**(b)** 1 % of beam width

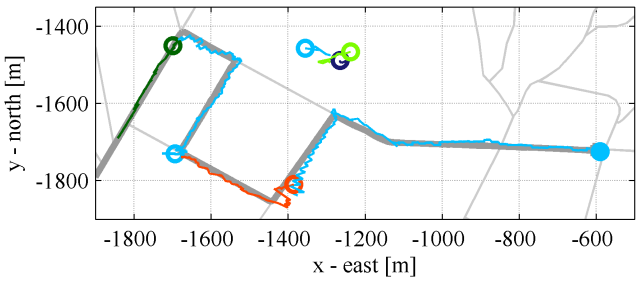


**(c)** 5 % of beam width

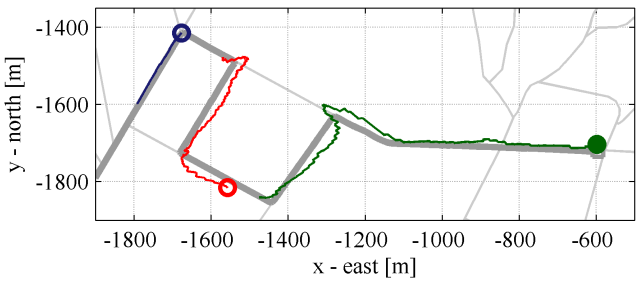


**(d)** 25 % of beamwidth

**Figure 8.11.:** Tracking results of the different configurations for target 1 for timesteps 14000 to 23000. The color for the display of each track is chosen arbitrarily. Source of the road map data: Openstreetmap

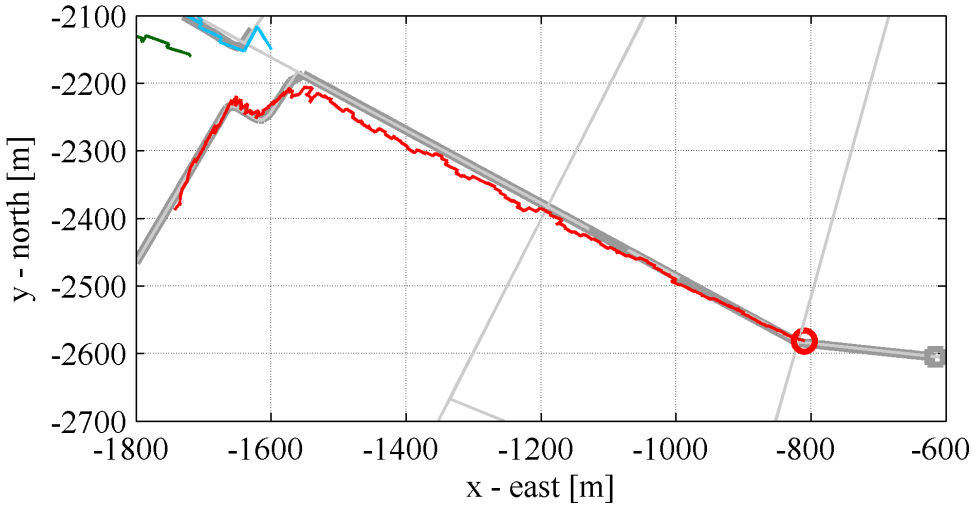


**(a)** MCMA

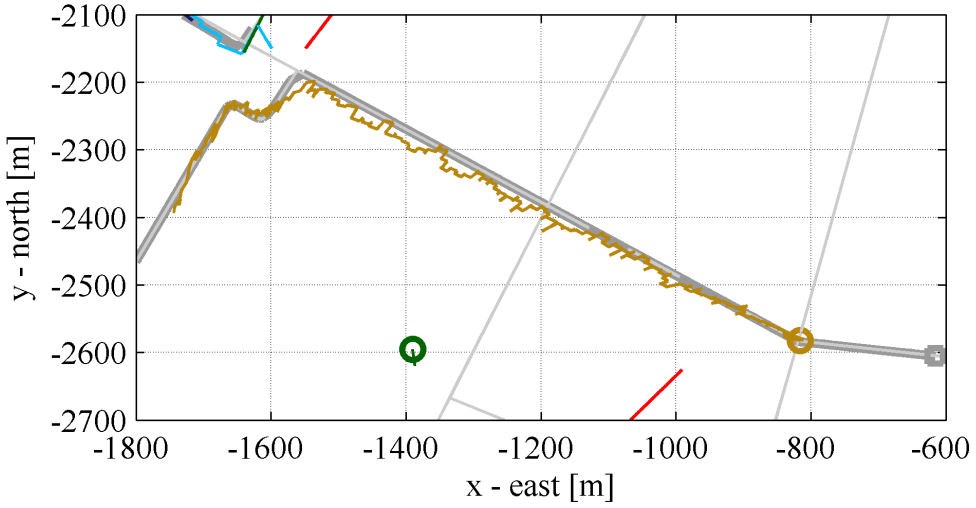


**(b)** 1 % of beam width

**Figure 8.12.:** Tracking results for target 2 for timesteps 12000 to 19000 (255 s to 404 s) for tracking with MCMA and a standard deviation that is set to 1 % of the beam width. The color for the display of each track is chosen arbitrarily. Source of the road map data: Openstreetmap

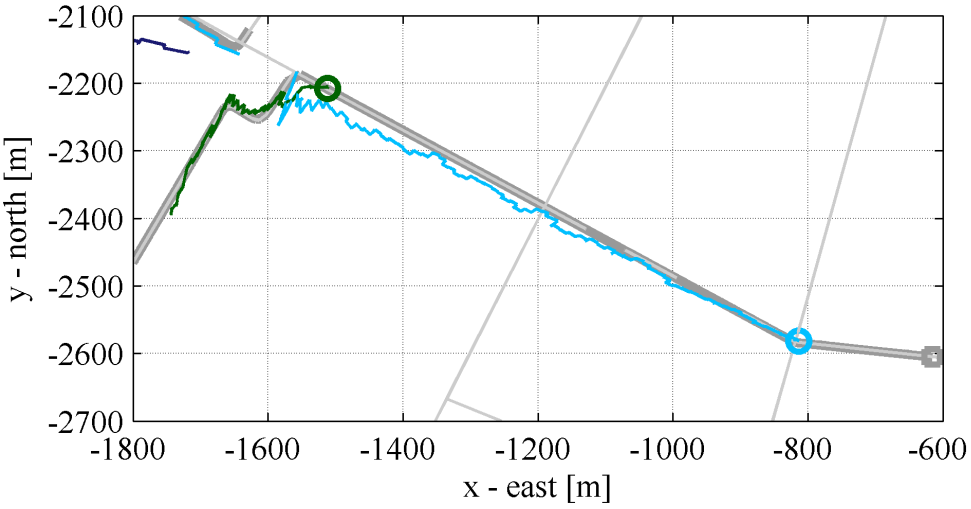


**(a)** 5 % of beam width

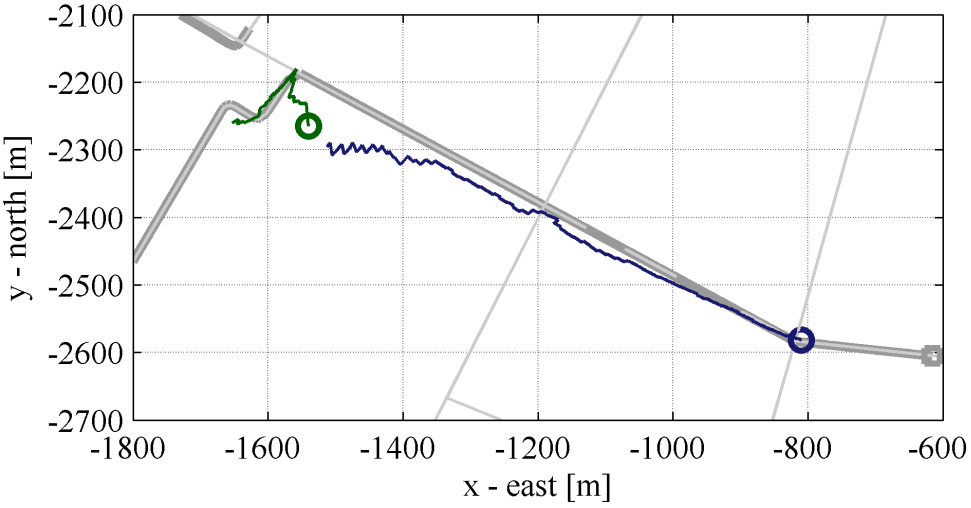


**(b)** 25 % of beam width

**Figure 8.13.:** Tracking results for target 2 for timesteps 12000 to 19000 (255 s to 404 s) for tracking with a standard deviation that is set to 5 % ans 25 % of the beam width. The color for the display of each track is chosen arbitrarily. Source of the road map data: Openstreetmap

**Discussion of experimental tracking performance** The tracking results with the three sub data sets lead to the following findings:

Standard tracking with the optimistic configuration (GM-PHD-OPT) causes very jittery tracks when the target moves on a straight line (see Figure 8.12a). On the other hand, the pessimistic configuration (GM-PHD-PESS) may react very slowly to turns of the target (see Figure 8.11d).

With the overly optimistic configuration track breakages occur. These were expected due to the simulative results. They are due to the fact that incoming measurements cannot be associated to existing tracks because the assumed accuracy is too high for both the track and the measurement. An example of this behavior are the swarm of tracks that is generated for the bike with GM-PHD-OPT (see Figure 8.9b). Another example is the breakage of the track of target 1 in Figure 8.10a. This breakage occurs at a time when the target is moving almost perpendicular to the line of sight to the platform. Thus, the DOA measurement accuracy is very low and even the intermediate configuration overestimates the measurement accuracy.

With GM-PHD-INT and GM-PHD-PESS another type of track breakages occurs *frequently* at target turns (see Figure 8.10b, 8.11c, 8.11d, 8.13a, 8.13b). In these cases the tracking algorithm attributes insufficient significance to detections that indicate a target turn. On the other hand, with MCMA, the accuracy assumption for the existing track and the measurements are better balanced. Thus, it performs more successful when a target changes course.

# 9. Conclusion

The original question of this thesis was whether radar signal processing and target tracking can be brought closer together in order to improve the final tracking result. Among various possible approaches to this question, this thesis has focused on the inclusion of an improved modeling of the direction of arrival estimation error in a tracking algorithm.

In the course of this investigation, numerous auxiliary, yet important tasks were completed: A specifically designed experiment with an airborne radar was conducted. A reference radar signal processing and a target tracking algorithm were implemented and documented in this thesis. Adaptations of standard tracking algorithms to the task of ground target tracking have been presented.

The investigation of the DOA error modeling has been based thoroughly on the experimental data set. It has shown that a simple, easily implementable method is very effective at modeling the DOA estimation error. Furthermore, it has shown with examples based on the experimental data that this modeling improves the tracking performance. Results were better or as least as good as tracking with a standard error model.

This thesis adds the first experimental verification of this error model to the body of literature. As such, it provides a significant extensions to the investigation that has been published earlier in [35] and [38]. Additionally, this thesis provides a treatise of the entire processing chain starting from the raw data up to tracking results. As existing publications only treat subfields, this in itself is an important addition to the literature.

Thus, this thesis is in general significant for any researcher in the field of ground moving target tracking. To researchers in the field of tracking, it provides an accessible presentation of the radar data acquisition process. To researchers in radar signal processing it details how the GMTI results are processed in the tracking step. More particular, this thesis is relevant for any engineer with the task of designing a ground moving target tracking algorithm. This thesis provides the incentive to at least strongly consider the error model that has been presented here.

Of course, every body of research has its limitations. With respect to the proposed DOA estimation error model, it is desirable to repeat an identical investigation with an even larger experimental data set. In particular, going beyond example results, it will be desirable to quantify the improved tracking performance with a high degree of confidence from a larger data set. More in general, other approaches for improving the tracking performance should be investigated in the future. These include the use of the tracking results in the clutter learning step in order to reduce target self nulling. Another interesting research direction is to adaptively modify the

allocated radar observation time depending on the detectability of the target. Furthermore, the experimental results of this thesis have shown the difficulty of target tracking in an urban area. Research into whether and how the tracking in urban areas can be improved is important. Seen more positively: For these investigations, this thesis will provide an excellent starting point.

# A. Algorithms

This Appendix gathers functions and algorithms that are defined or used in various parts of this thesis. Similarly to the use of variables in programming, the variable definitions shall only be valid in the context of each algorithm. While this in some cases makes the definitions more lengthy, it also ensures that each definition contains all equations and variables that are necessary for implementation.

- Section A.1 presents an algorithm for determining the geolocation of a target for which the range, directional of arrival and the prameters of a plane of which it is located are known. The Jacobian matrix with respect to all input parameters is also provided.

- Section A.2 presents a function that determines the magnitude of the measurable component of the velocity vector of a target that moves on a planar surface. The Jacobian matrix is given as well.

- Section A.3 presents a function that determines the range, radial velocity and directional cosine of a target based on the Cartesian coordiante and velocity of the target.

- Section A.4 presents a function that determines the Doppler frequency of clutter returns as a function of range and direction of arrival. This function is used for determining the J-hook and is important for preprocessing radar data prior to applying a STAP algorithm.

- Section A.5 presents functions that are used in the target tracking algorithm of this thesis. The main goal is to give the definition of two functions: First, the function $\boldsymbol{f}^{\mathcal{M}\leftarrow\mathrm{urv}}$ that converts a radar measurement vector to a measurement vector of the type that is passed to the tracking algorithm. Second, the function $\boldsymbol{h}_k$ that determines a synthetic measurements based on a track state and a measurement error vector.

  As Figure A.1 shows, these functions are defined with the help of various other functions. Some of the subfunctions are very simple. Still they are given here for completeness. Jacobian matrices of the functions that are required for the tracking algorithm are provided in Section A.6.

- Section A.7 presents functions for computing the Euler rotation matrix or its inverse for given yaw, pitch and roll angles. It also presents a function for performing a bilinear interpolation

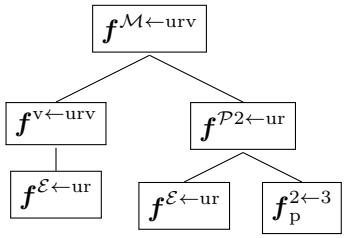


**(a)** Decomposition of the conversion of a radar measurement vector to a track measurement vector.

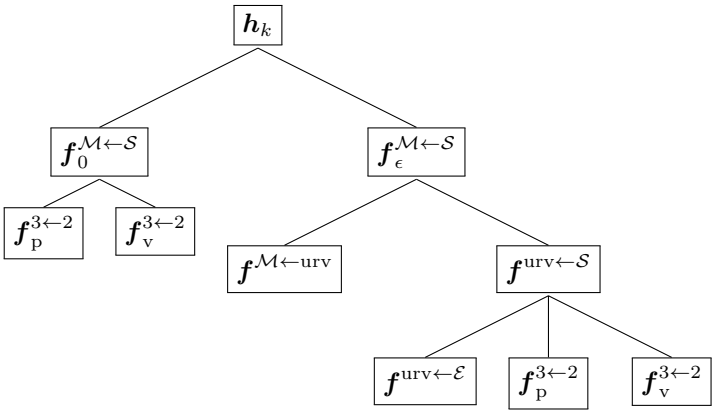


**(b)** Decomposition of the determination of the predicted measurement based on the track state.

**Figure A.1.:** Decomposition of the structure of the functions $\boldsymbol{f}^{\mathcal{M}\leftarrow\mathrm{urv}}$ and $\boldsymbol{h}_k$.

- Section A.8 presents functions that convert a track state that comprises two location and two velocity dimensions to a full ENU track state based on a digital elevation model. Jacobians of the conversion with respect to the original track state and DEM parameters are given.

To facilitate implementation of the content of this Appendix in a programming language, the order in which variable definitions are given here is the order in which they can be computed.

**Expansion of vector projections** In some of the algorithms the projection of a vector $\boldsymbol{x}$ on a plane with normal vector $\boldsymbol{n}_{\text{norm}}$ is performed as in

$$\boldsymbol{x}_{\text{p}} = \mathbf{P}_{\text{proj}} \boldsymbol{x}_{\text{org}} \,, \tag{A.1}$$

where

$$\mathbf{P}_{\text{proj}} = \mathbf{I} - \boldsymbol{n}_{\text{norm}} \left[\boldsymbol{n}_{\text{norm}}\right]^{\text{T}} \tag{A.2}$$

is the projection matrix. For later computations of the Jacobian of the vector $\boldsymbol{x}_{\text{p}}$ with respect to parameters of $\boldsymbol{x}_{\text{org}}$ or $\boldsymbol{n}_{\text{norm}}$, the expanded form

$$\begin{aligned} \boldsymbol{x}_{\text{p}} &= \left(\mathbf{I} - \boldsymbol{n}_{\text{norm}} \left[\boldsymbol{n}_{\text{norm}}\right]^{\text{T}}\right) \boldsymbol{x}_{\text{org}} \\ &= \boldsymbol{x}_{\text{org}} - \left[\boldsymbol{n}_{\text{norm}}\right]^{\text{T}} \boldsymbol{x}_{\text{org}} \boldsymbol{n}_{\text{norm}} \\ &= \boldsymbol{x}_{\text{org}} - \rho_{\text{proj}} \boldsymbol{n}_{\text{norm}} \,, \end{aligned} \tag{A.3}$$

of the projection will be more convenient. Here

$$\rho_{\text{proj}} = \left[\boldsymbol{n}_{\text{norm}}\right]^{\text{T}} \boldsymbol{x}_{\text{org}} \,. \tag{A.4}$$

The expanded expression avoids the use of matrices for which convential Jacobians are not defined.

# A.1. Geolocation of a target

## A.1.1. Function for the geolocation based on target range and directional cosine

This function determines the location of a target in Cartesian ENU coordinates based on the range $r$ and the directional cosine $u$ with respect to an axis, e.g. the antenna axis. For the geolocation it must be assumed that the target is located on a plane that is defined by its normal vector $\boldsymbol{n}^{\mathcal{E}}_{\text{plane}}$ and the distance $d^{\mathcal{E}}_{\text{plane}}$ of the plane to the origin of the coordinate system.

**Derivation** Due to the given range to the target and directional cosine to the target, the target must lie on a circle which is given in parameter form by

$$\boldsymbol{x}_{\mathrm{phi}}(\phi) = \boldsymbol{m}^{\mathcal{E}}_{\mathrm{circ}} + r_{\mathrm{circ}} \boldsymbol{e}^{\mathcal{E}}_{\mathrm{circ},1} \cos(\phi) + r_{\mathrm{circ}} \boldsymbol{e}^{\mathcal{E}}_{\mathrm{circ},2} \sin(\phi) \tag{A.5}$$

where $\phi$ is the running variable, $\boldsymbol{m}^{\mathcal{E}}_{\mathrm{circ}}$ is the center, $r_{\mathrm{circ}}$ is the radius, $\boldsymbol{e}^{\mathcal{E}}_{\mathrm{circ},1}$ and $\boldsymbol{e}^{\mathcal{E}}_{\mathrm{circ},2}$ are two unit vectors that span the circle. The second constraint is that the target lies on the plane. Combined with constraint (A.5) this yields

$$\left[\boldsymbol{n}^{\mathcal{E}}_{\mathrm{plane}}\right]^{\mathrm{T}} \boldsymbol{x}_{\mathrm{phi}}(\phi) = d^{\mathcal{E}}_{\mathrm{plane}} \,. \tag{A.6}$$

Rearanging this equation obtains

$$\left[\boldsymbol{n}^{\mathcal{E}}_{\mathrm{plane}}\right]^{\mathrm{T}} \boldsymbol{e}^{\mathcal{E}}_{\mathrm{circ},1} \cos(\phi) + \left[\boldsymbol{n}^{\mathcal{E}}_{\mathrm{plane}}\right]^{\mathrm{T}} \boldsymbol{e}^{\mathcal{E}}_{\mathrm{circ},2} \sin(\phi) = \frac{d^{\mathcal{E}}_{\mathrm{plane}} - \left[\boldsymbol{n}^{\mathcal{E}}_{\mathrm{plane}}\right]^{\mathrm{T}} \boldsymbol{m}^{\mathcal{E}}_{\mathrm{circ}}}{r_{\mathrm{circ}}} \,. \tag{A.7}$$

It can be sovled particularly easily for $\phi$ if $\boldsymbol{e}^{\mathcal{E}}_{\mathrm{circ},2}$ is selected such that its scalar product with $\boldsymbol{n}^{\mathcal{E}}_{\mathrm{plane}}$ is zero. In this case, the second summand in equation (A.7) disappears and the cosine of $\phi$ is given by

$$\cos(\phi) = \frac{d^{\mathcal{E}}_{\mathrm{plane}} - \left[\boldsymbol{n}^{\mathcal{E}}_{\mathrm{plane}}\right]^{\mathrm{T}} \boldsymbol{m}^{\mathcal{E}}_{\mathrm{circ}}}{r_{\mathrm{circ}} \left[\boldsymbol{n}^{\mathcal{E}}_{\mathrm{plane}}\right]^{\mathrm{T}} \boldsymbol{e}^{\mathcal{E}}_{\mathrm{circ},1}} \,. \tag{A.8}$$

In order to obtain the desired vanishing of the second summand, the first unit vector must be chosen such that it has the maximum correlation with the normal vector of the plane, i.e. it must be colinear to

$$\tilde{\boldsymbol{e}}^{\mathcal{E}}_{\mathrm{circ},1} = \mathbf{P}^{\mathcal{E}}_{\mathrm{cp}} \boldsymbol{n}^{\mathcal{E}}_{\mathrm{plane}} \,, \tag{A.9}$$

where $\mathbf{P}^{\mathcal{E}}_{\mathrm{cp}}$ is a matrix that projects into the plane of the circle. Based on this reasoning, the algorithm for determining the geolocation is given in the following.

**Notation**

$$\boldsymbol{x}^{\mathcal{E}}_{\mathrm{grd},n} = \boldsymbol{f}^{\mathcal{E}\leftarrow\mathrm{ur}}_{n}\left(u, r, \boldsymbol{x}^{\mathcal{E}}_{\mathrm{ant}}, \boldsymbol{\gamma}^{\mathcal{A}\leftarrow\mathcal{E}}_{\mathrm{yp}}, \boldsymbol{n}^{\mathcal{E}}_{\mathrm{plane}}, d^{\mathcal{E}}_{\mathrm{plane}}\right) \tag{A.10a}$$

**Implementation** Unit vector of the orientation of the main axis of the linear antenna

$$\boldsymbol{e}^{\mathcal{E}} = \begin{bmatrix} \cos(\gamma_{\mathrm{yaw}}) \cos(\gamma_{\mathrm{pitch}}) \\ \sin(\gamma_{\mathrm{yaw}}) \cos(\gamma_{\mathrm{pitch}}) \\ -\sin(\gamma_{\mathrm{pitch}}) \end{bmatrix} \tag{A.10b}$$

where the angles are given by

$$\boldsymbol{\gamma}_{\mathrm{yp}}^{\mathcal{A}\leftarrow\mathcal{E}} = \begin{bmatrix} \gamma_{\mathrm{yaw}} \\ \gamma_{\mathrm{pitch}} \end{bmatrix}. \tag{A.10c}$$

Matrix which projects into the plane of the range cone circle:

$$\mathbf{P}_{\mathrm{cp}}^{\mathcal{E}} = \mathbf{I} - \boldsymbol{e}^{\mathcal{E}} \left[\boldsymbol{e}^{\mathcal{E}}\right]^{\mathrm{T}} \tag{A.10d}$$

Scalar product between antenna main axis and normal vector of the plane:

$$\rho_{\mathrm{en}} = \left[\boldsymbol{e}^{\mathcal{E}}\right]^{\mathrm{T}} \boldsymbol{n}_{\mathrm{plane}}^{\mathcal{E}} \tag{A.10e}$$

A vector that is colinear to the first unit vector that spans the circle:

$$\tilde{\boldsymbol{e}}_{\mathrm{circ},1}^{\mathcal{E}} = \mathbf{P}_{\mathrm{cp}}^{\mathcal{E}} \boldsymbol{n}_{\mathrm{plane}}^{\mathcal{E}} = \boldsymbol{n}_{\mathrm{plane}}^{\mathcal{E}} - \left[\boldsymbol{e}^{\mathcal{E}}\right]^{\mathrm{T}} \boldsymbol{n}_{\mathrm{plane}}^{\mathcal{E}} \boldsymbol{e}^{\mathcal{E}} \tag{A.10f}$$

$$= \boldsymbol{n}_{\mathrm{plane}}^{\mathcal{E}} - \rho_{\mathrm{en}} \boldsymbol{e}^{\mathcal{E}} \tag{A.10g}$$

First unit vector that spans the circle:

$$\boldsymbol{e}_{\mathrm{circ},1}^{\mathcal{E}} = \frac{\mathbf{P}_{\mathrm{cp}}^{\mathcal{E}} \boldsymbol{n}_{\mathrm{plane}}^{\mathcal{E}}}{\|\mathbf{P}_{\mathrm{cp}}^{\mathcal{E}} \boldsymbol{n}_{\mathrm{plane}}^{\mathcal{E}}\|} = \frac{\tilde{\boldsymbol{e}}_{\mathrm{circ},1}^{\mathcal{E}}}{\|\tilde{\boldsymbol{e}}_{\mathrm{circ},1}^{\mathcal{E}}\|} \tag{A.10h}$$

Second unit vector that spans the circle:

$$\boldsymbol{e}_{\mathrm{circ},2}^{\mathcal{E}} = \boldsymbol{e}_{\mathrm{circ},1}^{\mathcal{E}} \times \boldsymbol{e}^{\mathcal{E}} \tag{A.10i}$$

Radius of the circle:

$$r_{\mathrm{circ}} = r\sqrt{1-u^2} \tag{A.10j}$$

Center of the circle:

$$\boldsymbol{m}_{\mathrm{circ}}^{\mathcal{E}} = \boldsymbol{x}^{\mathcal{E}} + ur\boldsymbol{e}^{\mathcal{E}} \tag{A.10k}$$

Scalar product of the normal vector of the surface plane and the first unit vector spanning the circle:

$$\rho_{\mathrm{nc1}} = \left[\boldsymbol{n}_{\mathrm{plane}}^{\mathcal{E}}\right]^{T} \boldsymbol{e}_{\mathrm{circ},1}^{\mathcal{E}} = \sqrt{1-\rho_{\mathrm{en}}^2} \tag{A.10l}$$

Cosine of the angle $\phi$ that determines the target location in ENU coordinates:

$$v = \frac{d_{\mathrm{plane}}^{\mathcal{E}} - \left[\boldsymbol{n}_{\mathrm{plane}}^{\mathcal{E}}\right]^{\mathrm{T}} \boldsymbol{m}_{\mathrm{circ}}^{\mathcal{E}}}{r_{\mathrm{circ}}\rho_{\mathrm{nc1}}} \tag{A.10m}$$

If $|v| > 1$ it is impossible to determine a location that is compatible with the given range and directional cosine and lies on the surface plane.
Corresponding sine. There are in general two solutions.

$$w_1 = +\sqrt{1-v^2} \tag{A.10n}$$

$$w_2 = -\sqrt{1-v^2} \tag{A.10o}$$

$$\tag{A.10p}$$

Finally, the two solutions for the Cartesian ENU target coordinate:

$$\boldsymbol{x}^{\mathcal{E}}_{\mathrm{grd},n} = \boldsymbol{m}^{\mathcal{E}}_{\mathrm{circ}} + r_{\mathrm{circ}}\boldsymbol{e}^{\mathcal{E}}_{\mathrm{circ},1}v + r_{\mathrm{circ}}\boldsymbol{e}^{\mathcal{E}}_{\mathrm{circ},2}w_n \,, n = 1, 2. \tag{A.10q}$$

## A.1.2. Jacobian of the geolocation function

A function that computes the solutions for the geolocation of a target based on the range to the target and a directional cosine with respect to an axis has been derived in Section A.1.1. This function accepts several parameters. Here the Jacobian of this function with respect to the vector

$$\begin{aligned}\boldsymbol{\Phi} &= \left[ \left[\boldsymbol{x}^{\mathcal{E}}_{\mathrm{ant}}\right]^T \ \left[\boldsymbol{\gamma}^{\mathcal{A}\leftarrow\mathcal{E}}_{\mathrm{yp}}\right]^T \ \left[\boldsymbol{n}^{\mathcal{E}}_{\mathrm{plane}}\right]^T d^{\mathcal{E}}_{\mathrm{plane}} \ \left[\boldsymbol{z}_{\mathrm{ur}}\right]^T \right]^T \\ &= \big[x^{\mathcal{E}}_{\mathrm{ant},1} \ x^{\mathcal{E}}_{\mathrm{ant},2} \ x^{\mathcal{E}}_{\mathrm{ant},3} \ \gamma^{\mathcal{A}\leftarrow\mathcal{E}}_{\mathrm{yaw}} \ \gamma^{\mathcal{A}\leftarrow\mathcal{E}}_{\mathrm{pitch}} \\ &\qquad n^{\mathcal{E}}_{\mathrm{plane},1} \ n^{\mathcal{E}}_{\mathrm{plane},2} \ n^{\mathcal{E}}_{\mathrm{plane},3} \ d^{\mathcal{E}}_{\mathrm{plane}} \ u \ r \ \big]^{\mathrm{T}}\end{aligned} \tag{A.11}$$

that comprises all parameters is presented.

### Notation

$$\frac{\partial \boldsymbol{x}^{\mathcal{E}}_{\mathrm{gr},n}}{\partial \boldsymbol{\Phi}} = \mathbf{f}^{\mathcal{E}\leftarrow\mathrm{ur}}_{J,n}\left(u, r, \boldsymbol{x}^{\mathcal{E}}_{\mathrm{ant}}, \boldsymbol{\gamma}^{\mathcal{A}\leftarrow\mathcal{E}}_{\mathrm{yp}}, \boldsymbol{n}^{\mathcal{E}}_{\mathrm{plane}}, d^{\mathcal{E}}_{\mathrm{plane}}\right) \tag{A.12a}$$

**Implementation** First, compute all variables of Section A.1.1.
Jacobians of the function parameters with respect to the parameter vector:

$$\begin{aligned}\frac{\partial u}{\partial \boldsymbol{\Phi}} &= [\ \mathbf{0}_{1\times 9} \ \mathbf{I}_{1\times 1}\mathbf{0}_{1\times 1}] \\ \frac{\partial r}{\partial \boldsymbol{\Phi}} &= [\mathbf{0}_{1\times 10} \ \mathbf{I}_{1\times 1} \ ] \\ \frac{\partial \boldsymbol{x}^{\mathcal{E}}_{\mathrm{ant}}}{\partial \boldsymbol{\Phi}} &= [\mathbf{I}_{3\times 3} \ \mathbf{0}_{3\times 8}] \\ \frac{\partial \boldsymbol{\gamma}^{\mathcal{A}\leftarrow\mathcal{E}}_{\mathrm{yp}}}{\partial \boldsymbol{\Phi}} &= [\mathbf{0}_{2\times 3} \ \mathbf{I}_{2\times 2} \ \mathbf{0}_{3\times 6}] \\ \frac{\partial \boldsymbol{n}^{\mathcal{E}}_{\mathrm{plane}}}{\partial \boldsymbol{\Phi}} &= [\mathbf{0}_{3\times 5} \ \mathbf{I}_{3\times 3} \ \mathbf{0}_{3\times 3}] \\ \frac{\partial d^{\mathcal{E}}_{\mathrm{plane}}}{\partial \boldsymbol{\Phi}} &= [\mathbf{0}_{1\times 8} \ \mathbf{I}_{1\times 1} \ \mathbf{0}_{1\times 2}]\end{aligned} \tag{A.12b}$$

Jacobian of the unit vector that describes the orientation of the antenna axis:

$$\frac{\partial \boldsymbol{e}^{\mathcal{E}}}{\partial \boldsymbol{\Phi}} = \left[\mathbf{0}_{3\times 3} \quad \frac{\partial \boldsymbol{e}^{\mathcal{E}}}{\partial \gamma_{\mathrm{yaw}}} \quad \frac{\partial \boldsymbol{e}^{\mathcal{E}}}{\partial \gamma_{\mathrm{pitch}}}\mathbf{0}_{3\times 7}\right]^{\mathrm{T}}, \tag{A.12c}$$

where

$$\frac{\partial \boldsymbol{e}^{\mathcal{E}}}{\partial \gamma_{\mathrm{yaw}}} = \begin{bmatrix} -\sin(\gamma_{\mathrm{yaw}})\cos(\gamma_{\mathrm{pitch}}) \\ \cos(\gamma_{\mathrm{yaw}})\cos(\gamma_{\mathrm{pitch}}) \\ 0 \end{bmatrix} \tag{A.12d}$$

and

$$\frac{\partial \boldsymbol{e}^{\mathcal{E}}}{\partial \gamma_{\text{pitch}}} = \begin{bmatrix} -\cos(\gamma_{\text{yaw}})\sin(\gamma_{\text{pitch}}) \\ -\sin(\gamma_{\text{yaw}})\sin(\gamma_{\text{pitch}}) \\ -\cos(\gamma_{\text{pitch}}) \end{bmatrix}. \tag{A.12e}$$

Jacobian of the correlation between the antenna orientation vector and the normal vector of the surface plane:

$$\frac{\partial \rho_{\text{en}}}{\partial \boldsymbol{\Phi}} = \left[\boldsymbol{e}^{\mathcal{E}}\right]^{\text{T}} \frac{\partial \boldsymbol{n}^{\mathcal{E}}_{\text{plane}}}{\partial \boldsymbol{\Phi}} + \left[\boldsymbol{n}^{\mathcal{E}}_{\text{plane}}\right]^{T} \frac{\partial \boldsymbol{e}^{\mathcal{E}}}{\partial \boldsymbol{\Phi}} \tag{A.12f}$$

Jacobian of the projection of the normal vector of the surface plane onto the plane of the cone range circle

$$\frac{\partial \tilde{\boldsymbol{e}}^{\mathcal{E}}_{\text{circ},1}}{\partial \boldsymbol{\Phi}} = \frac{\partial \boldsymbol{n}^{\mathcal{E}}_{\text{plane}}}{\partial \boldsymbol{\Phi}} - \boldsymbol{e}^{\mathcal{E}} \frac{\partial \rho_{\text{en}}}{\partial \Phi} - \rho_{\text{en}} \frac{\partial \boldsymbol{e}_{\text{ant},1}}{\partial \boldsymbol{\Phi}} \tag{A.12g}$$

Jacobian of the first unit vector which spans the range cone circle

$$\frac{\partial \boldsymbol{e}^{\mathcal{E}}_{\text{circ},1}}{\partial \boldsymbol{\Phi}} = \frac{\left\|\tilde{\boldsymbol{e}}^{\mathcal{E}}_{\text{circ},1}\right\| \frac{\partial \tilde{\boldsymbol{e}}^{\mathcal{E}}_{\text{circ},1}}{\partial \boldsymbol{\Phi}} - \tilde{\boldsymbol{e}}^{\mathcal{E}}_{\text{circ},1} \frac{\left[\tilde{\boldsymbol{e}}^{\mathcal{E}}_{\text{circ},1}\right]^{T} \frac{\partial \tilde{\boldsymbol{e}}^{\mathcal{E}}_{\text{circ},1}}{\partial \boldsymbol{\Phi}}}{\left\|\tilde{\boldsymbol{e}}^{\mathcal{E}}_{\text{circ},1}\right\|}}{\left\|\tilde{\boldsymbol{e}}^{\mathcal{E}}_{\text{circ},1}\right\|^{2}} \tag{A.12h}$$

Jacobian matrix of the second vector which spans the range cone circle:

$$\frac{\partial \boldsymbol{e}^{\mathcal{E}}_{\text{circ},2}}{\partial \boldsymbol{\Phi}} = \left[\frac{\partial \boldsymbol{e}^{\mathcal{E}}_{\text{circ},2}}{\partial \Phi_k}\right]_{k=1\ldots11} \tag{A.12i}$$

where

$$\frac{\partial \boldsymbol{e}^{\mathcal{E}}_{\text{circ},2}}{\partial \Phi_k} = \frac{\partial \boldsymbol{e}^{\mathcal{E}}_{\text{circ},1}}{\partial \Phi_k} \times \boldsymbol{e}^{\mathcal{E}} + \boldsymbol{e}^{\mathcal{E}}_{\text{circ},1} \times \frac{\partial \boldsymbol{e}^{\mathcal{E}}}{\partial \Phi_k} \tag{A.12j}$$

is the $k$-th column of the Jacobian matrix.
Jacobian of the radius of the range cone circle:

$$\frac{\partial r_{\text{circ}}}{\partial \boldsymbol{\Phi}} = \sqrt{1-u^2} \frac{\partial r}{\partial \boldsymbol{\Phi}} - r \frac{u}{\sqrt{1-u^2}} \frac{\partial u}{\partial \boldsymbol{\Phi}} \tag{A.12k}$$

Jacobian of the center of the cone circle:

$$\frac{\partial \boldsymbol{m}^{\mathcal{E}}_{\text{circ}}}{\partial \boldsymbol{\Phi}} = \frac{\partial \boldsymbol{x}^{\mathcal{E}}_{\text{ant}}}{\partial \boldsymbol{\Phi}} + ur \frac{\partial \boldsymbol{e}^{\mathcal{E}}}{\partial \boldsymbol{\Phi}} + \boldsymbol{e}^{\mathcal{E}} r \frac{\partial u}{\partial \boldsymbol{\Phi}} + \boldsymbol{e}^{\mathcal{E}} u \frac{\partial r}{\partial \boldsymbol{\Phi}} \tag{A.12l}$$

Jacobian of the correlation between the normal vector of the surface plane and the first vector which spans the circle:

$$\frac{\partial \rho_{\text{nc1}}}{\partial \boldsymbol{\Phi}} = -\frac{\rho_{\text{en}}}{\sqrt{1-\rho^2_{\text{en}}}} \frac{\partial \rho_{\text{en}}}{\partial \boldsymbol{\Phi}} \tag{A.12m}$$

Jacobian of $v$, the cosine of the solution for $\phi$:

$$\frac{\partial v}{\partial \boldsymbol{\Phi}} = \left(d^{\mathcal{E}}_{\text{plane}} - \left[\boldsymbol{n}^{\mathcal{E}}_{\text{plane}}\right]^{\mathrm{T}} \boldsymbol{m}^{\mathcal{E}}_{\text{circ}}\right) \left(-\frac{1}{r_{\text{circ}}\rho^2_{\text{nc1}}}\frac{\partial \rho_{\text{nc1}}}{\partial \boldsymbol{\Phi}} - \frac{1}{r^2_{\text{circ}}\rho_{\text{nc1}}}\frac{\partial r_{\text{circ}}}{\partial \boldsymbol{\Phi}}\right) + \frac{1}{r_{\text{circ}}\rho_{\text{nc1}}}\left(\frac{\partial d^{\mathcal{E}}_{\text{plane}}}{\partial \boldsymbol{\Phi}} - \left[\boldsymbol{n}^{\mathcal{E}}_{\text{plane}}\right]^{\mathrm{T}}\frac{\partial \boldsymbol{m}^{\mathcal{E}}_{\text{circ}}}{\partial \boldsymbol{\Phi}} - \left[\boldsymbol{m}^{\mathcal{E}}_{\text{circ}}\right]^{\mathrm{T}}\frac{\partial \boldsymbol{n}^{\mathcal{E}}_{\text{plane}}}{\partial \boldsymbol{\Phi}}\right) \tag{A.12n}$$

Jacobians of $w_1$ and $w_2$, the corresponding sine values:

$$\frac{\partial w_1}{\partial \boldsymbol{\Phi}} = -\frac{v}{\sqrt{1-v^2}}\frac{\partial v}{\partial \boldsymbol{\Phi}} \tag{A.12o}$$

$$\frac{\partial w_2}{\partial \boldsymbol{\Phi}} = +\frac{v}{\sqrt{1-v^2}}\frac{\partial v}{\partial \boldsymbol{\Phi}} \tag{A.12p}$$

Finally, the Jacobian of the target's Cartesian ENU coordinate:

$$\begin{aligned}\frac{\partial \boldsymbol{x}^{\mathcal{E}}_{\text{gr},n}}{\partial \boldsymbol{\Phi}} =& \frac{\partial \boldsymbol{m}^{\mathcal{E}}_{\text{circ}}}{\partial \boldsymbol{\Phi}} \\ &+ \boldsymbol{e}^{\mathcal{E}}_{\text{circ},1} r_{\text{circ}}\frac{\partial v}{\partial \boldsymbol{\Phi}} + \boldsymbol{e}^{\mathcal{E}}_{\text{circ},1} v\frac{\partial r_{\text{circ}}}{\partial \boldsymbol{\Phi}} + r_{\text{circ}} v\frac{\partial \boldsymbol{e}^{\mathcal{E}}_{\text{circ},1}}{\partial \boldsymbol{\Phi}} \\ &+ \boldsymbol{e}^{\mathcal{E}}_{\text{circ},2} r_{\text{circ}}\frac{\partial w_n}{\partial \boldsymbol{\Phi}} + \boldsymbol{e}^{\mathcal{E}}_{\text{circ},2} w_n\frac{\partial r_{\text{circ}}}{\partial \boldsymbol{\Phi}} + r_{\text{circ}} w_n\frac{\partial \boldsymbol{e}^{\mathcal{E}}_{\text{circ},2}}{\partial \boldsymbol{\Phi}}\end{aligned} \tag{A.12q}$$

### A.1.3. Function for selecting one solution of the possible target geolocations

In general there are two solutions for the geolocation of a target. In most practial cases, one of the solution lies in the back lobe of the antenna. As almost no energy is returned from the back lobe, this solution can be excluded. This function returns the index of a solution which does not lie in the antenna back lobe.

#### Notation

$$n_{\text{tgt,ch}} = \boldsymbol{f}_{\text{tgt,ch}}\left(\boldsymbol{x}^{\mathcal{E}}_{\text{grd},1}, \boldsymbol{x}^{\mathcal{E}}_{\text{grd},2}, \boldsymbol{x}^{\mathcal{E}}_{\text{ant}}, \boldsymbol{\gamma}_{\text{yrp}}\right) \tag{A.13a}$$

where $\boldsymbol{x}^{\mathcal{E}}_{\text{grd},n}$, $n = 1, 2$ are 2 solutions.

**Implementation** Compute direction vectors for each solution:

$$\boldsymbol{u}^{\mathcal{E}}_{\text{at},n} = \frac{\boldsymbol{x}^{\mathcal{E}}_{\text{grd},n} - \boldsymbol{x}^{\mathcal{E}}_{\text{ant}}}{\|\boldsymbol{x}^{\mathcal{E}}_{\text{grd},n} - \boldsymbol{x}^{\mathcal{E}}_{\text{ant}}\|} \tag{A.13b}$$

Determine rotation matrix to antenna coordinate system:

$$\mathbf{T}^{\mathcal{A}\leftarrow\mathcal{E}} = \mathbf{T}_{\text{Euler}}(\boldsymbol{\gamma}_{\text{yrp}}) \tag{A.13c}$$

The direction vector in antenna coordinates:

$$\boldsymbol{u}_{\mathrm{at},n}^{\mathcal{A}} = \mathbf{T}^{\mathcal{A}\leftarrow\mathcal{E}}\boldsymbol{u}_{\mathrm{at},n}^{\mathcal{E}} \tag{A.13d}$$

The vector components are denoted as

$$\boldsymbol{u}_{\mathrm{at},n}^{\mathcal{A}} = \begin{bmatrix} \boldsymbol{u}_{\mathrm{at},n,1}^{\mathcal{A}} \\ \boldsymbol{u}_{\mathrm{at},n,2}^{\mathcal{A}} \\ \boldsymbol{u}_{\mathrm{at},n,3}^{\mathcal{A}} \end{bmatrix} \tag{A.13e}$$

if $\boldsymbol{u}_{\mathrm{at},1,3}^{\mathcal{A}} > 0$, then solution 1 is not in the back lobe, proceed to return $n_{\mathrm{grd,choice}} = 1$, else choose $n_{\mathrm{grd,choice}} = 2$.

### A.1.4. Function for a unique solution for the geolocation of the target

This function uses definition of Section A.1.3 to provide a unique solution for the geolocation of a target.

#### Notation

$$\boldsymbol{x}_{\mathrm{grd}}^{\mathcal{E}} = \boldsymbol{f}^{\mathcal{E}\leftarrow\mathrm{ur}}\left(u_{\mathrm{dc}}, r, \boldsymbol{x}_{\mathrm{ant}}^{\mathcal{E}}, \boldsymbol{\gamma}_{\mathrm{yp}}^{\mathcal{A}\leftarrow\mathcal{E}}, \boldsymbol{n}_{\mathrm{plane}}^{\mathcal{E}}, d_{\mathrm{plane}}^{\mathcal{E}}\right) \tag{A.14a}$$

**Implementation** Compute both solutions:

$$\boldsymbol{x}_{\mathrm{grd},n}^{\mathcal{E}} = \boldsymbol{f}_{\mathrm{rc},n}^{\mathcal{E}\leftarrow\mathrm{ur}}\left(u_{\mathrm{dc}}, r, \boldsymbol{x}_{\mathrm{ant}}^{\mathcal{E}}, \boldsymbol{\gamma}_{\mathrm{yp}}^{\mathcal{A}\leftarrow\mathcal{E}}, \boldsymbol{n}_{\mathrm{plane}}^{\mathcal{E}}, d_{\mathrm{plane}}^{\mathcal{E}}\right) \tag{A.14b}$$

Index of the chosen solution:

$$n_{\mathrm{grd,choice}} = \boldsymbol{f}_{\mathrm{grd,choice}}(\boldsymbol{x}_{\mathrm{grd},1}^{\mathcal{E}}, \boldsymbol{x}_{\mathrm{grd},2}^{\mathcal{E}}, \boldsymbol{\vartheta}) \tag{A.14c}$$

Chosen ground location:

$$\boldsymbol{x}_{\mathrm{grd}}^{\mathcal{E}} = \boldsymbol{x}_{\mathrm{grd},n_{\mathrm{grd,choice}}}^{\mathcal{E}} \tag{A.14d}$$

## A.2. Measurable velocity component

### A.2.1. Function for the measurable velocity component of a target constrained to a plane

The radial velocity of a target is the sum of two components – one due to the antenna velocity and one due to the target velocity. After the geolocation of the target, it is possible to compensate for the antenna motion component in order to determine the pure target motion component of the radial velocity. As it is additionally known that the targets motion is constrained to a surface plane, the scalar magnitude of one of the two velocity components that lie within this plane can be found (see Section 3.3.2). The orientation of vector that corresponds to the scalar magnitude is given by the projection of the line of sight between the antenna and the target onto the surface plane. Since there are in general two solutions for the geolocation of the target, there are also

two solutions for the target's velocity component. In the following, the function that computes the scalar magnitude is presented.

**Notation**

$$v_{\mathrm{t,pl},n} = \boldsymbol{f}_n^{\mathrm{v}\leftarrow\mathrm{urv}}\left(u_{\mathrm{dc}}, r, v_{\mathrm{rad}}, \boldsymbol{x}_{\mathrm{ant}}^{\mathcal{E}}, \boldsymbol{v}_{\mathrm{ant}}^{\mathcal{E}}, \boldsymbol{\gamma}_{\mathrm{yp}}^{\mathcal{A}\leftarrow\mathcal{E}}, \boldsymbol{n}_{\mathrm{plane}}^{\mathcal{E}}, d_{\mathrm{plane}}^{\mathcal{E}}\right) \tag{A.15a}$$

**Implementation** Location of the target in Cartesian ENU coordinates ($n = 1, 2$ is the index of the two solutions):

$$\boldsymbol{x}_{\mathrm{grd},n}^{\mathcal{E}} = \boldsymbol{f}_{\mathrm{rc},n}^{\mathcal{E}\leftarrow\mathrm{ur}}\left(u_{\mathrm{dc}}, r, \boldsymbol{x}_{\mathrm{ant}}^{\mathcal{E}}, \boldsymbol{e}^{\mathcal{E}}, \boldsymbol{n}_{\mathrm{plane}}^{\mathcal{E}}, d_{\mathrm{plane}}^{\mathcal{E}}\right) \tag{A.15b}$$

Matrix that projects on the surface plane:

$$\mathbf{P}_{\mathrm{plane}}^{\mathcal{E}} = \mathbf{I} - \boldsymbol{n}_{\mathrm{plane}}^{\mathcal{E}}\left[\boldsymbol{n}_{\mathrm{plane}}^{\mathcal{E}}\right]^T \tag{A.15c}$$

Difference vector between antenna and target position:

$$\Delta\boldsymbol{x}_{\mathrm{at},n}^{\mathcal{E}} = \boldsymbol{x}_{\mathrm{grd},n}^{\mathcal{E}} - \boldsymbol{x}_{\mathrm{ant}}^{\mathcal{E}} \tag{A.15d}$$

Range to the targets:

$$r = \|\Delta\boldsymbol{x}_{\mathrm{at},n}^{\mathcal{E}}\| \tag{A.15e}$$

Unit vector that points to the target location:

$$\boldsymbol{u}_{\mathrm{at},n}^{\mathcal{E}} = \frac{\Delta\boldsymbol{x}_{\mathrm{at},n}^{\mathcal{E}}}{\|\Delta\boldsymbol{x}_{\mathrm{at},n}^{\mathcal{E}}\|} \tag{A.15f}$$

Scalar product between the normal vector of the surface plane and the unit direction vector:

$$\rho_{\mathrm{pl,at},n} = \left[\boldsymbol{n}_{\mathrm{plane}}^{\mathcal{E}}\right]^T \boldsymbol{u}_{\mathrm{at},n}^{\mathcal{E}} \tag{A.15g}$$

Projection of the unit direction vector onto the plane:

$$\tilde{\boldsymbol{u}}_{\mathrm{at,p},n}^{\mathcal{E}} = \mathbf{P}_{\mathrm{plane}}^{\mathcal{E}}\boldsymbol{u}_{\mathrm{at},n}^{\mathcal{E}} \tag{A.15h}$$

$$= \boldsymbol{u}_{\mathrm{at},n}^{\mathcal{E}} - \rho_{\mathrm{pl,at},n}\boldsymbol{n}_{\mathrm{plane}}^{\mathcal{E}} \tag{A.15i}$$

Target component of the radial velocity:

$$v_{\mathrm{t,rad},n} = v_{\mathrm{rad}} + \left[\boldsymbol{u}_{\mathrm{at},n}^{\mathcal{E}}\right]^{\mathrm{T}} \boldsymbol{v}_{\mathrm{ant}}^{\mathcal{E}} \tag{A.15j}$$

Measurable component of the target velocity within the plane:

$$v_{\mathrm{t,pl},n} = \frac{v_{\mathrm{t,rad},n}}{\|\tilde{\boldsymbol{u}}_{\mathrm{at,p},n}^{\mathcal{E}}\|} \tag{A.15k}$$

### A.2.2. Jacobian of the meausurable velocity with respect to the ENU parameters

In Section A.2.1 an algorithm for determining the scalar value of the measurable velocity component of target in the surface plane was presented. Here, the Jacobian of this function with respect to the vector

$$\begin{aligned}\boldsymbol{\Theta} &= \left[ \left[\boldsymbol{x}_{\text{ant}}^{\mathcal{E}}\right]^T \ \left[\boldsymbol{\gamma}_{\text{yp}}^{\mathcal{A}\leftarrow\mathcal{E}}\right]^T \ \left[\boldsymbol{n}_{\text{plane}}^{\mathcal{E}}\right]^T d_{\text{plane}}^{\mathcal{E}} \ \left[\boldsymbol{z}_{\text{urv}}\right]^T \right]^T \\ &= \big[ x_{\text{ant},1}^{\mathcal{E}} \ x_{\text{ant},2}^{\mathcal{E}} \ x_{\text{ant},3}^{\mathcal{E}} \ \gamma_{\text{yaw}}^{\mathcal{A}\leftarrow\mathcal{E}} \ \gamma_{\text{pitch}}^{\mathcal{A}\leftarrow\mathcal{E}} \\ &\quad n_{\text{plane},1}^{\mathcal{E}} \ n_{\text{plane},2}^{\mathcal{E}} \ n_{\text{plane},3}^{\mathcal{E}} \ d_{\text{plane}}^{\mathcal{E}} \ u \ r \ v_{\text{rad}} \ \big]^{\text{T}}\end{aligned} \tag{A.16}$$

which comprises all input parameters is given.

#### Notation

$$\frac{\partial v_{\text{t,pl},n}}{\partial \boldsymbol{\Theta}} = \mathbf{f}_{J,n}^{v\leftarrow\text{urv}}\left(u_{\text{dc}}, r, v_{\text{rad}}, \boldsymbol{x}_{\text{ant}}^{\mathcal{E}}, \boldsymbol{v}_{\text{ant}}^{\mathcal{E}}, \boldsymbol{\gamma}_{\text{yp}}^{\mathcal{A}\leftarrow\mathcal{E}}, \boldsymbol{n}_{\text{plane}}^{\mathcal{E}}, d_{\text{plane}}^{\mathcal{E}}\right) \tag{A.17a}$$

**Implementation** Jacobians of the input parameters with respect to the parameter vector:

$$\begin{aligned}\frac{\partial u}{\partial \boldsymbol{\Theta}} &= [\ \mathbf{0}_{1\times 9} \ \mathbf{I}_{1\times 1}\mathbf{0}_{1\times 2}] \\ \frac{\partial r}{\partial \boldsymbol{\Theta}} &= [\mathbf{0}_{1\times 10} \ \mathbf{I}_{1\times 1} \ \mathbf{0}_{1\times 1}] \\ \frac{\partial v_{\text{rad}}}{\partial \boldsymbol{\Theta}} &= [\mathbf{0}_{1\times 11} \ \mathbf{I}_{1\times 1}] \\ \frac{\partial \boldsymbol{x}_{\text{ant}}^{\mathcal{E}}}{\partial \boldsymbol{\Theta}} &= [\mathbf{I}_{3\times 3} \ \mathbf{0}_{3\times 9}] \\ \frac{\partial \boldsymbol{\gamma}_{\text{yp}}^{\mathcal{A}\leftarrow\mathcal{E}}}{\partial \boldsymbol{\Theta}} &= [\mathbf{0}_{2\times 3} \ \mathbf{I}_{2\times 2} \ \mathbf{0}_{3\times 7}] \\ \frac{\partial \boldsymbol{n}_{\text{plane}}^{\mathcal{E}}}{\partial \boldsymbol{\Theta}} &= [\mathbf{0}_{3\times 5} \ \mathbf{I}_{3\times 3} \ \mathbf{0}_{3\times 4}] \\ \frac{\partial d_{\text{plane}}^{\mathcal{E}}}{\partial \boldsymbol{\Theta}} &= [\mathbf{0}_{1\times 8} \ \mathbf{I}_{1\times 1} \ \mathbf{0}_{1\times 3}]\end{aligned} \tag{A.17b}$$

Jacobian of the target location with respect to parameter vector $\boldsymbol{\Phi}$ of Section A.1.2:

$$\frac{\partial \boldsymbol{x}_{\text{gr},n}^{\mathcal{E}}}{\partial \boldsymbol{\Phi}} = \mathbf{f}_{J,\text{rc},n}^{\mathcal{E}\leftarrow\text{ur}}\left(u, r, \boldsymbol{x}_{\text{ant}}^{\mathcal{E}}, \boldsymbol{\gamma}_{\text{yp}}^{\mathcal{A}\leftarrow\mathcal{E}}, \boldsymbol{n}_{\text{plane}}^{\mathcal{E}}, d_{\text{plane}}^{\mathcal{E}}\right) \tag{A.17c}$$

Jacobian of the target location with respect to parameter vector $\boldsymbol{\Theta}$:

$$\frac{\partial \boldsymbol{x}_{\text{gr},n}^{\mathcal{E}}}{\partial \boldsymbol{\Theta}} = \left[\frac{\partial \boldsymbol{x}_{\text{gr},n}^{\mathcal{E}}}{\partial \boldsymbol{\Phi}} \quad \mathbf{0}_{3\times 1}\right] \tag{A.17d}$$

Determine all variables of the algorithm of Section A.2.1.
Jacobian of the difference between the target and antenna location:

$$\frac{\partial \Delta \boldsymbol{x}_{\mathrm{at},n}^{\mathcal{E}}}{\partial \boldsymbol{\Theta}} = \frac{\partial \boldsymbol{x}_{\mathrm{grd},n}^{\mathcal{E}}}{\partial \boldsymbol{\Theta}} - \frac{\partial \boldsymbol{x}_{\mathrm{ant}}^{\mathcal{E}}}{\partial \boldsymbol{\Theta}} \tag{A.17e}$$

Jacobian of the range to the target:

$$\frac{\partial r_n}{\partial \boldsymbol{\Theta}} = \frac{\left[\Delta \boldsymbol{x}_{\mathrm{at},n}^{\mathcal{E}}\right]^T \frac{\partial \Delta \boldsymbol{x}_{\mathrm{at},n}^{\mathcal{E}}}{\partial \boldsymbol{\Theta}}}{\|\Delta \boldsymbol{x}_{\mathrm{at},n}^{\mathcal{E}}\|} \tag{A.17f}$$

Jacobian of the unit direction vector that points from the antenna to the target:

$$\begin{aligned}\frac{\partial \boldsymbol{u}_{\mathrm{at},n}^{\mathcal{E}}}{\partial \,\mathrm{d}\,\boldsymbol{\Theta}} &= \frac{\|\Delta \boldsymbol{x}_{\mathrm{at},n}^{\mathcal{E}}\| \frac{\partial \Delta \boldsymbol{x}_{\mathrm{at},n}^{\mathcal{E}}}{\partial \,\mathrm{d}\,\boldsymbol{\Theta}} - \Delta \boldsymbol{x}_{\mathrm{at},n}^{\mathcal{E}} \frac{\partial \|\Delta \boldsymbol{x}_{\mathrm{at},n}^{\mathcal{E}}\|}{\partial \,\mathrm{d}\,\boldsymbol{\Theta}}}{\|\Delta \boldsymbol{x}_{\mathrm{at},n}^{\mathcal{E}}\|^2} \\ &= \frac{r_n \frac{\partial \Delta \boldsymbol{x}_{\mathrm{at},n}^{\mathcal{E}}}{\partial \,\mathrm{d}\,\boldsymbol{\Theta}} - \Delta \boldsymbol{x}_{\mathrm{at},n}^{\mathcal{E}} \frac{\partial r_n}{\partial \,\mathrm{d}\,\boldsymbol{\Theta}}}{r_n^2}\end{aligned} \tag{A.17g}$$

Jacobian of the target component of the radial velocity:

$$\frac{\partial v_{\mathrm{t,rad},n}}{\partial \boldsymbol{\Theta}} = \frac{\partial \hat{v}_{\mathrm{rad}}}{\partial \,\mathrm{d}\,\boldsymbol{\Theta}} + \left[\boldsymbol{u}_{\mathrm{at},n}^{\mathcal{E}}\right]^{\mathrm{T}} \frac{\partial \boldsymbol{v}_{\mathrm{ant}}^{\mathcal{E}}}{\partial \boldsymbol{\Theta}} + \left[\boldsymbol{v}_{\mathrm{ant}}^{\mathcal{E}}\right]^T \frac{\partial \boldsymbol{u}_{\mathrm{at},n}^{\mathcal{E}}}{\partial \boldsymbol{\Theta}} \tag{A.17h}$$

Jacobian of the scalar product of the direction vector and the normal vector of the surface plane:

$$\frac{\partial \rho_{\mathrm{pl,at},n}}{\partial \boldsymbol{\Theta}} = \left[\boldsymbol{n}_{\mathrm{plane}}^{\mathcal{E}}\right]^T \frac{\partial \boldsymbol{u}_{\mathrm{at},n}^{\mathcal{E}}}{\partial \boldsymbol{\Theta}} + \left[\boldsymbol{u}_{\mathrm{at},n}^{\mathcal{E}}\right]^T \frac{\partial \boldsymbol{n}_{\mathrm{plane}}^{\mathcal{E}}}{\partial \boldsymbol{\Theta}} \tag{A.17i}$$

Jacobian of the projection of the direction vector onto the surface plane:

$$\begin{aligned}\frac{\partial \tilde{\boldsymbol{u}}_{\mathrm{at,p},n}^{\mathcal{E}}}{\partial \boldsymbol{\Theta}} =& \frac{\partial \boldsymbol{u}_{\mathrm{at},n}^{\mathcal{E}}}{\partial \boldsymbol{\Theta}} - \boldsymbol{n}_{\mathrm{plane}}^{\mathcal{E}} \frac{\partial \rho_{\mathrm{pl,at},n}}{\partial \boldsymbol{\Theta}} \\ &- \rho_{\mathrm{pl,at},n} \frac{\partial \boldsymbol{n}_{\mathrm{plane}}^{\mathcal{E}}}{\partial \boldsymbol{\Theta}}\end{aligned} \tag{A.17j}$$

Jacobian of the norm of the projection of the direction vector onto the surface plane:

$$\frac{\partial \|\tilde{\boldsymbol{u}}_{\mathrm{at,p},n}^{\mathcal{E}}\|}{\partial \boldsymbol{\Theta}} = \frac{\left[\tilde{\boldsymbol{u}}_{\mathrm{at,p},n}^{\mathcal{E}}\right]^T \frac{\partial \tilde{\boldsymbol{u}}_{\mathrm{at,p},n}^{\mathcal{E}}}{\partial \boldsymbol{\Theta}}}{\|\tilde{\boldsymbol{u}}_{\mathrm{at,p},n}^{\mathcal{E}}\|} \tag{A.17k}$$

Finally, the Jacobian of the scalar magnitude of the measurable target velocity component:

$$\frac{\partial v_{\mathrm{t,pl},n}}{\partial \boldsymbol{\Theta}} = \frac{\frac{\partial v_{\mathrm{t,rad},n}}{\partial \boldsymbol{\Theta}} \|\tilde{\boldsymbol{u}}_{\mathrm{at,p},n}^{\mathcal{E}}\| - v_{\mathrm{t,rad},n} \frac{\partial \|\tilde{\boldsymbol{u}}_{\mathrm{at,p},n}^{\mathcal{E}}\|}{\partial \boldsymbol{\Theta}}}{\|\tilde{\boldsymbol{u}}_{\mathrm{at,p},n}^{\mathcal{E}}\|^2} \tag{A.17l}$$

### A.2.3. Determine a unique solution for the surface velocity component: $\boldsymbol{f}^{\mathrm{v}\leftarrow\mathrm{urv}}$

As there are two solutions for the geolocation of a target, there are also two solutions for the magnitude of the measurable target velocity component. This function returns the velocity solution which corresponds to the unique solution of Section A.1.4.

**Notation**

$$v_{\mathrm{t,pl}} = \boldsymbol{f}^{\mathrm{v}\leftarrow\mathrm{urv}}\left(u_{\mathrm{dc}}, r, v_{\mathrm{rad}}, \boldsymbol{x}^{\mathcal{E}}_{\mathrm{ant}}, \boldsymbol{v}^{\mathcal{E}}_{\mathrm{ant}}, \boldsymbol{\gamma}^{\mathcal{A}\leftarrow\mathcal{E}}_{\mathrm{yp}}, \boldsymbol{n}^{\mathcal{E}}_{\mathrm{plane}}, d^{\mathcal{E}}_{\mathrm{plane}}\right) \tag{A.18a}$$

**Implementation** Compute both solutions for the velocity component

$$v_{\mathrm{t,pl},n} = \boldsymbol{f}^{\mathrm{v}\leftarrow\mathrm{urv}}_{n}\left(u_{\mathrm{dc}}, r, v_{\mathrm{rad}}, \boldsymbol{x}^{\mathcal{E}}_{\mathrm{ant}}, \boldsymbol{v}^{\mathcal{E}}_{\mathrm{ant}}, \boldsymbol{\gamma}^{\mathcal{A}\leftarrow\mathcal{E}}_{\mathrm{yp}}, \boldsymbol{n}^{\mathcal{E}}_{\mathrm{plane}}, d^{\mathcal{E}}_{\mathrm{plane}}\right) \tag{A.18b}$$

Compute both solutions for the geolocated target position

$$\boldsymbol{x}^{\mathcal{E}}_{\mathrm{grd},n} = \boldsymbol{f}^{\mathcal{E}\leftarrow\mathrm{ur}}_{\mathrm{rc},n}\left(u_{\mathrm{dc}}, r, \boldsymbol{x}^{\mathcal{E}}_{\mathrm{ant}}, \boldsymbol{\gamma}^{\mathcal{A}\leftarrow\mathcal{E}}_{\mathrm{yp}}, \boldsymbol{n}^{\mathcal{E}}_{\mathrm{plane}}, d^{\mathcal{E}}_{\mathrm{plane}}\right) \tag{A.18c}$$

Determine which solution to choose

$$n_{\mathrm{grd,choice}} = \boldsymbol{f}_{\mathrm{grd,choice}}(\boldsymbol{x}^{\mathcal{E}}_{\mathrm{grd},1}, \boldsymbol{x}^{\mathcal{E}}_{\mathrm{grd},2}, \boldsymbol{\vartheta}) \tag{A.18d}$$

Chosen ground location

$$v_{\mathrm{t,pl}} = v_{\mathrm{t,pl},n_{\mathrm{grd,choice}}} \tag{A.18e}$$

## A.3. Range, radial velocity and directional cosine of a target

### A.3.1. Function $\boldsymbol{f}^{\mathrm{urv}\leftarrow\mathcal{E}}$

This function determines the directional cosine, range and radial velocity of a target. It accepts the target location and velocity in Cartesian ENU coordinates and the antenna location, velocity and attitude as input parameters.

**Notation**

$$\boldsymbol{z}_{\mathrm{urv}} = \boldsymbol{f}^{\mathrm{urv}\leftarrow\mathcal{E}}\left(\boldsymbol{x}^{\mathcal{E}}, \boldsymbol{v}^{\mathcal{E}}; \boldsymbol{x}^{\mathcal{E}}_{\mathrm{ant}}, \boldsymbol{v}^{\mathcal{E}}_{\mathrm{ant}}, \boldsymbol{\gamma}^{\mathcal{A}\leftarrow\mathcal{E}}_{\mathrm{yp}}\right) \tag{A.19a}$$

**Implementation** Difference between target and antenna location:

$$\Delta\boldsymbol{x}^{\mathcal{E}} = \boldsymbol{x}^{\mathcal{E}} - \boldsymbol{x}^{\mathcal{E}}_{\mathrm{ant}} \tag{A.19b}$$

Range to the target¿

$$r = \|\Delta\boldsymbol{x}^{\mathcal{E}}\| \tag{A.19c}$$

Direction vector in ENU coordinates:

$$\boldsymbol{u}^{\mathcal{E}} = \frac{\Delta \boldsymbol{x}^{\mathcal{E}}}{\|\Delta \boldsymbol{x}^{\mathcal{E}}\|} \tag{A.19d}$$

Orientation of the axis of the antenna:

$$\boldsymbol{e}^{\mathcal{E}} = \begin{bmatrix} \cos(\gamma_{\text{yaw}})\cos(\gamma_{\text{pitch}}) \\ \sin(\gamma_{\text{yaw}})\cos(\gamma_{\text{pitch}}) \\ -\sin(\gamma_{\text{pitch}}) \end{bmatrix} \tag{A.19e}$$

where the angles are given by

$$\boldsymbol{\gamma}_{\text{yp}}^{\mathcal{A}\leftarrow\mathcal{E}} = \begin{bmatrix} \gamma_{\text{yaw}} \\ \gamma_{\text{pitch}} \end{bmatrix}. \tag{A.19f}$$

First component of the direction vector in antenna coordinates:

$$u_1^{\mathcal{A}} = \left[\boldsymbol{e}^{\mathcal{E}}\right]^{\text{T}} \boldsymbol{u}^{\mathcal{E}} \tag{A.19g}$$

Difference of target and platform velocity:

$$\Delta \boldsymbol{v}^{\mathcal{E}} = \boldsymbol{v}^{\mathcal{E}} - \boldsymbol{v}_{\text{ant}}^{\mathcal{E}} \tag{A.19h}$$

Radial velocity of the target :

$$v_{\text{rad}} = \left[\boldsymbol{u}^{\mathcal{E}}\right]^{T} \Delta \boldsymbol{v}^{\mathcal{E}} \tag{A.19i}$$

Arrangement of directional cosine, range and radial velocity to one vector:

$$\boldsymbol{z}_{\text{urv}} = \begin{bmatrix} u_1^{\mathcal{A}} \\ r \\ v_{\text{rad}} \end{bmatrix} \tag{A.19j}$$

## A.3.2. Jacobian of $\boldsymbol{f}^{\text{urv}\leftarrow\mathcal{E}}$

Section A.3.1 presents a function for computing the directional cosine, range and radial velocity of a target. Here, the Jacobian of this function with respect to the vector

$$\boldsymbol{\Psi} = \left[ \left[\boldsymbol{x}_{\text{ant}}^{\mathcal{E}}\right]^{T} \ \left[\boldsymbol{v}_{\text{ant}}^{\mathcal{E}}\right]^{T} \ \left[\boldsymbol{\gamma}_{\text{yp}}^{\mathcal{A}\leftarrow\mathcal{E}}\right]^{T} \ \left[\boldsymbol{x}^{\mathcal{E}}\right]^{T} \ \left[\boldsymbol{v}^{\mathcal{E}}\right]^{T} \right]^{T}. \tag{A.20}$$

### Notation

$$\frac{\partial \boldsymbol{z}_{\text{urv}}}{\partial \boldsymbol{\Psi}} = \boldsymbol{f}_{\text{J}}^{\text{urv}\leftarrow\mathcal{E}}\left(\boldsymbol{x}^{\mathcal{E}}, \boldsymbol{v}^{\mathcal{E}}; \boldsymbol{x}_{\text{ant}}^{\mathcal{E}}, \boldsymbol{v}_{\text{ant}}^{\mathcal{E}}, \boldsymbol{\gamma}_{\text{yp}}^{\mathcal{A}\leftarrow\mathcal{E}}\right) \tag{A.21a}$$

**Implementation** Jacobians of the input variables with respect to the parameter vector:

$$\begin{aligned}
\frac{\partial \boldsymbol{x}_{\text{ant}}^{\mathcal{E}}}{\partial \boldsymbol{\Psi}} &= [\mathbf{I}_{3\times 3}\ \mathbf{0}_{3\times 11}] \\
\frac{\partial \boldsymbol{v}_{\text{ant}}^{\mathcal{E}}}{\partial \boldsymbol{\Psi}} &= [\mathbf{0}_{3\times 3}\ \mathbf{I}_{3\times 3}\ \mathbf{0}_{3\times 8}] \\
\frac{\partial \boldsymbol{\gamma}_{\text{yp}}^{\mathcal{A}\leftarrow\mathcal{E}}}{\partial \boldsymbol{\Psi}} &= [\mathbf{0}_{2\times 6}\ \mathbf{I}_{2\times 2}\ \mathbf{0}_{2\times 6}] \\
\frac{\partial \boldsymbol{x}^{\mathcal{E}}}{\partial \boldsymbol{\Psi}} &= [\mathbf{0}_{3\times 8}\ \mathbf{I}_{3\times 3}\ \mathbf{0}_{3\times 3}] \\
\frac{\partial \boldsymbol{v}^{\mathcal{E}}}{\partial \boldsymbol{\Psi}} &= [\mathbf{0}_{3\times 11}\ \mathbf{I}_{3\times 3}]
\end{aligned} \tag{A.21b}$$

Jacobian of the orientation of the unit vector that describes the orientation of the linear antenna:

$$\frac{\partial \boldsymbol{e}^{\mathcal{E}}}{\partial \boldsymbol{\Psi}} = \left[\mathbf{0}_{3\times 6} \quad \frac{\partial \boldsymbol{e}^{\mathcal{E}}}{\partial \gamma_{\text{yaw}}} \quad \frac{\partial \boldsymbol{e}^{\mathcal{E}}}{\partial \gamma_{\text{pitch}}} \mathbf{0}_{3\times 6}\right]^{\text{T}} \tag{A.21c}$$

where

$$\frac{\partial \boldsymbol{e}^{\mathcal{E}}}{\partial \gamma_{\text{yaw}}} = \begin{bmatrix} -\sin(\gamma_{\text{yaw}})\cos(\gamma_{\text{pitch}}) \\ \cos(\gamma_{\text{yaw}})\cos(\gamma_{\text{pitch}}) \\ 0 \end{bmatrix} \tag{A.21d}$$

and

$$\frac{\partial \boldsymbol{e}^{\mathcal{E}}}{\partial \gamma_{\text{pitch}}} = \begin{bmatrix} -\cos(\gamma_{\text{yaw}})\sin(\gamma_{\text{pitch}}) \\ -\sin(\gamma_{\text{yaw}})\sin(\gamma_{\text{pitch}}) \\ -\cos(\gamma_{\text{pitch}}) \end{bmatrix}. \tag{A.21e}$$

Jacobian of the difference between target and antenna location

$$\frac{\partial \Delta\boldsymbol{x}^{\mathcal{E}}}{\partial \boldsymbol{\Psi}} = \frac{\partial \boldsymbol{x}^{\mathcal{E}}}{\partial \boldsymbol{\Psi}} - \frac{\partial \boldsymbol{x}_{\text{ant}}^{\mathcal{E}}}{\partial \boldsymbol{\Psi}} \tag{A.21f}$$

Jacobian of the range to the target:

$$\frac{\partial r}{\partial \boldsymbol{\Psi}} = \frac{\left[\Delta\boldsymbol{x}^{\mathcal{E}}\right]^{T} \frac{\partial \Delta\boldsymbol{x}^{\mathcal{E}}}{\partial \boldsymbol{\Psi}}}{\|\Delta\boldsymbol{x}^{\mathcal{E}}\|} \tag{A.21g}$$

Jacobian of the direction vector in ENU coordinates:

$$\frac{\partial \boldsymbol{u}^{\mathcal{E}}}{\partial \boldsymbol{\Psi}} = \frac{r\frac{\partial \Delta\boldsymbol{x}^{\mathcal{E}}}{\partial \boldsymbol{\Psi}} - \Delta\boldsymbol{x}^{\mathcal{E}}\frac{\partial r}{\partial \boldsymbol{\Psi}}}{r^2} \tag{A.21h}$$

Jacobian of the first component of the direction vector in antenna coordinates:

$$\frac{\partial u_1^{\mathcal{A}}}{\partial \boldsymbol{\Psi}} = \left[\boldsymbol{e}^{\mathcal{E}}\right]^{\text{T}} \frac{\partial \boldsymbol{u}^{\mathcal{E}}}{\partial \boldsymbol{\Psi}} + \left[\boldsymbol{u}^{\mathcal{E}}\right]^{\text{T}} \frac{\partial \boldsymbol{e}^{\mathcal{E}}}{\partial \boldsymbol{\Psi}} \tag{A.21i}$$

Jacobian of the difference of target and platform velocity:

$$\frac{\partial \Delta \boldsymbol{v}^{\mathcal{E}}}{\partial \boldsymbol{\Psi}} = \frac{\partial \boldsymbol{v}^{\mathcal{E}}}{\partial \boldsymbol{\Psi}} - \frac{\partial \boldsymbol{v}^{\mathcal{E}}_{\mathrm{ant}}}{\partial \boldsymbol{\Psi}} \tag{A.21j}$$

Jacobian of the radial velocity of the target:

$$\frac{\partial v_{\mathrm{rad}}}{\partial \boldsymbol{\Psi}} = \left[\boldsymbol{u}^{\mathcal{E}}\right]^T \frac{\partial \Delta \boldsymbol{v}^{\mathcal{E}}}{\partial \boldsymbol{\Psi}} + \left[\Delta \boldsymbol{v}^{\mathcal{E}}\right]^T \frac{\partial \boldsymbol{u}^{\mathcal{E}}}{\partial \boldsymbol{\Psi}} \tag{A.21k}$$

Jacobian of the vector of directional cosine, range and radial velocity:

$$\frac{\partial \boldsymbol{z}_{\mathrm{urv}}}{\partial \boldsymbol{\Psi}} = \begin{bmatrix} \frac{\partial u_1^{\mathcal{A}}}{\partial \boldsymbol{\Psi}} \\ \frac{\partial r}{\partial \boldsymbol{\Psi}} \\ \frac{\partial v_{\mathrm{rad}}}{\partial \boldsymbol{\Psi}} \end{bmatrix} \tag{A.21l}$$

## A.4. Clutter Doppler frequency versus range and directional cosine

This function computes the Doppler frequency that corresponds to a pair of a range and a directional cosine value for *clutter* returns.

### Notation

$$f_n = f_n^{\mathrm{f}\leftarrow\mathrm{ur}}\left(u, r, \boldsymbol{x}^{\mathcal{E}}_{\mathrm{ant}}, \boldsymbol{\gamma}_{\mathrm{yp}}^{\mathcal{A}\leftarrow\mathcal{E}}, \boldsymbol{n}^{\mathcal{E}}_{\mathrm{plane}}, d^{\mathcal{E}}_{\mathrm{plane}}; \lambda_0\right) \tag{A.22a}$$

**Implementation** Compute the location of the clutter return in ENU coordinates

$$\boldsymbol{x}^{\mathcal{E}}_{\mathrm{grd},n} = \boldsymbol{f}_{\mathrm{rc},n}^{\mathcal{E}\leftarrow\mathrm{ur}}\left(u, r, \boldsymbol{x}^{\mathcal{E}}_{\mathrm{ant}}, \boldsymbol{\gamma}_{\mathrm{yp}}^{\mathcal{A}\leftarrow\mathcal{E}}, \boldsymbol{n}^{\mathcal{E}}_{\mathrm{plane}}, d^{\mathcal{E}}_{\mathrm{plane}}\right) \tag{A.22b}$$

Compute the measruement vaiables

$$\boldsymbol{z}_{\mathrm{urv},n} = \begin{bmatrix} u_n \\ r_n \\ v_{\mathrm{rad},n} \end{bmatrix} = \boldsymbol{f}^{\mathrm{urv}\leftarrow\mathcal{E}}\left(\boldsymbol{x}^{\mathcal{E}}_{\mathrm{grd},n}, \boldsymbol{v}^{\mathcal{E}}; \boldsymbol{x}^{\mathcal{E}}_{\mathrm{ant}}, \boldsymbol{v}^{\mathcal{E}}_{\mathrm{ant}}, \boldsymbol{\gamma}_{\mathrm{yp}}^{\mathcal{A}\leftarrow\mathcal{E}}\right) \tag{A.22c}$$

Convert the radial velocity measurement to the Doppler frequency

$$f_n = -\frac{2 v_{\mathrm{rad},n}}{\lambda_0} \tag{A.22d}$$

## A.5. Functions that are used by the tracking algorithm

### A.5.1. Radar measurement to track measurement conversion: $\boldsymbol{f}^{\mathcal{M}\leftarrow\mathbf{urv}}$

This function converts the measurement vector that is determined by the radar system to the measurement vector that is accepted by the tracking algorithm of this thesis.

#### Notation

$$\boldsymbol{z} = \boldsymbol{f}^{\mathcal{M}\leftarrow\mathrm{urv}}\left(u, r, v_{\mathrm{rad}}, \boldsymbol{x}^{\mathcal{E}}_{\mathrm{ant}}, \boldsymbol{v}^{\mathcal{E}}_{\mathrm{ant}}, \boldsymbol{\gamma}^{\mathcal{A}\leftarrow\mathcal{E}}_{\mathrm{yp}}, \boldsymbol{n}^{\mathcal{E}}_{\mathrm{plane}}, d^{\mathcal{E}}_{\mathrm{plane}}\right) \tag{A.23a}$$

**Implementation** Target location on the tracking plane:

$$\boldsymbol{x}^{\mathcal{P}2}_{\mathrm{tgt}} = \boldsymbol{f}^{\mathcal{P}2\leftarrow\mathrm{ur}}\left(u, r, v_{\mathrm{rad}}, \boldsymbol{x}^{\mathcal{E}}_{\mathrm{ant}}, \boldsymbol{\gamma}^{\mathcal{A}\leftarrow\mathcal{E}}_{\mathrm{yp}}, \boldsymbol{n}^{\mathcal{E}}_{\mathrm{plane}}, d^{\mathcal{E}}_{\mathrm{plane}}\right) \tag{A.23b}$$

Scalar magnitude of the measurable target velocity surface component:

$$v_{\mathrm{t,pl}} = \boldsymbol{f}^{\mathrm{v}\leftarrow\mathrm{urv}}\left(u, r, v_{\mathrm{rad}}, \boldsymbol{x}^{\mathcal{E}}_{\mathrm{ant}}, \boldsymbol{v}^{\mathcal{E}}_{\mathrm{ant}}, \boldsymbol{\gamma}^{\mathcal{A}\leftarrow\mathcal{E}}_{\mathrm{yp}}, \boldsymbol{n}^{\mathcal{E}}_{\mathrm{plane}}, d^{\mathcal{E}}_{\mathrm{plane}}\right) \tag{A.23c}$$

Arrangement of both variables to the track measurement vector:

$$\boldsymbol{z} = \begin{bmatrix} \boldsymbol{x}^{\mathcal{P}2} \\ v_{\mathrm{t,pl}} \end{bmatrix} \tag{A.23d}$$

### A.5.2. Definition of the measurement function: $\boldsymbol{h}_k$

In nonlinear target tracking the equation

$$\boldsymbol{z} = \boldsymbol{h}_k(\boldsymbol{x}^{\mathcal{S}}, \boldsymbol{\epsilon}) \tag{A.24}$$

describes how the target state $\boldsymbol{x}^{\mathcal{S}}$ and measurement noise $\boldsymbol{\epsilon}$ are related to a measurement $\boldsymbol{z}$. Tracking with an extended Kalman filter like algorithm requires the evaluation of $\boldsymbol{h}_k(\boldsymbol{x}^{\mathcal{S}}, \mathbf{0})$ (see equation 4.24) and the Jacobian matrices $\frac{\partial \boldsymbol{h}_k}{\partial \boldsymbol{x}}(\boldsymbol{x}, \mathbf{0})$ and $\frac{\partial \boldsymbol{h}_k}{\partial \boldsymbol{\epsilon}}(\boldsymbol{x}, \boldsymbol{\epsilon})$ (see equation (4.30)). In the following, the definition of $\boldsymbol{h}_k$ is provided for the ground moving target tracking algorithm of this thesis.

In this specific application, $\boldsymbol{h}_k$ is significantly more simple for a zero noise vector than for an arbitrary noise vector. Thus, two different definitions are provided: One for $\boldsymbol{\epsilon} = \mathbf{0}$ and one for arbitrary $\boldsymbol{\epsilon}$. The definition for a zero noise vector is later used for computing the Jacobian with respect to the track state.

The definition basically consists only of a call to one of the functions $\boldsymbol{f}_0^{\mathcal{M}\leftarrow\mathcal{S}}$ or $\boldsymbol{f}_{\epsilon}^{\mathcal{M}\leftarrow\mathcal{S}}$. This is to make the dependency of $\boldsymbol{h}_k$ on time step dependent antenna parameters explicit.

#### Notation

$$\boldsymbol{z} = \boldsymbol{h}_k(\boldsymbol{x}^{\mathcal{S}}, \boldsymbol{\epsilon}) \tag{A.25a}$$

**Implementation** If the noise term is a vector of zeros:

$$\boldsymbol{h}_k(\boldsymbol{x}^{\mathcal{S}}, \boldsymbol{0}) = \boldsymbol{f}_0^{\mathcal{M}\leftarrow\mathcal{S}}\left(\boldsymbol{x}^{\mathcal{S}}; \hat{\boldsymbol{x}}^{\mathcal{E}}_{\mathrm{ant},k}, \hat{\boldsymbol{v}}^{\mathcal{E}}_{\mathrm{ant},k}, \hat{\boldsymbol{\gamma}}^{\mathcal{A}\leftarrow\mathcal{E}}_{\mathrm{yp},k}\right) \tag{A.25b}$$

else:

$$\boldsymbol{h}_k(\boldsymbol{x}^{\mathcal{S}}, \boldsymbol{\epsilon}) = \boldsymbol{f}_\epsilon^{\mathcal{M}\leftarrow\mathcal{S}}\left(\boldsymbol{x}^{\mathcal{S}}; \hat{\boldsymbol{x}}^{\mathcal{E}}_{\mathrm{ant},k}, \hat{\boldsymbol{v}}^{\mathcal{E}}_{\mathrm{ant},k}, \hat{\boldsymbol{\gamma}}^{\mathcal{A}\leftarrow\mathcal{E}}_{\mathrm{yp},k}, \boldsymbol{\epsilon}\right) \tag{A.25c}$$

### A.5.3. Track measurement based on target state including measurement errors: $\boldsymbol{f}_\epsilon^{\mathcal{M}\leftarrow\mathcal{S}}$

This function computes the track measurement based on the target state. It is required for computing the Jacobian of $\boldsymbol{h}_k$ with respect to the measurement vector. This Jacobian is employed in extended Kalman filter like tracking algorithms.

In order to include radar measurements, the computation is performed in two step. In the first step, the track state is converted to radar measurements. In the second step, the radar measurements are converted to the track measurement. In this second step, measurement errors are added to the input variables.

**Notation**

$$\boldsymbol{z} = \boldsymbol{f}_\epsilon^{\mathcal{M}\leftarrow\mathcal{S}}\left(\boldsymbol{x}^{\mathcal{S}}; \boldsymbol{x}^{\mathcal{E}}_{\mathrm{ant}}, \boldsymbol{v}^{\mathcal{E}}_{\mathrm{ant}}, \boldsymbol{\gamma}^{\mathcal{A}\leftarrow\mathcal{E}}_{\mathrm{yp}}, \boldsymbol{\epsilon}\right) \tag{A.26a}$$

**Implementation** Partitioning of the error terms:

$$\boldsymbol{\epsilon} = [\epsilon_u\ \epsilon_r\ \epsilon_v\ \boldsymbol{\epsilon}^{\mathcal{E}}_{p,\mathrm{ant}}\ \boldsymbol{\epsilon}^{\mathcal{E}}_{v,\mathrm{ant}}\ \boldsymbol{\epsilon}^{\mathcal{A}\leftarrow\mathcal{E}}_{\mathrm{yp}}]^{\mathrm{T}} \tag{A.26b}$$

Computation of the radar measurement variables (see Sec. A.5.10):

$$\boldsymbol{z}_{\mathrm{urv}} = \boldsymbol{f}^{\mathrm{urv}\leftarrow\mathcal{S}}\left(\boldsymbol{x}^{\mathcal{E}}, \boldsymbol{v}^{\mathcal{E}}; \boldsymbol{x}^{\mathcal{E}}_{\mathrm{ant}}, \boldsymbol{v}^{\mathcal{E}}_{\mathrm{ant}}, \boldsymbol{\gamma}^{\mathcal{A}\leftarrow\mathcal{E}}_{\mathrm{yp}}\right) \tag{A.26c}$$

Computation of the track measuremnt variables, including additional error terms (see A.5.1):

$$\begin{aligned}\boldsymbol{z} = \boldsymbol{f}^{\mathcal{M}\leftarrow\mathrm{urv}}\big(&u + \epsilon_u, r + \epsilon_r, v_{\mathrm{rad}} + \epsilon_v, \boldsymbol{x}^{\mathcal{E}}_{\mathrm{ant}} + \boldsymbol{\epsilon}^{\mathcal{E}}_{\mathrm{p,ant}},\\ &\boldsymbol{v}^{\mathcal{E}}_{\mathrm{ant}} + \boldsymbol{\epsilon}^{\mathcal{E}}_{\mathrm{v,ant}}, \boldsymbol{\gamma}^{\mathcal{A}\leftarrow\mathcal{E}}_{\mathrm{yp}} + \boldsymbol{\epsilon}_{\mathrm{yp,ant}}, \boldsymbol{n}^{\mathcal{E}}_{\mathrm{plane}}, d^{\mathcal{E}}_{\mathrm{plane}}\big)\end{aligned} \tag{A.26d}$$

### A.5.4. Track measurement based on the track state without effect of measurement noise: $\boldsymbol{f}_0^{\mathcal{M}\leftarrow\mathcal{S}}$

This function computes the track measurement based on the track state. Unlike the function $\boldsymbol{f}_\epsilon^{\mathcal{M}\leftarrow\mathcal{S}}$ it does not account for measurement error. It is used by the function $\boldsymbol{h}_k$ if there is no measurement error. Hence, it is employed in the tracking algorithm for computing the predicted measurement and for determining the Jacobian of the measurement function with respect to the track state.

**Notation**

$$\boldsymbol{z} = \boldsymbol{f}_0^{\mathcal{M}\leftarrow\mathcal{S}}\left(\boldsymbol{x}^{\mathcal{S}}; \boldsymbol{x}_{\text{ant}}^{\mathcal{E}}, \boldsymbol{v}_{\text{ant}}^{\mathcal{E}}, \boldsymbol{\gamma}_{\text{yp}}^{\mathcal{A}\leftarrow\mathcal{E}}\right) \tag{A.27a}$$

**Implementation** Partitioning of the track state vector:

$$\boldsymbol{x}^{\mathcal{S}} = \begin{bmatrix} \boldsymbol{x}^{\mathcal{P}2} \\ \boldsymbol{v}^{\mathcal{P}2} \end{bmatrix} \tag{A.27b}$$

Cartesian ENU target position (see Sec. A.5.5):

$$\boldsymbol{x}^{\mathcal{E}} = \boldsymbol{f}_{\text{p}}^{3\leftarrow2}\left(\boldsymbol{x}^{\mathcal{P}2}; \boldsymbol{x}_{\mathcal{P}3,\text{origin}}^{\mathcal{E}}, \boldsymbol{\gamma}^{\mathcal{E}\leftarrow\mathcal{P}3}\right) \tag{A.27c}$$

Cartesian ENU target velocity (see Sec. A.5.6):

$$\boldsymbol{v}^{\mathcal{E}} = \boldsymbol{f}_{\text{v}}^{3\leftarrow2}\left(\boldsymbol{v}^{\mathcal{P}2}; \boldsymbol{\gamma}^{\mathcal{E}\leftarrow\mathcal{P}3}\right) \tag{A.27d}$$

Matrix that projects on the tracking plane:

$$\mathbf{P}_{\text{plane}}^{\mathcal{E}} = \mathbf{I} - \boldsymbol{n}_{\text{plane}}^{\mathcal{E}}\left[\boldsymbol{n}_{\text{plane}}^{\mathcal{E}}\right]^T \tag{A.27e}$$

Difference vector between platform and ground position:

$$\Delta\boldsymbol{x}_{\text{at}}^{\mathcal{E}} = \boldsymbol{x}^{\mathcal{E}} - \boldsymbol{x}_{\text{ant}}^{\mathcal{E}} \tag{A.27f}$$

Projection of the difference vector onto the tracking plane:

$$\Delta\boldsymbol{x}_{\text{at,p}}^{\mathcal{E}} = \mathbf{P}_{\text{plane}}^{\mathcal{E}}\Delta\boldsymbol{x}_{\text{at}}^{\mathcal{E}} = \Delta\boldsymbol{x}_{\text{at}}^{\mathcal{E}} - \left[\boldsymbol{n}_{\text{plane}}^{\mathcal{E}}\right]^T\Delta\boldsymbol{x}_{\text{at}}^{\mathcal{E}}\boldsymbol{n}_{\text{plane}}^{\mathcal{E}} \tag{A.27g}$$

$$= \Delta\boldsymbol{x}_{\text{at}}^{\mathcal{E}} - \tilde{\rho}_{\text{pl,at}}\boldsymbol{n}_{\text{plane}}^{\mathcal{E}} \tag{A.27h}$$

Normalized projection of the direction vector onto the plane:

$$\boldsymbol{u}_{\text{at,p}}^{\mathcal{E}} = \frac{\mathbf{P}_{\text{plane}}^{\mathcal{E}}\Delta\boldsymbol{x}_{\text{at}}^{\mathcal{E}}}{\|\mathbf{P}_{\text{plane}}^{\mathcal{E}}\Delta\boldsymbol{x}_{\text{at}}^{\mathcal{E}}\|} = \frac{\Delta\boldsymbol{x}_{\text{at,p}}^{\mathcal{E}}}{\|\Delta\boldsymbol{x}_{\text{at,p}}^{\mathcal{E}}\|} \tag{A.27i}$$

Measurable velocity component:

$$v_{\text{t,pl}} = \left[\boldsymbol{u}_{\text{at,p}}^{\mathcal{E}}\right]^T\boldsymbol{v}^{\mathcal{E}} \tag{A.27j}$$

Arrange computed values into measurement vector:

$$\boldsymbol{z} = \begin{bmatrix} x_1^{\mathcal{S}} \\ x_2^{\mathcal{S}} \\ v_{\text{t,pl}} \end{bmatrix} \tag{A.27k}$$

## A.5.5. Conversion of a location from 2 to 3 dimensions: $\boldsymbol{f}_{\text{p}}^{3\leftarrow2}$

**Notation**

$$\boldsymbol{x}^{\mathcal{E}} = \boldsymbol{f}_{\text{p}}^{3\leftarrow2}\left(\boldsymbol{x}^{\mathcal{P}2}; \boldsymbol{x}_{\mathcal{P}3,\text{origin}}^{\mathcal{E}}, \boldsymbol{\gamma}^{\mathcal{E}\leftarrow\mathcal{P}3}\right) \tag{A.28a}$$

**Implementation**

$$\mathbf{T}^{\mathcal{E}\leftarrow\mathcal{P}3} = \mathbf{T}_{\text{Euler}}\left(\boldsymbol{\gamma}^{\mathcal{E}\leftarrow\mathcal{P}3}\right) \tag{A.28b}$$

$$\mathbf{T}^{D3\leftarrow D2} = \begin{bmatrix} 1 & 0 \\ 0 & 1 \\ 0 & 0 \end{bmatrix} \tag{A.28c}$$

$$\boldsymbol{x}^{\mathcal{E}} = \boldsymbol{x}^{\mathcal{E}}_{\mathcal{P}3,\text{origin}} + \mathbf{T}^{\mathcal{E}\leftarrow\mathcal{P}3}\ \mathbf{T}^{D3\leftarrow D2}\ \boldsymbol{x}^{\mathcal{P}2} \tag{A.28d}$$

## A.5.6. Conversion of a velocity vector from 2 to 3 dimensions: $\boldsymbol{f}_{\mathsf{v}}^{3\leftarrow 2}$

**Notation**

$$\boldsymbol{v}^{\mathcal{E}} = \boldsymbol{f}_{\text{v}}^{3\leftarrow 2}\left(\boldsymbol{v}^{\mathcal{P}2}; \boldsymbol{\gamma}^{\mathcal{E}\leftarrow\mathcal{P}3}\right) \tag{A.29a}$$

**Implementation**

$$\mathbf{T}^{\mathcal{E}\leftarrow\mathcal{P}3} = \mathbf{T}_{\text{Euler}}\left(\boldsymbol{\gamma}^{\mathcal{E}\leftarrow\mathcal{P}3}\right) \tag{A.29b}$$

$$\mathbf{T}^{D3\leftarrow D2} = \begin{bmatrix} 1 & 0 \\ 0 & 1 \\ 0 & 0 \end{bmatrix} \tag{A.29c}$$

Velocity in ENU coordinates

$$\boldsymbol{v}^{\mathcal{E}} = \mathbf{T}^{\mathcal{E}\leftarrow\mathcal{P}3}\ \mathbf{T}^{D3\leftarrow D2}\ \boldsymbol{v}^{\mathcal{P}2} \tag{A.29d}$$

## A.5.7. Conversion of a 3d location to 2 dimensions: $\boldsymbol{f}^{2\leftarrow 3}$

**Notation**

$$\boldsymbol{x}^{\mathcal{P}2} = \boldsymbol{f}^{2\leftarrow 3}\left(\boldsymbol{x}^{\mathcal{E}}; \boldsymbol{x}^{\mathcal{E}}_{\mathcal{P},\text{origin}}, \boldsymbol{\gamma}^{\mathcal{E}\leftarrow\mathcal{P}3}\right) \tag{A.30a}$$

**Implementation**

$$\mathbf{T}^{\mathcal{P}3\leftarrow\mathcal{E}} = \mathbf{T}^{\text{inv}}_{\text{Euler}}\left(\boldsymbol{\gamma}^{\mathcal{E}\leftarrow\mathcal{P}3}\right) \tag{A.30b}$$

$$\mathbf{T}^{D2\leftarrow D3} = \begin{bmatrix} 1 & 0 & 0 \\ 0 & 1 & 0 \end{bmatrix} \tag{A.30c}$$

$$\boldsymbol{x}^{\mathcal{P}2} = \mathbf{T}^{D2\leftarrow D3}\mathbf{T}^{\mathcal{P}3\leftarrow\mathcal{E}}\left(\boldsymbol{x}^{\mathcal{E}} - \boldsymbol{x}^{\mathcal{E}}_{\mathcal{P},\text{origin}}\right) \tag{A.30d}$$

### A.5.8. Conversion of a 3d velocity vector to 2 dimensions $\boldsymbol{f}^{\mathcal{P}2\leftarrow\mathcal{E}}$

**Notation**

$$\boldsymbol{v}^{\mathcal{P}2} = \boldsymbol{f}^{\mathcal{P}2\leftarrow\mathcal{E}}\left(\boldsymbol{v}^{\mathcal{E}}; \boldsymbol{\gamma}^{\mathcal{E}\leftarrow\mathcal{P}3}\right) \tag{A.31a}$$

**Implementation**

$$\mathbf{T}^{\mathcal{P}3\leftarrow\mathcal{E}} = \mathbf{T}^{\text{inv}}_{\text{Euler}}\left(\boldsymbol{\gamma}^{\mathcal{E}\leftarrow\mathcal{P}3}\right) \tag{A.31b}$$

$$\mathbf{T}^{D2\leftarrow D3} = \begin{bmatrix} 1 & 0 & 0 \\ 0 & 1 & 0 \end{bmatrix} \tag{A.31c}$$

$$\boldsymbol{v}^{\mathcal{P}2} = \mathbf{T}^{D2\leftarrow D3}\mathbf{T}^{\mathcal{P}3\leftarrow\mathcal{E}}\boldsymbol{v}^{\mathcal{E}} \tag{A.31d}$$

### A.5.9. Locate a target in the tracking plane based on range and DOA measurement

**Notation**

$$\boldsymbol{x}^{\mathcal{P}2}_{\text{tgt}} = \boldsymbol{f}^{\mathcal{P}2\leftarrow\text{ur}}\left(u, r, \boldsymbol{x}^{\mathcal{E}}_{\text{ant}}, \boldsymbol{\gamma}^{\mathcal{A}\leftarrow\mathcal{E}}_{\text{yp}}, \boldsymbol{n}^{\mathcal{E}}_{\text{plane}}, d^{\mathcal{E}}_{\text{plane}}\right) \tag{A.32a}$$

**Implementation** Compute the 3d geolocation (see Section A.1.4)

$$\boldsymbol{x}^{\mathcal{E}}_{\text{tgt}} = \boldsymbol{f}^{\mathcal{E}\leftarrow\text{ur}}\left(u_{\text{dc}}, r, \boldsymbol{x}^{\mathcal{E}}_{\text{ant}}, \boldsymbol{\gamma}^{\mathcal{A}\leftarrow\mathcal{E}}_{\text{yp}}, \boldsymbol{n}^{\mathcal{E}}_{\text{plane}}, d^{\mathcal{E}}_{\text{plane}}\right) \tag{A.32b}$$

Convert this geolocated position to the tracking plane

$$\boldsymbol{x}^{\mathcal{P}2}_{\text{tgt}} = \boldsymbol{f}^{\mathcal{P}2\leftarrow\mathcal{E}}\left(\boldsymbol{x}^{\mathcal{E}}_{\text{tgt}}; \boldsymbol{x}^{\mathcal{E}}_{\mathcal{P},\text{origin}}, \boldsymbol{\gamma}^{\mathcal{E}\leftarrow\mathcal{P}3}\right) \tag{A.32c}$$

### A.5.10. Radar measurements based on track state: $\boldsymbol{f}^{\text{urv}\leftarrow\mathcal{S}}$

This function determines the radar measurement vector that is associated with the given track state vector.

**Notation**

$$\boldsymbol{z}_{\text{urv}} = \boldsymbol{f}^{\text{urv}\leftarrow\mathcal{S}}\left(\boldsymbol{x}^{\mathcal{S}}, \boldsymbol{x}^{\mathcal{E}}_{\text{ant}}, \boldsymbol{v}^{\mathcal{E}}_{\text{ant}}, \boldsymbol{\gamma}^{\mathcal{A}\leftarrow\mathcal{E}}_{\text{yp}}\right) \tag{A.33a}$$

**Implementation** Partitioning of the track state:

$$\boldsymbol{x}^{\mathcal{S}} = \begin{bmatrix} \boldsymbol{x}^{\mathcal{P}2} \\ \boldsymbol{v}^{\mathcal{P}2} \end{bmatrix} \tag{A.33b}$$

Cartesian ENU location:

$$\boldsymbol{x}^{\mathcal{E}} = \boldsymbol{f}_{\mathrm{p}}^{3\leftarrow 2}\left(\boldsymbol{x}^{\mathcal{P}2}; \boldsymbol{x}_{\mathcal{P}3,\mathrm{origin}}^{\mathcal{E}}, \boldsymbol{\gamma}^{\mathcal{E}\leftarrow\mathcal{P}3}\right) \tag{A.33c}$$

Cartesian ENU velocity vector:

$$\boldsymbol{v}^{\mathcal{E}} = \boldsymbol{f}_{\mathrm{v}}^{3\leftarrow 2}\left(\boldsymbol{v}^{\mathcal{P}2}; \boldsymbol{\gamma}^{\mathcal{E}\leftarrow\mathcal{P}3}\right) \tag{A.33d}$$

Radar measurement vector:

$$\boldsymbol{z}_{\mathrm{urv}} = \boldsymbol{f}^{\mathrm{urv}\leftarrow\mathcal{E}}\left(\boldsymbol{x}^{\mathcal{E}}, \boldsymbol{v}^{\mathcal{E}}; \boldsymbol{x}_{\mathrm{ant}}^{\mathcal{E}}, \boldsymbol{v}_{\mathrm{ant}}^{\mathcal{E}}, \boldsymbol{\gamma}_{\mathrm{yp}}^{\mathcal{A}\leftarrow\mathcal{E}}\right) \tag{A.33e}$$

### A.5.11. Radar measurement based on track measurement: $\boldsymbol{f}^{\mathrm{urv}\leftarrow\mathcal{M}}$

This function determines the radar measurement vector based on the track measurement vector.

#### Notation

$$\boldsymbol{z}_{\mathrm{urv}} = \boldsymbol{f}^{\mathrm{urv}\leftarrow\mathcal{M}}\left(\boldsymbol{z}, \boldsymbol{x}_{\mathrm{ant}}^{\mathcal{E}}, \boldsymbol{v}_{\mathrm{ant}}^{\mathcal{E}}, \boldsymbol{\gamma}_{\mathrm{yp}}^{\mathcal{A}\leftarrow\mathcal{E}}\right) \tag{A.34a}$$

**Implementation** Partitioning of the track measurement:

$$\boldsymbol{z} = \begin{bmatrix} \boldsymbol{x}^{\mathcal{P}2} \\ v_{\mathrm{t,pl}} \end{bmatrix} \tag{A.34b}$$

Cartesian ENU location:

$$\boldsymbol{x}^{\mathcal{E}} = \boldsymbol{f}_{\mathrm{p}}^{3\leftarrow 2}\left(\boldsymbol{x}^{\mathcal{P}2}; \boldsymbol{x}_{\mathcal{P}3,\mathrm{origin}}^{\mathcal{E}}, \boldsymbol{\gamma}^{\mathcal{E}\leftarrow\mathcal{P}3}\right) \tag{A.34c}$$

Difference between target and antenna location:

$$\Delta\boldsymbol{x}^{\mathcal{E}} = \boldsymbol{x}^{\mathcal{E}} - \boldsymbol{x}_{\mathrm{ant}}^{\mathcal{E}} \tag{A.34d}$$

Range to the target:

$$r = \|\Delta\boldsymbol{x}^{\mathcal{E}}\| \tag{A.34e}$$

Direction vector in ENU coordinates:

$$\boldsymbol{u}^{\mathcal{E}} = \frac{\Delta\boldsymbol{x}^{\mathcal{E}}}{\|\Delta\boldsymbol{x}^{\mathcal{E}}\|} \tag{A.34f}$$

Determine orientation of the x-axis of the antenna coordinate system:

$$\boldsymbol{e}^{\mathcal{E}} = \begin{bmatrix} \cos\left(\gamma_{\mathrm{yaw}}\right)\cos\left(\gamma_{\mathrm{pitch}}\right) \\ \sin\left(\gamma_{\mathrm{yaw}}\right)\cos\left(\gamma_{\mathrm{pitch}}\right) \\ -\sin\left(\gamma_{\mathrm{pitch}}\right) \end{bmatrix} \tag{A.34g}$$

where the angles are given by

$$\boldsymbol{\gamma}_{\mathrm{yp}}^{\mathcal{A}\leftarrow\mathcal{E}} = \begin{bmatrix} \gamma_{\mathrm{yaw}} \\ \gamma_{\mathrm{pitch}} \end{bmatrix}. \tag{A.34h}$$

First component of the direction vector in antenna coordinates:

$$u_1^{\mathcal{A}} = \left[\boldsymbol{e}^{\mathcal{E}}\right]^{\mathrm{T}} \boldsymbol{u}^{\mathcal{E}} \tag{A.34i}$$

Scalar product of the normal vector of the plane and line of sight vector:

$$\rho_{\mathrm{pl,at}} = \left[\boldsymbol{n}_{\mathrm{plane}}^{\mathcal{E}}\right]^{T} \boldsymbol{u}^{\mathcal{E}} \tag{A.34j}$$

Projection of the antenna to target pointing vector onto the plane:

$$\tilde{\boldsymbol{u}}^{\mathcal{E}} = \mathbf{P}_{\mathrm{plane}}^{\mathcal{E}} \boldsymbol{u}^{\mathcal{E}} \tag{A.34k}$$

$$= \boldsymbol{u}^{\mathcal{E}} - \rho_{\mathrm{pl,at}} \boldsymbol{n}_{\mathrm{plane}}^{\mathcal{E}} \tag{A.34l}$$

Target component of the radial velocity:

$$v_{\mathrm{t,rad}} = v_{\mathrm{t,pl}} \|\tilde{\boldsymbol{u}}^{\mathcal{E}}\| \tag{A.34m}$$

Radial velocity including antenna component:

$$v_{\mathrm{rad}} = v_{\mathrm{t,rad}} - \left[\boldsymbol{u}^{\mathcal{E}}\right]^{\mathrm{T}} \boldsymbol{v}_{\mathrm{ant}}^{\mathcal{E}} \tag{A.34n}$$

Arrangement of all measurements to one vector:

$$\boldsymbol{z}_{\mathrm{urv}} = \begin{bmatrix} u_1^{\mathcal{A}} \\ r \\ v_{\mathrm{rad}} \end{bmatrix} \tag{A.34o}$$

## A.6. Jacobians of functions that are used by the tracking algorithm

### A.6.1. Jacobian of the functions that converts a 3d location to a 2d location

Jacobian of the function (see A.5.7)

$$\boldsymbol{f}^{2\leftarrow 3}\left(\boldsymbol{x}^{\mathcal{E}}; \boldsymbol{x}_{\mathcal{P},\mathrm{origin}}^{\mathcal{E}}, \boldsymbol{\gamma}^{\mathcal{E}\leftarrow\mathcal{P}3}\right) \tag{A.35}$$

#### Notation

$$\frac{\partial \boldsymbol{x}^{\mathcal{P}2}}{\partial \boldsymbol{x}^{\mathcal{E}}} = \mathbf{f}_{\mathrm{J,p}}^{2\leftarrow 3}\left(\boldsymbol{\gamma}^{\mathcal{E}\leftarrow\mathcal{P}3}\right) \tag{A.36a}$$

**Implementation** Compute $\mathbf{T}^{D2\leftarrow D3}$ and $\mathbf{T}^{\mathcal{P}3\leftarrow\mathcal{E}}$ of Section A.5.7

$$\frac{\partial \boldsymbol{x}^{\mathcal{P}2}}{\partial \boldsymbol{x}^{\mathcal{E}}} = \mathbf{T}^{D2\leftarrow D3}\mathbf{T}^{\mathcal{P}3\leftarrow\mathcal{E}} \tag{A.36b}$$

### A.6.2. Jacobian of the function that converts the range Doppler measurement to a location in the tracking plane

Jacobian of the function

$$\boldsymbol{f}^{\mathcal{P}2\leftarrow\mathrm{ur}}\left(u, r, \boldsymbol{x}_{\mathrm{ant}}^{\mathcal{E}}, \boldsymbol{\gamma}_{\mathrm{yp}}^{\mathcal{A}\leftarrow\mathcal{E}}, \boldsymbol{n}_{\mathrm{plane}}^{\mathcal{E}}, d_{\mathrm{plane}}^{\mathcal{E}}\right) \tag{A.37}$$

with respect to the vector $\boldsymbol{\Phi}$ which is defined in Section A.1.2.

#### Notation

$$\frac{\partial \boldsymbol{x}^{\mathcal{P}2}}{\partial \boldsymbol{\Phi}} = \frac{\partial \boldsymbol{f}^{\mathcal{P}2\leftarrow\mathrm{ur}}}{\partial \boldsymbol{\Phi}}\left(u, r, \boldsymbol{x}_{\mathrm{ant}}^{\mathcal{E}}, \boldsymbol{\gamma}_{\mathrm{yp}}^{\mathcal{A}\leftarrow\mathcal{E}}, \boldsymbol{n}_{\mathrm{plane}}^{\mathcal{E}}, d_{\mathrm{plane}}^{\mathcal{E}}\right) \tag{A.38a}$$

**Implementation** Determine the Jacobian of the geolocation in 3 dimensions (see Section A.1.2)

$$\frac{\partial \boldsymbol{x}_{\mathrm{gr}}^{\mathcal{E}}}{\partial \boldsymbol{\Phi}} = \mathbf{f}_{J,\mathrm{rc}}^{\mathcal{E}\leftarrow\mathrm{ur}}\left(u, r, \boldsymbol{x}_{\mathrm{ant}}^{\mathcal{E}}, \boldsymbol{\gamma}_{\mathrm{yp}}^{\mathcal{A}\leftarrow\mathcal{E}}, \boldsymbol{n}_{\mathrm{plane}}^{\mathcal{E}}, d_{\mathrm{plane}}^{\mathcal{E}}\right) \tag{A.38b}$$

Determine the Jacobian of the location in the tracking plane with respect to the 3d location

$$\frac{\partial \boldsymbol{x}^{\mathcal{P}2}}{\partial \boldsymbol{x}^{\mathcal{E}}} = \frac{\partial \boldsymbol{f}^{2\leftarrow 3}}{\partial \boldsymbol{x}^{\mathcal{E}}}\left(\boldsymbol{\gamma}^{\mathcal{E}\leftarrow\mathcal{P}3}\right) \tag{A.38c}$$

Determine the derivative with respect to $\boldsymbol{\Phi}$ with the chain rule

$$\frac{\partial \boldsymbol{x}^{\mathcal{P}2}}{\partial \boldsymbol{\Phi}} = \frac{\partial \boldsymbol{x}^{\mathcal{P}2}}{\partial \boldsymbol{x}^{\mathcal{E}}}\frac{\partial \boldsymbol{x}_{\mathrm{gr}}^{\mathcal{E}}}{\partial \boldsymbol{\Phi}} \tag{A.38d}$$

### A.6.3. Jacobian of the function that converts the radar measurment to the track input measurement

Jacobian of (see Section A.5.1)

$$\boldsymbol{f}^{\mathcal{M}\leftarrow\mathrm{urv}}\left(u, r, v_{\mathrm{rad}}, \boldsymbol{x}_{\mathrm{ant}}^{\mathcal{E}}, \boldsymbol{v}_{\mathrm{ant}}^{\mathcal{E}}, \boldsymbol{\gamma}_{\mathrm{yp}}^{\mathcal{A}\leftarrow\mathcal{E}}, \boldsymbol{n}_{\mathrm{plane}}^{\mathcal{E}}, d_{\mathrm{plane}}^{\mathcal{E}}\right) \tag{A.39}$$

The Jacobian is determined with respect to

$$\boldsymbol{\theta}_{\mathrm{pt}} = \begin{bmatrix} \boldsymbol{\theta} \\ \boldsymbol{z}_{\mathrm{urv}} \end{bmatrix} \tag{A.40}$$

where

$$\begin{aligned}\boldsymbol{\theta} &= \left[\left[\boldsymbol{x}_{\mathrm{ant}}^{\mathcal{E}}\right]^T \ \left[\boldsymbol{v}_{\mathrm{ant}}^{\mathcal{E}}\right]^T \ \left[\boldsymbol{\gamma}^{\mathcal{A}\leftarrow\mathcal{E}}\right]^T\right]^T \\ &= \left[x_{\mathrm{ant},1}^{\mathcal{E}} \ x_{\mathrm{ant},2}^{\mathcal{E}} \ x_{\mathrm{ant},3}^{\mathcal{E}} \ v_{\mathrm{ant},1}^{\mathcal{E}} \ v_{\mathrm{ant},2}^{\mathcal{E}} \ v_{\mathrm{ant},3}^{\mathcal{E}} \ \gamma_{\mathrm{yaw}}^{\mathcal{A}\leftarrow\mathcal{E}} \ \gamma_{\mathrm{pitch}}^{\mathcal{A}\leftarrow\mathcal{E}} \ \gamma_{\mathrm{roll}}^{\mathcal{A}\leftarrow\mathcal{E}}\right]^T\end{aligned}$$

is the antenna location and attitude parameter vector.

**Notation**

$$\frac{\partial \boldsymbol{z}}{\partial \boldsymbol{\theta}_{\mathrm{pt}}} = \mathbf{f}_{J,\theta_{\mathrm{pt}}}^{\mathcal{M}\leftarrow\mathrm{urv}}\left(u, r, v_{\mathrm{rad}}, \boldsymbol{x}_{\mathrm{ant}}^{\mathcal{E}}, \boldsymbol{v}_{\mathrm{ant}}^{\mathcal{E}}, \boldsymbol{\gamma}_{\mathrm{yp}}^{\mathcal{A}\leftarrow\mathcal{E}}, \boldsymbol{n}_{\mathrm{plane}}^{\mathcal{E}}, d_{\mathrm{plane}}^{\mathcal{E}}\right) \tag{A.41a}$$

**Implementation** Compute the derivative of the location of the target in the tracking plane (see Section A.5.9)

$$\frac{\partial \boldsymbol{x}^{\mathcal{P}2}}{\partial \boldsymbol{\Phi}} = \frac{\partial \boldsymbol{f}^{\mathcal{P}2\leftarrow\mathrm{ur}}}{\partial \boldsymbol{\Phi}}\left(u, r, \boldsymbol{x}_{\mathrm{ant}}^{\mathcal{E}}, \boldsymbol{\gamma}_{\mathrm{yp}}^{\mathcal{A}\leftarrow\mathcal{E}}, \boldsymbol{n}_{\mathrm{plane}}^{\mathcal{E}}, d_{\mathrm{plane}}^{\mathcal{E}}\right) \tag{A.41b}$$

Use the chain rule to convert to the derivative with respect to $\boldsymbol{\theta}_{\mathrm{pt}}$

$$\frac{\partial \boldsymbol{x}^{\mathcal{P}2}}{\partial \boldsymbol{\theta}_{\mathrm{pt}}} = \frac{\partial \boldsymbol{x}^{\mathcal{P}2}}{\partial \boldsymbol{\Phi}} \frac{\partial \boldsymbol{\Phi}}{\partial \boldsymbol{\theta}_{\mathrm{pt}}} \tag{A.41c}$$

Determine the Jacobian of the measurable velocity with respect to $\boldsymbol{\Phi}$:

$$\frac{\partial v_{\mathrm{t,pl},n}}{\partial \boldsymbol{\Phi}} = \mathbf{f}_{J,n}^{v\leftarrow\mathrm{urv}}\left(u_{\mathrm{dc}}, r, v_{\mathrm{rad}}, \boldsymbol{x}_{\mathrm{ant}}^{\mathcal{E}}, \boldsymbol{v}_{\mathrm{ant}}^{\mathcal{E}}, \boldsymbol{\gamma}_{\mathrm{yp}}^{\mathcal{A}\leftarrow\mathcal{E}}, \boldsymbol{n}_{\mathrm{plane}}^{\mathcal{E}}, d_{\mathrm{plane}}^{\mathcal{E}}\right) \tag{A.41d}$$

and use the chain rule to convert to a derivative with respect to $\boldsymbol{\theta}_{\mathrm{pt}}$

$$\frac{\partial v_{\mathrm{t,pl},n}}{\partial \boldsymbol{\theta}_{\mathrm{pt}}} = \frac{\partial v_{\mathrm{t,pl},n}}{\partial \boldsymbol{\Phi}} \frac{\partial \boldsymbol{\Phi}}{\partial \boldsymbol{\theta}_{\mathrm{pt}}} \tag{A.41e}$$

Concatanate to one matrix to obtain the Jacobian of the entire track measurement

$$\frac{\partial \boldsymbol{z}}{\partial \boldsymbol{\theta}_{\mathrm{pt}}} = \begin{bmatrix} \frac{\partial \boldsymbol{x}^{\mathcal{P}2}}{\partial \boldsymbol{\theta}_{\mathrm{pt}}} \\ \frac{\partial v_{\mathrm{t,pl},n}}{\partial \boldsymbol{\theta}_{\mathrm{pt}}} \end{bmatrix} \tag{A.41f}$$

### A.6.4. Jacobian of the track measurement with respect to measurement noise

Determine the Jacobian of (see Section A.5.3)

$$\boldsymbol{f}_{\epsilon}^{\mathcal{M}\leftarrow\mathcal{S}}\left(\boldsymbol{x}^{\mathcal{S}}; \boldsymbol{x}_{\mathrm{ant}}^{\mathcal{E}}, \boldsymbol{v}_{\mathrm{ant}}^{\mathcal{E}}, \boldsymbol{\gamma}_{\mathrm{yp}}^{\mathcal{A}\leftarrow\mathcal{E}}, \boldsymbol{\epsilon}\right) \tag{A.42}$$

with respect to the noise term $\boldsymbol{\epsilon}$

**Notation**

$$\frac{\partial \boldsymbol{z}}{\partial \boldsymbol{\epsilon}} = \mathbf{f}_{J,\epsilon}^{\mathcal{M}\leftarrow\mathcal{S}}\left(\boldsymbol{x}^{\mathcal{S}}; \boldsymbol{x}_{\mathrm{ant}}^{\mathcal{E}}, \boldsymbol{v}_{\mathrm{ant}}^{\mathcal{E}}, \boldsymbol{\gamma}_{\mathrm{yp}}^{\mathcal{A}\leftarrow\mathcal{E}}, \boldsymbol{\epsilon}\right) \tag{A.43a}$$

**Implementation** First, determine the synthetic DOA, range and radial velocity measurements (see Section A.5.10)

$$\boldsymbol{z}_{\mathrm{urv}} = \boldsymbol{f}^{\mathrm{urv}\leftarrow\mathcal{S}}\left(\boldsymbol{x}^{\mathcal{E}}, \boldsymbol{v}^{\mathcal{E}}; \boldsymbol{x}_{\mathrm{ant}}^{\mathcal{E}}, \boldsymbol{v}_{\mathrm{ant}}^{\mathcal{E}}, \boldsymbol{\gamma}_{\mathrm{yp}}^{\mathcal{A}\leftarrow\mathcal{E}}\right) \tag{A.43b}$$

Determine the Jacobian of the track measurement when determined with the synthetic radar measurement (see Section A.6.3). The application of the chain rule shows that it is given by

$$\begin{aligned}\frac{\partial \boldsymbol{z}}{\partial \boldsymbol{\epsilon}} = \mathbf{f}_{J,\theta_{\mathrm{pt}}}^{\mathcal{M}\leftarrow\mathrm{urv}} \big(&u+\epsilon_u, r+\epsilon_r, v_{\mathrm{rad}}+\epsilon_v, \boldsymbol{x}_{\mathrm{ant}}^{\mathcal{E}}+\boldsymbol{\epsilon}_{p,\mathrm{ant}}^{\mathcal{E}},\\ &\boldsymbol{v}_{\mathrm{ant}}^{\mathcal{E}}+\boldsymbol{\epsilon}_{v,\mathrm{ant}}^{\mathcal{E}}, \boldsymbol{\gamma}_{\mathrm{yp}}^{\mathcal{A}\leftarrow\mathcal{E}}+\boldsymbol{\epsilon}_{\mathrm{yp}}^{\mathcal{A}\leftarrow\mathcal{E}}, \boldsymbol{n}_{\mathrm{plane}}^{\mathcal{E}}, d_{\mathrm{plane}}^{\mathcal{E}}\big)\end{aligned} \tag{A.43c}$$

## A.6.5. Jacobian of the synthetic measurement with respect to the track state in the abscence of noise

This function determines the Jacobian of the synthetic measurement with respect to the track state in the abscene of noise (see Section A.5.4)

$$\boldsymbol{f}_0^{\mathcal{M}\leftarrow\mathcal{S}} \left(\boldsymbol{x}^{\mathcal{S}}; \boldsymbol{x}_{\mathrm{ant}}^{\mathcal{E}}, \boldsymbol{v}_{\mathrm{ant}}^{\mathcal{E}}, \boldsymbol{\gamma}_{\mathrm{yp}}^{\mathcal{A}\leftarrow\mathcal{E}}\right) \tag{A.44}$$

### Notation

$$\frac{\partial \boldsymbol{z}}{\partial \boldsymbol{x}^{\mathcal{S}}} = \mathbf{f}_{J,0}^{\mathcal{M}\leftarrow\mathcal{S}} \left(\boldsymbol{x}^{\mathcal{S}}; \boldsymbol{x}_{\mathrm{ant}}^{\mathcal{E}}, \boldsymbol{v}_{\mathrm{ant}}^{\mathcal{E}}, \boldsymbol{\gamma}_{\mathrm{yp}}^{\mathcal{A}\leftarrow\mathcal{E}}\right) \tag{A.45}$$

**Implementation** Jacobian of the 3d target location with respect to the track state

$$\frac{\partial \boldsymbol{x}^{\mathcal{E}}}{\partial \boldsymbol{x}^{\mathcal{S}}} = \begin{bmatrix}\mathbf{T}^{\mathcal{E}\leftarrow\mathcal{P}3}\mathbf{T}^{D3\leftarrow D2} & \mathbf{0}_{3\times 2}\end{bmatrix} \tag{A.46}$$

Jacobian of the difference of the target and platform location

$$\frac{\partial \Delta\boldsymbol{x}_{\mathrm{at}}^{\mathcal{E}}}{\partial \boldsymbol{x}^{\mathcal{S}}} = \frac{\partial \boldsymbol{x}^{\mathcal{E}}}{\partial \boldsymbol{x}^{\mathcal{S}}} \tag{A.47}$$

Jacobian of the scalar product of the difference vector and the normal vector of the plane

$$\frac{\partial \tilde{\rho}_{\mathrm{pl,at}}}{\partial \boldsymbol{x}^{\mathcal{S}}} = \left[\boldsymbol{n}_{\mathrm{plane}}^{\mathcal{E}}\right]^T \frac{\partial \Delta\boldsymbol{x}_{\mathrm{at}}^{\mathcal{E}}}{\partial \boldsymbol{x}^{\mathcal{S}}} \tag{A.48}$$

Jacobian of the projection of the difference vector on the tracking plane

$$\frac{\partial \Delta\boldsymbol{x}_{\mathrm{at,p}}^{\mathcal{E}}}{\partial \boldsymbol{x}^{\mathcal{S}}} = \frac{\partial \Delta\boldsymbol{x}_{\mathrm{at}}^{\mathcal{E}}}{\partial \boldsymbol{x}^{\mathcal{S}}} - \boldsymbol{n}_{\mathrm{plane}}^{\mathcal{E}} \frac{\partial \tilde{\rho}_{\mathrm{pl,at}}}{\partial \boldsymbol{x}^{\mathcal{S}}} \tag{A.49}$$

Jacobian of the norm of the projection of the difference vector

$$\frac{\partial \|\Delta\boldsymbol{x}_{\mathrm{at,p}}^{\mathcal{E}}\|}{\partial \boldsymbol{x}^{\mathcal{S}}} = \frac{\left[\Delta\boldsymbol{x}_{\mathrm{at,p}}^{\mathcal{E}}\right]^T \frac{\partial \Delta\boldsymbol{x}_{\mathrm{at,p}}^{\mathcal{E}}}{\partial \boldsymbol{x}^{\mathcal{S}}}}{\|\Delta\boldsymbol{x}_{\mathrm{at,p}}^{\mathcal{E}}\|} \tag{A.50}$$

Jacobian of the normalized projection of the differnce vector onto the plane

$$\frac{\partial \boldsymbol{u}_{\mathrm{at,p}}^{\mathcal{E}}}{\partial \boldsymbol{x}^{\mathcal{S}}} = \frac{\|\Delta \boldsymbol{x}_{\mathrm{at,p}}^{\mathcal{E}}\| \frac{\partial \Delta \boldsymbol{x}_{\mathrm{at,p}}^{\mathcal{E}}}{\boldsymbol{x}^{\mathcal{S}}} - \Delta \boldsymbol{x}_{\mathrm{at,p}}^{\mathcal{E}} \frac{\partial \|\Delta \boldsymbol{x}_{\mathrm{at,p}}^{\mathcal{E}}\|}{\partial \boldsymbol{x}^{\mathcal{S}}}}{\|\Delta \boldsymbol{x}_{\mathrm{at,p}}^{\mathcal{E}}\|^2} \tag{A.51}$$

Jacobian of the ENU velocity with respect to the track state

$$\frac{\partial \boldsymbol{v}^{\mathcal{E}}}{\partial \boldsymbol{x}^{\mathcal{S}}} = \begin{bmatrix} \mathbf{0}_{3\times 2} & \mathbf{T}^{\mathcal{E}\leftarrow\mathcal{P}3}\mathbf{T}^{D3\leftarrow D2} \end{bmatrix} \tag{A.52}$$

Jacobian of the measurable plane velocity component

$$\frac{\partial v_{\mathrm{t,pl}}}{\partial \boldsymbol{x}^{\mathcal{S}}} = \left[\boldsymbol{u}_{\mathrm{at,p}}^{\mathcal{E}}\right]^T \frac{\partial \boldsymbol{v}^{\mathcal{E}}}{\partial \boldsymbol{x}^{\mathcal{S}}} + \left[\boldsymbol{v}^{\mathcal{E}}\right]^T \frac{\partial \boldsymbol{u}_{\mathrm{at,p}}^{\mathcal{E}}}{\partial \boldsymbol{x}^{\mathcal{S}}} \tag{A.53}$$

Finally, the Jacobian of the track measurement

$$\frac{\partial \boldsymbol{z}}{\partial \boldsymbol{x}^{\mathcal{S}}} = \begin{bmatrix} 1 & 0 & 0 & 0 \\ 0 & 1 & 0 & 0 \\ \text{—} & \frac{\partial v_{\mathrm{t,pl}}}{\partial \boldsymbol{x}^{\mathcal{S}}} & \text{—} \end{bmatrix} \tag{A.54}$$

## A.6.6. Jacobian of the radar measurements with respect to the track state

converts the track state to the radar measurement

### Notation

$$= \boldsymbol{f}_{\mathrm{J}}^{\mathrm{urv}\leftarrow\mathcal{S}}\left(\boldsymbol{x}^{\mathcal{E}}, \boldsymbol{v}^{\mathcal{E}}; \boldsymbol{x}_{\mathrm{ant}}^{\mathcal{E}}, \boldsymbol{v}_{\mathrm{ant}}^{\mathcal{E}}, \boldsymbol{\gamma}_{\mathrm{yp}}^{\mathcal{A}\leftarrow\mathcal{E}}\right) \tag{A.55a}$$

converts the track state to the radar measurement

**Implementation** Partitioning of the track state

$$\boldsymbol{x}^{\mathcal{S}} = \begin{bmatrix} \boldsymbol{x}^{\mathcal{P}2} \\ \boldsymbol{v}^{\mathcal{P}2} \end{bmatrix} \tag{A.55b}$$

Compute 3d ENU location

$$\boldsymbol{x}^{\mathcal{E}} = \boldsymbol{f}_{\mathrm{p}}^{3\leftarrow 2}\left(\boldsymbol{x}^{\mathcal{P}2}; \boldsymbol{x}_{\mathcal{P}3,\mathrm{origin}}^{\mathcal{E}}, \boldsymbol{\gamma}^{\mathcal{E}\leftarrow\mathcal{P}3}\right) \tag{A.55c}$$

Compute the 3d ENU velocity vector

$$\boldsymbol{v}^{\mathcal{E}} = \boldsymbol{f}_{\mathrm{v}}^{3\leftarrow 2}\left(\boldsymbol{v}^{\mathcal{P}2}; \boldsymbol{\gamma}^{\mathcal{E}\leftarrow\mathcal{P}3}\right) \tag{A.55d}$$

Compute the radar measurement

$$\boldsymbol{z}_{\mathrm{urv}} = \boldsymbol{f}^{\mathrm{urv}\leftarrow\mathcal{E}}\left(\boldsymbol{x}^{\mathcal{E}}, \boldsymbol{v}^{\mathcal{E}}; \boldsymbol{x}_{\mathrm{ant}}^{\mathcal{E}}, \boldsymbol{v}_{\mathrm{ant}}^{\mathcal{E}}, \boldsymbol{\gamma}_{\mathrm{yp}}^{\mathcal{A}\leftarrow\mathcal{E}}\right) \tag{A.55e}$$

## A.6.7. Jacobian of the radar measurement with respect to the track measurement

Determine the Jacobian of the radar measurement with respect to the track measurement (see Section A.5.11)

### Notation

$$\frac{\partial \boldsymbol{z}_{\mathrm{urv}}}{\partial \boldsymbol{z}} = \boldsymbol{f}_{\mathrm{J}}^{\mathrm{urv}\leftarrow\mathcal{M}}\left(\boldsymbol{z}, \boldsymbol{x}_{\mathrm{ant}}^{\mathcal{E}}, \boldsymbol{v}_{\mathrm{ant}}^{\mathcal{E}}, \boldsymbol{\gamma}_{\mathrm{yp}}^{\mathcal{A}\leftarrow\mathcal{E}}\right) \tag{A.56a}$$

**Implementation** Compute variables of Section A.5.11 Jacobian of the track measurement component $v_{\mathrm{t,pl}}$ with respect to the track measurement

$$\frac{\partial v_{\mathrm{t,pl}}}{\partial \boldsymbol{z}} = [0 \quad 0 \quad 1] \tag{A.56b}$$

$$\frac{\partial \boldsymbol{x}^{\mathcal{E}}}{\partial \boldsymbol{z}} = \left[\mathbf{T}^{\mathcal{E}\leftarrow\mathcal{P}3}\mathbf{T}^{D3\leftarrow D2} \quad \mathbf{0}_{3\times 1}\right] \tag{A.56c}$$

Jacobian of the difference between the target and antenna location

$$\frac{\partial \Delta\boldsymbol{x}^{\mathcal{E}}}{\partial \boldsymbol{z}} = \frac{\partial \boldsymbol{x}^{\mathcal{E}}}{\partial \boldsymbol{z}} \tag{A.56d}$$

Jacobian of the range to the target

$$\frac{\partial r}{\partial \boldsymbol{z}} = \frac{\left[\Delta\boldsymbol{x}^{\mathcal{E}}\right]^{T}\frac{\partial \Delta\boldsymbol{x}^{\mathcal{E}}}{\partial \boldsymbol{z}}}{\|\Delta\boldsymbol{x}^{\mathcal{E}}\|} \tag{A.56e}$$

Jacobian of the direction vector of the target

$$\frac{\partial \boldsymbol{u}^{\mathcal{E}}}{\partial \boldsymbol{z}} = \frac{r\frac{\partial \Delta\boldsymbol{x}^{\mathcal{E}}}{\partial \boldsymbol{z}} - \Delta\boldsymbol{x}^{\mathcal{E}}\frac{\partial r}{\partial \boldsymbol{z}}}{r^2} \tag{A.56f}$$

Derivative of the direction vector

$$\frac{\partial u_1^{\mathcal{A}}}{\partial \boldsymbol{z}} = \left[\boldsymbol{e}^{\mathcal{E}}\right]^{\mathrm{T}}\frac{\partial \boldsymbol{u}^{\mathcal{E}}}{\partial \boldsymbol{z}} \tag{A.56g}$$

Derivative of the correlation between the direction vector and the normal vector of the plane

$$\frac{\partial \rho_{\mathrm{pl,at}}}{\partial \boldsymbol{z}} = \left[\boldsymbol{n}_{\mathrm{plane}}^{\mathcal{E}}\right]^{T}\frac{\partial \boldsymbol{u}^{\mathcal{E}}}{\partial \boldsymbol{z}} \tag{A.56h}$$

Jacobian of the projection of the direction vector onto the plane

$$\frac{\partial \tilde{\boldsymbol{u}}^{\mathcal{E}}}{\partial \boldsymbol{z}} = \frac{\partial \boldsymbol{u}^{\mathcal{E}}}{\partial \boldsymbol{z}} - \frac{\partial \rho_{\mathrm{pl,at}}}{\partial \boldsymbol{z}}\boldsymbol{n}_{\mathrm{plane}}^{\mathcal{E}} \tag{A.56i}$$

Derivative of the norm of the projection vector

$$\frac{\partial \|\tilde{\boldsymbol{u}}^{\mathcal{E}}\|}{\partial \boldsymbol{z}} = \frac{\left[\tilde{\boldsymbol{u}}^{\mathcal{E}}\right]^{T} \frac{\partial \tilde{\boldsymbol{u}}^{\mathcal{E}}}{\partial \boldsymbol{z}}}{\|\tilde{\boldsymbol{u}}^{\mathcal{E}}\|} \tag{A.56j}$$

Derivative of the target component of the radial velocity:

$$\frac{\partial v_{\mathrm{t,rad}}}{\partial \boldsymbol{z}} = v_{\mathrm{t,pl}} \frac{\partial \|\tilde{\boldsymbol{u}}^{\mathcal{E}}\|}{\partial \boldsymbol{z}} + \frac{\partial v_{\mathrm{t,pl}}}{\partial \boldsymbol{z}} \|\tilde{\boldsymbol{u}}^{\mathcal{E}}\| \tag{A.56k}$$

Derivative of the radial velocity including antenna component:

$$\frac{\partial v_{\mathrm{rad}}}{\partial \boldsymbol{z}} = \frac{\partial v_{\mathrm{t,rad}}}{\partial \boldsymbol{z}} - \left[\boldsymbol{v}_{\mathrm{ant}}^{\mathcal{E}}\right]^{\mathrm{T}} \frac{\partial \boldsymbol{u}^{\mathcal{E}}}{\partial \boldsymbol{z}} \tag{A.56l}$$

Arrangement of all derivatives to the Jacobi matrix

$$\frac{\partial \boldsymbol{z}_{\mathrm{urv}}}{\partial \boldsymbol{z}} = \begin{bmatrix} \frac{\partial u_1^{\mathcal{A}}}{\partial \boldsymbol{z}} \\ \frac{\partial r}{\partial \boldsymbol{z}} \\ \frac{\partial v_{\mathrm{rad}}}{\partial \boldsymbol{z}} \end{bmatrix} \tag{A.56m}$$

## A.7. Other functions

### A.7.1. Euler rotation matrix

The Euler rotation matrix is given in [21, Sec. 4.5, p. 116].

#### Notation

$$\mathbf{T} = \mathbf{T}_{\mathrm{Euler}}\left(\boldsymbol{\gamma}_{\mathrm{ypr}}\right) \tag{A.57a}$$

**Implementation** The parameter vector includes the yaw, pitch and roll angles:

$$\boldsymbol{\gamma}_{\mathrm{ypr}} = \begin{bmatrix} \gamma_{\mathrm{yaw}} \\ \gamma_{\mathrm{pitch}} \\ \gamma_{\mathrm{roll}} \end{bmatrix} \tag{A.57b}$$

Definition of the components of the Euler matrix:

$$\mathbf{T}_{\mathrm{r}}(\gamma_{\mathrm{roll}}) = \begin{bmatrix} 1 & 0 & 0 \\ 0 & \cos(\gamma_{\mathrm{roll}}) & \sin(\gamma_{\mathrm{roll}}) \\ 0 & -\sin(\gamma_{\mathrm{roll}}) & \cos(\gamma_{\mathrm{roll}}) \end{bmatrix} \tag{A.57c}$$

$$\mathbf{T}_{\mathrm{p}}(\gamma_{\mathrm{pitch}}) = \begin{bmatrix} \cos(\gamma_{\mathrm{pitch}}) & 0 & -\sin(\gamma_{\mathrm{pitch}}) \\ 0 & 1 & 0 \\ \sin(\gamma_{\mathrm{pitch}}) & 0 & \cos(\gamma_{\mathrm{pitch}}) \end{bmatrix} \tag{A.57d}$$

$$\mathbf{T}_{\mathrm{y}}(\gamma_{\mathrm{yaw}}) = \begin{bmatrix} \cos(\gamma_{\mathrm{yaw}}) & \sin(\gamma_{\mathrm{yaw}}) & 0 \\ -\sin(\gamma_{\mathrm{yaw}}) & \cos(\gamma_{\mathrm{yaw}}) & 0 \\ 0 & 0 & 1 \end{bmatrix}. \tag{A.57e}$$

Use the definition of the yaw, pitch and roll rotations to compute the Euler matrix:

$$\mathbf{T} = \mathbf{T}_{\mathrm{r}}(\gamma_{\mathrm{roll}})\mathbf{T}_{\mathrm{p}}(\gamma_{\mathrm{pitch}})\mathbf{T}_{\mathrm{y}}(\gamma_{\mathrm{yaw}}) \tag{A.57f}$$

## A.7.2. Inverse Euler rotation matrix

### Notation

$$\mathbf{T}^{\mathrm{inv}} = \mathbf{T}^{\mathrm{inv}}_{\mathrm{Euler}}\left(\boldsymbol{\gamma}_{\mathrm{ypr}}\right) \tag{A.58a}$$

**Implementation** The parameter vector includes the yaw, pitch and roll angles:

$$\boldsymbol{\gamma}_{\mathrm{ypr}} = \begin{bmatrix} \gamma_{\mathrm{yaw}} \\ \gamma_{\mathrm{pitch}} \\ \gamma_{\mathrm{roll}} \end{bmatrix} \tag{A.58b}$$

Use the definition of the yaw, pitch and roll rotations of Algorithm A.7.1 to compute the inverse Euler matrix

$$\mathbf{T}^{\mathrm{inv}} = \mathbf{T}_{\mathrm{y}}(-\gamma_{\mathrm{yaw}})\mathbf{T}_{\mathrm{p}}(-\gamma_{\mathrm{pitch}})\mathbf{T}_{\mathrm{r}}(-\gamma_{\mathrm{roll}})\,. \tag{A.58c}$$

## A.7.3. Bilinear interpolation

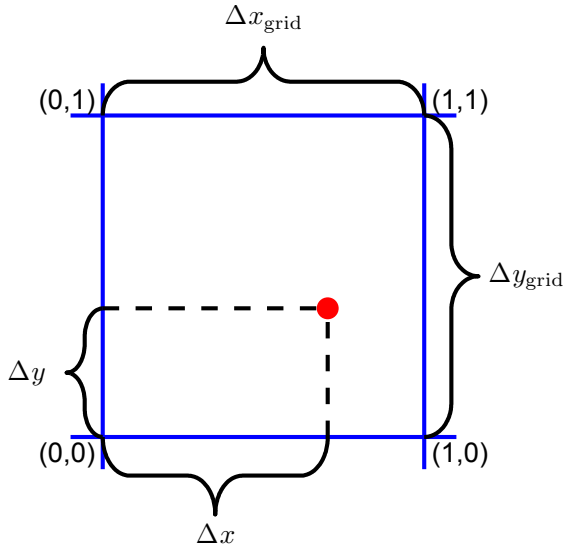


**Figure A.2.:** One quadrant of the lattice on which the function values of $g$ are provided. The location at which the interpolated value is sought is highlighted by a red dot.

This function performs a bilinear interpolation: it approximates the value of a function $g$ at a location $\boldsymbol{x}^{\mathrm{2d}}$. Functions values of $g$ are known for a lattice with spacing $\Delta x_{\mathrm{grid}}$ and $\Delta y_{\mathrm{grid}}$.

**Notation**

$$z = f_{\text{bilin}}\left(\boldsymbol{x}^{2\text{d}}, \boldsymbol{\theta}_{\text{grid}}\right) \tag{A.59a}$$

**Implementation**

- Determine the quadrant where $\boldsymbol{x}^{2\text{d}}$ is located
- Determine the location of $\boldsymbol{x}^{2\text{d}}$ within this quadrant. The x and y location with respect to edge (0,0) of the quadrant shall be denoted $\Delta x$ and $\Delta y$.
- Determine the values of the function $g$ at the edges. Denote them by

$$\boldsymbol{z}_{\text{grid}} = \begin{bmatrix} z_{\text{grid},0,0} & z_{\text{grid},0,1} & z_{\text{grid},1,0} & z_{\text{grid},1,1} \end{bmatrix}^T \tag{A.59b}$$

- Determine the elements of $4 \times 1$ vector $\boldsymbol{b}$ which is used for computing the interpolated value

$$\begin{aligned} b_1 &= z_{\text{grid},0,0} \\ b_2 &= z_{\text{grid},1,0} - z_{\text{grid},0,0} \\ b_3 &= z_{\text{grid},0,1} - z_{\text{grid},0,0} \\ b_3 &= z_{\text{grid},0,0} - z_{\text{grid},1,0} - z_{\text{grid},0,1} + z_{\text{grid},1,1} \end{aligned} \tag{A.59c}$$

- Compute the interpolated value

$$z = b_1 + b_2 \frac{\Delta x}{\Delta x_{\text{grid}}} + b_3 \frac{\Delta y}{\Delta y_{\text{grid}}} + b_4 \frac{\Delta x \Delta y}{\Delta x_{\text{grid}} \Delta y_{\text{grid}}} \tag{A.59d}$$

# A.8. Conversions with a digital elevation model

## A.8.1. Mapping from the planar location to ENU location

This function converts a two dimensional location state to a full three dimensional location by using a digital elevation model. Basicaly, this function performs a bilinear interpolation to find the z-coordiante of the DEM. The expanded notation inlcudes the bilinear interpolation. It is given in order to facicilate the computation of the Jacobian matrix of this function in Section A.9.

**Notation**

$$\boldsymbol{x}^{\mathcal{E}} = \boldsymbol{f}_{\text{p,dem}}^{3\leftarrow 2}\left(\boldsymbol{x}^{\mathcal{P}2}, \boldsymbol{\theta}_{\text{dem}}\right) \tag{A.60a}$$

**Implementation**

$$\boldsymbol{x}^{\mathcal{E}} = \begin{bmatrix} \boldsymbol{x}^{\mathcal{P}2} \\ f_{\text{bilin}}\left(\boldsymbol{x}^{\mathcal{P}2}, \boldsymbol{\theta}_{\text{dem}}\right) \end{bmatrix} \tag{A.60b}$$

**Expanded notation**

- Compute the components of the parameter vector $\boldsymbol{b}$ of the bilinear interpolation.

$$\begin{aligned} b_1 &= z_{\mathrm{dem},0,0} \\ b_2 &= z_{\mathrm{dem},1,0} - z_{\mathrm{dem},0,0} \\ b_3 &= z_{\mathrm{dem},0,1} - z_{\mathrm{dem},0,0} \\ b_3 &= z_{\mathrm{dem},0,0} - z_{\mathrm{dem},1,0} - z_{\mathrm{dem},0,1} + z_{\mathrm{dem},1,1} \end{aligned} \tag{A.60c}$$

- Determine the location of the $\boldsymbol{x}^{\mathcal{P}2}$ within the quadrant of the DEM

$$\begin{aligned} \Delta x &= \mathrm{mod}\left(x_1^{\mathcal{P}2}, \Delta x_{\mathrm{dem}}\right) \\ \Delta y &= \mathrm{mod}\left(x_2^{\mathcal{P}2}, \Delta y_{\mathrm{dem}}\right) \end{aligned} \tag{A.60d}$$

- Determine the interpolated value

$$x_3^{\mathcal{E}} = b_1 + b_2\frac{\Delta x}{\Delta x_{\mathrm{dem}}} + b_3\frac{\Delta y}{\Delta y_{\mathrm{dem}}} + b_4\frac{\Delta x \Delta y}{\Delta x_{\mathrm{dem}}\Delta y_{\mathrm{dem}}} \tag{A.60e}$$

## A.8.2. Mapping from the track velocity to ENU velocity

Using a DEM model, this function converts a two dimenensional velocity state to a three dimensional velocity state. The expanded notation is given for the later computation of Jacobian matrices of this functin.

**Notation**

$$\boldsymbol{v}^{\mathcal{E}} = \boldsymbol{f}_{\mathrm{v,dem}}^{3\leftarrow 2}(\boldsymbol{x}^{\mathcal{S}}, \boldsymbol{\theta}_{\mathrm{dem}}) \tag{A.61a}$$

**Implementation** Compute the Jacobian of the ENU location with respect to the location (see Section A.9.1)

$$\mathbf{T}^{3\leftarrow 2} = \frac{\partial \boldsymbol{f}_{\mathrm{p,dem}}^{3\leftarrow 2}}{\partial \boldsymbol{x}^{\mathcal{P}2}}(\boldsymbol{x}^{\mathcal{P}2}, \boldsymbol{\theta}_{\mathrm{dem}}) \tag{A.61b}$$

Return value:

$$\boldsymbol{v}^{\mathcal{E}} = \mathbf{T}^{3\leftarrow 2}\boldsymbol{v}^{\mathcal{P}2} \tag{A.61c}$$

**Expanded notation** Jacobian of the z-component of the 3D location with respect to the 2D location vector:

$$\boldsymbol{g}^{\mathrm{T}} = \begin{bmatrix} \dfrac{b_2}{\Delta x_{\mathrm{grid}}} + \dfrac{b_4 \Delta y}{\Delta x_{\mathrm{grid}}\Delta y_{\mathrm{grid}}} & \dfrac{b_3}{\Delta y_{\mathrm{grid}}} + \dfrac{b_4 \Delta x}{\Delta x_{\mathrm{grid}}\Delta y_{\mathrm{grid}}} \end{bmatrix} \tag{A.61d}$$

Columns of $\mathbf{T}^{3\leftarrow 2}$

$$\boldsymbol{a}_{\mathrm{v},1} = \begin{bmatrix} 1 \\ 0 \\ g_1 \end{bmatrix}, \ \boldsymbol{a}_{\mathrm{v},2} = \begin{bmatrix} 1 \\ 0 \\ g_2 \end{bmatrix} \tag{A.61e}$$

where $g_1$ and $g_2$ are the elements of the vector $\boldsymbol{g}$ of equation (A.61d). Return value:

$$\boldsymbol{v}^{\mathcal{E}} = \boldsymbol{a}_{\mathrm{v},1} v_1^{\mathcal{P}2} + \boldsymbol{a}_{\mathrm{v},2} v_2^{\mathcal{P}2} \tag{A.61f}$$

## A.9. Jacobians of the conversion between ENU and track coordinate systems

In order to perform error propagation, Jacobians of the functions $\boldsymbol{f}_{\mathrm{p,dem}}^{3\leftarrow 2}$, $\boldsymbol{f}_{\mathrm{v,dem}}^{3\leftarrow 2}$ and $\boldsymbol{f}_{\mathrm{s,dem}}^{3\leftarrow 2}$ with respect to the location, velocity and DEM parameters are required. In the following, these Jacobians are given.

### A.9.1. Jacobian of the location conversion with respect to the location

#### Notation

$$\mathbf{T}_{\mathrm{p,p}}^{3\leftarrow 2} = \frac{\partial \boldsymbol{f}_{\mathrm{p,dem}}^{3\leftarrow 2}}{\partial \boldsymbol{x}^{\mathcal{P}2}}(\boldsymbol{x}^{\mathcal{P}2}, \boldsymbol{\theta}_{\mathrm{dem}}) \tag{A.62a}$$

#### Implementation

- Determine the parameters $b_1$ to $b_4$ that are used in the bilinear interpolation (see equation A.59c).
- Determine the positions $\Delta x$ and $\Delta y$ within the grid.
- Jacobian of the z component of the ENU coordinate

$$\boldsymbol{g}^{\mathrm{T}} = \frac{\partial f_{\mathrm{bilin}}}{\partial \boldsymbol{x}}(\boldsymbol{x}, \boldsymbol{\theta}_{\mathrm{grid}}) = \left[ \frac{b_2}{\Delta x_{\mathrm{grid}}} + \frac{b_4 \Delta y}{\Delta x_{\mathrm{grid}} \Delta y_{\mathrm{grid}}} \quad \frac{b_3}{\Delta y_{\mathrm{grid}}} + \frac{b_4 \Delta x}{\Delta x_{\mathrm{grid}} \Delta y_{\mathrm{grid}}} \right] \tag{A.62b}$$

- Jacobian of the entire ENU location vector

$$\mathbf{T}_{\mathrm{p,p}}^{3\leftarrow 2} = \begin{bmatrix} \mathbf{I}_{2\times 2} \\ \boldsymbol{g}^{\mathrm{T}} \end{bmatrix} \tag{A.62c}$$

### A.9.2. Jacobian of the location conversion with respect to the DEM model parameters

**Notation** Jacobian of the ENU location with respect the four neighboring grid points:

$$\mathbf{T}_{\mathrm{p,dem}}^{3\leftarrow 2} = \frac{\partial \boldsymbol{f}_{\mathrm{dem}}^{3\leftarrow 2}}{\partial \boldsymbol{z}_{\mathrm{dem}}}(\boldsymbol{x}^{\mathcal{P}2}, \boldsymbol{\theta}_{\mathrm{dem}}) \tag{A.63a}$$

**Implementation** Jacobian of values $b_1$ to $b_4$ with respect to four neighboring grid points:

$$\frac{\partial \boldsymbol{b}}{\partial \boldsymbol{z}_{\mathrm{dem}}} = \begin{bmatrix} 1 & 0 & 0 & 0 \\ -1 & 1 & 0 & 0 \\ -1 & 0 & 1 & 0 \\ 1 & -1 & -1 & 1 \end{bmatrix}. \tag{A.63b}$$

Jacobian of interpolated valued with respect to parameters $b_1$ to $b_4$:

$$\frac{\partial f_{\mathrm{bilin}}}{\partial \boldsymbol{b}} \left(\boldsymbol{x}^{\mathcal{P}2}, \boldsymbol{\theta}_{\mathrm{grid}}\right) = \begin{bmatrix} 1 & \dfrac{\Delta x}{\Delta x_{\mathrm{dem}}} & \dfrac{\Delta y}{\Delta y_{\mathrm{dem}}} & \dfrac{\Delta x \Delta y}{\Delta x_{\mathrm{dem}} \Delta y_{\mathrm{dem}}} \end{bmatrix} \tag{A.63c}$$

Jacobian of the interpolated value with respect to the four neighboring edge points:

$$\frac{\partial f_{\mathrm{bilin}}}{\partial \boldsymbol{z}} \left(\boldsymbol{x}^{\mathcal{P}2}, \boldsymbol{\theta}_{\mathrm{dem}}\right) = \frac{\partial f_{\mathrm{bilin}}}{\partial \boldsymbol{b}} \left(\boldsymbol{x}^{\mathcal{P}2}, \boldsymbol{\theta}_{\mathrm{dem}}\right) \frac{\partial \boldsymbol{b}}{\partial \boldsymbol{z}_{\mathrm{dem}}}, \tag{A.63d}$$

Return value:

$$\mathbf{T}^{3\leftarrow 2}_{\mathrm{p,dem}} = \begin{bmatrix} \mathbf{0}_{2\times 4} \\ \frac{\partial f_{\mathrm{bilin}}}{\partial \boldsymbol{z}} \left(\boldsymbol{x}^{\mathcal{P}2}_{\mathrm{p}}, \boldsymbol{\theta}_{\mathrm{dem}}\right) \end{bmatrix} \tag{A.63e}$$

### A.9.3. Jacobian of the location conversion with respect to track state and DEM model parameters

Jacobian of $\boldsymbol{f}^{3\leftarrow 2}_{\mathrm{p,dem}}$ with respect to the vector

$$\boldsymbol{\theta}_{\mathrm{S}} = \begin{bmatrix} \boldsymbol{x}^{\mathcal{S}} \\ \boldsymbol{z}_{\mathrm{dem}} \end{bmatrix} \tag{A.64}$$

which combines the target state and the DEM parameters.

**Notation**

$$\mathbf{T}^{3\leftarrow 2}_{\mathrm{p,s}} = \frac{\partial \boldsymbol{f}^{3\leftarrow 2}_{\mathrm{v,dem}}}{\partial \boldsymbol{\theta}_{\mathrm{s}}} (\boldsymbol{x}^{\mathcal{P}2}, \boldsymbol{\theta}_{\mathrm{dem}}) \tag{A.65a}$$

**Implementation** Compute the Jacobian with respect to the location (see Section A.9.1)

$$\mathbf{T}^{3\leftarrow 2}_{\mathrm{p,p}} = \frac{\partial \boldsymbol{f}^{3\leftarrow 2}_{\mathrm{p,dem}}}{\partial \boldsymbol{x}^{\mathcal{P}2}} (\boldsymbol{x}^{\mathcal{P}2}, \boldsymbol{\theta}_{\mathrm{dem}}) \tag{A.65b}$$

Compute the Jacobian with respect to the DEM model parameters (see Section A.9.2)

$$\mathbf{T}^{3\leftarrow 2}_{\mathrm{p,dem}} = \frac{\partial \boldsymbol{f}^{3\leftarrow 2}_{\mathrm{dem}}}{\partial \boldsymbol{z}_{\mathrm{dem}}} (\boldsymbol{x}^{\mathcal{P}2}, \boldsymbol{\theta}_{\mathrm{dem}}) \tag{A.65c}$$

Return value: Combine both results

$$\mathbf{T}^{3\leftarrow 2}_{\mathrm{p,s}} = \begin{bmatrix} \mathbf{T}^{3\leftarrow 2}_{\mathrm{p,p}} & \mathbf{0}_{3\times 2} & \mathbf{T}^{3\leftarrow 2}_{\mathrm{p,dem}} \end{bmatrix} \tag{A.65d}$$

## A.9.4. Jacobian of ENU velocity with resepect to the DEM parameters

**Notation**

$$\mathbf{T}_{\mathrm{v,dem}}^{3\leftarrow 2} = \frac{\partial \boldsymbol{f}_{\mathrm{v,dem}}^{3\leftarrow 2}}{\partial \boldsymbol{z}_{\mathrm{dem}}}(\boldsymbol{x}^{\mathcal{S}}, \boldsymbol{\theta}_{\mathrm{dem}}) \tag{A.66a}$$

**Implementation** Jacobian of $\boldsymbol{g}$ with respect to the DEM parameter vector $\boldsymbol{b}$

$$\frac{\partial \boldsymbol{g}}{\partial \boldsymbol{b}} = \begin{bmatrix} 0 & \frac{1}{\Delta x_{\mathrm{grid}}} & 0 & \frac{\Delta y}{\Delta x_{\mathrm{grid}} \Delta y_{\mathrm{grid}}} \\ 0 & 0 & \frac{1}{\Delta y_{\mathrm{grid}}} & \frac{\Delta x}{\Delta x_{\mathrm{grid}} \Delta y_{\mathrm{grid}}} \end{bmatrix}, \tag{A.66b}$$

Jacobian of $\boldsymbol{a}_{\mathrm{v},1}$ and $\boldsymbol{a}_{\mathrm{v},2}$ with respect to the DEM parameter vector $\boldsymbol{b}$

$$\frac{\partial \boldsymbol{a}_{\mathrm{v},1}}{\partial \boldsymbol{b}} = \begin{bmatrix} \mathbf{0}_{2\times 4} \\ [1 \quad 0] \frac{\partial \boldsymbol{g}}{\partial \boldsymbol{b}} \end{bmatrix}, \frac{\partial \boldsymbol{a}_{\mathrm{v},2}}{\partial \boldsymbol{b}} = \begin{bmatrix} \mathbf{0}_{2\times 4} \\ [0 \quad 1] \frac{\partial \boldsymbol{g}}{\partial \boldsymbol{b}} \end{bmatrix} \tag{A.66c}$$

$$\frac{\partial \boldsymbol{f}_{\mathrm{v,dem}}^{3\leftarrow 2}}{\partial \boldsymbol{b}} = v_1^{\mathcal{P}2} \frac{\partial \boldsymbol{a}_{\mathrm{v},1}}{\partial \boldsymbol{b}} + v_2^{\mathcal{P}2} \frac{\partial \boldsymbol{a}_{\mathrm{v},2}}{\partial \boldsymbol{b}} \tag{A.66d}$$

Return value (see equation (A.63b) for the computation of $\frac{\partial \boldsymbol{b}}{\partial \boldsymbol{z}_{\mathrm{dem}}}$):

$$\mathbf{T}_{\mathrm{v,dem}}^{3\leftarrow 2} = \frac{\partial \boldsymbol{f}_{\mathrm{v,dem}}^{3\leftarrow 2}}{\partial \boldsymbol{b}} \frac{\partial \boldsymbol{b}}{\partial \boldsymbol{z}_{\mathrm{dem}}} \tag{A.66e}$$

## A.9.5. Jacobian of ENU velocity with resepect to the track location

The Jacobian of the velocity conversion function with respect to the 2d position is found similarly to the Jacobian with respect to the DEM parameters.

**Notation**

$$\mathbf{T}_{\mathrm{v,p}}^{3\leftarrow 2} = \frac{\partial \boldsymbol{f}_{\mathrm{v,dem}}^{3\leftarrow 2}}{\partial \boldsymbol{x}^{\mathcal{P}2}}(\boldsymbol{x}^{\mathcal{S}}, \boldsymbol{\theta}_{\mathrm{dem}}) \tag{A.67a}$$

**Implementation** Jacobian of $\boldsymbol{g}$ with respect to the track location

$$\frac{\partial \boldsymbol{g}}{\partial \boldsymbol{x}^{\mathcal{P}2}} = \begin{bmatrix} 0 & \frac{b_4}{\Delta x_{\mathrm{grid}} \Delta y_{\mathrm{grid}}} \\ \frac{b_4}{\Delta x_{\mathrm{grid}} \Delta y_{\mathrm{grid}}} & 0 \end{bmatrix} \tag{A.67b}$$

Jacobian of the vectors $\boldsymbol{a}_{v,1}$ and $\boldsymbol{a}_{v,2}$

$$\frac{\partial \boldsymbol{a}_{\mathrm{v},1}}{\partial \boldsymbol{x}^{\mathcal{P}2}} = \begin{bmatrix} \mathbf{0}_{2\times 2} \\ [1 \quad 0]^{\mathrm{T}} \frac{\partial \boldsymbol{g}}{\partial \boldsymbol{x}^{\mathcal{P}2}} \end{bmatrix}, \frac{\partial \boldsymbol{a}_{\mathrm{v},2}}{\partial \boldsymbol{x}^{\mathcal{P}2}} = \begin{bmatrix} \mathbf{0}_{2\times 2} \\ [0 \quad 1]^{\mathrm{T}} \frac{\partial \boldsymbol{g}}{\partial \boldsymbol{x}^{\mathcal{P}2}} \end{bmatrix} \tag{A.67c}$$

Return value

$$\mathbf{T}_{\mathrm{v,p}}^{3\leftarrow 2} = v_1^{\mathcal{P}2} \frac{\partial \boldsymbol{a}_{\mathrm{v},1}}{\partial \boldsymbol{x}^{\mathcal{P}2}} + v_2^{\mathcal{P}2} \frac{\partial \boldsymbol{a}_{\mathrm{v},2}}{\partial \boldsymbol{x}^{\mathcal{P}2}} \tag{A.67d}$$

### A.9.6. Jacobian of ENU velocity with resepect to the track velocity

**Notation**

$$\mathbf{T}_{\mathrm{v,v}}^{3\leftarrow 2} = \frac{\partial \boldsymbol{f}_{\mathrm{v,dem}}^{3\leftarrow 2}}{\partial \boldsymbol{v}^{\mathcal{P}2}}(\boldsymbol{x}^{\mathcal{S}}, \boldsymbol{\theta}_{\mathrm{dem}}) \tag{A.68a}$$

**Implementation** Return value

$$\mathbf{T}_{\mathrm{v,v}}^{3\leftarrow 2} = \frac{\partial \boldsymbol{f}_{\mathrm{p,dem}}^{3\leftarrow 2}}{\partial \boldsymbol{x}^{\mathcal{P}2}}(\boldsymbol{x}^{\mathcal{P}2}, \boldsymbol{\theta}_{\mathrm{dem}}) \tag{A.68b}$$

### A.9.7. Jacobian of the ENU velocity with respect to the entire track state and the DEM parameters

Jacobian of $\boldsymbol{f}_{\mathrm{v,dem}}^{3\leftarrow 2}$ with respect to the vector

$$\boldsymbol{\theta}_{\mathrm{S}} = \begin{bmatrix} \boldsymbol{x}^{\mathcal{S}} \\ \boldsymbol{z}_{\mathrm{dem}} \end{bmatrix} \tag{A.69}$$

**Notation**

$$\mathbf{T}_{\mathrm{v},\theta}^{3\leftarrow 2} = \frac{\partial \boldsymbol{f}_{\mathrm{v,dem}}^{3\leftarrow 2}}{\partial \boldsymbol{\theta}_{\mathrm{s}}}(\boldsymbol{x}^{\mathcal{S}}, \boldsymbol{\theta}_{\mathrm{dem}}) \tag{A.70a}$$

**Implementation** Compute the Jacobian with respect to the track location

$$\mathbf{T}_{\mathrm{v,p}}^{3\leftarrow 2} = \frac{\partial \boldsymbol{f}_{\mathrm{v,dem}}^{3\leftarrow 2}}{\partial \boldsymbol{x}^{\mathcal{P}2}}(\boldsymbol{x}^{\mathcal{S}}, \boldsymbol{\theta}_{\mathrm{dem}}) \tag{A.70b}$$

Compute the Jacobian with respect to the track velocity

$$\mathbf{T}_{\mathrm{v,v}}^{3\leftarrow 2} = \frac{\partial \boldsymbol{f}_{\mathrm{v,dem}}^{3\leftarrow 2}}{\partial \boldsymbol{v}^{\mathcal{P}2}}(\boldsymbol{x}^{\mathcal{S}}, \boldsymbol{\theta}_{\mathrm{dem}}) \tag{A.70c}$$

Compute the Jacobian with respect to the DEM parameters

$$\mathbf{T}_{\mathrm{v,dem}}^{3\leftarrow 2} = \frac{\partial \boldsymbol{f}_{\mathrm{v,dem}}^{3\leftarrow 2}}{\partial \boldsymbol{z}_{\mathrm{dem}}}(\boldsymbol{x}^{\mathcal{S}}, \boldsymbol{\theta}_{\mathrm{dem}}) \tag{A.70d}$$

Return value: Combine results

$$\mathbf{T}_{\mathrm{v},\theta}^{3\leftarrow 2} = \begin{bmatrix} \mathbf{T}_{\mathrm{v,p}}^{3\leftarrow 2} & \mathbf{T}_{\mathrm{v,v}}^{3\leftarrow 2} & \mathbf{T}_{\mathrm{v,dem}}^{3\leftarrow 2} \end{bmatrix} \tag{A.70e}$$

### A.9.8. Jacobian of entire ENU state with respect to the entire track state and the DEM parameters

Jacobian of $\boldsymbol{f}_{\mathrm{s,dem}}^{3\leftarrow 2}$ with respect to the vector

$$\boldsymbol{\theta}_{\mathrm{S}} = \begin{bmatrix} \boldsymbol{x}^{\mathcal{S}} \\ \boldsymbol{z}_{\mathrm{dem}} \end{bmatrix} \tag{A.71}$$

**Notation**

$$\mathbf{T}_{\mathrm{v},\theta}^{3\leftarrow 2} = \frac{\partial \boldsymbol{f}_{\mathrm{v,dem}}^{3\leftarrow 2}}{\partial \boldsymbol{\theta}_{\mathrm{s}}}(\boldsymbol{x}^{\mathcal{S}}, \boldsymbol{\theta}_{\mathrm{dem}}) \tag{A.72a}$$

**Implementation** Compute the Jacobian of the ENU location with respect to the $\boldsymbol{\theta}_{\mathrm{s}}$

$$\mathbf{T}_{\mathrm{p},\theta}^{3\leftarrow 2} = \frac{\partial \boldsymbol{f}_{\mathrm{p,dem}}^{3\leftarrow 2}}{\partial \boldsymbol{\theta}_{\mathrm{s}}}(\boldsymbol{x}^{\mathcal{P}2}, \boldsymbol{\theta}_{\mathrm{dem}}) \tag{A.72b}$$

Compute the Jacobian of the ENU velocity with respect to the $\boldsymbol{\theta}_{\mathrm{s}}$

$$\mathbf{T}_{\mathrm{v},\theta}^{3\leftarrow 2} = \frac{\partial \boldsymbol{f}_{\mathrm{v,dem}}^{3\leftarrow 2}}{\partial \boldsymbol{\theta}_{\mathrm{s}}}(\boldsymbol{x}^{\mathcal{S}}, \boldsymbol{\theta}_{\mathrm{dem}}) \tag{A.72c}$$

Return value: Combine Jacobians

$$\mathbf{T}_{\mathrm{v},\theta}^{3\leftarrow 2} = \begin{bmatrix} \mathbf{T}_{\mathrm{p},\theta}^{3\leftarrow 2} \\ \mathbf{T}_{\mathrm{v},\theta}^{3\leftarrow 2} \end{bmatrix} \tag{A.72d}$$

# Bibliography


[1] M. Arulampalam, N. Gordon, M. Orton, and B. Ristic. A variable structure multiple model particle filter for GMTI tracking. In *Proceedings of the Fifth International Conference on Information Fusion*, volume 2, pages 927 – 934, 2002. doi:10.1109/ICIF.2002.1020911.

[2] M. S. Arulampalam, S. Maskell, N. Gordon, and T. Clapp. A tutorial on particle filters for online nonlinear/non-Gaussian Bayesian tracking. *IEEE Transactions on Signal Processing*, 50(2):174–188, 2002.

[3] Y. Bar-Shalom. Tracking methods in a multitarget environment. *IEEE Transactions on Automatic Control*, 23(4):618 – 626, Aug. 1978. ISSN 0018-9286. doi:10.1109/TAC.1978.1101790.

[4] Y. Bar-Shalom, X. R. Li, and T. Kirubarajan. *Estimation with applications to Tracking and Navigation*. John Wiley & Sons, Inc., 2001.

[5] Y. Barniv. Dynamic programming solution for detecting dim moving targets. *IEEE Transactions on Aerospace and Electronic Systems*, AES-21(1):144 –156, Jan. 1985. ISSN 0018-9251. doi:10.1109/TAES.1985.310548.

[6] K. Benameur, B. Pannetier, and V. Nimier. A comparative study on the use of road network information in GMTI tracking. In *8th International Conference on Information Fusion*, volume 1, page 8 pp., 2005. doi:10.1109/ICIF.2005.1591941.

[7] S. Blackman and R. Popoli. *Design and Analysis of Modern Tracking Systems*. Artech House, 1999.

[8] S. S. Blackman. Multiple hypothesis tracking for multiple target tracking. *IEEE Transactions on Aerospace and Electronic Systems*, 19:5–18, 2004.

[9] A. R. Brenner and J. H. G. Ender. Demonstration of advanced reconnaissance techniques with the airborne SAR/GMTI sensor PAMIR. *IEE Proceedings Radar, Sonar and Navigation*, 153(2):152–162, 2006.

[10] J. F. Böhme. *Stochastische Signale*. Teubner, Stuttgart, 1998.

[11] D. Cerutti-Maori, J. Klare, A. R. Brenner, and J. H. G. Ender. Wide-area traffic monitoring with the SAR/GMTI system PAMIR. *IEEE Transactions on Geoscience and Remote Sensing*, 46:3019–3030, Oct. 2008. ISSN 0196-2892. doi:10.1109/TGRS.2008.923026.

[12] Y. Cheng and T. Singh. Efficient particle filtering for road-constrained target tracking. *IEEE Transactions on Aerospace and Electronic Systems*, 43(4):1454 –1469, 2007. ISSN 0018-9251. doi:10.1109/TAES.2007.4441751.

[13] C.-Y. Chong, D. Garren, and T. P. Grayson. Ground target tracking-a historical perspective. In *IEEE Aerospace Conference Proceedings*, volume 3, pages 433–448, Big Sky, MT, USA, 2000. doi:10.1109/AERO.2000.879870.

[14] J. Clark, P. Kountouriotis, and R. Vinter. A methodology for incorporating the Doppler blind zone in target tracking algorithms. In *11th International Conference on Information Fusion*, July 2008. doi:10.1109/ICIF.2008.4632386.

[15] J. Clark, P.-A. Kountouriotis, and R. Vinter. A new Gaussian mixture algorithm for GMTI tracking under a minimum detectable velocity constraint. *IEEE Transactions on Automatic Control*, 54(12):2745 –2756, 2009. ISSN 0018-9286. doi:10.1109/TAC.2009.2031720.

[16] S. Davey, M. Rutten, and B. Cheung. A comparison of detection performance for several track-before-detect algorithms. *EURASIP Journal on Advances in Signal Processing*, 2008(1):428036, 2008. ISSN 1687-6180. doi:10.1155/2008/428036. URL `http://asp.eurasipjournals.com/content/2008/1/428036`.

[17] M. R. Ducoff and B. W. Tietjen. Pulse compression radar. In *Radar Handbook*, chapter 8, page 8.1 to 8.44. McGraw-Hill, 2008.

[18] J. H. G. Ender. Space-time processing for multichannel synthetic aperture radar. *Electronics & Communication Engineering Journal*, 11(1):29–38, Feb. 1999. ISSN 0954-0695.

[19] J. H. G. Ender, C. H. Gierull, and D. Cerutti-Maori. Improved space-based moving target indication via alternate transmission and receiver switching. *IEEE Transactions on Geoscience and Remote Sensing*, 46(12):3960–3974, Dec. 2008. ISSN 0196-2892. doi:10.1109/TGRS.2008.2002266.

[20] J. Entzminger, J. N., C. A. Fowler, and W. J. Kenneally. JointSTARS and GMTI: past, present and future. *IEEE Transactions on Aerospace and Electronic Systems*, 35(2):748–761, Apr. 1999. ISSN 0018-9251. doi:10.1109/7.766956.

[21] B. Etkin. *Dynamcis of Atmospheric Flight*. John Wiley & Sons, Inc, 1972.

[22] A. Fosbury, T. Singh, J. Crassidis, and C. Springen. Ground target tracking using terrain information. In *10th International Conference on Information Fusion*, 2007. doi:10.1109/ICIF.2007.4408079.

[23] S. Gattein, B. Pannetier, and P. Vannoorenberghe. Analysis and integration of road projection methods for multiple ground target tracking. In *8th International Conference on Information Fusion*, volume 1, 2005. doi:10.1109/ICIF.2005.1591859.

[24] K. Gerlach. Outlier resistant adaptive matched filtering. *IEEE Transactions on Aerospace and Electronic Systems*, 38(3):885–901, July 2002. ISSN 0018-9251. doi:10.1109/TAES.2002.1039406.

[25] J. R. Guerci. *Space-Time Adaptive Processing for Radar*. Artech House Boston, 2003.

[26] R. Guo, Z. Qin, and C. Chen. An adaptive unscented particle filter for tracking ground maneuvering target. In *International Conference on Mechatronics and Automation*, pages 2138–2143, Harbin,, Aug. 2007. doi:10.1109/ICMA.2007.4303882.

[27] L. Hong, N. Cui, M. Pronobis, and S. Scott. Local motion feature aided ground moving target tracking with GMTI and HRR measurements. *IEEE Transactions on Automatic Control*, 50(1):127–133, 2005. ISSN 0018-9286. doi:10.1109/TAC.2004.841119(410) 50.

[28] L. Hong, N. Cui, M. Bakich, and J. Layne. Multirate interacting multiple model particle filter for terrain-based ground target tracking. *IEE Proceedings Control Theory and Applications*, 153(6):721–731, 2006.

[29] R. Horn, A. Nottensteiner, A. Reigber, J. Fischer, and R. Scheiber. F-SAR: DLR's new multi-frequency polarimetric airborne SAR. In *IEEE International Geoscience and Remote Sensing Symposium*, volume 2, pages II–902–II–905, July 2009. doi:10.1109/IGARSS.2009.5418244.

[30] G. J. Joyner. Measure of effectiveness for JSTARS ground moving target indicator: A value focused thinking approach. Master's thesis, Air Force Institute of Technology, 2011. URL `http://oai.dtic.mil/oai/oai?verb=getRecord&metadataPrefix=html&identifier=ADA541226`.

[31] K. Kastella and C. Kreucher. Multiple model nonlinear filtering for low signal ground target applications. *IEEE Transactions on Aerospace and Electronic Systems*, 41(2):549–564, Apr. 2005. ISSN 0018-9251. doi:10.1109/TAES.2005.1468747.

[32] T. Kirubarajan, Y. Bar-Shalom, K. Pattipati, and I. Kadar. Ground target tracking with variable structure IMM estimator. *IEEE Transactions on Aerospace and Electronic Systems*, 36(1):26–46, 2000. doi:10.1109/7.826310.

[33] Y. Kirubarajan, T.; Bar-Shalom. Tracking evasive move-stop-move targets with a GMTI radar using a VS-IMM estimator. *IEEE Transactions on Aerospace and Electronic Systems*, 39(3):1098–1103, July 2003. ISSN 0018-9251. doi:10.1109/TAES.2003.1238762.

[34] R. Klemm. *Principles of space-time adaptive processing*. The Institution of Electrical Engineers, London, 2002.

[35] R. Klemm, U. Nickel, and W. Koch. Tracking of multiple ground targets with adaptive monopulse radar. part i: The sensor. In *International Radar Symposium*, 2006. doi:10.1109/IRS.2006.4338064.

[36] W. Koch. On exploiting 'negative' sensor evidence for target tracking and sensor data fusion. *Information Fusion*, 8(1):28–39, 2007. ISSN 1566-2535. doi:DOI: 10.1016/j.inffus.2005.09.002. URL `http://www.sciencedirect.com/science/article/B6W76-4HDG9MG-2/2/27402be1032673273c41be9e2739defd`.

[37] W. Koch and R. Klemm. Ground target tracking with STAP radar. 148(3):173–185, June 2001. ISSN 1350-2395. doi:10.1049/ip-rsn:20010381.

[38] W. Koch, R. Klemm, and U. Nickel. Tracking of multiple ground moving targets with adaptive monopulse radar. part ii: The tracker. In *International Radar Symposium*, 2006. doi:10.1109/IRS.2006.4338065.

[39] R. Kohlleppel. Ground moving target tracking of PAMIR detections with a Gaussian Mixture-PHD filter. In *Proceedings International Radar Symposium*, pages 193 –198, 2011. URL `http://ieeexplore.ieee.org/stamp/stamp.jsp?tp=&arnumber=6042117&isnumber=6041611`.

[40] R. Kohlleppel. Ground moving target tracking with amplitude derived direction of arrival estimation accuracy information. In *9th European Conference on Synthetic Aperture Radar*, pages 267 –270, april 2012. URL `http://ieeexplore.ieee.org/stamp/stamp.jsp?tp=&arnumber=6217048&isnumber=6215928`.

[41] R. Kohlleppel. Ground target tracking with signal adaptive measurement error covariance matrix. In *Proceedings of the 2012 15th International Conference on Information Fusion*, pages 550–557, 2012. URL `http://ieeexplore.ieee.org/stamp/stamp.jsp?tp=&arnumber=6289850&isnumber=6289713`.

[42] O. Kreyenkamp and R. Klemm. Doppler compensation in forward-looking STAP radar. *IEE Proceedings Radar, Sonar and Navigation*, 148(5):253–258, oct 2001. ISSN 1350-2395. doi:10.1049/ip-rsn:20010557.

[43] X. Li and Y. Bar-Shalom. Stability evaluation and track life of the PDAF for tracking in clutter. *IEEE Transactions on Automatic Control*, 36(5):588–602, May 1991. ISSN 0018-9286. doi:10.1109/9.76364.

[44] X. R. Li and V. P. Jilkov. A survey of maneuvering target tracking—part iii: Measurement models. In *Proceedings of SPIE Conference on Signal and Data Processing of Small Targets, San Diego*, July-August 2001.

[45] L. Lin, Y. Bar-Shalom, and T. Kirubarajan. New assignment-based data association for tracking move-stop-move targets. *IEEE Transactions on Aerospace and Electronic Systems*, 40(2):714–725, 2004. ISSN 0018-9251. doi:10.1109/TAES.2004.1310016.

[46] D. Manolakis, V. Ingle, and S. Kogon. *Statistical and adaptive signal processing: spectral estimation, signal modeling, adaptive filtering, and array processing*. McGraw-Hill series in electrical and computer engineering. McGraw-Hill, 2000. ISBN 9780070400511.

[47] E. Mazor, A. Averbuch, Y. Bar-Shalom, and J. Dayan. Interacting multiple model methods in target tracking: a survey. *IEEE Transactions on Aerospace and Electronic Systems*, 34(1): 103–123, Jan. 1998. ISSN 0018-9251. doi:10.1109/7.640267.

[48] W. L. Melvin. Space-time adaptive radar performance in heterogeneous clutter. *IEEE Transactions on Aerospace and Electronic Systems*, 36(2):621–633, Apr. 2000. ISSN 0018-9251. doi:10.1109/7.845251.

[49] W. L. Melvin. A STAP overview. *IEEE Aerospace and Electronic Systems Magazine*, 19: 19–35, 2004. doi:10.1109/MAES.2004.1263229.

[50] W. L. Melvin and J. R. Guerci. Knowledge-aided signal processing: a new paradigm for radar and other advanced sensors. *IEEE Transactions on Aerospace and Electronic Systems*, 42(3):983–996, July 2006. ISSN 0018-9251. doi:10.1109/TAES.2006.248215.

[51] M. Mertens and R. Kohlleppel. Ground target tracking with experimental data of the PAMIR system. In *Proceedings of the 17th International Conference on Information Fusion, Salamanca*, 2014.

[52] J. H. Michels, B. Himed, and M. Rangaswamy. Robust STAP detection in a dense signal airborne radar environment. *Signal Processing*, 84(9):1625–1636, 2004. doi:10.1016/j.sigpro.2004.05.005.

[53] U. Nickel. Monopulse estimation with adaptive arrays. *Radar and Signal Processing, IEE Proceedings F*, 140(5):303–308, Oct 1993. ISSN 0956-375X. URL `http://ieeexplore.ieee.org/stamp/stamp.jsp?tp=&arnumber=238225&isnumber=6117`.

[54] U. Nickel. Performance analysis of space-time-adaptive monopulse. *Signal Processing*, 84(9): 1561–1579, September 2004. doi:10.1016/j.sigpro.2004.05.025.

[55] U. Nickel, E. Chaumette, and P. Larzabal. Statistical performance prediction of generalized monopulse estimation. *IEEE Transactions on Aerospace and Electronic Systems*, 47(1):381 –404, January 2011. ISSN 0018-9251. doi:10.1109/TAES.2011.5705682.

[56] A. V. Oppenheim and R. W. Schafer. *Discrete-Time Signal Processing*. Prentince Hall International, Inc., 1999.

[57] U. Orguner, T. Schon, and F. Gustafsson. Improved target tracking with road network information. In *IEEE Aerospace conference*, pages 1 –11, Mar. 2009. doi:10.1109/AERO.2009.4839490.

[58] G. Palubinskas and H. Runge. Radar signatures of a passenger car. *IEEE Geoscience and Remote Sensing Letters*, 4(4):644–648, Oct. 2007. ISSN 1545-598X. doi:10.1109/LGRS.2007.903074.

[59] B. Pannetier and M. Rombaut. Terrain obscuration managment for multiple ground target tracking. In *10th International Conference on Information Fusion*, 2007. doi:10.1109/ICIF.2007.4408065.

[60] B. Pannetier, K. Benameur, V. Nimier, and M. Rombaut. Ground moving target tracking with road constraint. volume 5429, pages 138–149. SPIE, 2004. doi:10.1117/12.543635. URL `http://link.aip.org/link/?PSI/5429/138/1`.

[61] M. Rangaswamy. Statistical analysis of the nonhomogeneity detector for non-Gaussian interference backgrounds. *IEEE Transactions on Signal Processing*, 53(6):2101–2111, 2005. doi:10.1109/TSP.2005.847843.

[62] D. Reid. An algorithm for tracking multiple targets. *IEEE Transactions on Automatic Control*, 24(6):843 – 854, dec 1979. ISSN 0018-9286. doi:10.1109/TAC.1979.1102177.

[63] A. Reigber, M. Jager, J. Fischer, R. Horn, R. Scheiber, P. Prats, and A. Nottensteiner. Performance of the L- and P-band subsystems of the F-SAR airborne SAR instrument. In *9th European Conference on Synthetic Aperture Radar*, pages 286–289, April 2012. URL `http://ieeexplore.ieee.org/stamp/stamp.jsp?tp=&arnumber=6217058&isnumber=6215928`.

[64] F. C. Robey, D. R. Fuhrmann, E. J. Kelly, and R. Nitzberg. A CFAR adaptive matched filter detector. *IEEE Transactions on Aerospace and Electronic Systems*, 28(1):208–216, Jan. 1992. ISSN 0018-9251. doi:10.1109/7.135446.

[65] Y. Ruan and L. Hong. Feature-aided tracking with GMTI and HRR measurements via mixture density estimation. *IEE Proceedings Control Theory and Applications*, 153(3):342 – 356, May 2006. ISSN 1350-2379. doi:10.1049/ip-cta:20045099.

[66] O. Ruault du Plessis, J. Nouvel, R. Baque, G. Bonin, P. Dreuillet, C. Coulombeix, and H. Oriot. ONERA SAR facilities. *IEEE Aerospace and Electronic Systems Magazine*, 26(11): 24–30, Nov 2011. ISSN 0885-8985. doi:10.1109/MAES.2011.6070278.

[67] M. Rutten, N. Gordon, and S. Maskell. Recursive track-before-detect with target amplitude fluctuations. *IEE Proceedings Radar, Sonar and Navigation*, 152(5):345–352, 2005. doi:10.1049/ip-rsn:20045041.

[68] W. W. Shrader and V. Gregers-Hansen. MTI radar. In *Radar Hanbook*, chapter 2, pages 2.1–2.102. McGraw-Hill, 2008.

[69] R. Singer. Estimating optimal tracking filter performance for manned maneuvering targets. *IEEE Transactions on Aerospace and Electronic Systems*, AES-6(4):473 –483, July 1970. ISSN 0018-9251. doi:10.1109/TAES.1970.310128.

[70] M. Skolnik. An introduction and overview of radar. In *Radar Handbook*, chapter 1, pages 1.1–1.24. McGraw-Hill, 2008.

[71] M. I. Skolnik. Radar information from the partial derivatives of the echo signal phase from a point scatterer. Technical report, Naval Research Lab Washington DC, 1988. URL `http://oai.dtic.mil/oai/oai?verb=getRecord&metadataPrefix=html&identifier=ADA193402`.

[72] M. I. Skolnik, editor. *Radar Handbook*. McGraw-Hill Companies, New York, 2nd edition, 1990.

[73] M. I. Skolnik. *Introduction to Radar*. McGraw-Hill, Singapore, 3rd edition, 2001.

[74] A. R. Smith. Color gamut transform pairs. In *Proceedings of the 5th annual conference on Computer graphics and interactive techniques*, 1978. doi:10.1145/800248.807361.

[75] J. P. Stralka and W. G. Fedarko. Pulse doppler radar. In *Radar Handbook*, chapter 4, pages 4.1–4.53. McGraw-Hill, 2008.

[76] R. L. Streit, M. L. Graham, and M. J. Walsh. Multitarget tracking of distributed targets using histogram-PMHT. *Digital Signal Processing*, 12(2-3):394–404, 2002. doi:10.1006/dspr.2002.0440.

[77] H. L. V. Trees. *Detection, Estimation and Modulation Theory*. John Wiley & Sons, Inc., 1968.

[78] M. Ulmke, O. Erdinc, and P. Willett. Gaussian mixture cardinalized PHD filter for ground moving target tracking. In *10th International Conference on Information Fusion*, July 2007. doi:10.1109/ICIF.2007.4408105.

[79] G. Van Keuk and S. S. Blackman. On phased-array radar tracking and parameter control. *IEEE Transactions on Aerospace and Electronic Systems*, 29(1):186–194, 1993. doi:10.1109/7.249124.

[80] B. N. Vo and W. K. Ma. The Gaussian Mixture Probability Hypothesis Density Filter. *IEEE Transactions on Signal Processing*, 54(11):4091–4104, Nov. 2006. ISSN 1053-587X. doi:10.1109/TSP.2006.881190.

[81] B. N. Vo, S. Singh, and A. Doucet. Sequential Monte Carlo methods for multitarget filtering with random finite sets. *IEEE Transactions on Aerospace and Electronic Systems*, 41(4): 1224–1245, Oct. 2005. ISSN 0018-9251. doi:10.1109/TAES.2005.1561884.

[82] B.-N. Vo, B.-T. Vo, N.-T. Pham, and D. Suter. Joint detection and estimation of multiple objects from image observations. *IEEE Transactions on Signal Processing*, 58(10):5129 –5141, Oct. 2010. ISSN 1053-587X. doi:10.1109/TSP.2010.2050482.

[83] J. Ward. Space-time adaptive processing for airborne radar. Technical report, Lincoln Laboratory, Massachusetts Institute of Technology, 1994.

[84] T. A. Weil and M. Skolnik. The radar transmitter. In *Radar Handbook*, chapter 10, pages 10.1–10.30. McGraw-Hill, 2008.

[85] D. Zei, F. Mele, P. Tellini, A. Montanari, A. Fusaroli, P. Di Grazia, and G. Annessi. Real time MTI STAP first results from SOSTAR-X flight trials. In *IEEE Radar Conference*, pages 1 –6, May 2008. doi:10.1109/RADAR.2008.4720858.